

Modelling the energy balance of high altitude glacierised basins in the Central Andes

Javier González Corripio

Doctor of Philosophy
The University of Edinburgh
2002

Abstract

Water as a result of snow and glacier melt is an important resource in the Central Andes of Chile and Argentina, which in terms of precipitation are close to climatic deserts, yet they support large populations and a rich agriculture. In spite of this, little is known of the processes at play and the variability over time. In particular, the specific mechanisms of energy balance and melt on high altitude glaciers in this region have been the subject of limited research. Another particularity of the region is the ablation of most of the snow cover into penitentes or pinnacles of snow and ice about 2 m in height.

Meteorological data from one automatic weather station installed on two different glaciers at 3335 m and 4667 m in the Chilean Central Andes demonstrate the relative importance of turbulent heat transfer in the energy balance equation, accounting for 10 to 20% of the net energy balance. Intense evaporation, together with effective radiative cooling, dew point well below freezing and intense solar radiation favour differential ablation of the snow surface, which results in the formation of snow penitentes, these unique forms result in a further modification of the energy balance. Stable conditions and a clear atmosphere permit effective incorporation of fully distributed solar radiative models with good results. Melt rates are compared with theoretical models, showing that while evaporation is enhanced in the Andes, surface morphology decreases total ablation. Modelling work suggests that penitentes enhance conservation of snow cover and the consequences of their loss, due to changes in the initial climatic conditions, might be increased ablation over the whole season, decreased glacier mass balance and faster depletion of water resources.

To implement distributed energy balance models both at the basin scale and at the microtopography scale, two additional tools were developed. One is a set of algorithms for the computation of terrain parameters from digital elevation models (DEMs) suitable for rough topography. These algorithms, together with those developed for shading and insolation, permit the treatment of overhanging surfaces, such as the penitentes. Another tool is a flexible and inexpensive remote sensing tool for albedo estimation using conventional terrestrial photography. The technique consists in georeferencing oblique photographs to a digital elevation model (DEM), defining a mapping function between the pixel of the image and the corresponding cell on the DEM. Once the image is georeferenced, the reflectance values recorded by the film or digital camera are corrected for topographic and atmospheric influences and for the effect of the photographic process. By comparing these to a surface of known albedo, the spatial distribution of albedos is calculated. The validation of the technique on Alpine terrain shows good agreement with measured values.

Acknowledgements

This work was possible thanks to a Scholarship from the Carnegie Trust for the Universities of Scotland. Field work in the Andes was possible thanks to a research grant from the Carnegie Trust. Fieldwork in the French Alps was supported by a grant from Kodak UK, research and development. Field work in the Swiss Alps was possible thanks to the logistical and economical support of the Swiss Federal Institute of Technology, ETH Zürich. I would like to thank Research Systems Inc. for their support with IDL software.

I am grateful to the dedication of my supervisors: Ross Purves who improved the quality of this work by his sharp and accurate comments, even when he was a thousand miles away, and David Sugden and Nick Hulton who bore the hassle of the last minute race against time.

Field work in the Andes was greatly improved thanks to dedicated field assistants and superb mountaineers Cameron Thomson and Carlitos Gómez. It would be difficult to forget the hospitality of Jessica and Felipe Orrego and their family, the support of Alejandra Tovar and many other friends in that great country. Invaluable help was given by the Laboratorio de Glaciología, University of Chile, especially by Andrés Rivera and Jorge Quinteros. The Arolla team: Uli Strasser, Francesca Pellicciotti, Ben Brock, Paolo Burlando and Martin Funk made the best of my time in the Alps. I am indebted to Chamonix mountain guide Ricardo Mora and his family for their hospitality in the Alps, and for looking at ways of improving the access to the field sites, always by the most difficult, vertical and enjoyable route.

I would like to thank the Chamonix Meteorological Office for providing meteorological data as well as the Chilean Dirección General de Aguas, and last but not least, to all those in Geography that made my job easier, specially by ‘pushing’ me into the local pub after long hours at the computer to keep the balance between modelling and fieldwork.

DECLARATION

I declare that this thesis has been composed by myself and the work within it is my own, except where otherwise indicated.

Javier González Corripio

2002

Nomenclature

Symbol	Definition
F_t	correction term for the angle of incidence of sun on the slope
F_{ms}	diffuse radiation due to multiple scattering between ground and sky
F_{sk}	diffuse radiation from the sky
G	acceleration due to gravity 9.8066 ms^{-2}
H	sensible turbulent flux
I_d	diffuse solar irradiance (Wm^2)
I_i	incoming global solar radiation flux (Wm^2)
I_n	direct normal solar irradiance (Wm^2)
I_r	reflected global solar radiation flux
I_{da}	aerosol-scattered diffuse irradiance after the first pass through the atmosphere
I_{dm}	diffuse irradiance from multip[le reflections between the earth and the atmosphere
I_{dr}	Rayleigh-scattered diffuse irradiance after the first pass through the atmosphere
I_{sc}	solar constant (mean value: 1367 Wm^2)
L	Obukhov's stability length
$L \downarrow$	long-wave downward radiative flux
$L \uparrow$	long-wave upward radiative flux
L_s	latent heat of sublimation
$L_s E$	latent turbulent heat flux
L_v	latent heat of evaporation
$L_v E$	latent turbulent heat flux
M_d	molecular weight of dry air 28.966
P_0	standard sea-level atmospheric pressure $1.013250e5 \text{ Pa}$
Q_s	heat diffusion within the snow pack
R	mean distance Sun - Earth ($1.496 \times 10^{11} \text{ m}$)
$(R/R_0)^2$	reciprocal of the square of the radius vector of the earth
R	reflected radiation flux
R^*	universal gas constant $8.31432 \text{ Jmol}^{-1} \text{ K}^{-1}$
R_0	actual distance Sun - Earth
R_n	pixel reflectance
R_{ref}	reference pixel reflectance
SW	short-wave radiative flux
T_0	standard sea-level temperature 288.15 K
T_a	air temperature at screen level
T_s	snow temperature
Ω	solid angle of a receptor's pixel field of view

$\Psi_{sh}(\zeta)$	stability correction for heat
$\Psi_{sm}(\zeta)$	stability correction for momentum
$\Psi_{sq}(\zeta)$	stability correction for water vapour
α	albedo
α_g	ground albedo
α_{sk}	atmospheric albedo
α_s	snow albedo
\mathbf{C}	camera coordinates
\mathbf{T}	target coordinates
δ	solar declination angle
ℓ	grid cell length
γ	$= \pi/2 - \varphi$, angle between topocentric Z -axis (along the earth radius at the observer position) and the axis of rotation of the earth
λ	wavelength
μ	coefficient of dynamic viscosity for air (1.78×10^{-5} Kg m $^{-1}$ s $^{-1}$)
ν	kinematic viscosity of air
ω	hour angle, zero at noon and positive before noon
ω_v	max mixing ratio for water vapour
ϕ	azimuth angle or aspect
ϕ	half the vertical field of view of the camera
ρ	density
ρ	density of moist air
ρ_d	density of dry air
ρ_v	density of water vapour
τ_a	transmittance function due to aerosols
τ_g	transmittance function due to uniformly mixed gases
τ_o	transmittance function due to ozone
τ_r	transmittance function for Rayleigh scattering
τ_w	transmittance function due to water vapour
$\tau_{Rey.}$	Reynolds stress
τ_i	transmittance function through the atmosphere
τ_t	transmittance functions through the atmosphere from the camera to the target
θ	solar zenith angle (radians)
θ_a	potential temperature of air at screen level
θ_s	potential temperature at the snow surface
θ_s	angle between sun and normal to surface or relative solar zenith angle
$\hat{\mathbf{n}}$	unit vector in the direction of \mathbf{n}
$\hat{\mathbf{s}}$	unit vector in the direction of the sun
$\hat{\mathbf{s}}_0$	unit vector in the direction of the sun at noon LAT
φ	half the horizontal field of view of the camera

φ	latitude
ς	slope gradient
n	vector normal to the grid cell surface
\vec{N}	unit vector in the viewing direction
\vec{U}	near horizontal unit vector perpendicular to \vec{N}
\vec{V}	near vertical unit vector perpendicular to \vec{N}
ζ	solar zenith angle (degrees)
a_v	ratio of eddy diffusivity to eddy viscosity for water vapour
a_h	ratio of eddy diffusivity to eddy viscosity for heat
a_m	ratio of eddy diffusivity to eddy viscosity for momentum
c_p	specific heat of dry air at constant pressure ($= 1004.67 \text{ JKg}^{-1}\text{K}^{-1}$)
d_0	zero-plane displacement
f	focal length
f_{df}	ratio of diffuse to total incoming radiation
f_{rt}	ratio of direct to total incoming radiation
f_{sv}	ratio of snow covered to total visible surrounding terrain
f_s	ratio of snow covered to total surrounding terrain
f_v	skyview factor
g	acceleration due to gravity 9.8066 ms^{-2}
h	film height (24 mm for 35 m photography)
k	von Karman constant ($= 0.40$)
q_a	specific humidity of air at screen level
q_s	specific humidity at the snow surface
r	mean earth's radius ($= 6.356766 \times 10^6 \text{ m}$)
r_0	effective radius of the earth at a specific latitude (for calculating geopotential altitude)
u_*	friction velocity
w	film width (36 mm for 35 m photography)
w_p	precipitable water, cm
z	altitude above sea level
z_0	roughness length for momentum
$z_0 h$	roughness length for heat
$z_0 q$	roughness length for water vapour
z_q	humidity measurement height
z_t	temperature measurement height
z_u	wind measurement height

Contents

1	Introduction	1
1.1	Aim	1
1.2	Background and rationale	2
1.3	The problems	3
1.4	Plan of work	3
2	Site of study and methodology	6
2.1	The Dry Andes: climatic setting	6
2.2	Economic and social importance of glaciers in the region	8
2.3	Snow and ice penitentes	10
2.3.1	The origin of penitentes	12
2.4	Methodology	13
2.5	Instrumentation and data recording	16
3	Modelling the energy balance at the snow surface	18
3.1	Introduction	18
3.2	Short-wave radiation	19
3.2.1	Background theory	19

3.2.2	Bird and Hulstrom (Iqbal) parametric model	21
3.2.3	Diffuse reflected radiation	27
3.3	Long–Wave radiation	27
3.4	Turbulent heat transfer	30
3.4.1	Background theory	31
3.5	Internal heat fluxes	35
3.6	Temperature fluctuation	35
3.7	Model validation and applicability	37
3.7.1	Short–wave validation	37
3.7.2	Long–wave validation	37
3.7.3	Snow temperature model validation	39
3.7.4	Net energy balance and melt validation	41
4	Modelling solar radiation over complex topography: I DEM tools	45
4.1	Introduction	45
4.2	Vector defining an inclined surface	46
4.3	Comparison with other methods of calculating slope	52
4.4	Vector defining the position of the sun	55
4.4.1	Angle of incidence of the sun on inclined surfaces	58
4.5	Shaded relief	60
4.6	Sky view factor	62
5	Modelling solar radiation over complex topography: II. Albedo estimation using terrestrial photography	65
5.1	Aim	65
5.2	Introduction	65

5.3	Methodology	66
5.3.1	Georeferencing terrestrial photography	67
5.3.2	Conversion from reflectance to albedo	76
5.3.3	Data format	81
5.4	Experimental set up	82
5.5	Results and discussion	84
6	Model implementation and results	89
6.1	Boundary and initial conditions	91
6.2	Input data	91
6.2.1	Elevation data	100
6.3	Distributed energy balance model	100
6.3.1	Distributed modelling of short-wave radiation	100
6.3.2	Distributed modelling of long-wave radiation	102
6.3.3	Distributed modelling of turbulent fluxes	102
6.4	Sensitivity analysis	105
6.4.1	short-wave radiation model sensitivity	105
6.4.2	Long-wave radiation model sensitivity	107
6.4.3	Turbulent heat fluxes model sensitivity	108
6.5	Energy balance at the microtopographical scale	109
6.5.1	Penitentes digital elevation model	110
6.6	Results and discussion	112
6.6.1	Effect of topography	116
6.6.2	Effect of penitentes	117
6.7	Response under changing climatic conditions	124

7 Conclusions and future work	128
7.1 Future work	129
A Appendix	132

List of Tables

2.1	Instruments, range and accuracy of meteorological measurements.	17
3.1	Values of the coefficients in the polynomials (equation: 3.55) that predict z_0/z for temperature and water vapour (Andreas 1987) for smooth, transition and rough surfaces. . .	35
4.1	Correlation between slopes derived mathematically from a synthetic surface and those calculated using the vector algebra algorithm and a 3x3 kernel algorithm.	53
6.1	Recorded meteorological variables and calculated dew point.	93
6.2	Energy balance partition for flat snow and penitentes (Wm^{-2})	120
6.3	Modelled melt and evaporation on flat snow and penitente snow at Loma Larga, 4667m on day 37.	121

List of Figures

1.1	Penitentes field on the middle section of the Loma Larga glacier, at about 4500 m a.s.l. The whole glacier above 4000 m is covered in these snow pinnacles, which restricts the movement of mountaineers and researchers and alters the surface energy balance of the glacier.	4
1.2	Penitentes about 2 m in height on a clean snow field at 4300 m a.s.l. in the Central Andes.	5
2.1	The area of study in the Chilean Andes, about 33° S 70° W. Map source: South America map from the GLOBE project, NOAA, NGDC.	7
2.2	Aster image of the Juncal Norte glacier. The near infrared band was the only one that was not completely saturated in the upper section of the glacier covered in snow with high albedo. The location of the AWS is indicated by an arrow, the image correspond to a different time of the year than the survey, and the lower section of the glacier is free of snow. Data from NASA EOS Data Gateway: http://edcdaac.usgs.gov/aster/ast_11a.html	8
2.3	Aster image of the Loma Larga glacier. The location of the AWS is indicated by an arrow, the large dam to the northwest of the image is the Rio Yeso dam, the main water reservoir supplying Santiago de Chile.	9
2.4	Surface sea level pressure averaged from December 2000 to February 2001 and relative humidity reanalysis data. The image is a visualisation of NCEP/NCAR reanalysis data provided by the NOAA-CIRES Climate Diagnostics Center, Boulder, Colorado, from their web site at http://www.cdc.noaa.gov/ .	9
2.5	Clear skies short wave downward flux and mean wind speed averaged from December 2000 to February 2001. NCEP/NCAR reanalysis data (se Figure 2.4).	10

2.6	Penitentes about 2 m in height on a snow field at about 4300 m a.s.l. The photograph is taken looking west, and shows the inclination of the penitentes toward the north. Note that for this latitude and time of the year, the sun is due west at 17:10h, the approximate time at which the photograph was taken, with an elevation angle of 44°.	11
2.7	Ice blocks sculpted into pinnacles, probably by the action of the sun rays, at Loma larga glacier, about 3500 m a.s.l. The prominent pinnacle in the centre is about 10 m height.	11
2.8	Schematic representation of the feedback mechanisms that enhance penitentes growth. Solar radiation is more intense at the bottom of penitentes due to multiple reflections, net long-wave radiation decreases with height due to larger sky visibility and net turbulent fluxes are more negative at the peaks where sublimation prevails producing intense cooling. In this way peaks survive and troughs are deepened.	13
2.9	Micropenitentes or initial stage in the formation of penitentes at different locations in the Central Andes. Darker areas correspond to lower reflectance in wetter areas or because lower light interception, as in the steep walls (upper right figure).	14
2.10	Digitally enhanced image of a small area covered in micropenitentes a few cm deep. The dark square is an A4 photographic greyscale card (21x29cm). The darker snow on the top of pinnacles and blades is a thin crust of bonded snow grains but no dirt.	15
2.11	Large suncups on Loma Larga glacier at about 3900 m, probably resulting from the decay of penitentes formed earlier in the ablation season.	15
3.1	schematic representation of the effect of the earth's atmosphere on the short-wave radiation from the sun. The attenuation, absorption transmittance and scattering, either forward to ground, back to space and multiple scattering are formidable problems to solve for a real atmosphere. An empirical solution with satisfactory results will be presented in the following sections. Adapted from Iqbal (1983).	19
3.2	Comparison between modelled and measured radiation spectral distribution outside the atmosphere and on the ground for two sites near Edinburgh, 55.92 °N, 3.17°W, in summer. The modelled values are the output of the radiative transfer model MODTRAN using estimated visibility and incorporated model atmospheres, measurements were performed by the author with a GER 3700 spectroradiometer.	22
3.3	Distribution of skylight and upward radiation for three different surface albedos A, from Coulson (1959) as cited by Paltridge and Platt (1976, p. 114). The sun's elevation is 53°, its position is given by the symbol $\leftarrow \odot$. Right figure is sky luminance distribution as quoted by Robison (1966), cited by Paltridge and Platt (1976, p. 115)	26

3.4	Measured and modelled short-wave radiation at the Haut Glacier d'Arolla, 2900m a.s.l., Swiss Alps, on a typical clear day. Diffuse radiation is separated into that from sky and that from surrounding slopes. The fit is better than the accuracy of the pyranometer (10%). 7 LINES ONLY 6 LEGEND	38
3.5	Measured and modelled short-wave radiation at Loma Larga glacier, 4667 m a.s.l. Diffuse radiation is separated into that from sky and that from surrounding slopes. For the aerosol transmittance, visibility is assumed to be 100 km through the whole day, whereas for other transmittances, meteorological variables recorded at 10 minute interval were used. The fit is better than the accuracy of the pyranometer (10%). Cast shadows and the fraction of shaded surrounding slopes are not computed at this stage.	38
3.6	Modelled and measured net long-wave radiation for a 2-week period in summer 2001 at the Haut Glacier d'Arolla, Swiss Alps. Note that the pronounced troughs in measured long-wave are likely to be instrumental artifacts, as explained in the text, and that values are modelled only for clear skies, so peaks under cloudy conditions are not reproduced. The average difference between modelled and measured values under cloudless skies, after discharging near sunset and near sunrise values, is less than 1%.	39
3.7	Comparison between modelled and measured temperatures on the surface of Loma Larga glacier, 4667 m.a.s.l. The surface was covered in snow penitentes and the measurement sites at T1 (closer to the bottom of penitentes) and T2 (closer to the penitentes' peak) had a slightly different net energy flux. Site T2 was likely to undergo a more intense radiative cooling. Initial modelled temperature was set to -73.15 °C (200 K) to assess the stability of the model and the rapid convergence of modelled values to measured ones.	40
3.8	Comparison between modelled and measured temperatures on the surface of Loma Larga glacier, as in Figure 3.7, but modelled for the uppermost surface layer, about 2 cm depth.	40
3.9	Energy fluxes on a clear day on Loma Larga glacier, 4667 m a.s.l. DOY 37, 6th of February. Note the increasing albedo in the afternoon, when the apparent position of the sun changes from north to south (see Figure 3.10), an explanatory hypothesis is given in the text.	42
3.10	Solar path for the day 37 (6 February, 2001) at 33°S, 10°W. The sun crosses to the southern apparent position at about 18:00, when the recorded albedo starts to increase (see text for tentative explanation). I have made the IDL code for plotting the solar path available at the IDL user contributed library at www.rsinc.com/	42

3.11	Energy balance components, modelled melt and measured snow depth at the Haut Glacier d’Arolla for a 2 week period in July 2001.	44
3.12	Energy balance components, modelled melt and measured snow lowering from ablation stakes on Juncal Norte glacier, 3035 m a.s.l. for a 11-day period in November–December, 2000. Note the maximum values of turbulent heat fluxes that correspond to wind speeds higher than 10ms^{-1} and relative humidity lower than 20%.	44
4.1	Vector normal to grid surface	47
4.2	Relative grey-scale representation of the values of coordinates x, y, z for the vector normal to surface in a digital elevation model of the Mont Blanc Massif. To make the coordinates agree with solar position convention, white is a high positive eastwards, southwards and upward component. The grid is 338 columns by 444 rows, with a resolution of 50 m (16.9 x 22.2 km). The inverted Y-shaped feature in the lower centre is the Mer de Glace, the largest glacier in the French Alps. The sharp border on the right and lower areas is the national boundary plus a buffer area, as the relief of Italy and Switzerland is not shown, and the main Valley running NE to SW is the Valley of Chamonix. North is up.	50
4.3	Relative grey-scale representation of surface aspects in the Mont Blanc DEM. White is northeast and black is southwest.	51
4.4	Synthetic DEM, a surface of highly variable relief generated by Equation 4.6. Z values are in the range ± 1.07474 , horizontal cell spacing is $2\pi/100$ units.	52
4.5	Scattergrams of slope values generated with the algorithm described in this paper and a 3x3 kernel algorithm compared to the slopes derived mathematically from a synthetic surface (Figure 4.4 and Equation 4.8).	53
4.6	Gray-scale representation of the spatial distribution of errors in the computation of slope for the synthetic DEM. a) is between mathematically generated slopes and vector algorithm, b) is the difference with the 3x3 kernel algorithm. Note that the location of errors is similar but these are accentuated in the right image. Values range from -2.91 to 3.78 and from -8.19 to 8.12. Neutral gray is no error, darker is overestimation and whiter is underestimation of slope.	54

4.7	Rotation of the topocentric coordinate system XYZ an angle ω , from time t_0 to time t_1 . This movement can be decomposed in three rotations: i) rotation around axis X an angle $\gamma = \pi/2 - \varphi$, where φ is the latitude; ii) rotation around axis Z an angle ω ; and iii) rotation back around axis X an angle $-\gamma$. Translation is ignored as the maximum parallax of the earth is 8.8 seconds of arc (Nautical Almanac Office 1974), and therefore negligible for most solar radiation applications.	55
4.8	Color coded map of insolation received at the Mont Blanc Massif at the spring equinox. Incoming solar radiation is modelled for clear skies at 15 minutes interval from sunrise to sunset following Iqbal's (1983) parametric model. Incident solar radiation for every grid cell is evaluated according to the angle of incidence of the sun and the shading of surrounding terrain. Diffuse incoming solar radiation is evaluated according to the hemispherical portion of sky visible from every grid cell. Reflected radiation from surrounded terrain is not computed. Values range from 2.2 to 29.96 MJm^{-2}	59
4.9	Hillshading. As the sun can be considered as a point source at infinite distance, all solar rays are parallel and cross the plane SP perpendicularly. By checking the projection of a grid cell over this plane we can determine whether a point is in the sun or in the shade of a previous cell. In the figure the projection of P_1 , that is, P'_1 has a value higher than any previous one (as it is the first point to be scanned), so it is in the sun. Similarly for P'_2 and P'_3 , however, P'_4 has a lower value than P'_3 and therefore is in its shadow. The projection of a point P'_i on the 'solar plane' SP is the dot product of the vector \overrightarrow{OP}_i and the vector s_p , which is a unit vector perpendicular to s , the unit vector in the direction of the sun.	60
4.10	Hillshading of Mont Blanc DEM. The incident light is modified according to the cosine angle of incidence of the sun on the slope. A minimum illuminance of 18% is introduced to account for diffuse radiation. Illumination is from the northwest at 45^0 elevation.	61
4.11	Sky view factor: the fraction of sky visible from any point is evaluated as the ratio of the projected area of the visible hemisphere to the area of the base of a unit sphere. The figure illustrates the calculation for a given cell $z_{i,j}$ with visibility obstructed by neighbouring cells $z_{m,n}$ and $z_{p,q}$, where the portion of visible sky is the shaded area. The sky view factor will be $r^2/R^2 = r^2 = \sin^2 \bar{\theta}$, where $\bar{\theta}$ is the average zenithal angle for all azimuth directions. Note that for clarity in the illustration the projected visible surface area is selected only for two points and not for the average, thus the resulting geometry is an ellipse instead of a circle.	63

4.12	Relative grey-scale representation of sky view factor for the Mont Blanc DEM. Dark areas have lower sky visibility, while white ones, such as higher ridges, have unobstructed visibility of the upper hemisphere. Values range from 0.5 to 1, with the lowest value corresponding to the steepest slope, 81° , on the western face of Les Drus, centre right of the image.	64
5.1	Simplified scheme of image formation in the camera. ϕ is half the angle of the vertical field of view, w is the width of the film (36 mm) and h is its height (24 mm).	67
5.2	Change from world to camera coordinate system. DEM coordinates are referenced to the main reference system XYZ in the figure, while the image taken by camera at point C is referenced to the coordinate system defined by the three orthogonal unit vectors $\vec{U} \vec{N} \vec{V}$. \vec{N} is the viewing direction of the camera, calculated from the camera and target positions. \vec{U} is the unit vector of the cross product of \vec{N} and \vec{N}_{xy} , which is the projection of \vec{N} on the horizontal plane. \vec{V} is $\vec{U} \times \vec{N}$. See Section 5.3.1.	69
5.3	Simplified geometry of the perspective projection for one single point. A point P in tridimensional space is mapped (projected) to a point P' in a two-dimensional viewing window representing the camera film. The distance f to the origin of coordinates C in camera coordinate system is equivalent to the lens focal length. This perspective projection produces a virtual photograph of the DEM, which is then mapped to the pixels in the photograph. By conserving the link between P and P' the information in the flat two dimensional photograph can be mapped to the original three-dimensional points in the DEM. See Section 5.3.1 for details.	70
5.4	Perspective projection of a DEM of the lower section of the Mer de Glace, Mont Blanc. Every dot represent a grid cell after a viewing transformation and perspective projection. The frame is the camera field of view. Axis units are pixels in the original photograph: 720x480 within the frame, at a resolution of 200 dots per cm.	71
5.5	Super imposition of the perspective projection of a DEM of the Mer de Glace glacier (Figure 5.4) over a photograph of the area. Red dots are the perspective projections of the original DEM grid cells, green dots are ground control points. The photograph is taken from the Refuge du Requin looking east-northeast.	71
5.6	Flow chart of the georeferencing process.	72
5.7	Georeferenced image of the lower middle section of the Mer de Glace. Reflectance values are extracted from photograph in Figure 5.5. Black areas (holes) are not visible from the camera position.	73

5.8	Detail of lower section of Mer de Glace. Georeferenced image using a resampled 10 m resolution DEM to show the potential of this technique for landform and pattern recognition. Note the dark and white ogives or Forbes bands on the glacier, which are characteristic of the lower tongue of the Mer de Glace.	73
5.9	Example of mismatch between the perspective projection of the DEM (dotted line) and the photographic image (continuous line) due to roll of the camera. The correction for this displacement is explained in Section 5.3.1	75
5.10	Digital Number (DN) versus reflectance. The output of the scanned photographic image is conditioned by the whole photographic process, camera, lenses and scanner characteristics. In order to relate the input light to the output values an empirical approach was followed. Solid line shows the relationship between input light and output DN values and dashed line is a regression fit excluding areas of very low reflectance. The regression is then linear, and the exclusion of very low (dark) values is justified as we are dealing with snow, which has high reflectance values, in the region where the function is linear.	81
5.11	Albedometer setting. The white oval, above and left the camera tripod is the albedometer, made up of two Kipp & Zonen opposed pyranometers. The output is read in two voltmeters connected at the extreme of the cable, held by the skier-operator in the image.	82
5.12	Map of the area of study in the French Alps, $45^{\circ} 50' N$, $7^{\circ} E$. Mer de Glace glacier is the inverted Y-shaped glacier in the lower centre of the image. Coloured dots are albedo measurements. The DEM only covers the French side of the area, with no values for Italy and Switzerland.	83
5.13	Colour coded composite map of albedo values derived from three georeferenced photographs of the Mer de Glace. Coloured crosses are measured values, a first inspection reveals good agreement between measured and estimated values. Actual values are plotted in Figure 5.15. The inset is a detail of the lower section of the Mer de Glace, corresponding to Figure 5.8, showing the albedo variability among the glacier ogives.	86
5.14	Measured versus estimated albedo values for areas in Figure 5.13. The maximum difference is 6.5%, while the average is 2%, which is less than the accuracy of the albedometer. Measured points on the X-axis are ordered from west to east.	87
5.15	Inter-pixel variability of the albedo values for three arbitrary transects on the upper, medium and lower (ice covered) areas of the glacier. High variability in a relatively small space is a large source of errors in the photography derived albedos.	87

5.16	Relief representation of a georeferenced photograph taken from the north of Haut Glacier d'Arolla looking south, wrapped over the digital elevation model of the area.	88
5.17	Evolution of snow cover during from 25 May 2001 to 25 July 2001 on the Haut Glacier d'Arolla, Swiss Alps. Note that the image has enough resolution to detect small avalanches on the rightmost section of the central image.	88
6.1	Schematic flow diagram of the energy balance modelling. Albedo in brackets indicates an optional input when it is available or an estimation or extrapolation when direct or derived measurements are not available.	90
6.2	Air temperature measured on Juncal Norte glacier at 3335 m.	94
6.3	Air temperature measured on Loma Larga glacier at 4667 m.	94
6.4	Relative humidity measured on Juncal Norte glacier at 3335 m.	95
6.5	Relative humidity measured on Loma Larga glacier at 4667 m.	95
6.6	Dew point calculated according to Jacobson (1999) 2.56 on Juncal Norte glacier at 3335 m.	96
6.7	Dew point calculated according to Jacobson (1999) 2.56 on Loma Larga glacier at 4667 m.	96
6.8	Wind speed measured on Juncal Norte glacier at 3335 m.	97
6.9	Wind speed measured on Loma Larga glacier at 4667 m.	97
6.10	Wind rose of relative frequency for all the measuring period (day 335 to 346) on Juncal Norte glacier at 3335 m. Grey lines indicate wind mean speed for every radial sector. The maximum frequency follows the orientation of the lower section of glacier, as can be seen in Figure 2.2	98
6.11	Wind rose of relative frequency for all the measuring period (day 22 to 53) on Loma Larga glacier at 4667 m. Grey lines indicate wind mean speed for every radial sector. The main orientation of the glacier is East–West and the predominant winds in this case seems to be from the valley, the northeast component of the glacier winds may be influenced by the more extent snow cover of the south-facing slopes, to the north of the AWS.	98
6.12	Shortwave incoming and outgoing solar radiation measured on Juncal Norte glacier at 3335 m.	99

6.13 Shortwave incoming and outgoing solar radiation measured on Loma Larga glacier at 4667 m.	99
6.14 Relief shading and contour map of the Loma Larga area. The AWS is indicated by the red flag and the red star shows Cerro Loma Larga, at 5404 m. Projection is UTM, grids are 2 km apart, as indicated by the labels. A close inspection of the DEM reveals artifacts following the contour levels, generated by the interpolating algorithm. Note as well the spurious data on grid 408000,6268000 (circled), due to a missing contour value in the original map, which also shows large blank areas, probably due to poor definition of steep regions in the original aerial photograph. For these reasons detailed conclusions derived from the analysis of digital elevation models in the area should be treated with care.	101
6.15 Variation of short-wave atmospheric direct and diffuse radiation with altitude, independent of topography. The line shows the modelled values at 1 m interval, while the equation shows the best linear fit and correlation coefficient.	102
6.16 Comparison between modelled and measured temperatures on the surface of Loma Larga glacier, 4667 m. using Greuell and Konzelmann's (1994) modified formulation. Compared with Figure 3.7, here minimum values are slightly lower, but realistic, and the convergence of the model to measured values is slower than using the Monin-Obukhov length. Net short wave radiation (not to scale) is plotted to show day and night periods	104
6.17 Modelled variation of incoming solar radiation, direct and diffuse components, for increasing altitude (a) and for increasing visibility(b).	106
6.18 Modelled variation of the direct and diffuse components of incoming solar radiation for changing values of O ₃ and relative humidity	106
6.19 Modelled variation of the direct and diffuse components of incoming solar radiation for increasing temperature (a) and the corresponding change in individual transmittances. In (b) all transmittances overlap except for water vapour.	107
6.20 Modelled variation of long-wave radiation as a function of air and snow temperature (a) and as a function of relative humidity (b).	107
6.21 Modelled variation of long-wave radiation as a function of altitude (a) and sky view factor (b).	108
6.22 Modelled variation of the turbulent heat fluxes for changes in the the wind speed (a) and in the roughness parameter(b).	109

6.23 Details of penitentes on a snow field about 4300 m The tops tend to sharpen into a peak shape, but the overall blade structure is conserved.	111
6.24 Digital elevation model at 1cm resolution of the penitentes-covered snow surface. The world reference system is rotated southth to avoid overhanging surfaces, to model the solar radiation the solar vector is defined according to the new reference system.	111
6.25 Energy contributions of every component in the energy balance for the whole recording period at Loma larga glacier. SW is short-wae, LW long-wave, Q_S turbulent sensible heat flux, Q_L turbulent latent heat flux, Q_net is turbulent net heat flux and Net energy is for the local measured albedo.	112
6.26 Spatial distribution of the daily cumulative short-wave direct (a) and diffuse (b) components of incoming solar radiation. Loma Larga site, averaged from day of the year (DOY) 22 to day 53.	113
6.27 Spatial distribution of the daily cumulative incoming short-wave radiation reflected from surrounding slopes (a) and the total value (b). Loma Larga site, averaged from DOY 22 to day 53.	113
6.28 Spatial distribution of the daily cumulative long-wave radiation, (a) is incoming flux, (b) is outgoing and (c) is net flux. Loma Larga site, averaged from DOY 22 to day 53.	114
6.29 Spatial distribution of the daily cumulative turbulent sensible and latent heat flux on Loma Larga glacier. Loma Larga site, averaged from DOY 22 to day 53.	115
6.30 Spatial distribution of the daily cumulative net turbulent and total net heat flux on Loma Larga glacier. Loma Larga site, averaged from DOY 22 to day 53.	115
6.31 Variation with elevation of the mean daily distributed values at different altitudinal belts of the energy balance components for the whole recording periods on the Loma Larga (days 22 to 54) and the Juncal Norte areas (days 345 to 355). Outgoing long-wave are absolute values, the actual value is negative. Main differences are due to increased absolute values of turbulent fluxes in Juncal Norte due to stronger winds.	117
6.32 Variation of the energy balance components with height for mean recorded values at the lower AWS (3035 m) applying a standard lapse rate (-0.0065Km ⁻¹). Net values are right axis. Values do not take into account energy absorbed at different surface or subsurface layers in this case. Short-wave global radiation is modified primarily by albedo, which in this case was simplified to a constant value. The right figure shows the results for an average increase in wind speed of 2 ms ⁻¹	117

6.33 Variation with slope of the mean daily distributed values of the energy balance components on Loma Larga and Juncal glaciers.	118
6.34 Variation with aspect of the slope of the mean daily distributed values of the energy balance components on Loma Larga and Juncal glaciers.	118
6.35 Average daily value of total insolation (direct, diffuse and reflected) modelled on penitentes for the 37th day of the year at Loma Larga glacier.	119
6.36 Histogram of insolation values in Figure 6.35 showing a bimodal distribution corresponding to the north facing and south facing slopes. Values are MJm ⁻²	119
6.37 Spatial distribution of snow ablation, including evaporation, both at the basin scale and the penitentes scale. Note increased ablation on the right side of the north walls of penitentes.	122
6.38 Net energy balance of penitentes for the 37th day of the year.	123
6.39 Temperature fluctuations for a two week period modelled on the surface of penitentes at Loma Larga glacier. Temperature on the south facing walls (away from the sun) barely reaches 0°C, indicating little or no melting, despite positive air temperatures and strong solar radiation.	123
6.40 Penitentes on a former shallow snow field at 4300 m Snow in the troughs has disappeared, but the penitentes survive for a long time despite the strong solar radiation and day temperatures above freezing level.	124
6.41 Output of the HadCM3 coupled atmosphere-ocean general circulation model showing the differences between present and projected surface temperature by the end of the 21st Century. URL: http://www.cru.uea.ac.uk/	126
6.42 Output of the HadCM2 coupled atmosphere-ocean general circulation model showing the differences between mean temperatures from 1961-1990 and projected surface temperature by 2080. URL: http://www.cru.uea.ac.uk/	126
6.43 Uppermost surface layer net energy balance at Juncal Norte Glacier on the day of the year 335 (1st December). Thick contours are 3000 m, 4000 m and 5000 m, The net energy balance becomes negative at about 3800 m, the height where first penitentes were observed.	127
A.1 Air temperature measured on Juncal Norte glacier at 3335 m.	133
A.2 Air temperature measured on Loma Larga glacier at 4667 m.	133

A.3	Relative humidity measured on Juncal Norte glacier at 3335 m.	134
A.4	Relative humidity measured on Loma Larga glacier at 4667 m.	134
A.5	Dew point calculated according to Jacobson (1999) 2.56 on Juncal Norte glacier at 3335 m.	135
A.6	Dew point calculated according to Jacobson (1999) 2.56 on Loma Larga glacier at 4667 m.	135
A.7	Wind speed measured on Juncal Norte glacier at 3335 m.	136
A.8	Wind speed measured on Loma Larga glacier at 4667 m.	136
A.9	Wind rose of relative frequency for all the measuring period (day 335 to 346) on Juncal Norte glacier at 3335 m a.s.l. Grey lines indicate wind mean speed for every radial sector. The maximum frequency follows the orientation of the lower section of glacier, as can be seen in Figure 2.2 This figure is repeated from Figure 6.10 for completeness. . .	137
A.10	Wind rose of relative frequency for all the measuring period (day 22 to 53) on Loma Larga glacier at 4667 m. Grey lines indicate wind mean speed for every radial sector. The main orientation of the glacier is East–West and the predominant winds in this case seems to be from the valley, the northeast component of the glacier winds may be influenced by the more extent snow cover of the south-facing slopes, to the north of the AWS. This figure is repeated from Figure 6.11 for completeness. . .	137
A.11	Shortwave incoming and outgoing solar radiation measured on Juncal Norte glacier at 3335 m.	138
A.12	Shortwave incoming and outgoing solar radiation measured on Loma Larga glacier at 4667 m.	138

Chapter 1

Introduction

1.1 Aim

The main aim of this thesis is a better understanding of the energy balance, sensitivity and climatic response of high altitude glaciers in the Central Andes, focusing on the interaction of the glacier system with the atmosphere, climate and topography. The particular ablation morphology (penitentes) on the glaciers of this region alters the energy balance of the snow cover and requires detailed treatment and modelling. This understanding will be helpful in the assessment of wider implications for water resources in the region and for the use of glaciers as climatic indicators.

The specific objectives are:

- the measurement and modelling of local meteorological variables
- the development of analytical tools for the computation of the terrain parameters that define the influence of topography on energy balance
- the development of inexpensive techniques of field survey, such as albedo estimation using land based oblique photograph
- the extrapolation of modelling results to practical information on snow cover depletion and water resources

1.2 Background and rationale

The Andes is the longest mountain range on the surface of Earth, stretching the length of South America for over 7500 km. Yet, there are very few studies on the dynamics and energy balance of glaciers in these mountains. Most glaciological studies outside the poles are focused on high latitude glaciers, mainly on the northern hemisphere. The significance of this gap in glaciological research is stressed by the fact that some of the most dramatic climatic gradients on earth occurs here (Schwerdtfeger 1976, Lliboutry 1998).

Mountain glaciers are excellent indicators of climatic change (e.g. Oerlemans et al. 1998); however, glaciers in the Southern hemisphere are underrepresented in the global monitoring strategies. The last mass balance bulletin of the World Glacier Monitoring Service (Haeberli et al. 2001) or the comprehensive Glacier Mass Balance and Regime of the Institute of Arctic and Alpine Research (Dyurgerov 2002) give information for only five glaciers in the whole Andes outside the Patagonia Ice Fields. A contribution toward a better understanding of the energy balance of glaciers in these areas will improve the understanding of glacier response to global climatic change.

Water is a very scarce resource in this region, with mean precipitation values below 180 mm per year in the eastern side of the Cordillera (Schwerdtfeger 1976). Yet agriculture is an important element in the economy of Chile and the Andean provinces of Argentina, as well as hydroelectric production, which is only possible thanks to the meltwater runoff of snow accumulated during the winter and stored in the glacier ice. The importance of glaciers as water reservoirs is stressed if we consider their areal extension in the region: more than 1900 km² in the Central Dry Andes alone, or about 65% of the total area of the glaciers in the Alps (Dyurgerov 2002).

Energy balance modelling has been proven to be a useful tool in many fields of glaciology, namely: predicting runoff from glacierised basins (Hock 1998, Wagnon et al. 1999, Strasser et al. 2002), assessing the stability of the snow pack for avalanche forecasting (Brun et al. 1989), studying the sensitivity and response of glaciers to climatic change and the role of glaciers as climatic indicators (Greuell and Oerlemans 1986, Oerlemans 1986, Oerlemans 1989, Oerlemans 1994, Oerlemans 2001). It is a first step in modelling glacier dynamics, which is important for paleoclimatic reconstructions. Glacier dynamics are also important for the safety of inhabitants in the region. This was manifest in the floods of 1934, resulting from the breakdown of an ice dam produced by the Nevado del Plomo glacier surge, and the sudden release of over 60 million cubic metres of accumulated water, which reached the city of Mendoza (1.2 million inhabitants), 150 km downriver. A similar event, without tragic consequences, happened again in 1984 and it is likely to occur in the future (King 1934, Helbling 1935, Espizúa 1986, Leiva et al. 1989).

1.3 The problems

We face two main problems when studying the Andean glaciers. One is the lack of data and direct observations; the other is the formation of snow penitentes on the surface that changes the energy balance of the whole snow-covered areas and complicates the application of existing energy balance and melt models to the region.

To approach these problems additional work needs to be done to find appropriate and reliable models that can build on the sparse data. In this work much of the effort is focused on modelling adequately the most important source of energy for the snow ablation, that of the direct solar radiation. As topography plays an important role in the energy balance of these glaciers, models should incorporate an efficient evaluation of the topographical effects.

The most striking characteristic of the snow cover in this region is the general presence of penitentes (Figures 1.1 and 1.2). They appear on all glaciers and snow fields about 3700 m at the beginning of the ablation season, rising to about 4000 m as the mean air temperature increases. Their presence completely changes the snow surface energy balance (Kotlyakov and Lebedeva 1974). As Lliboutry (1954a, p. 466) put it: “penitentes are not a simple curiosity of this region, but the basis of all the glaciological processes”. Traditional snow melt models are of questionable utility under these circumstances, as the energy balance should be considered at the microtopographical scale.

1.4 Plan of work

Chapter 2 describes the area of study, its climatic setting and the more specific location where meteorological data were collected. These are two glaciers of the Chilean side of the Andes at 33°South, 70°West, at altitudes of 3335 m above sea level (a.s.l.) and 4667 m respectively. Data were collected intermittently from November, 2000 to February, 2001. The instrumentation used is briefly summarised, while all the data collected are shown graphically in the appendices.

Chapter 3 is a brief review of the background theory for modelling the different energy terms that affect the total energy balance at the surface of the snow. The selected modelling tools and their performance are evaluated by comparing the modelling results to measured data. Additional data from cooperative campaigns in the Alps (Haut Glacier d’Arolla) are also be used to assess the wider application of the modelling tools.

Chapter 4 focuses on the development of mathematical tools for the evaluation of terrain parameters using digital elevation models (DEMs). These tools have been developed taking into consideration the particularities of mountain topography, with strong relief and sudden changes of slope. They are applied to a wide range of scales, from large basins to the microtopography of the surface ablation morphology.



Figure 1.1. Penitentes field on the middle section of the Loma Larga glacier, at about 4500 m a.s.l. The whole glacier above 4000 m is covered in these snow pinnacles, which restricts the movement of mountaineers and researchers and alters the surface energy balance of the glacier.

Their implementation is efficient, fast and compensates for the computational demands of distributed modelling over large areas. This chapter forms the basis of a paper published in the International Journal of Geographical Information Science (Corripi 2003).

Solar radiation is the main energy input to snow and glaciers in these high mountains with extremely clear atmosphere and stable weather during the ablation season. For this reason the albedo of the snow is an important parameter to consider. Thus in Chapter 5 a novel technique for the estimation of snow surface albedo using terrestrial photography is described. The validation of this technique was carried out in the Alps, and most of the examples are given for Alpine regions. The method can be applied to any area with a relatively smooth snow surface, but unfortunately, as soon as penitentes begin to form on the surface, the results of this technique are highly questionable. Nonetheless, it is useful for measuring the albedo of flat snow and bare ice surfaces, and for monitoring temporal variations of snow cover and snow line retreat. It is an inexpensive tool, which is always an advantage in regions where the general



Figure 1.2. Penitentes about 2 m in height on a clean snow field at 4300 m a.s.l. in the Central Andes.

economic situation makes expensive field campaigns anything but a priority. This chapter forms the basis of a paper submitted for publication to the International Journal of Remote Sensing.

Chapter 6 focuses on the implementation of the model at two scales, the broad glacier basin scale and the more detailed microtopographical scale, in order to evaluate the energy balance for the penitentes layer. This chapter is in part adapted from Corripio and Purves (2003), a book chapter submitted for publication as a cooperative effort between meteorological and hydrological disciplines at the European Geophysical Society for the International Year of the Mountains.

Chapter 2

Site of study and methodology

The selected glaciers are near the latitude of Santiago de Chile (Figures 2.1, 2.2 and 2.3). The Juncal Norte glacier (32.98° S, 69.95° W) flows northward of Nevado Juncal peak from 6100 m to 2900 m, near the border with Argentina and south of the Portillo pass. Here, an automatic weather station (AWS) was installed on the snow-covered glacier surface at 3335 m and collected data from 30 November to 11 December, 2000. The second glacier is Loma Larga glacier, on the headwaters of the Maipo river (33.69° S, 70.00° W), where the AWS was installed at 4667 m a.s.l. and recorded data from 22 January to 24 February, 2001. The upper section of the glacier reaches 5404 m and extends to 2900 m, where the ice becomes completely covered in debris. Fieldwork presented some logistic problems such as transport to remote areas of the Andes and the lack of adequate information and maps. Transport was arranged with local arrieros (mule drivers), but proved to be a time-consuming exercise. Mules cannot, obviously, climb up glaciers, although we had the chance of seeing ingenius snow shoes and crampons for mules developed by the mountain section of the Chilean army. Thus the transport of the instruments to the adequate location relied on the help of local mountaineers. The most reliable maps of the area were still those produced by Lliboutry (1956) almost half a century ago; despite their age they were a very useful resource in planning the exploration and selection of the most adequate areas to set up the AWS.

2.1 The Dry Andes: climatic setting

Along the 33° S parallel, annual average precipitation ranges from 459 mm in Valparaiso (33.02° S, 71.63° W, 41 m) on the Pacific coast, to 356 mm in Santiago (33.45° S, 70.70° W, 520 m) and 180 mm in Mendoza (32.89° S, 68.83° W, 769 m) on the Argentinian side of the Cordillera (Prohaska 1976, Miller 1976). In this region climatic seasonality is well defined, with dry summers and most of the

2.1. The Dry Andes: climatic setting

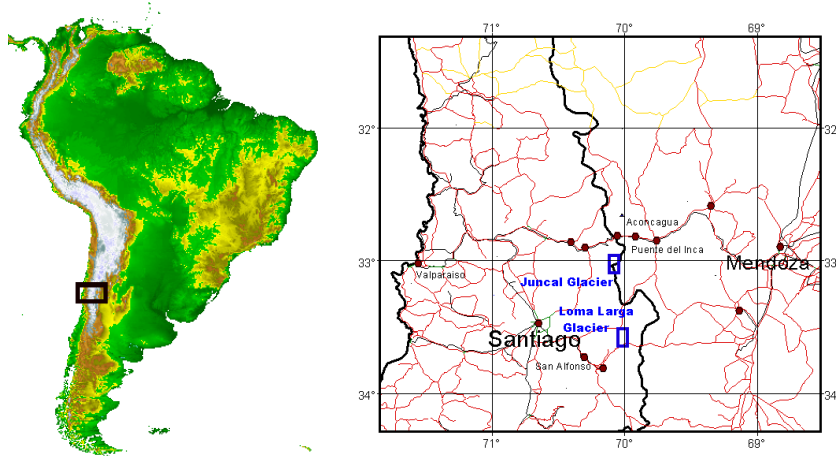


Figure 2.1. The area of study in the Chilean Andes, about 33° S 70° W. Vertical grid separation is about 111 km (1° latitude). Map source: South America map from the GLOBE project, NOAA, NGDC, URL:<http://www.ngdc.noaa.gov/seg/topo/globe.shtml>.

Detailed map from the Digital Chart of The World, URL:<http://www.maproom.psu.edu/dcw/>.

precipitation occurring during the winter months. The southwestern Pacific perturbations reach the mountains only during the winter, producing variable precipitation, which is always in the form of snow at high altitude (Lliboutry 1965). During the summer the weather is extremely dry and stable, characterised by the constant presence of the Pacific anticyclone over the region. In fact, less than 1% of the annual total precipitation is recorded during the December–February period. Frontal activity is infrequent, and precipitation, both on the mountain range and in the lee of the mountains, is mainly due to convective activity (Miller 1976).

The synoptic situation during fieldwork is summarised in Figure 2.4, which shows the surface sea level pressure over South America. As indicated by Lliboutry (1998), a belt of stationary high pressure extends across the Pacific Ocean west of South America, preventing intrusion of moisture-laden air masses to the continent. This stationary anticyclone is also responsible for a minimum in relative humidity over central Chile during the summer months. The same reanalysis data show a relative humidity value of about 25% on the western coast of Chile at about 33° latitude south, the minimum for the southern hemisphere outside Antarctica (Figure 2.4). The solar radiation is very intense, with a daily average of over 400 W m^{-2} for the same period and is a maximum for both hemispheres during the summer months excluding the South Pole (Figure 2.5).

The climatic regime of the Dry Central Andes is clearly different from that of the subtropical Andes of Bolivia and Peru, further north, characterised by convective intrusions of moist air masses from the Amazon basin during the summer (Vuille et al. 1998). Here the ablation season is well defined and characterised by long periods of clear and stable weather. This climatic setting seems to be responsible for the formation of a very peculiar ablation morphology, the snow penitentes, common to all the central Andes and to other dry high mountains like the Pamirs (Lliboutry 1965, Kotlyakov and Lebedeva 1974).



Figure 2.2. Aster image of the Juncal Norte glacier. The near infrared band was the only one that was not completely saturated in the upper section of the glacier covered in snow with high albedo. The location of the AWS is indicated by an arrow, the image correspond to a different time of the year than the survey, and the lower section of the glacier is free of snow. Data from NASA EOS Data Gateway: http://edcdaac.usgs.gov/aster/ast_11a.html

2.2 Economic and social importance of glaciers in the region

The eastern regions of the Dry Central Andes, stretching from latitude 31° S to 35° S, are climatic deserts, yet they support rich agriculture and large urban centres thanks to melt water from glaciers and snow-covered mountains. Most of the agriculture of the Chilean Central Valley is irrigated (Miller 1976), and all drinking water for Santiago de Chile, with over five million inhabitants (one third of the population of Chile), comes from water reservoirs fed by snow and ice melt during the summer. On the Argentinian side of the Andes, with barely 180 mm of annual precipitation, the provinces of Mendoza (population over 1.5 million) and San Juan are the country's main wine producers and the region has rich agricultural farms. This production is only possible thanks to a well developed irrigation system making efficient use of the summer melt water from the Cordillera. The contrast between the natural desert vegetation and the lush green of the cultivated farms is evident over the whole province, stressing the vital role of the mountains as "water towers of the world for the 21st Century" (Liniger et al. 1998).

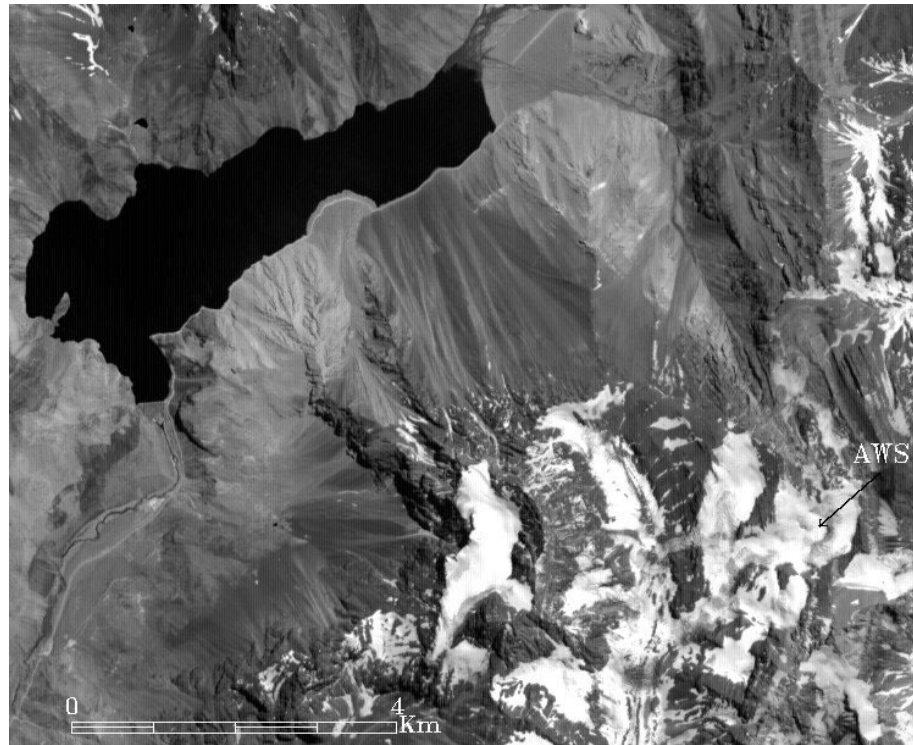


Figure 2.3. Aster image of the Loma Larga glacier. The location of the AWS is indicated by an arrow, the large dam to the northwest of the image is the Rio Yeso dam, the main water reservoir supplying Santiago de Chile.

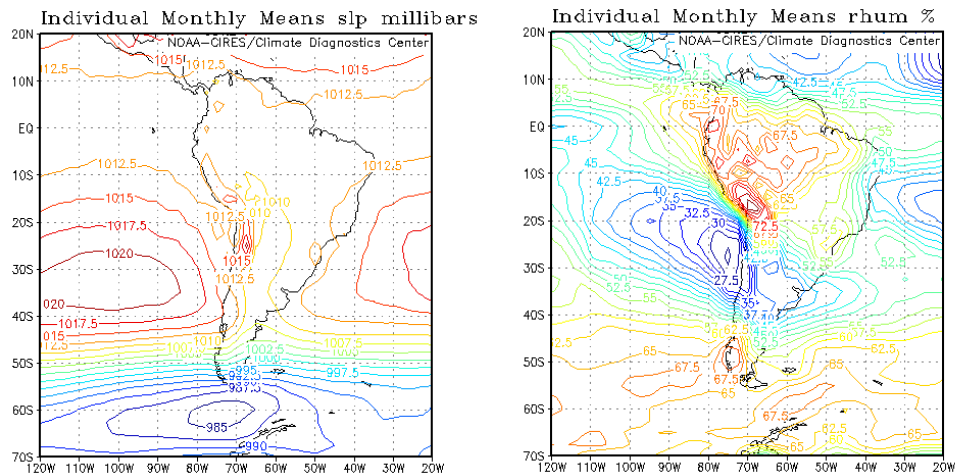


Figure 2.4. Surface sea level pressure averaged from December 2000 to February 2001 and relative humidity reanalysis data. The image is a visualisation of NCEP/NCAR reanalysis data provided by the NOAA-CIRES Climate Diagnostics Center, Boulder, Colorado, from their web site at <http://www.cdc.noaa.gov/>.

2.3. Snow and ice penitentes

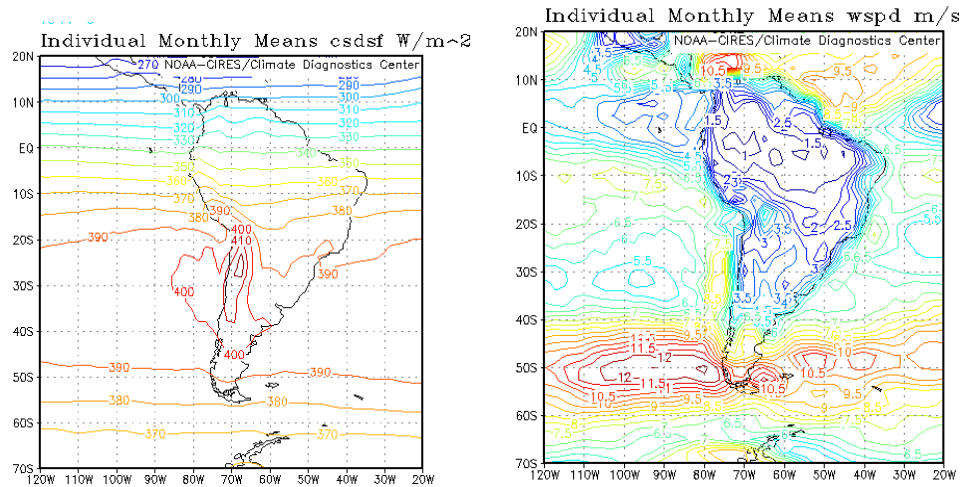


Figure 2.5. Clear skies short wave downward flux and mean wind speed averaged from December 2000 to February 2001. NCEP/NCAR reanalysis data (see Figure 2.4).

2.3 Snow and ice penitentes

Penitentes are a labyrinth of ice and snow pinnacles, towers, spires and blades, apparently chaotic in distribution, but actually showing a common pattern in their orientation that reflects the mechanism for their origin. They are invariably oriented toward the zenithal angle of the sun at noon, with walls aligned preferentially from east to west (Figure 2.6). Penitentes were first described in the literature by Darwin (1839). On March 22, 1835 he had to squeeze his way through snowfields covered in penitentes near the Piuquenes pass, on the way from Santiago de Chile to the Argentinian city of Mendoza, and reported the local belief (continuing to the present day) that they were formed by the strong winds of the Andes. These pinnacles of snow or ice grow over most glaciated and snow covered areas in the Dry Andes. They range in size from a few cm to over five metres. (Lliboutry 1965, Naruse and Leiva 1997). Larger forms, up to 30 m, reported by Roch (1954) in the Himalayas are likely to be remnants of seracs or ice avalanches sculpted into a pinnacle form by the effect of direct solar radiation. Similar cases were observed in the Loma Larga glacier in the Andes, where large blocks of dislodged ice were differentially ablated into pinnacles up to 15 m in height (Figure 2.7). Penitentes are not exclusive to the Dry Andes, but they also appear in mountains with similar climatic conditions, such as the Pamirs, and can develop in many other ranges under long spells of dry, stable and relatively cold, but sunny weather. They have been described in the tropical Andes, the Himalayas, the highest peaks of the Sierra Nevada of California, the high mountains of equatorial Africa, especially the Kilimanjaro, and even on the snow cover Pico del Teide, in Tenerife (Workman 1914, Troll 1942, Lliboutry 1954b, Lliboutry 1965, Kotlyakov and Lebedeva 1974, Hastenrath and Koci 1981, Becht 1991, Lliboutry 1998).

2.3. Snow and ice penitentes



Figure 2.6. Penitentes about 2 m in height on a snow field at about 4300 m a.s.l. The photograph is taken looking west, and shows the inclination of the penitentes toward the north. Note that for this latitude and time of the year, the sun is due west at 17:10h, the approximate time at which the photograph was taken, with an elevation angle of 44° .



Figure 2.7. Ice blocks sculpted into pinnacles, probably by the action of the sun rays, at Loma larga glacier, about 3500 m a.s.l. The prominent pinnacle in the centre is about 10 m height.

2.3.1 The origin of penitentes

Lliboutry (1954a, 1954b, 1965, 1998) noted that the key climatic condition for the differential ablation that leads to the formation of penitentes is that dew point is always below zero. Thus, snow will sublime, and this requires higher energy input than melting, resulting in a cooling of the surface. Once the process of differential ablation starts, the surface geometry of the evolving penitente produces a positive feedback mechanism, and radiation is trapped by multiple reflections between the walls. The hollows become almost a black body for radiation, while decreased wind due to increased roughness lengths leads to air saturation, increasing dew point temperature and the onset of melting. In this way peaks, where mass loss is due only to sublimation, will remain, as well as the steep walls, which intercept only a minimum of solar radiation. In the troughs ablation is enhanced, leading to a downward growth of penitentes. It should be noticed, though, that even when dew point is always below zero in areas covered by penitentes, this is not a sufficient condition. In the same way that we can melt snow on a stove in Antarctica or on the South Col of Everest at much lower temperature and dew point, because the rate of energy input exceeds the rate of energy output (surface cooling), it is possible to observe melt and liquid water even if the dew point at screen level is below zero. This involves an extreme humidity gradient from the surface to the measurement instruments. Such a situation was observed almost daily at the lower AWS on Juncal Norte, and thus, to determine whether melting occurs or not, it is necessary to assess the whole energy interchange at the snow surface. A mathematical model of the process of snow ablation that leads to the survival of perturbations of a determined wavelength, related to the penitente size, has been developed by Betterton (2001). However, the physical processes at the initial stage of penitente growth from granular snow to micropenitentes (Figures 2.9 and 2.10), still remain unclear. A schematic representation of the mechanisms that intervene in the formation of penitentes and their growth is summarised in Figure 2.8.

Lliboutry (1954b) reported different theories to explain penitente formation, ranging from the electromagnetic orientation of snow crystals to the effects of the wind, rain or avalanches. The most popular of all was probably wind, a widespread belief among the local inhabitants in the present day, as it was 160 years ago according to Darwin's reports. Lliboutry (1954a, 1954b, 1965) stressed the different energies required for melting and sublimation as the initial stage in the formation of penitentes, and the positive feedback mechanism produced by reduced air circulation in the troughs and multiple reflection of light between the penitente walls as an explanation of their subsequent growth. Soon afterwards Amstutz (1955) published a critique of Lliboutry's theories. He questioned whether penitentes grow by ablation or by upward ice deposition and suggested a study of the isotopic composition to determine this. In the four months of field work in the Andes, and in previous scientific and mountaineering campaigns, the author never observed hoar or rime deposition; furthermore the dew point and modelled latent heat fluxes were always negative, which suggest no condensation, and therefore no deposition.

Kotlyakov and Lebedeva (1974) studied penitentes in the Pamirs and stressed the importance of radiative cooling in the energy balance of the snow surface. They suggested that the original micro-slopes

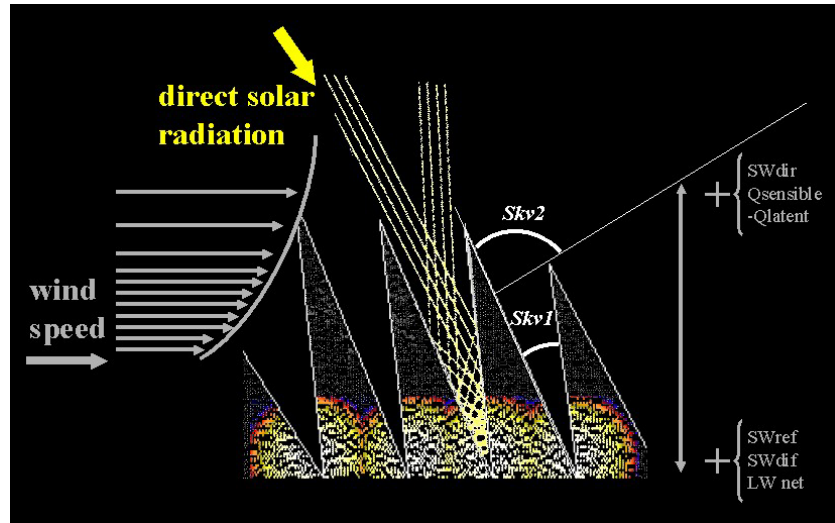


Figure 2.8. Schematic representation of the feedback mechanisms that enhance penitentes growth. Solar radiation is more intense at the bottom of penitentes due to multiple reflections, net long-wave radiation decreases with height due to larger sky visibility and net turbulent fluxes are more negative at the peaks where sublimation prevails producing intense cooling. In this way peaks survive and troughs are deepened.

in the irregular surface of the snow is the key to the initiation of differential ablation that leads to penitentes. Rhodes et al. (1987) considered penitentes as an extreme form of ablation hollows, increasing in depth as at higher altitudes. After experiments carried out on the snow fields of Mount Rainier they concluded that the key factor in the formation of both is the dirt content of the snow. In the Andes we observed large suncups (Figure 2.11) probably formed from decaying penitentes as the temperature increased during the ablation season, but never the inverse process. The importance of the dirt content of the snow is stressed by Kirkbride (1995), and it is an essential point in the modelling approach undertaken by Betterton (2001). However, Lliboutry (1954b) stressed a long time ago, that penitentes can grow over both clean or dirty ice snow, and that their origin is unrelated to and unaffected by a moderate concentration of dirt. During fieldwork we observed penitentes growth in snow completely clean and flat as far as detailed observation with the naked eye and with a 10x magnifier can tell (Figure 2.9). The unimportant role of dirt has recently been confirmed in laboratory experiments by Betterton and Bergeron (personal communication) who replicated the penitente growth in a cold laboratory at the École Normale in Paris.

2.4 Methodology

The methodological approach is the combination of numerical modelling and field data collection. A modelling exercise without direct observation of the modelled processes may result in unrealistic results. It is therefore necessary to maintain the links with the observed phenomena to determine which possible



Figure 2.9. Micropenitentes or initial stage in the formation of penitentes at different locations in the Central Andes. Darker areas correspond to lower reflectance in wetter areas or because lower light interception, as in the steep walls (upper right figure).

results are realistic and which are not. As Oerlemans (2001, p. 145) put it, “working with models is the only way to quantify processes and put these processes into perspective”. Another advantage of modelling is that it allows running experiments that permit quantifying the relative importance of the variables affecting the system and their overall sensitivity (Hulton et al. 2002).

The most important part of a model is its explanatory power, and its aim is not so much to replicate reality as to help understanding it. In other words: “fitting for fittings’s sake seems a vacuous pursuit” (Hulton et al. 2002). The disagreement or poor fit with observed data helps the identification of poorly understood areas in the behaviour of the modelled system. This misfit is a positive contribution rather than an invalidation of the model, even when data are scarce or uncertain. Quoting Oerlemans (2001, p. 145): “the argument is frequently heard that there is no point in modelling a particular glacier because field data are too scanty. This makes just as much sense as stating that it is useless to perform measurements on a glacier because no model is available. Modelling and making observations should be combined. Measurements always yield useful constraints on modelling - modelling provides basic information about the dynamic properties of the a glacier and may give hints as to what is important to measure”.



Figure 2.10. Digitally enhanced image of a small area covered in micropenitentes a few cm deep. The dark square is an A4 photographic greyscale card (21x29cm). The darker snow on the top of pinnacles and blades is a thin crust of bonded snow grains but no dirt.

For the modelling approach two additional tools were developed during this work. One is a series of vector algebra algorithms to improve the terrain analysis and solar radiation modelling using digital



Figure 2.11. Large suncups on Loma Larga glacier at about 3900 m, probably resulting from the decay of penitentes formed earlier in the ablation season.

elevation models (DEMs), and the other is a remote sensing tool to assess snow cover extension, snow cover changes and derive the albedo of the snow surface using terrestrial photography.

The fieldwork consisted in the collection of meteorological data by installing an automatic weather station (AWS) in the field, together with detailed observation of the structure, distribution and morphometry of the penitentes. These data and observations were used to apply both point and spatially distributed energy balance models that incorporate the effect of surrounding topography. The approximate validation of the models with data from the Alps and the Andes adds confidence to its heuristic ability, which is employed to assess the rate of snow cover ablation and their sensitivity to climatic parameters.

2.5 Instrumentation and data recording

On Juncal Norte glacier an automatic weather station (AWS) was installed on the snow covered glacier surface at 3335 m and about 1.5 km from the glacier snout (Figure 2.2). It collected data from 30 November to 11 December 2000, when the snow depth was insufficient to maintain the AWS in a stable position. The area was relatively flat with an average of less than 2° slope for the 20m DEM cell. The AWS support structure was an aluminum ice corer with a modular extension of three tubes one metre long. The ice corer was efficient in compact snow but resisted any attempt to drill through glacier ice; thus the station was installed in areas where snow depth was at least 1.5m to guarantee stability of the structure. Additional stability was gained by using guys anchored to the snow. On Loma Larga glacier the AWS was installed at 4667 m a.s.l. and recorded data from 22 January to 23 February 2000 (Figure 2.3). The area was completely covered in penitentes ranging from 1 m to 1.80 m.

The meteorological variables recorded were: incoming shortwave solar radiation, outgoing reflected shortwave solar radiation, wind speed, wind direction, relative humidity, air temperature and snow temperature at different depths. A summary of sensor characteristics is given in table 2.1. Additional measurements were made on snow depth variation and snow surface ablation forms. Depth was estimated by measuring manually the lowering of the snow surface in relation to several ablation stakes. Stakes were used successfully only on Juncal glacier. Here the bottom of the stake reached the surface of the glacier ice, in this way, errors derived from sinking of the stake are unlikely, but still some uncertainty remains due to the different thermal properties of bamboo and snow, which caused enhanced melting in the vicinity of the stake. Meteorological measurements were performed every 10 minutes, at this point the average and standard deviation of 20 instantaneous continuous measurements were stored in the memory of a Campbell CR10 data logger.

It has long been recognised that under strong radiative conditions, measurements of temperature may be distorted if the sensors are not ventilated (e.g Georges and Kaser 2002). The situation is aggravated when the upwelling radiation is intense, as in the case of snow covered ground with high albedo.

2.5. Instrumentation and data recording

Table 2.1. Instruments, range and accuracy of meteorological measurements.

variable	Sensor	Range	Accuracy
shortwave radiation	CM3 Pyranometer sensor Kipp & Zonen thermopile	305 - 2800 nm	daily sums 10%
air temperature	Vaisala 50Y 1000Ω Platinum Resistance Temperature detector (PRT)	-40 to +60°C	±0.35°C at -10°C, ±0.6°C at +60°C
snow temperature	107 temperature probe thermistor	-40 to 56°C	-23 to 48 <0.1°C
relative humidity	Vaisala 50Y capacity humidity sensor INTERCAP®	0 to 100% RH	±2% at 10%, ±3% at 90%, ±6% at 90-100%
wind speed	05103 Young Wind monitor 4-blade polypropylene helicoid propeller	1 to 60 ms ⁻¹ survival up to 100 ms ⁻¹	±0.1 ms ⁻¹ , 1 to 60 ms ⁻¹ ; ±1.0 ms ⁻¹ , 60 to 100 ms ⁻¹
wind direction	05103 Young Wind monitor Balanced van	0-360°	±3°

The measurements in the present campaign were made with screened but unventilated sensors, simply because ventilation systems were not available. However, wind speed was fairly constant, with averages of 3.95 ms⁻¹ and 2.52 ms⁻¹ for the lower (Juncal) and upper (Loma Larga) AWS respectively. This produced a natural ventilation of the sensors, although probably not sufficiently intense for the upper AWS (Georges and Kaser 2002). The values of measured meteorological variables and the calculated dew point are shown in the Appendix A.

Additional measurements of snow density were made at both glaciers and at the Haut Glacier d’Arolla. In the Andes density was calculated from the weight of a recipient of known volume full of snow, in Arolla density was measured at different depths and locations using both a corer of known volume and a cylindric container. Density spatial distribution was rather uniform in Arolla and Juncal Norte, with values around in the range 500 to 560 kg m⁻³, while in Loma Larga mean density was closer to 400 kg m⁻³.

Chapter 3

Modelling the energy balance at the snow surface

This chapter presents a review of background theory to compute the components of the energy balance at the snow surface. Most of the time analytical solutions to the problems described in the theory are rather difficult to implement. In this cases the modelling tools and empirical or semi-empirical approaches, will be described and the reason for choosing any particular approach highlighted. The models will be tested against data collected not only in the Andes, but also in the Alps, which may add reliability to the wider application of the selected tool.

The incorporation of topography into the energy balance will be addressed in chapters 4 and 6. The effect of albedo variability will be addressed in Chapter 5 and the energy balance at a microtopographical scale, that of the surface ablation forms, in Chapter 6.

3.1 Introduction

The net energy flux Q at the surface of the glacier can be expressed as:

$$Q = I_G(1 - \alpha) + L \downarrow - L \uparrow + H + L_v E + Q_s \quad (3.1)$$

where I_G is global short-wave radiation, α is snow albedo, L is long-wave radiation, arrows indicating downward or upward fluxes, H and $L_v E$ are sensible and latent turbulent fluxes with the atmosphere and Q_s is internal heat flux within the snow pack. Following the general convention, fluxes toward the surface are positive.

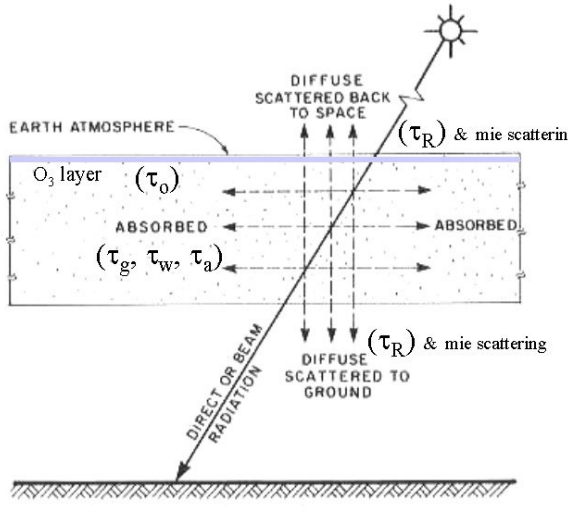


Figure 3.1. schematic representation of the effect of the earth's atmosphere on the short-wave radiation from the sun. The attenuation, absorption transmittance and scattering, either forward to ground, back to space and multiple scattering are formidable problems to solve for a real atmosphere. An empirical solution with satisfactory results will be presented in the following sections. Adapted from Iqbal (1983).

3.2 Short-wave radiation

As we have seen in Chapter 2, the input of solar radiation during the ablation season in the Central Andes is one of the highest in the world. Short-wave solar fluxes are the main energy input for ablation, as in many mountain glaciers (e.g. Wagnon et al. 1999), and given the lack of observations and permanent meteorological stations in this geographical area, it would be desirable to find a model of solar radiation that can be applied with confidence to a glacierised basin in the region. The advantage here is that the ablation season is generally stable, with clean and clear atmospheres, which make the modelling task easier.

3.2.1 Background theory

To estimate the solar radiation falling on the glacier surface, we need to calculate the absorption, reflection and transmission through the atmospheric path between the snow surface and the top of the atmosphere; it is equivalent to solving the radiative transfer equation through that path (Figure 3.1).

Let us consider first the case where only absorption occurs. It is generally assumed that absorptance of a monochromatic beam (N_λ) through an infinitesimal distance ds is independent of N_λ but proportional to the density of the transmitter $\rho(s)$, which will be denoted simply by ρ from now on, and to ds (Paltridge and Platt 1976), thus:

$$dN_\lambda/N_\lambda = -\kappa_{a\lambda}\rho ds \quad (3.2)$$

where $\kappa_{a\lambda}$ is defined as the spectral absorption coefficient of the medium. Integrating along a finite path

from x_1 to x_2 gives:

$$N_\lambda = N_{\lambda 0} e^{-\kappa_a \lambda \int_{x_1}^{x_2} \rho ds} \quad (3.3)$$

which is formally known as Beer's Law. When the spectral absorption coefficient is a function of position it should be written inside the integral. The quantity $\int_{x_1}^{x_2} \rho(s) ds$ (dimensions $kg\ m^{-2}$) is defined as the optical path and the dimensionless quantity $-\kappa_a \lambda \int_{x_1}^{x_2} \rho(s) ds$ is called the optical depth (Paltridge and Platt 1976). When considering the atmosphere in reference to the direct solar beam, the optical path is called the absolute optical air mass:

$$m_a = \int_0^\infty \rho ds \quad (3.4)$$

For the vertical direction, ds is substituted by dz , the increment in vertical height. For an oblique trajectory of the solar beam the relative optical air mass is defined as the ratio of the optical path along the oblique trajectory to the vertical path in the zenith direction:

$$m_a = \int_0^\infty \rho ds / \int_0^\infty \rho dz \quad (3.5)$$

A similar situation can be described for a pure scattering medium:

$$N_\lambda = N_{\lambda 0} e^{-\int_{x_1}^{x_2} \beta_{sc} \rho ds} \quad (3.6)$$

where β_{sc} is the volume scattering coefficient (dimensions m^{-1}).

A beam traversing a medium in a given direction is subjected to both attenuation and augmentation processes. Augmentation may happen due to forward scattering and by radiative emission of the medium. In the latter case, the main radiative contribution along the atmospheric path is likely to be in the thermal radiation band, which will be considered in Section 3.3.

The scattering process becomes more complicated when we consider the actual composition of the atmosphere and atmospheric particles. In theory, the scattering of radiation by spherical particles can be derived from the solution of Maxwell's electromagnetic equations in spherical polar coordinates. One of those solutions is given by Rayleigh's theory, which applies to air molecules of size smaller than one tenth of the wavelength of light. The mathematical treatment of light scattering can be classified according to the parameter $2\pi r/\lambda$ and the index of refraction n , where r is the radius of the particle and λ the wavelength in micrometres. We have then three cases (Iqbal 1983):

- $2\pi r/\lambda < 0.6/n$, scattered is described by Rayleigh's theory;
- $2\pi r/\lambda > 5$ uncommon in the earth's atmosphere;
- $0.6/n < 2\pi r/\lambda < 5$ scattering described by Mie's Theory.

For simplicity, Iqbal's (1983) expression has been reproduced, but it should be noted that the refraction index is a complex number. Mie theory gives a solution for the scatter produced by an isolated sphere, and it is in principle possible to treat also irregular particles by considering that due to their

random orientation their average behaviour can be represented as a sphere of equivalent size (Paltridge and Platt 1976). This is not true for preferentially aligned particles, like ice crystals in cirrus clouds, although it can be acceptable for cloudless atmospheres.

The analytical solution of the radiative transfer equation including absorption and scattering can be formidable, and therefore different numerical solutions and simplifications have been developed. Two of these are the two-stream and Eddington approximations. For an overview the reader is directed to the work of Paltridge and Platt (1976, chapter 4) and Jacobson (1999, Section 10.8.3), where extensive references are supplied.

We have been dealing, up to now, with monochromatic radiation, a single wavelength, but for the practical purpose of estimating the energy balance at the snow surface we are more interested in the total energy supplied by the short-wave broadband radiation flux as a whole. The spectral distribution, however, is useful for deriving snow properties and for the remote sensing of the snow cover. There are models that, by applying semi-analytical and numerical solutions to the radiative transfer problem, successfully calculate the transmittances for any given wavelength band (Berk et al. 1989, Vermote et al. 1994, Vermote et al. 1997). The accuracy of these models, based on a line-by-line calculation and extensive databases of atmospheric components, is remarkable (Figure 3.2), however their application is rather time consuming and computer demanding. In order to model the solar radiation over a large time span, its daily or hourly variation and to incorporate the effect of topography, we need a simpler, yet accurate model. This is also needed in other fields of research, such as plant ecology, solar engineering and architecture or the implementation of general circulation models. Therefore considerable effort has been made successfully in that direction. A review of different parametric models to estimate solar short-wave radiation is given by Niemelä et al. (2001b), and the model that, despite its simplicity, gives better results in that intercomparison is Iqbal's (1983) model. This latter model is actually a slight modification of Bird and Hulstrom model (Bird and Hulstrom 1981a, Bird and Hulstrom 1981b), that somehow has passed to history as Iqbal's model.

3.2.2 Bird and Hulstrom (Iqbal) parametric model

Bird and Hulstrom compare the outputs of seven simple models with that of the rigorous model SOLTRAN, based on the atmospheric transmission model LOWTRAN. In this latter model the band absorption model is based on laboratory measurements and theoretical molecular line constants in line-by-line calculations (Bird and Hulstrom 1981a); absorption coefficients from different absorbers are stored at a 5 cm^{-1} wavenumber (the inverse of wavelength) intervals and the transmittance is calculated with a resolution of 20 cm^{-1} interval. The scattering and absorption by aerosols is computed according to MIE theory and is stored in the code as a function of wavelength. For the atmospheric profile the model allows the input of radiosonde data or the use of four standard aerosol models. For a more recent version of this model, which is continually updated, see Berk et al. (1989).

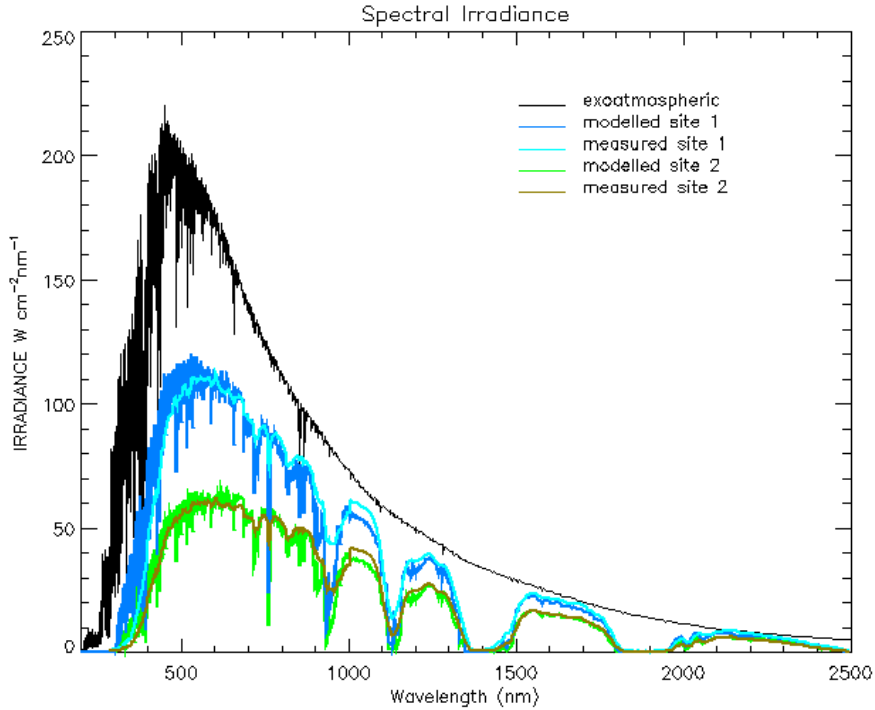


Figure 3.2. Comparison between modelled and measured radiation spectral distribution outside the atmosphere and on the ground for two sites near Edinburgh, 55.92°N, 3.17°W, in summer. The modelled values are the output of the radiative transfer model MODTRAN using estimated visibility and incorporated model atmospheres, measurements were performed by the author with a GER 3700 spectroradiometer.

Direct radiation

The expressions from the seven simple models compared by Bird and Hulstrom were tuned to get the best least squares fit to the output of the SOLTRAN model. The expression of direct normal irradiance was further modified in the present work to:

$$I_n = 0.9751 I_0 (\tau_r \tau_o \tau_g \tau_w \tau_a + \beta(z)) \quad (3.7)$$

where the factor 0.9751 is the ratio of the extraterrestrial irradiance in the spectral interval considered by the SOLTRAN model (0.3 μm to 3.0 μm) to the solar constant I_{sc} ; $I_0 = I_{sc} (R_0/R)^2$ is the extraterrestrial solar radiation or solar constant corrected for the eccentricity of the earth's orbit by multiplying it by the reciprocal of the square of the radius vector of the earth, calculated following Spencer (1971), as shown in Equation 5.19; the τ functions are transmittance functions for Rayleigh scattering and transmittance due to ozone, uniformly mixed gases, water vapour and aerosols respectively; and β_z is a correction term for altitude explained below.

This expression differs slightly from Bird and Hulstrom's formulation in two ways. Firstly the

factor 0.9751 was originally 0.9662 as the original computation followed Thekaekara's (1973) value of 1353 Wm^{-2} for the solar constant. Iqbal corrected the value for the more updated NASA/ASTM solar constant of 1367 Wm^{-2} and its spectral distribution. The present-day accepted value of the solar constant is 1366.1 Wm^{-2} computed as the mean of daily averages from six different satellites over the 1978-1998 time period. (Fröhlich and Lean 1998). The second difference is the correction for increased transmittance with altitude: $\beta(z)$ (units: m^{-1}). This term is introduced following Bintanja (1996) who applied it to the parameterisation of radiative fluxes in Antarctica:

$$\begin{aligned}\beta(z) &= 2.2 \times 10^{-5} z && \text{for } z \leq 3000 \text{ m} \\ \beta(z) &= 2.2 \times 3000 \times 10^{-5} && \text{for } z > 3000 \text{ m}\end{aligned}\quad (3.8)$$

where z is the altitude above sea level. $\beta(z)$ is strongly linear up to 3000 m and fairly constant up to 5-6000 m.

Note that the spectral interval is from $0.3 \mu\text{m}$ to $3.0 \mu\text{m}$ and this ignores some of the incoming solar radiation, actually about 14 Wm^{-2} in the ultraviolet and 24 Wm^{-2} in the near infrared, in total about 2.8% of the total extraterrestrial radiant flux according to data from the World Radiation Centre (WRC) in Davos, Switzerland (Iqbal 1983, pp. 46-47). The ultraviolet band is entirely absorbed by the ozone layer before reaching the altitudes in which we are working. In relation to the near infrared region of the spectrum it is interesting to notice, as remarked by Paltridge and Platt (1976), that outside the atmosphere only 0.4% of the radiant energy is in wavelengths longer than $5 \mu\text{m}$, whereas in the infrared band, only 0.4% of the energy is within wavelengths shorter than $5 \mu\text{m}$, and the transition after atmospheric absorption is at a point closer to $2 \mu\text{m}$. Therefore the solar and terrestrial radiation bands can be treated independently and the sensitivity range of the pyranometers used here seem appropriate for the solar radiation treatment.

Firstly, we calculate the relative optical air mass (m_r) according to Iqbal (1983), which gives a formula that approximate values of a model atmosphere as:

$$m_r = 1.0 / (\cos \theta + 0.15(93.885 - \theta_d)^{-1.253}) \quad (3.9)$$

where θ_d is $\theta (180/2\pi)$ or zenith angle in degrees.

The solution of Equation 3.5, the formal definition of airmass, can only be obtained if the vertical density variation of the actual atmosphere is known. This approximation is for standard pressure, a further approximation for local conditions at pressure p_z is given by the relative optical air mass pressure corrected (m_a):

$$m_a = m_r \frac{p_z}{1013.25} \quad (3.10)$$

Pressure as a function of altitude was calculated following the equation derived for the US standard

atmosphere 1976 (U.S. NOAA 1976, p. 12 & 13):

$$p_z = \left(\frac{p_0 T_0}{T_0 + L_M (H - H_b)} \right) \frac{g'_0 M_d}{R^* L_M} \quad (3.11)$$

where H is geopotential altitude as defined in Equation 3.12, H_b is reference pressure level, which is 0 m for the first 11 km in the atmosphere and L_M is the molecular scale temperature gradient in K/km' (-6.5 °K), where m' is the standard geopotential metre. g'_0 is a dimensional constant to relate the standard geopotential meter to geometric height. It is numerically equal to g_0 , the sea level value of the acceleration of gravity (= 9.80665 m/s²), which applies precisely to a latitude of 45 ° 32' 33". M_d is the molecular weight of dry air (= 0.028966 kg mol⁻¹) and R^* is the universal gas constant (= 8.31432 Jmol⁻¹K⁻¹). The geopotential altitude is calculated as:

$$H = \frac{r_0 z}{r_0 + z} \quad (3.12)$$

where r_0 is the effective earth's radius at a specific latitude (= 6.356766 × 10⁶ m for the US standard atmosphere). The value of r_0 takes into account the centrifugal acceleration at the particular latitude to be consistent with the sea-level value of the acceleration of gravity. z is altitude above sea level.

The calculation of the individual transmittances follows Bird and Hulstrom (1981b). Transmittance by ozone:

$$\tau_o = 1.0 - [0.1611 lm_r (1.0 + 139.48 lm_r)^{-0.035} - 0.002715 lm_r (1.0 + 0.044 lm_r + 0.0003 (lm_r)^2)^{-1}] \quad (3.13)$$

$$(3.14)$$

where l is the vertical ozone layer thickness in cm, which is updated according to data from the Total Ozone Mapping Spectrometer–Earth Probe (TOMS–EP 2001).

Transmittance by uniformly mixed gases:

$$\tau_g = e^{-0.0127 m_a^{0.26}} \quad (3.15)$$

Transmittance by water vapour:

$$\tau_w = 1.0 - 2.4959 w m_r [(1.0 + 79.034 w m_r^{0.6828} + 6.385 w m_r)^{-1}] \quad (3.16)$$

where w is precipitable water in cm calculated after Prata (1996) as in Equation 3.28

The transmittance by aerosols is a complicated task when there is no direct information on atmospheric turbidity. Thus some surrogate variable, easily measurable in the field, needs to be used. For

the implementation of the present model, Iqbal's formulation relies on visibility, which is derived from Mächler's (1983) work. Visibility is calculated as the maximum distance at which the naked eye can distinguish objects. This is a rather subjective value, especially when considering that aerosol transmittance is probably the most important parameter affecting atmospheric extinction of short-wave radiation (Bird and Hulstrom 1981b). However, the advantage of the study site is that skies are normally very transparent, with visibility ranges in excess of 100 km. Transmittance by aerosols is computed as:

$$\tau_a = [0.97 - 1.265 (Vis)^{-0.66}]^{m_a^{0.9}} \quad (3.17)$$

where Vis is visibility in km.

Diffuse radiation from the sky

For the diffuse component of solar radiation, Bird and Hulstrom (1981a) give the following parametric equations:

The Rayleigh-scattered diffuse irradiance after the first pass through the atmosphere is given by:

$$I_{dr} = 0.79 I_0 \cos \theta \tau_o \tau_g \tau_w \tau_{aa} 0.5 (1.0 - \tau_r) / (1.0 - m_a + m_a^{1.02}) \quad (3.18)$$

where τ_{aa} is the transmittance of direct radiation due to aerosol absorptance:

$$\tau_{aa} = 1.0 - (1.0 - \omega_0)(1.0 - m_a + m_a^{1.06})(1.0 - \tau_a) \quad (3.19)$$

ω_0 is the single scattering albedo, the fraction of the incident energy scattered to total attenuation by aerosols, taken as 0.9 (Hoyt 1978, Bird and Hulstrom 1981b, Iqbal 1983).

The aerosol-scattered diffuse irradiance after the first pass through the atmosphere is:

$$I_{da} = 0.79 I_0 \cos \theta \tau_o \tau_g \tau_w \tau_{aa} F_c (1.0 - \tau_{as}) / (1.0 - m_a + m_a^{1.02}) \quad (3.20)$$

where $\tau_{as} = \tau_a / \tau_{aa}$ and F_c is the fraction of forward scattering to total scattering. If no information on aerosols is available, Iqbal's model recommends a value of 0.84.

To compute the multiply-reflected irradiance, the atmospheric albedo is computed as:

$$\alpha'_a = 0.0685 + (1.0 - F_c)(1.0 - \tau_{as}) \quad (3.21)$$

The diffuse irradiance from multiple reflections between the earth and the atmosphere is calculated as:

$$I_{dm} = (I_n \cos \theta + I_{dr} + I_{da}) \alpha_g \alpha'_a / (1.0 - \alpha_g \alpha'_a), \quad (3.22)$$

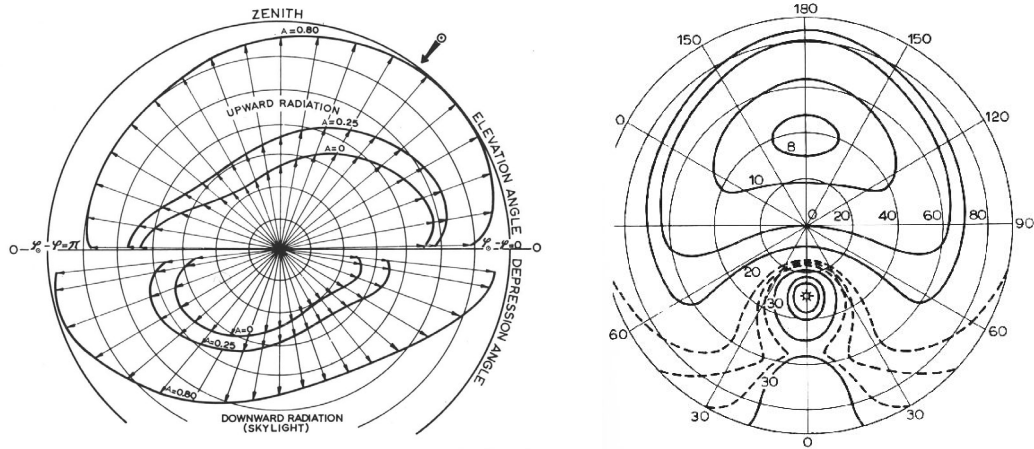


Figure 3.3. Distribution of skylight and upward radiation for three different surface albedos A, from Coulson (1959) as cited by Paltridge and Platt (1976, p. 114). The sun's elevation is 53° , its position is given by the symbol $\leftarrow \odot$. Right figure is sky luminance distribution as quoted by Robison (1966), cited by Paltridge and Platt (1976, p. 115)

where α_g is the albedo of the ground. The value of α_g is estimated from local knowledge of the average snow cover in a few km around the site of interest, as explained by Greuell et al. (1997) and shown in Chapter 5, Equation 5.25.

Finally, total diffuse radiation is:

$$I_d = I_{dr} + I_{da} + I_{dm} \quad (3.23)$$

The diffuse component of solar radiation in the atmosphere is considered as having an isotropic distribution. This is far from reality, as can be seen even by the naked eye when comparing the sky luminosity near the horizon with the circumsolar region, or the area at 90° to the sun. This is further confirmed by a simple experiment, such as comparing the readings of the light meter of a reflex camera on the aforementioned regions of the sky. The volume distribution of incoming and outgoing diffuse radiation has been investigated for a long time (e.g. Kondratiev 1969) and results for model atmospheres are exemplified in Figures 3.3, taken from Coulson (1959). However, as the objective in this work is to calculate total energy falling on a inclined surface surrounded by rough topography, it is intuitive that the integration of the anisotropic diffuse radiation field over a whole day will be approximately equivalent to an isotropic field. Furthermore, at high altitude the diffuse component is much reduced, and therefore the errors derived from an isotropic approach are smaller.

3.2.3 Diffuse reflected radiation

In mountainous terrain, especially when covered in snow, an important component of the total diffuse radiation is due to the reflection of light on the surrounding slopes. Ignoring this component may lead to gross errors in the estimation of the energy balance terms (Klok and Oerlemans 2002).

The effect of topography is twofold; firstly, it reduces part of the diffuse radiation coming from the sky by sheltering a fraction of the sky near the horizon, and secondly, it enhances diffuse radiation by reflecting global radiation onto the surrounding slopes. Both effects are opposed but do not cancel each other out and the diffuse reflected component can be very important when the surrounding slopes have a high albedo. Thus, the global incoming flux density I_G at any given zenith angle θ will be:

$$I_G = I_{dir} \cos \theta + \int I_{dif} d\omega \quad (3.24)$$

where the first term is direct solar beam and the second is diffuse radiation integrated over all solid angles (ω) of the upper hemisphere (Paltridge and Platt 1976). This is a formidable computational task even for idealised relief (Peterson et al. 1985). The task is even more complex for an area of irregular topography, and a simplification is necessary. The problem is tackled by introducing the concept of skyview factor (Section 4.6), and the approach is explained in Section 5.3.2, Equations 5.22 onwards.

Despite the necessary simplifications this model performs very well in clean atmospheres like those at high altitude in the Andes, as can be seen from figure 3.5, which compares modelled and measured data at 4667 m a.s.l. The modelled data include direct, diffuse and diffuse reflected radiation, but do not include cast shadows, which will be incorporated later in Section 4.5.

3.3 Long-Wave radiation

The downwelling long-wave radiative flux at the surface of the glacier for clear skies depends on the temperature, constitution and vertical profile of the overlying atmosphere, plus the emitted radiation from surrounding slopes. A good approximation to the atmospheric component is:

$$L \downarrow = - \int_0^\infty \int_{p_s}^0 \pi B_\gamma [T(p)] \frac{dt_\gamma(p_s, p)}{dp} dp d_\gamma \quad (3.25)$$

where p is pressure, p_s is surface pressure, T is temperature, γ is wavelength, B_γ is the monochromatic Planck function and $t_\gamma(p_s, p)$ is the monochromatic flux transmissivity from p to p_s (Niemelä et al. 2001a). A rigorous solution to this equation requires a detailed knowledge of the vertical variation in T , p and $t_\gamma(p_s, p)$, which was not available for the present case studies. Thus, an approximate solution based on meteorological variables recorded at screen level is desirable.

Niemelä et al. (2001a) has done a comprehensive evaluation of several parameterisations and compared them to *measured* values in Finland over a temperature range of -49°C to $+11^{\circ}\text{C}$. The italics are to stress that the actual downward long-wave flux was estimated from measured net total flux, measured net short-wave and estimated surface temperature. The possible errors in this estimation are given in Niemelä et al. (2001a, Equation 16 onwards). From this intercomparison, the best results were obtained from parameterisations used in the numerical weather prediction models (NWP), which require vertical atmospheric profile inputs. The following best results were the formulae proposed by Prata (1996) and Dilley and O'Brien (1998). Dilley and O'Brien's (1998) model performs better in wet environments, while Prata's (1996) approach is better suited to dry atmospheres (Dilley and O'Brien 1998, Niemelä et al. 2001a). It also includes a correction for non sea level pressures different, which makes it more appropriate for use in mountain environments.

The approach of both authors is to calculate the emissivity term ϵ_a considering the whole atmosphere as a *grey body* radiator:

$$\epsilon_a = \frac{L \downarrow}{\sigma T^4} \quad (3.26)$$

where σ is the Stephan-Boltzmann's constant. Prata (1996) and Niemelä et al. (2001a) review different equations, which are based in empirical observations, with some methods having their basis in the radiative transfer theory (Niemelä et al. 2001a). These parameterisations calculated emissivity either as a function of water vapor pressure e_0 , screen temperature T , or both. As a result Prata proposed a new formulation, based on precipitable water, *i.e.* indirectly on both e_0 and T :

$$\epsilon_a = 1 - (1 + w_p) e^{-(1.2 + 3w_p)^{0.5}} \quad (3.27)$$

where precipitable water (w_p) is calculated following an empirical equation given also by Prata (1996):

$$w_p = 46.5 \frac{e_0}{T_a} \quad (3.28)$$

where T_a is screen level air temperature in K. The actual vapour pressure is $e_0 = e^* RH$, where e^* is saturated vapour pressure computed following Lowe's (1977) polynomials (Equation 3.30), and RH is relative humidity from 0.0 to 1.0. This equation best fits extensive data from radiosonde stations around the world, and it is for standard pressure, which certainly is not the case in the Andes. The column of water above the site of interest is much smaller at 4600 m than at sea level, and therefore this correction needs to be taken into account. Prata gives a precise derivation of the relationship between vapor pressure and precipitable water, which requires knowledge of the scale height of the atmosphere and the lapse rate, and the solution is a degenerate hypergeometric function (for a general description of this type of function see for example Weisstein (1999), and for a detailed discussion see Gradshteyn and Ryzhik (1980)). For simplicity, speed of implementation and because of the lack of information about the atmospheric conditions aloft, an empirical formula suggested by Paltridge and Platt (1976) is used

here. Thus, the correction of precipitable water to the datum conditions is:

$$w_p = w' \left(\frac{p_z}{103.25} \right)^{3/4} \left(\frac{273}{T_a} \right)^{1/2} \quad (3.29)$$

here w' is the result of Equation 3.28 and p_z is local pressure at height z .

Lowe's (1977) polynomials for the calculation of saturation vapour pressure are as follows:

Over water:

$$\begin{aligned} a_0 &= 6984.505294 \\ a_1 &= -188.9039310 \\ a_2 &= 2.133357675 \\ a_3 &= -1.288580973e - 2 \\ a_4 &= 4.393587233e - 5 \\ a_5 &= -8.023923082e - 8 \\ a_6 &= 6.136820929e - 11 \end{aligned}$$

$$e^* = a_0 + T(a_1 + T(a_2 + T(a_3 + T(a_4 + T(a_5 + T a_6))))) \quad (3.30)$$

For the saturation vapour pressure over ice, the polynomials are:

$$\begin{aligned} T &= T - 273.15 \\ a_0 &= 6.109177956 \\ a_1 &= 5.03469897e - 1 \\ a_2 &= 1.886013408e - 2 \\ a_3 &= 4.176223716e - 4 \\ a_4 &= 5.824720280e - 6 \\ a_5 &= 4.838803174e - 8 \\ a_6 &= 1.838826904e - 10 \end{aligned}$$

and then also are applied to Equation 3.30

Finally the effect of sky obstruction and long-wave emission by surrounding slopes is considered in a similar way as for short-wave radiation, using the sky view factor. This approach has been widely used before (Olyphant 1986b, Duguay 1995, Plüss and Ohmura 1997). Incoming Long-wave radiation is:

$$L \downarrow = \epsilon_a \sigma T^4 f_v + \epsilon_s \sigma T^4 (1 - f_v) \quad (3.31)$$

where, ϵ_s is snow emissivity, taken as 0.99, σ is the Stephan-Boltzman constant and the sky view factor f_v is defined in Section 4.6.

Different parameterisations have been proposed to evaluate the effect of cloudiness on downward long-wave radiation (Brutsaert 1982, pp. 142–144; for a review see Oke 1987). These parameterisations require information on the type of clouds, fraction of sky covered by all or every type, and ideally the base height and temperature of the cloud. This information is not available for the present study.

3.4 Turbulent heat transfer

Interchange of energy between the snow surface and the lower part of the atmospheric boundary layer (surface sublayer) takes place mainly in the form of vertical transfer by convective motion. By comparison, molecular diffusivity is insignificant, and about five orders of magnitude smaller (Paterson 1994). In the present study we are interested in the transfer of two entities: heat and water vapour. Transfer of water vapour means evaporation or condensation, and the related absorption or liberation of latent heat. The associated energy flux is computed by multiplying the mass interchange of water vapour by the latent heat of sublimation when the snow is dry or by the latent heat of evaporation when there is water present (Grenell and Konzelmann 1994). The best approach to evaluate convective fluxes is by the eddy fluctuation or eddy correlation method (Oke 1987, Munro 1989). This method requires delicate instruments that can detect instantaneous variation in the vertical velocity of wind and of any entity under study (e.g. water vapour), and recording equipment capable of processing large amounts of information. It is clear that these requirements render the method inappropriate for a light expedition to high altitude glaciers, and therefore an alternative method is necessary. A second approach is using an aerodynamic profile, which requires the measurement of wind, temperature and humidity at various levels above the surface. This approach necessitates a moderate amount of instrumentation but is very sensitive to instrumental error, and as Denby and Grenell (2000) have shown its theoretical application is highly questionable over a glacier in the presence of katabatic winds.

The method employed in this study was the bulk-transfer method, as explained by Munro (1989), using the Monin–Obukhov stability length with the formulation presented by Brutsaert (1982), and the scalar roughness lengths corrections suggested by Andreas (1986). The approach has been used successfully in areas of similar climatic conditions, where evaporation is likely to be important (Marks and Dozier 1992, Aizen et al. 1997). In this approach temperature, wind speed and humidity are measured at one single level, usually at 2 m above the surface. Humidity at the snow surface is considered to be at the saturation point for the corresponding temperature of the snow, which is zero for melting conditions and very problematic to determine for non-melting snow as we will see later. Wind speed is assumed to become zero near the surface, depending on roughness length.

3.4.1 Background theory

The concept of atmospheric boundary layer (ABL) was introduced by Prandtl (1904) for the transport of momentum in the neighbourhood of a solid wall. It is assumed that the horizontal scales are much larger than the vertical and that the horizontal gradients and vertical velocities are negligible compared to the vertical gradients and horizontal velocities (Brutsaert 1982, p. 52). In the surface sublayer of the ABL, where turbulence is modulated or generated by wind shear near the ground, the vertical flux of horizontal momentum is:

$$\tau_{xz} = -\bar{\rho} \overline{w' u'}_s \quad \text{and} \quad \tau_{yz} = -\bar{\rho} \overline{w' v'}_s \quad (3.32)$$

where u, v, w are the Cartesian components of the wind vector, τ is stress and x, y, z the Cartesian axes, the overbar denotes mean values and prima denotes instantaneous values. The subscript s denotes values measured near the surface. The turbulent momentum flux acts like a stress (Stull 1988, p. 65), called the Reynold stress:

$$\tau_{Rey.} = [\tau_{xz}^2 + \tau_{yz}^2]^{1/2} \quad (3.33)$$

It is useful to introduce now a velocity scale, the friction velocity, which by definition is:

$$u_*^2 = [\overline{w' u'}_s^2 + \overline{w' v'}_s^2] \quad (3.34)$$

$$u_* = (\tau_{Rey.}/\rho)^{1/2} \quad (3.35)$$

The logarithmic wind profile law, also introduced by Prandtl (1932), and based on dimensional analysis, states that in a plan-parallel flow, wind mean speed increasing in the vertical direction ($d\bar{u}/dz$) indicates downward momentum flux and a sink at the surface. Measurements confirm that the profile is logarithmic in near-neutral atmospheres in the first few metres above the surface (Paterson 1994). Thus, in the dynamic sublayer, the fully turbulent region closer to the surface where Coriolis forces and buoyancy are negligible, we have:

$$\frac{u_*}{(z - d_0)(d\bar{u}/dz)} = k \quad (3.36)$$

integrating:

$$\bar{u} = \frac{u_*}{k} \ln \left(\frac{z - d_0}{z_0} \right) \quad (3.37)$$

where z_0 , the roughness length, is an integration constant that can be interpreted as the height above surface where the wind speed becomes zero (typical values over snow and ice range from 0.001 mm to a few cm (Paterson 1994)); the term d_0 (Paeschke 1937) is the zero-plane displacement height, introduced for rough surfaces, where the zero level reference is at a certain height between the base and the top of the roughness elements; following Brutsaert (1982) it is computed as $(2/3.0)7.35z_0$; k is the von Karman's constant, an empirical constant the value of which is 0.40, although some other values have been suggested. A similar approach can be used for deriving expressions for specific humidity and

other scalar admixtures whose presence do not affect the dynamics of flow (Brutsaert 1982):

$$\frac{E}{u_*(z - d_0)\rho(d\bar{q}/dz)} = -a_v k \quad (3.38)$$

where a_v is the ratio of eddy diffusivity to eddy viscosity for water vapour and \bar{q} is mean specific humidity. Similarly, for the flux of sensible heat H :

$$\frac{H}{u_*(z - d_0)\rho c_p(d\bar{\theta}/dz)} = -a_h k \quad (3.39)$$

where c_p is the specific heat of dry air at constant pressure ($= 1004.67 \text{ JK}^{-1}\text{K}^{-1}$) and a_h is the ratio of eddy diffusivity to eddy viscosity for heat. Although some experiments suggest that $a_h = a_v > a_m$, a_m for momentum, Stull (1988, p. 204) finds no theoretical reason for this and suggest some pressure correlation contamination effect in the measurements. A value of 1.0 will be used here.

In the surface sublayer, the lower part of the ABL above the roughness obstacles, flow is relatively unaffected by roughness elements and Coriolis forces, but buoyancy due to density gradient must be considered. Following Brutsaert (1982) the vertical acceleration of an air parcel, can be approximated to:

$$\ddot{z} = -\frac{g}{T_a} \left(\frac{\partial \theta}{\partial z} + 0.61 T_a \frac{\partial q}{\partial z} \right) \quad (3.40)$$

and the contribution of buoyancy to turbulent kinetic energy in a horizontally homogeneous surface sublayer is, to a close approximation:

$$\frac{g}{\rho T_a} \left[\left(\frac{H}{c_p} \right) + 0.61 T_a E \right] \quad (3.41)$$

Equations 3.40 and 3.41 describe the effect of atmospheric stability on turbulent transport. From the dimensionless analysis and equations 3.36, 3.38 and 3.39 the dimensionless characteristics of the turbulence depends on $z - d_0$, τ_0 , ρ and buoyancy (Equation 3.41) (Brutsaert 1982). The combination of these four quantities into one dimensionless variable was proposed by Monin and Obukhov (1954) as:

$$\zeta = \frac{z - d_0}{L} \quad (3.42)$$

where the Obukhov's stability length L is defined as:

$$L = \frac{-u_*^3 \rho}{kg \left[\left(\frac{H}{T_a C_p} \right) + 0.61 E \right]} \quad (3.43)$$

where g is the acceleration of gravity (Obukhov 1946, Businger and Yaglom 1971).

Finally we get the profiles for wind speed, water vapour and heat, considering measurements at one

level and at the surface, as:

$$u_* = \frac{\bar{u}k}{\ln\left(\frac{z-d_0}{z_{0m}}\right) - \Psi(\zeta)} \quad (3.44)$$

$$E = \frac{(q_a - q_s)a_v k u_* \rho}{\ln\left(\frac{z_q-d_0}{z_{0v}}\right) - \Psi_{sv}(\zeta)} \quad (3.45)$$

$$H = \frac{(\theta_a - \theta_s)a_h k u_* \rho C_p}{\ln\left(\frac{z_t-d_0}{z_{0h}}\right) - \Psi_{sh}(\zeta)} \quad (3.46)$$

Subscripts m, v, h refer to momentum, water vapour and heat respectively. The air density ρ for a given pressure is computed as the sum of densities of dry air ρ_d and water vapour ρ_v (Brutsaert 1982, Jacobson 1999):

$$\rho_d = p_d / (R_d * T_a) \quad (3.47)$$

$$\rho_v = 0.622 * e_0 / (R_d * T_a) \quad (3.48)$$

$$\rho = \rho_d + \rho_v \quad (3.49)$$

where the partial pressure of water vapour is $p_d = p_z - e_0$ and p_z is computed in Equation 3.11, R_d is the gas constant for dry air and $0.622 = 18.016/28.966$ is the ratio of the molecular weights of water and dry air. The specific humidity at screen level q_a and on the snow surface q_s is calculated as:

$$q = \rho_v / \rho \quad (3.50)$$

The Ψ_s functions are stability corrections, which depend on the Obukhov's stability length. There is some disagreement on their values, which have been obtained empirically (Brutsaert 1982, pp. 68-71). The values used here are similar to those used by Marks and Dozier (1992), also reported by Brutsaert (1982). Thus, for unstable conditions ($\zeta = (z_u - d_0)/L \leq 0$):

$$\Psi_{sv}(\zeta) = 2 \ln\left(\frac{1+\chi^2}{2}\right) \quad (3.51)$$

$$\Psi_{sm}(\zeta) = 2 \ln\left(\frac{1+\chi}{2}\right) + \ln\left(\frac{1+\chi^2}{2}\right) - 2 \arctan \chi + \frac{\pi}{2} \quad (3.52)$$

$$\Psi_{sh}(\zeta) = 2 \ln\left(\frac{1+\chi^2}{2}\right) \quad (3.53)$$

with $\chi = (1 - 16\zeta)^{1/4}$

For stable conditions ($\zeta = (z - d_0)/L > 0$):

$$\Psi_s(\zeta) = -\beta\zeta \quad \text{and} \quad \beta = 5 \quad (3.54)$$

A standard approach for the computation of the roughness length for momentum is to extrapolate the profiles of wind speed under neutral conditions to the level where wind speed equals zero (Stull 1988, Munro 1989, Greuell and Smeets 2001). However, this procedure requires measurements at at least two levels and is very sensitive to instrument errors. Furthermore, under katabatic winds the theoretical assumptions for estimating z_0 using the aerodynamical profile do not hold (Denby and Greuell 2000), therefore, a microtopographic survey is recommended. According to Brutsaert (1982), the value of z_0 is theoretically independent of the flow, except for flexible obstacles and waves), and only depends on the geometry of the surface. It was calculated as $z_0/h = 0.5\lambda$, where h is the roughness element height and λ is the frontal area index or vertical silhouette area per unit ground area (Lettau 1969). Data from wind tunnel experiments and atmospheric observations show that z_0/h increases linearly with λ for $\lambda < \lambda_{max}$ (Raupach 1992). The precise form of this function and the value of λ_{max} depends on the geometry of the roughness elements, but the above linear relationship was found satisfactory for very rough snow surfaces on Vatnajökull, Iceland, by Smeets et al. (1999). The frontal area index will change depending on wind direction, and so will the surface roughness length, sometimes on a very large range (Jackson and Carroll 1977). There is ample scope for inaccuracies using this method for variable roughness elements; however it is reassuring to notice that according to Denby and Greuell (2000), an order of magnitude error in the estimation of z_0 will only result in a 25% error in the turbulent fluxes estimation using the bulk method.

The transfer mechanisms of momentum and of other scalar admixtures are different at the surface, and consequently the roughness lengths have different values for momentum, water vapour and heat, which were calculated following Andreas (1987). He developed a fitting polynomial of the scalar roughness lengths over snow and sea ice (the coefficients for this are given in table 3.1):

$$\ln(z_s/z_0) = b_0 + b_1 \ln R_e + b_2 (\ln R_e)^2 \quad (3.55)$$

where z_s refers to water vapour or heat depending on the coefficients used. The Reynolds number R_e is a ratio of inertial to viscous forces (Stull 1988) defined as:

$$R_e = \frac{u_*}{z_0 \nu} \quad (3.56)$$

and $\nu = \mu/\rho$ is the kinematic viscosity of air, with μ the coefficient of dynamic viscosity for air.

	$R_e \leq 0.135$	$0.135 < R_e < 2.5$	$2.5 \leq R_e \leq 1000$
Temperature			
b_0	1.250	0.149	0.317
b_1	—	-0.550	-0.565
b_2	—	—	-0.183
Water vapour			
b_0	1.610	0.351	0.396
b_1	—	-0.628	-0.512
b_2	—	—	-0.180

Table 3.1. Values of the coefficients in the polynomials (equation: 3.55) that predict z_0/z for temperature and water vapour (Andreas 1987) for smooth, transition and rough surfaces.

3.5 Internal heat fluxes

Other energy inputs to the snow pack proceed from horizontal advection and conduction, heat due to ice deformation and in some cases geothermal heat. Except in the last case, which may be important, these fluxes are small compared to radiative and turbulent fluxes, and for simplicity they can be neglected (Greuell and Konzelmann 1994, Arnold et al. 1996).

3.6 Temperature fluctuation

From the previous formulation of long-wave radiative fluxes and for both latent and sensible turbulent fluxes it is clear that the temperature of the snow surface is a very relevant parameter. Measuring this temperature accurately and without perturbing the snow surface is a difficult task. Andreas (1986) proposed a new method for its measurement, but it requires additional instrumentation and may not be reliable under intense evaporation. When there is a mixture of snow and water under melting conditions, the whole surface is assumed to be at melting point, but at night and at high altitudes, where snow is dry, the estimation is more complicated. The sensors available for this study were thermistors, which have different emissivity than snow, and therefore are subject to a different rate of radiative cooling and heating (Brandt and Warren 1993). During the day, if they are exposed to direct solar radiation, their temperature raises considerably, melting surrounding snow and getting progressively buried. Thus, the recorded temperature may be approximate at night but unreliable during the day unless there is evidence of melting. The recorded temperature reflects the temperature of a thicker layer near the surface, and not the skin temperature. This layer is approximately equal to the largest dimension of the probe, as its position may change as it melts and gets buried. The actual value of snow surface temperature is only approximate.

To enable the modelling of the spatially distributed components of the energy balance for the whole

area of the glacier, which requires intense computation, a very simple approach was used to estimate snow surface temperature. The change in temperature of a given volume of snow is proportional to the energy input and to the thermal properties of the snow. For a one dimensional system atmosphere – snow surface layer – subsurface snow pack the thermodynamic equation describing the conservation of energy, neglecting melting and refreezing, can be described as (Koh and Jordan 1995, Greuell and Konzelmann 1994):

$$\rho_s c_s \frac{\partial T}{\partial t} = \frac{\partial}{\partial z} \left(k_s \frac{\partial T}{\partial z} \right) - \frac{\partial Q_s}{\partial z} \quad (3.57)$$

This equation is applied in a very simplified form following Oke (1987) and implemented using finite differences:

$$\frac{\Delta Q_s}{\Delta z} = C_s \frac{\Delta \bar{T}}{\Delta t} \quad (3.58)$$

where ΔQ_s is the flux density energy used to heat the snow at the surface, and C_s is the heat capacity of the snow $C_s = \rho_s c_s$, ρ_s is snow density and c_s is the specific heat of snow ($2.09 \times 10^3 \text{ J kg}^{-1} \text{ K}^{-1}$). As the main energy input comes from the surface, while the subsurface remains at a relatively stable temperature, we need to consider the thermal conductivity of the snow and the energy losses to subsurface layers:

$$Q_g = -\kappa_{Hs} C_s \frac{\partial \bar{T}}{\partial z} \simeq -k_s \frac{\Delta \bar{T}}{\Delta z} \quad (3.59)$$

where κ_{Hs} is the thermal diffusivity of the snow and k_s its thermal conductivity.

The volume of snow considered is that affected by the daily temperature changes at the surface. This temperature oscillation decreases exponentially with depth, and its amplitude at any given distance from the surface can be estimated according to Oke (1987) by

$$\Delta \bar{T}_z = \Delta \bar{T}_0 e^{-z(\pi \kappa_{Hs} P)^{1/2}} \quad (3.60)$$

where P is the wave period. Brutsaert (1982, equation 6.43) has shown that, roughly, 95% of the wave is damped at a depth of $3(2\kappa_{Hs}/\omega)^{1/2}$, where $\omega = 2\pi/P$. For a daily oscillation in the conditions of the present study this equation yields a value of 0.31 m. This figure agrees well with snow temperature profiles measured on other high altitude Andean glaciers (Wagnon 1999, Figure 3.11).

If we look in detail at the components of the energy fluxes at the surface, we can separate them into two groups, one that affects the uppermost surface layer and the other that can penetrate to a certain depth. In the first group are the turbulent heat interchange, the thermal radiation and the near infrared component of the short-wave radiation. Following Greuell and Konzelmann (1994), 36% of the total short-wave radiation is classified in the band below $0.8\mu\text{m}$, which is absorbed near the surface. The band above this wavelength penetrates the snow pack and in theory it should be attenuated following Beer's law. However, because the combined effect of absorption, scattering, and the rapid change of the spectral composition of the downward flux, the attenuation does not follow an exponential decay in approximately the first 40 cm (Warren 1982). The additional radiative cooling at the surface may result

in a temperature maximum located somewhere below the surface (Warren 1982, Brun et al. 1989, Koh and Jordan 1995), which in some cases may lead to subsurface melting. This case was detected by Koh and Jordan (1995) using a high frequency-modulated continuous radar wave, which, by detecting changes in the dielectric properties of the snow, can determine accurately the onset of melting in internal layers. In the high Andes it was observed that the uppermost layer about 2.5 cm thick, was almost permanently frozen, while snow underneath was loose, with grains unbounded. This was likely to be caused by radiative cooling and negative turbulent heat transfer at the surface, while shortwave radiation penetrates underneath the surface. In order to replicate this situation in a simplified model, the snow pack was divided in two layers, the first one about 2.5 cm depth from the surface and a second subsurface layer from -2.5cm to the depth where the daily temperature wave is almost damped (31 cm, 3.6). The energy fluxes and temperature variations modelled for both layers.

3.7 Model validation and applicability

To gain some confidence in the performance of the model and its application to a wide range of conditions, it was compared to data collected both in the Andes and at the Haut Glacier d'Arrolla.

3.7.1 Short-wave validation

Figure 3.4 shows the recorded and measured short-wave radiation. Modelled radiation is separated into direct, diffuse and diffuse-reflected components. At this stage the modelled values do not incorporate cast shadows but take into account the slope of the ground. The AWS was situated on a gently sloping section of the glacier (10° to the west). The modelled values derive this inclination from the gradient of the corresponding cell in the digital elevation model. Neglecting this slope results in a large error and a different distribution of incoming solar radiation during the day. Figure 3.5 shows the values of measured and modelled solar radiation for Loma Larga glacier, at 4667 m a.s.l. Errors in both cases are smaller than the pyranometer accuracy.

3.7.2 Long-wave validation

In the Andes direct measurements of long-wave radiation were not available, thus only data from Arolla is used here for the validation. Net long-wave radiation was estimated from the difference between measured net all-wave radiation and measured net short-wave radiation. Net all-wave radiation was measured with a Kipp & Zonen NR-Lite net radiometer and net short-wave radiation is derived from the values measured by two Kipp & Zonen opposed pyranometers. The NR-Lite net radiometer is a simple, low maintenance instrument, and even when daily values are within the nominal accuracy, the

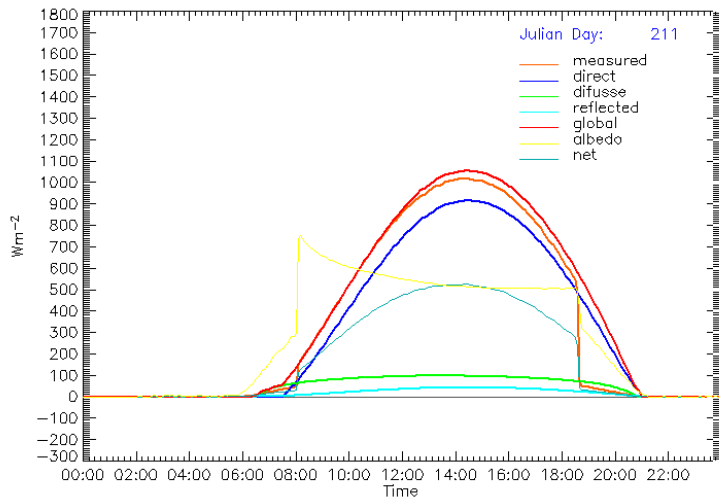


Figure 3.4. Measured and modelled short-wave radiation at the Haut Glacier d'Arolla, 2900m a.s.l., Swiss Alps, on a typical clear day. Diffuse radiation is separated into that from sky and that from surrounding slopes. The fit is better than the accuracy of the pyranometer (10%). 7 LINES ONLY 6 LEGEND

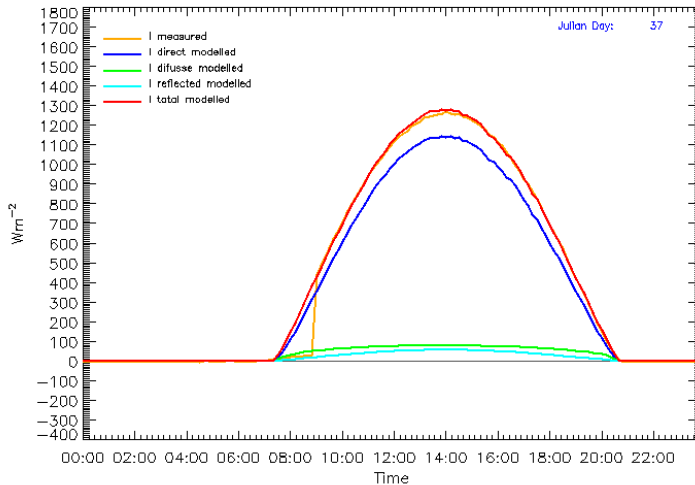


Figure 3.5. Measured and modelled short-wave radiation at Loma Larga glacier, 4667 m a.s.l. Diffuse radiation is separated into that from sky and that from surrounding slopes. For the aerosol transmittance, visibility is assumed to be 100 km through the whole day, whereas for other transmittances, meteorological variables recorded at 10 minute interval were used. The fit is better than the accuracy of the pyranometer (10%). Cast shadows and the fraction of shaded surrounding slopes are not computed at this stage.

different responses of the two instruments produces some artifacts in the data, as the pronounced troughs in Figure 3.6 near sunset and sunrise. After consultation with Campbell Scientific UK, it was concluded that these troughs are likely to be caused by the different cosine response of the net radiometer and the

pyranometers, plus some delay in the time response of the net radiometer.

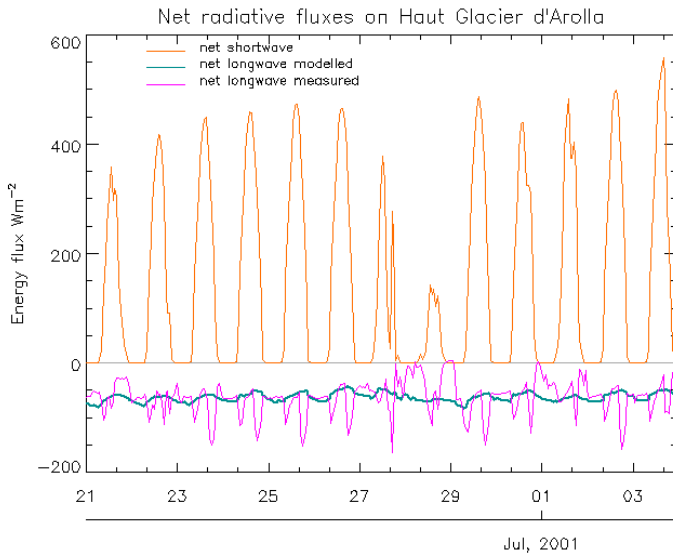


Figure 3.6. Modelled and measured net long-wave radiation for a 2-week period in summer 2001 at the Haut Glacier d'Arolla, Swiss Alps. Note that the pronounced troughs in measured long-wave are likely to be instrumental artifacts, as explained in the text, and that values are modelled only for clear skies, so peaks under cloudy conditions are not reproduced. The average difference between modelled and measured values under cloudless skies, after discharging near sunset and near sunrise values, is less than 1%.

3.7.3 Snow temperature model validation

The modelling of surface temperature requires a detailed knowledge of the energy balance, but the computation of the energy balance requires a detailed knowledge of the surface temperature. It would be a difficult problem to solve if it were not for the fact that the whole process is strongly stable and there are a number of feedbacks involved which tend to make all the related variables in the model converge to realistic values. Thus, if there are clear boundary conditions, the whole process of energy balance and snow surface temperature can be modelled within a narrow margin. The stability of the process is illustrated in figures 3.7 and 3.8, where the initial temperature was set to 200 K. Fluxes at any time step i are modelled with the temperature calculated at time step $i - 1$ and then T_i recalculated with the computed fluxes. Establishing an arbitrary low T_0 allows the testing of the convergence of the model to real values and also its stability. The convergence speed of modelled and measured values is inversely related to the thickness of the uppermost snow layer, but in any case it only takes a few timesteps.

Figure 3.7 shows the measured and modelled temperatures of the total surface layer for a two week period on Loma Larga glacier, 4667m a.s.l. The glacier was covered in penitentes, and the two measured temperatures were at different positions on the surface of penitentes (T_1 near the penitentes' trough and

3.7. Model validation and applicability

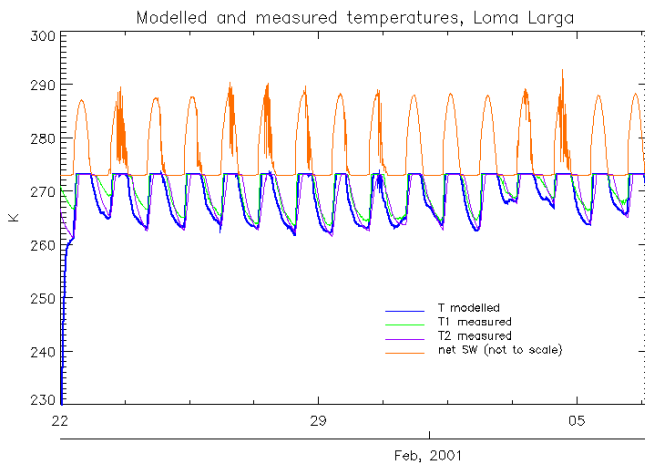


Figure 3.7. Comparison between modelled and measured temperatures on the surface of Loma Larga glacier, 4667 m.a.s.l. The surface was covered in snow penitentes and the measurement sites at T1 (closer to the bottom of penitentes) and T2 (closer to the penitentes' peak) had a slightly different net energy flux. Site T2 was likely to undergo a more intense radiative cooling. Initial modelled temperature was set to -73.15°C (200 K) to assess the stability of the model and the rapid convergence of modelled values to measured ones.

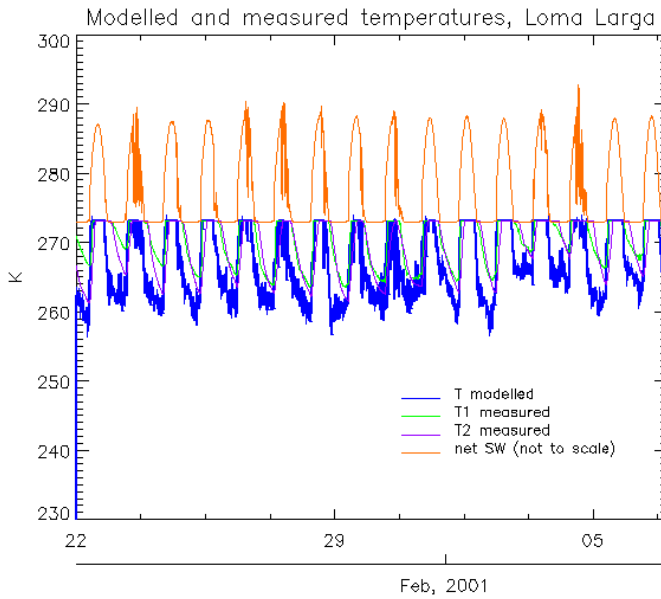


Figure 3.8. Comparison between modelled and measured temperatures on the surface of Loma Larga glacier, as in Figure 3.7, but modelled for the uppermost surface layer, about 2 cm depth.

T_2 closer to the peaks). This resulted in different sky view configurations and differences in the incoming and outgoing long-wave radiative fluxes, and therefore different rates of radiative cooling. Additional delays in the lowering of recorded temperature, especially when direct solar radiation decreases, may be

due to the presence of liquid water in the troughs between penitentes. Water has higher specific heat and therefore is likely to have a buffering effect in the temperature fluctuations. The modelled temperature is for an intermediate value of sky view factor and for the whole surface layer. Figure 3.8 shows modelled temperature for the uppermost surface layer, about 2.5 cm in depth. Here variation is faster and minimum temperatures are attained very soon. According to values of skin temperature measured with a hand held infrared thermometer, this second situation is likely to be more realistic. Values show a very rapid change within a range of a few degrees, normally associated with wind gusts, suggesting the importance of latent heat fluxes in the cooling of the surface. For the global evaluation of the energy balance, both surface and subsurface layers were considered, as indicated in Figure 3.7. However, the detailed variation of the thin, uppermost surface layer may be of interest to the initial process of snow metamorphism and micropenitentes formation. It would be desirable a precise recording of its temperature fluctuations in order to minimise errors derived from model simplifications. There are no snow surface temperature measurements for Arolla.

3.7.4 Net energy balance and melt validation

To assess all the modelled fluxes at the snow surface, the net energy balance is estimated and the corresponding melt computed. Figure 3.9 shows the measured and modelled fluxes at the AWS on Loma Larga glacier. An unusual pattern is observed in the last hours of the afternoon, when the albedo values rise sharply to almost 1.0. It may be the effect of a nearby icefall, which increases the diffuse radiation, or it could be explained by a sharp increase in reflected diffuse radiation as the sun hits the penitentes' slanting wall from the west at a very low angle. Snow is not a perfect lambertian reflector, the reflected diffuse radiation field having a prominent forward lobe at low incident angles (Warren 1982), thus at high zenith angles the upward component of the reflected radiation may increase considerably, especially when the sun hits the sloping back walls of the penitentes. The fact that the increase in albedo happens after 1800 h (Figure 3.10, when the solar azimuth enters the southwestern quadrant, adds support to this hypothesis.

There were no independent measurement of sensible and latent fluxes available for the present work, nor evaporation measurements; therefore it is impossible to make a strict and rigorous assessment of the accuracy of the method. However, it has been used successfully on snow research in previous cases, over a wide range of climatic conditions (Marks and Dozier 1992, Plüss and Mazzoni 1994, Arnold et al. 1996, Aizen et al. 1997, Brock and Arnold 2000, Obleitner 2000), and it seems appropriate for sites where evaporation is an important component of the energy balance (Marks and Dozier 1992, Aizen et al. 1997). Figure 3.11 shows the application of the whole energy balance to estimating melt at a point during a 2-week period in summer 2001 on the Haut Glacier d'Arolla. Ablation was measured with a Campbell SR50 ultrasonic snow depth gauge and compared to modelled ablation. Precipitation is included, but estimating the right amount of precipitation is problematic. Firstly rain gauges are not very accurate when rain or snow falls during windy conditions. Secondly the rain gauge was at the snout

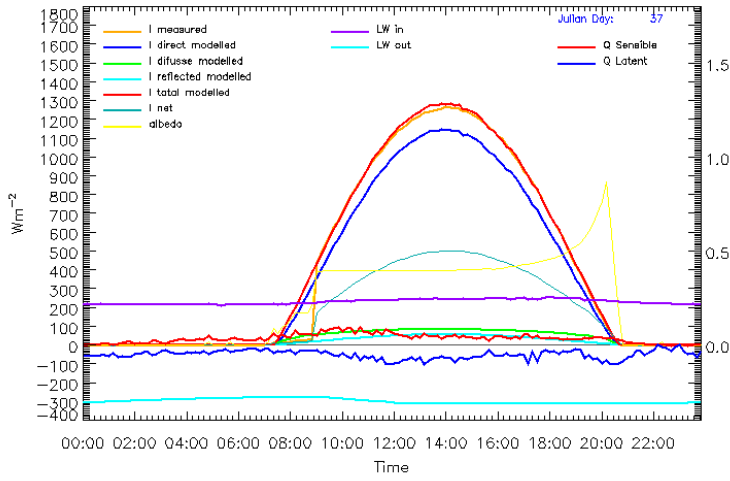


Figure 3.9. Energy fluxes on a clear day on Loma Larga glacier, 4667 m a.s.l. DOY 37, 6th of February. Note the increasing albedo in the afternoon, when the apparent position of the sun changes from north to south (see Figure 3.10), an explanatory hypothesis is given in the text.

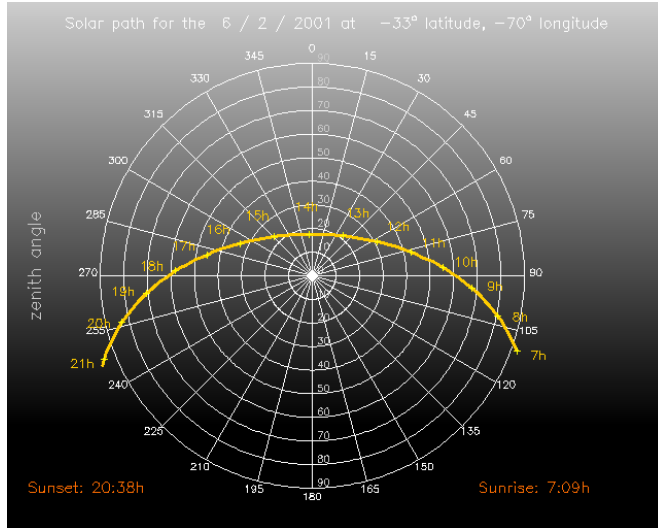


Figure 3.10. Solar path for the day 37 (6 February, 2001) at 33° S, 10° W. The sun crosses to the southern apparent position at about 18:00, when the recorded albedo starts to increase (see text for tentative explanation). I have made the IDL code for plotting the solar path available at the IDL user contributed library at www.rsinc.com/.

of the glacier, a few kilometres away from the ultrasonic gauge. Finally, the conversion of new snow to depth equivalent depends on snow density and wind redistribution, which are difficult to evaluate. From Figure 3.11 it seems that the pattern of modelled and measured melting follows a close relationship until day 29, a cloudy day, with little energy available for melting. Here the model underestimates total melting, and the cause could be an underestimation of turbulent fluxes or an anomalous high value of radiative cooling, as can be deduced from the very low trough in net radiation. This trough is also rather anomalous, one would expect a minimum value on very clear nights, and it could be hypothesized that such a situation is likely to happen after the pass of a perturbation and the clearing up of clouds in a

cleaner air. However a more sophisticated Kipp & Zonen CNR1 net radiometer in the lower section of the valley did not record this trough, which suggests an instrumental artifact. It is worth saying that Plüss and Mazzoni (1994) noted the underestimation of total melt energy using a bulk method when compared to total melt directly measured with a lysimeter, and Hock (2002) noted that calculated melt energy was underestimated in days with precipitation or dense fog in her study of Storglaciaren, in northern Sweden. These discrepancies recommend a more detailed survey of modelled and measured melt values, even when as in the examples given here, modelled results agree within a few percent of measured ones.

A comparison of calculated melt with sparse data from ablation stakes in Juncal Norte glacier near the lower AWS in the Andes campaign is shown in Figure 3.12, where the symbols show measured values from ablation stakes and the stepping line is modelled melt. The main uncertainties derive from the exact estimation of the snow density and surface temperature and from errors inherent in the stake ablation method, such as snow compaction, stake deepening, etc. Nonetheless, the difference between modelled and measured values over a 11-day period is less than 2 cm or 3.3%.

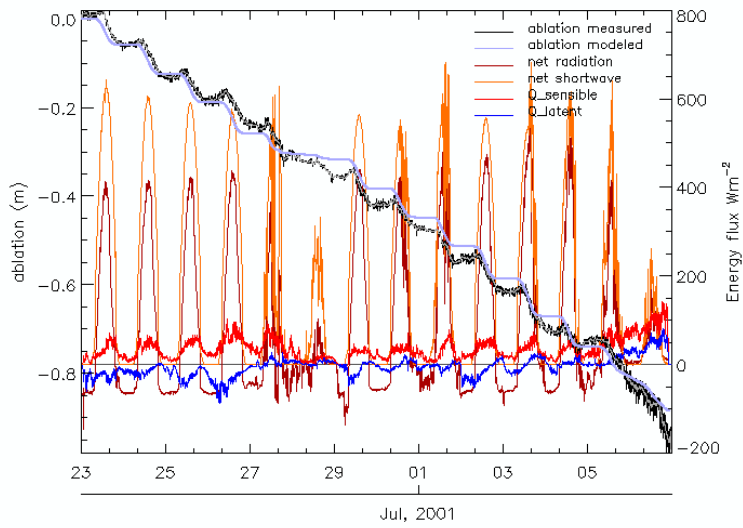


Figure 3.11. Energy balance components, modelled melt and measured snow depth at the Haut Glacier d'Arolla for a 2 week period in July 2001.

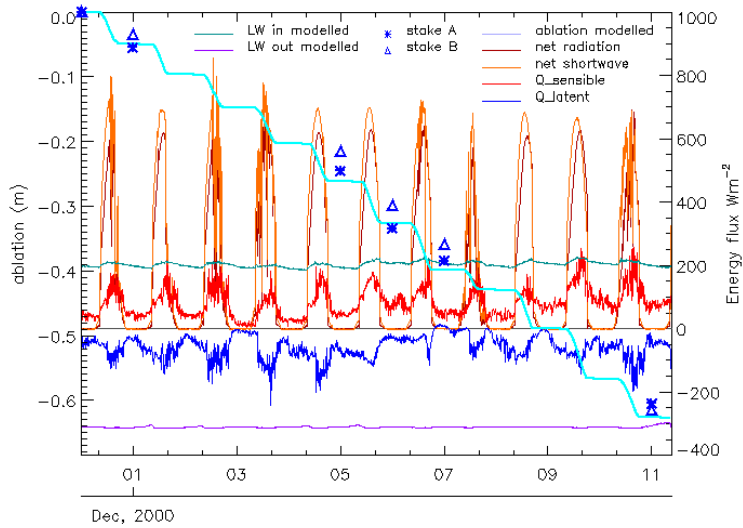


Figure 3.12. Energy balance components, modelled melt and measured snow lowering from ablation stakes on Juncal Norte glacier, 3035 m a.s.l. for a 11-day period in November–December, 2000. Note the maximum values of turbulent heat fluxes that correspond to wind speeds higher than 10 ms^{-1} and relative humidity lower than 20%.

Chapter 4

Modelling solar radiation over complex topography: I DEM tools

In this chapter a new set of vectorial algebra algorithms will be developed for the calculation of terrain parameters from digital elevation models and the solar radiation modelling in mountainous terrain.

4.1 Introduction

Digital elevation models (DEMs) are mathematical models of the earth's surface that, at present, are the most powerful method of representing relief (Stocks 1994). They are extensively used in environmental modelling and play an important role in geographic information systems (GIS).

Terrain parameters such as slope gradient and orientation of slope (aspect) are important controls in a number of surface processes, such as water runoff, erosion (Moore et al. 1993) and incoming solar radiation (Nuñez 1980, Barry 1992). These factors alone or combined are major controls in biological, glaciological and geomorphological processes, and thus have a decisive influence in biodiversity (Kumar and Skidmore 2000), tree line height (Kirckpatrick and Nuñez 1980), human settlement, fauna distribution (Stefanović and Wiersema 1985), tourism and recreation (e.g. ski slopes), local climatic conditions (Barry 1992), snow line and glacier mass balance (Willis et al. 1998, Brock, Willis, Sharp and Arnold 2000).

It is therefore understandable that considerable effort has been expended in developing fast and efficient algorithms to calculate the gradient of the surface from DEMs (for a review, see Skidmore 1989) and the variation of surface solar radiation with topography (Williams et al. 1972, Nuñez 1980, Dozier

and Frew 1990, Duguay 1995, Varley et al. 1996, Kumar et al. 1997).

Mountainous terrain is characterized by irregular and rapid changes in elevation over short distances. It is an environment where thresholds play an important role, for example in the influence of slope on landslides or avalanches (Wadge 1988, Dakhal et al. 2000). It is desirable to derive terrain parameters for these regions using algorithms that retain real extreme values minimizing any smoothing effect. Many methods for calculating slope from DEMs are based on a 3x3 kernel or ‘roving window’ displaced along the grid cells (Evans 1980, Horn 1981, Zevenbergen and Thorne 1987, Skidmore 1989). This approach has the advantage of minimising the effect of data errors in general, as it takes into consideration the 8 surrounding points to a given one (Horn 1981). However, as Hodgson (1995) has shown, the undesirable side effect is the computation of the slope for an equivalent area of up to twice the cell size. These methods also tend to underestimate slope on rough terrain and in coarse resolution grids (Chang and Tsai 1991, Gao 1997). According to Hodgson’s (1995) work, the most accurate algorithms for the combined estimation of surface and slope are those which use the four nearest neighbouring elevations in the grid. On most applications a compromise will be required between the original data quality and the accuracy or degree of smoothing of slope calculation algorithms. By using just one cell, the user keeps the final decision, as to whether the results are reliable or it is advisable to perform any further filtering or smoothing.

This paper presents an algorithm for calculating the gradient of the surface using the minimum areal unit in a DEM, that of the surface enclosed between 4 data points. To avoid confusion by the different definitions of the word gradient (Burrough 1986, p. 50), when used alone in this paper, the gradient is defined as a three dimensional unit vector perpendicular to the surface. From this vector slope and aspect can be calculated, although this step is unnecessary for solar radiation modelling using the sun position algorithm derived here. The sun position is defined as another unit vector in its direction, and thus, finding the angle between the sun and the normal to surface is equivalent to finding the solution to a dot product between both vectors. These algorithms make optimal use of the array handling power of modern computer programming languages, allowing fast implementation and running times. Furthermore the concept is easy to grasp and visualize.

4.2 Vector defining an inclined surface

We consider the smallest surface unit in a regularly gridded DEM as the plane enclosed by four data points: $z_{i,j}$, $z_{i+1,j}$, $z_{i,j+1}$, $z_{i+1,j+1}$, where $z_{i,j}$ is the elevation of a point at row i , column j (see Figure 4.1). Although it would be possible to extend the surface division into a triangular mesh (e.g. Wang, Robinson and White 2000), we prefer to keep the cell as the surface area unit for compatibility with other applications, such as raster information extracted from orthorectified photographs or satellite images, and for compatibility with existing models in glaciology, hydrology or snow studies, which are cell based (e.g. Arnold et al. 1996, Richards et al. 1996, Purves et al. 1998). It is also unreliable

interpolating values from the interior of a cell in mountain areas, characterised by non uniform change. However, as a plane is defined by three points in space, then the four points at the corners of the grid cell may delimit more than one single plane. As the resolution of the data does not permit defining the geometry of the area enclosed, a good approximation is to find an average between the two triangles at both sides of the cell diagonal. It can be shown that the result is the same whichever diagonal we choose. A vector normal to these surfaces is defined by half the sum of cross products of vectors along the sides of the grid cell, defined as in Equation 4.1. In Figure 4.1 these triangular surfaces are comprised between vectors \mathbf{a} \mathbf{b} and \mathbf{c} \mathbf{d} . The gradient will be the average of cross products $\mathbf{a} \times \mathbf{b}$ and $\mathbf{c} \times \mathbf{d}$. Ritter (1987) has previously used a vector based approach, although the approach taken in this paper differs in the selection of points to compute the slope and in the subdivision of the cell into two planes. The computation of surface area is also a new addition.

The resulting vector of a cross product has the length of the parallelogram whose sides are the vector factors. Thus, the modulus of the vector normal to surface calculated in this way will approximate the value of the surface area of the grid cell with accuracy proportional to the resolution of the grid.

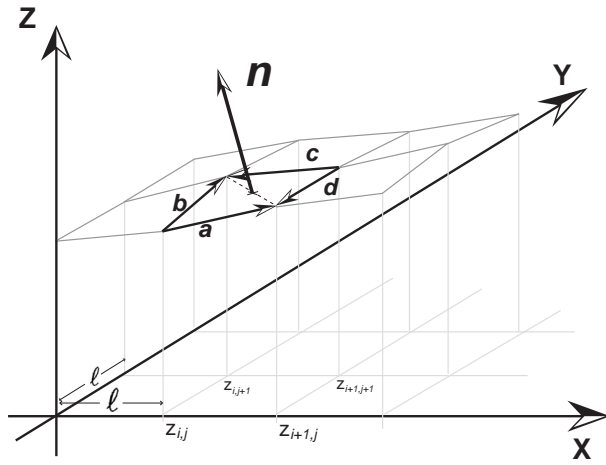


Figure 4.1. Vector normal to a grid cell surface. Vector \mathbf{n} is the average of cross products $\mathbf{a} \times \mathbf{b}$ and $\mathbf{c} \times \mathbf{d}$. Its length approximates the surface area of the grid cell with accuracy depending on resolution.

In a regular square grid of cell size ℓ , as in Figure 4.1, the x, y, z components of the vectors along the side of the grid cell are defined as:

$$\left\{ \begin{array}{ll} \mathbf{a} = (\ell, 0, \Delta z_a), & \text{with } \Delta z_a = z_{i+1,j} - z_{i,j} \\ \mathbf{b} = (0, \ell, \Delta z_b), & \text{with } \Delta z_b = z_{i,j+1} - z_{i,j} \\ \mathbf{c} = (-\ell, 0, \Delta z_c), & \text{with } \Delta z_c = z_{i,j+1} - z_{i+1,j+1} \\ \mathbf{d} = (0, -\ell, \Delta z_d), & \text{with } \Delta z_d = z_{i+1,j} - z_{i+1,j+1} \end{array} \right. \quad (4.1)$$

The vector normal to the grid cell, \mathbf{n} , will be:

$$\mathbf{n} = \frac{(\mathbf{a} \times \mathbf{b})}{2} + \frac{(\mathbf{c} \times \mathbf{d})}{2} = \frac{1}{2} \begin{vmatrix} \hat{\mathbf{i}} & \hat{\mathbf{j}} & \hat{\mathbf{k}} \\ \ell & 0 & \Delta z_a \\ 0 & \ell & \Delta z_b \end{vmatrix} + \frac{1}{2} \begin{vmatrix} \hat{\mathbf{i}} & \hat{\mathbf{j}} & \hat{\mathbf{k}} \\ -\ell & 0 & \Delta z_c \\ 0 & -\ell & \Delta z_d \end{vmatrix} \quad (4.2)$$

Simplifying the result of Equation 4.2 gives the components of the vector normal to surface in terms of grid elevation points and cell spacing as:

$$\mathbf{n} = \begin{pmatrix} 1/2 \ell (z_{i,j} - z_{i+1,j} + z_{i,j+1} - z_{i+1,j+1}) \\ 1/2 \ell (z_{i,j} + z_{i+1,j} - z_{i,j+1} - z_{i+1,j+1}) \\ \ell^2 \end{pmatrix} \quad (4.3)$$

The surface area of this cell will be $|\mathbf{n}|$, the length of vector \mathbf{n} . The unit vector in the direction of \mathbf{n} will be denoted \mathbf{n}_u .

This algorithm makes optimal use of the array handling capabilities of many computer languages and can be implemented very efficiently. The CPU time used for processing a DEM of about 250 000 cells, implementing the algorithm into IDL, on a Sun Enterprise 450 workstation was about 0.5 seconds excluding data input, and another half a second for the computation of the corresponding unit vectors and the area of every cell. Figure 4.2 shows a grey-scale representation of every component of the vector gradient for a DEM of the Mont Blanc Massif, French Alps, while Figure 4.3 shows the derived aspects.

If the slope and aspect of the surface need to be used, these can be calculated from the components of \mathbf{n}_u as follows:

$$\varsigma = \cos^{-1} \hat{n}_z \quad (4.4)$$

where ς is the slope and \hat{n}_z is the z coordinate of vector \mathbf{n}_u .

The aspect ϕ is not defined for slopes of 0 degrees, a vertical vector gradient. In any other case it can be calculated from the x, y components of \mathbf{n}_u . To make the gradient vector compatible with the sun vector, a left handed coordinate system has been chosen, with the X -axis (columns) increasing eastwards and the Y -axis (rows) increasing southwards. Counting clockwise from north, the aspect would be:

$$\phi = \frac{\pi}{2} + \tan^{-1} \frac{\hat{n}_y}{\hat{n}_x} \quad (4.5)$$

The sign of the coordinates needs to be taken into account to decide on which quadrant the vector lies in. The tangent is not defined when the horizontal projection of \hat{n} lies on the Y axis ($\text{unitvn}_x = 0$) and it is ambiguous when it lies on the X axis. Alternatively, the ratio between the sine and cosine of \hat{n}_{xy} could be used (e.g. Horn 1981). The above coordinate system is a mirror image of those commonly

used in DEMs, with the Y -axis increasing northwards. To apply Equation 4.5 in this case we only need to invert the y -coordinate of vector \hat{n} . The graphic visualisation of these results are shown in Figures 4.2 c and 4.3.

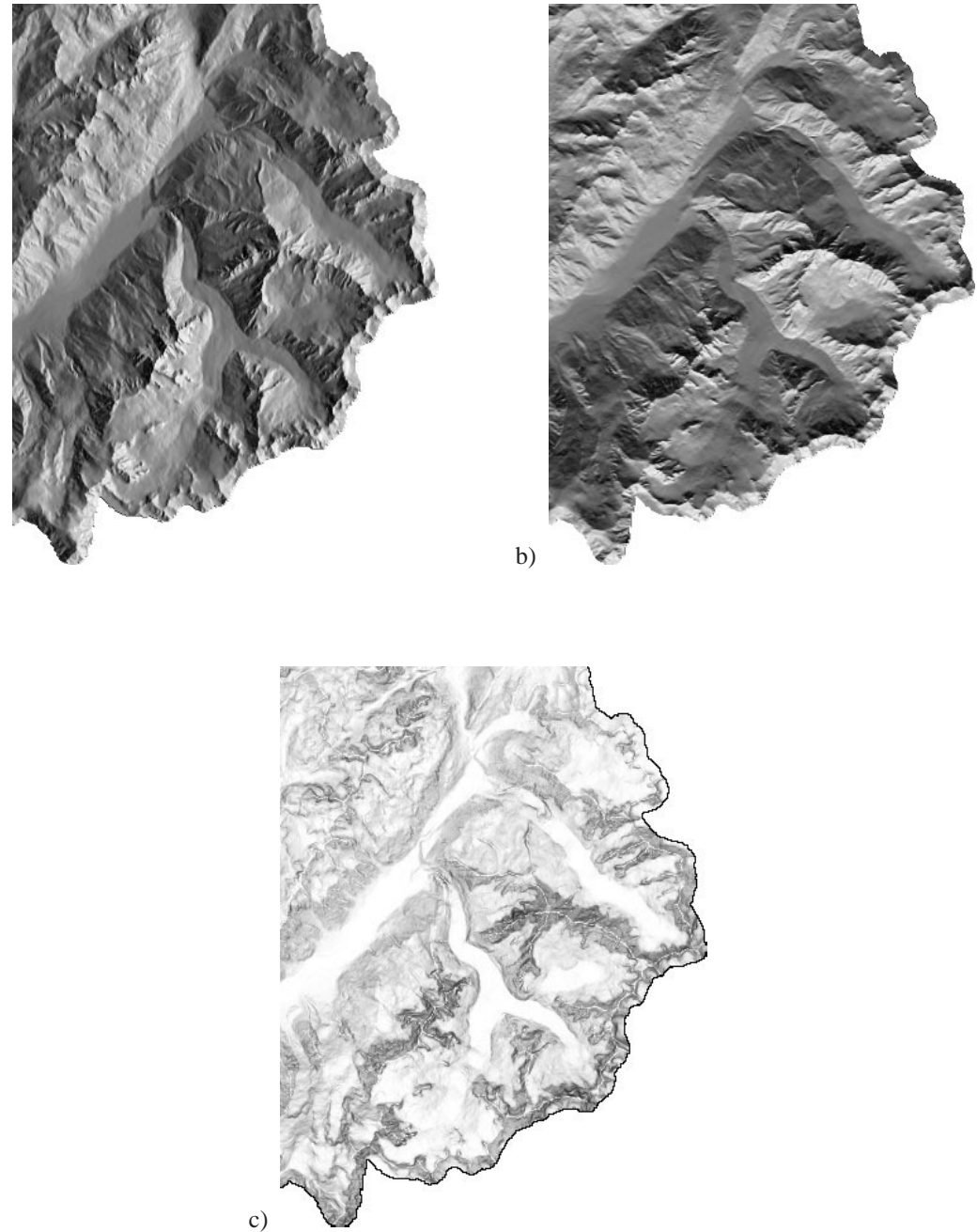


Figure 4.2. Relative grey-scale representation of the values of coordinates x, y, z for the vector normal to surface in a digital elevation model of the Mont Blanc Massif. To make the coordinates agree with solar position convention, white is a high positive eastwards, southwards and upward component. The grid is 338 columns by 444 rows, with a resolution of 50 m (16.9 x 22.2 km). The inverted Y-shaped feature in the lower centre is the Mer de Glace, the largest glacier in the French Alps. The sharp border on the right and lower areas is the national boundary plus a buffer area, as the relief of Italy and Switzerland is not shown, and the main Valley running NE to SW is the Valley of Chamonix. North is up.

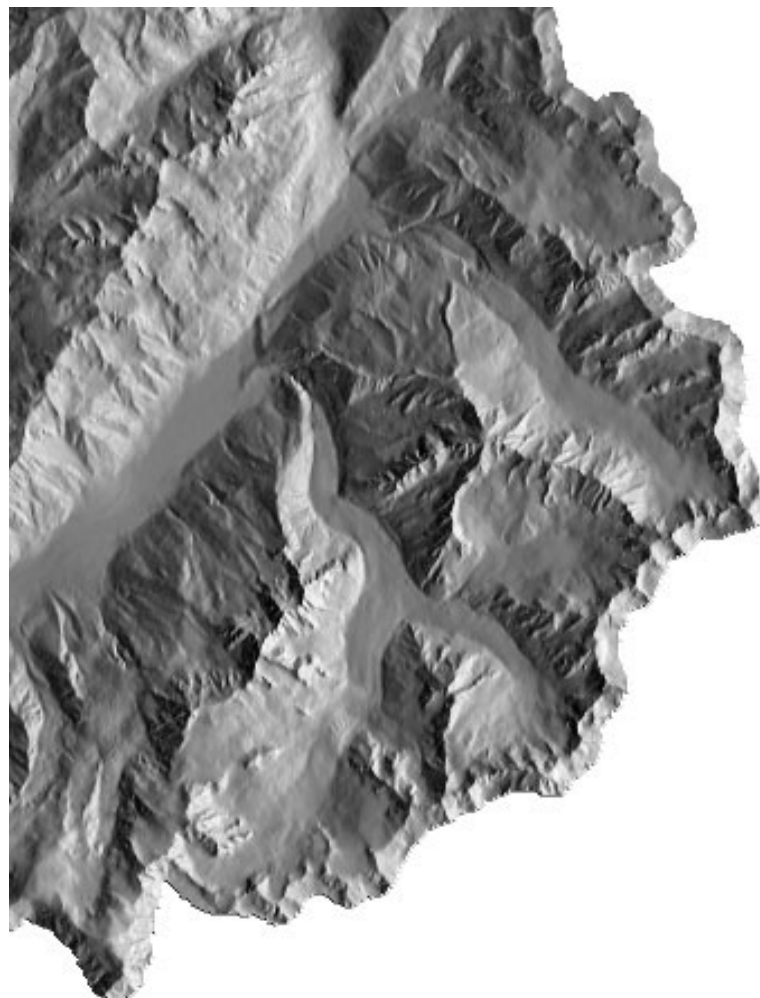


Figure 4.3. Relative grey-scale representation of surface aspects in the Mont Blanc DEM. White is northeast and black is southwest.

4.3 Comparison with other methods of calculating slope

It is questionable whether a synthetic surface is a valid comparison with real topography, but it has the advantage of providing error and artifact-free data. Similar approaches have been used successfully in the past (Hodgson 1995, Hodgson 1998). Additionally, by choosing a continuous differentiable function to generate the surface, the gradient can be derived mathematically at every point, thus providing an analytical value for comparison.

A simple trigonometrical function with two terms, one for the base elevation and a second one to add a surface of rapidly changing relief was chosen to generate a DEM of 10 000 cells sampled at regular intervals (Figure 4.4). The function generating this surface is:

$$f(x, y, z) = -\cos x \cos y - a \sin bx \sin by + z = 0 \quad (4.6)$$

where a and b are constants with values 0.1 and 10 respectively.

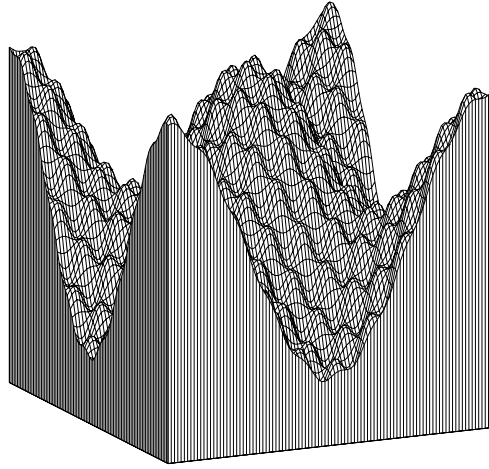


Figure 4.4. Synthetic DEM, a surface of highly variable relief generated by Equation 4.6. Z values are in the range ± 1.07474 , horizontal cell spacing is $2\pi/100$ units.

The gradient of function 4.6 is:

$$\nabla f(x, y, z) = \left(\frac{\partial f}{\partial x} \hat{i}, \frac{\partial f}{\partial y} \hat{j}, \frac{\partial f}{\partial z} \hat{k} \right) \quad (4.7)$$

Solving the partial derivatives gives the components of the vector normal to surface at any point:

$$\nabla f(x, y, z) = \begin{Bmatrix} (\sin x \cos y - ab \cos bx \sin by) \hat{i} \\ (\cos x \sin y - ab \sin bx \cos by) \hat{j} \\ \hat{k} \end{Bmatrix}, \quad (4.8)$$

4.3. Comparison with other methods of calculating slope

and from these, the slope, ς , is calculated as:

$$\varsigma = \cos^{-1} \frac{\nabla f_z}{|\nabla f|} \quad (4.9)$$

The results were compared to those obtained from the algorithms described here and with the output of a commonly used GIS software that uses a 3x3 kernel algorithm (ESRI 2000). The software manufacturer refers to Burrough (1986, p. 50, equation 3.4), which is based on Horn (1981, p. 18). Figure 4.5 shows a scattergram comparing the slope values. Both algorithms underestimate the slope, although the vectorial algorithm is closer to the mathematically derived slope, presents less dispersion, smaller root mean square error, smaller standard deviation and less mean absolute deviation (Table 4.1). Figure 4.6 shows a grey-scale representation of the spatial distribution of errors in the computation of slope for the synthetic DEM.

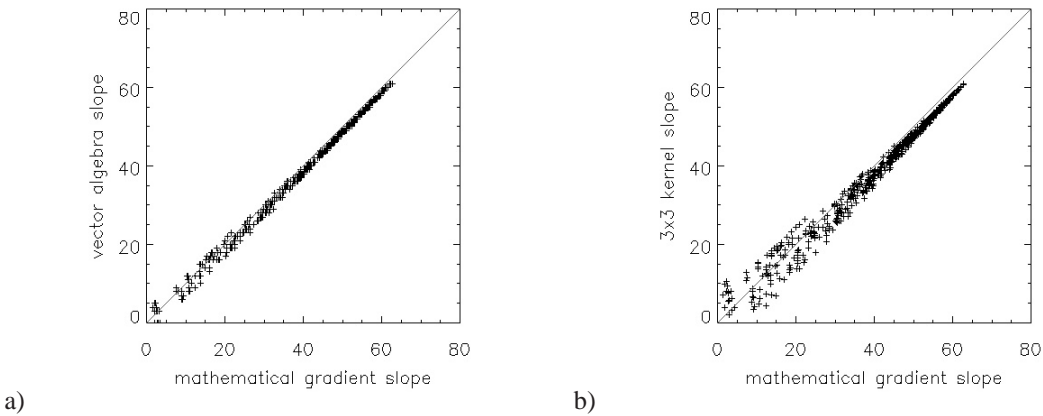


Figure 4.5. Scattergrams of slope values generated with the algorithm described in this paper and a 3x3 kernel algorithm compared to the slopes derived mathematically from a synthetic surface (Figure 4.4 and Equation 4.8).

Algorithm	Spearman's rank correlation	rms	σ	mean abs. dev.
math. gradient	—	—	—	—
vector algebra	0.993804	0.7089	1.7993	0.8205
3x3 kernel	0.980826	1.2430	3.2623	1.7720

Table 4.1. Correlation between slopes derived mathematically from a synthetic surface and those calculated using the vector algebra algorithm and a 3x3 kernel algorithm.

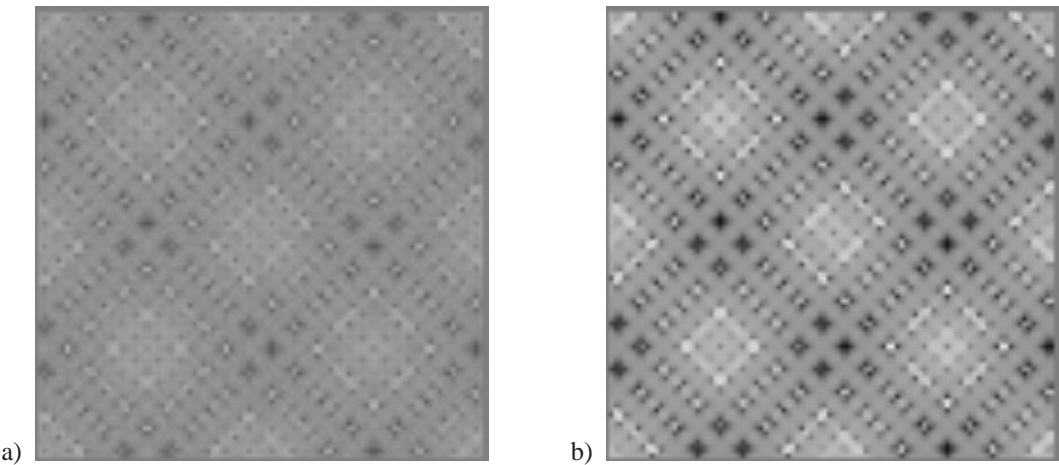


Figure 4.6. Gray-scale representation of the spatial distribution of errors in the computation of slope for the synthetic DEM. a) is between mathematically generated slopes and vector algorithm, b) is the difference with the 3x3 kernel algorithm. Note that the location of errors is similar but these are accentuated in the right image. Values range from -2.91 to 3.78 and from -8.19 to 8.12. Neutral gray is no error, darker is overestimation and whiter is underestimation of slope.

4.4 Vector defining the position of the sun

The vector in the direction of the sun can be calculated from the solar azimuth and zenith angles (e.g. Horn 1981, Peterson et al. 1985, Wang, White and Robinson 2000), and these angles can be calculated using spherical trigonometry (e.g. Nautical Almanac Office 1974, Iqbal 1983). However, for completeness and consistency with the vectorial approach, a new procedure is explained here. We define a topocentric coordinate system as an orthogonal reference system with origin at the observer position on the surface of the earth (Figure 4.7). To follow the conventions normally used in solar radiation studies regarding the position of the sun (e.g. Iqbal 1983, page 15), the coordinate axes are defined as follows:

- the X -axis is tangential to the earth surface in direction east–west and positive eastwards;
- the Y -axis is tangential in direction north-south and positive southwards;
- and the Z -axis lies along the earth’s radius and is positive upwards.

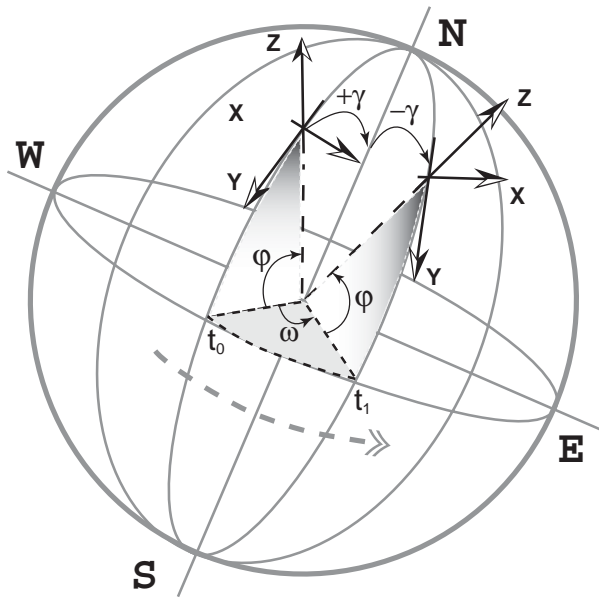


Figure 4.7. Rotation of the topocentric coordinate system XYZ an angle ω , from time t_0 to time t_1 . This movement can be decomposed in three rotations: i) rotation around axis X an angle $\gamma = \pi/2 - \varphi$, where φ is the latitude; ii) rotation around axis Z an angle ω ; and iii) rotation back around axis X an angle $-\gamma$. Translation is ignored as the maximum parallax of the earth is 8.8 seconds of arc (Nautical Almanac Office 1974), and therefore negligible for most solar radiation applications.

By definition, the sun lies on the ZY -plane (*i.e.* it is on the vertical plane) at noon local apparent time (LAT). At this time, the x -coordinate of a unit vector pointing to the sun (solar vector from now on) will be null. The solar declination (δ) is the angle between the solar rays and the plane of the earth’s equator. The geographical latitude (φ) is the angle between the radius of the earth at the observer position (that is the Z -axis in our coordinate system) and the equatorial plane. Thus, the solar vector, \hat{s}_0 , at noon LAT will be:

$$\hat{s}_0 = (0, \sin(\varphi - \delta), \cos(\varphi - \delta)) \quad (4.10)$$

At any given time t , the earth will have rotated away from noon an hour angle ω at an angular speed of 2π radians or 360 degrees per day. The hour angle is the angle between the observer meridian and the solar meridian, the convention is that ω is zero at noon and positive before noon (Iqbal 1983, page 15). At this time the topocentric coordinate system will have changed position in relationship to the sun at noon. This movement can be decomposed in three rotations (see Figure 4.7): one around the X -axis, to place the Z -axis parallel to the axis of rotation of the earth; a second rotation around the Z -axis an angle ω and a third rotation back around the X -axis to the observer position. To find the coordinates of the solar vector in the new, rotated reference system we multiply the original coordinates by 3 rotational matrices describing these movements. For a brief description of rotational matrices, a common procedure in computer graphics, see for example Foley et al. (1990) and related references. Thus, at any time, and assuming no atmospheric refraction, the solar vector \hat{s} will be:

$$\hat{s} = \mathbf{r}_x(\gamma) \mathbf{r}_z(\omega) \mathbf{r}_x(-\gamma) \hat{s}_0 \quad (4.11)$$

where \mathbf{r} is a rotation matrix around axis in subscript and angle in brackets, γ is the angle between earth's axis and the topocentric coordinate system Z -axis, and the hour angle ω is zero at noon and has the following value in radians at any time t (LAT) given in hours and decimal fraction:

$$\omega = \pi \left(\frac{t}{12} - 1 \right) \quad (4.12)$$

In matrix notation:

$$\hat{s} = \begin{pmatrix} 1 & 0 & 0 \\ 0 & \cos \gamma & -\sin \gamma \\ 0 & \sin \gamma & \cos \gamma \end{pmatrix} \begin{pmatrix} \cos \omega & -\sin \omega & 0 \\ \sin \omega & \cos \omega & 0 \\ 0 & 0 & 1 \end{pmatrix} \begin{pmatrix} 1 & 0 & 0 \\ 0 & \cos(-\gamma) & -\sin(-\gamma) \\ 0 & \sin(-\gamma) & \cos(-\gamma) \end{pmatrix} \begin{pmatrix} s_{0x} \\ s_{0y} \\ s_{0z} \end{pmatrix} \quad (4.13)$$

This rotation of the earth also involves a translation of the defined reference system, \hat{s}_0 , but the maximum parallax of the earth is $8.8''$ of arc (Nautical Almanac Office 1974), that is $4.4''$ if we take as reference noon for the hour angle. This is much smaller than the precision of other quantities involved, so the extra computational effort to account for this translation can be saved for most applications.

This equation can be fed directly into most programming languages, simplifying the programming effort, or can be solved for every coordinate. As γ is the angle between Z -axis (or earth radius at the observer) and the earth axis, it follows:

$$\gamma = \frac{\pi}{2} - \varphi \quad (4.14)$$

thus, Equation 4.13 can be expressed as:

$$\hat{s} = \begin{pmatrix} 1 & 0 & 0 \\ 0 & \sin \varphi & -\cos \varphi \\ 0 & \cos \varphi & \sin \varphi \end{pmatrix} \begin{pmatrix} \cos \omega & -\sin \omega & 0 \\ \sin \omega & \cos \omega & 0 \\ 0 & 0 & 1 \end{pmatrix} \begin{pmatrix} 1 & 0 & 0 \\ 0 & \sin \varphi & \cos \varphi \\ 0 & -\cos \varphi & \sin \varphi \end{pmatrix} \begin{pmatrix} \hat{s}_{0x} \\ \hat{s}_{0y} \\ \hat{s}_{0z} \end{pmatrix} \quad (4.15)$$

Using the equivalences for the y and z coordinates of \hat{s}_0 :

$$\hat{s}_{0y} = \sin(\varphi - \delta) = \sin \varphi \cos \delta - \cos \varphi \sin \delta \quad (4.16)$$

$$\hat{s}_{0z} = \cos(\varphi - \delta) = \cos \varphi \cos \delta + \sin \varphi \sin \delta \quad (4.17)$$

solving 4.15 and simplifying using $\sin^3 = \sin - \sin \cos^2$ and $\cos^3 = \cos - \cos \sin^2$, the x, y, z coordinates of the solar vector at hour angle ω will be:

$$\hat{s} = \begin{pmatrix} -\sin \omega \cos \delta \\ \sin \varphi \cos \omega \cos \delta - \cos \varphi \sin \delta \\ \cos \varphi \cos \omega \cos \delta + \sin \varphi \sin \delta \end{pmatrix} \quad (4.18)$$

From this equation, the solar zenithal angle θ can be calculated as:

$$\theta = \cos^{-1} s_z \quad (4.19)$$

and the solar azimuth ϕ as:

$$\phi = \frac{\pi}{2} + \tan^{-1} \frac{s_y}{s_x} \quad (4.20)$$

where s_x, s_y and s_z are the coordinates of the solar vector.

Due to the obliquity of the ecliptic, the declination can change from $-23^0 26' 12''$ at the winter solstice (Northern Hemisphere) to $+23^0 26' 12''$ at the summer solstice, with a variation of less than $10''$ over the next 20 years due to precession and nutation in the obliquity of the ecliptic and to general precession of the longitude of the sun (Nautical Almanac Office 1974). Calculating the declination is not a trivial problem, as its value is affected by long-term orbital changes (*i.e.* at Milankovitch time scales) and by the interaction with the moon and other planets.

Many authors have given different solutions to the problem of finding the solar declination with different degrees of accuracy (e.g. Spencer 1971, Walraven 1977, Page 1986). Here a Fourier series approximation derived by Bourges (1985) that estimates the declination with a mean error of 0.008^0 and a maximum error of 0.02^0 is used. Bourges explains clearly the procedure and astronomical assumptions, so that the series can be corrected for the required epoch. For the present day, we have:

$$\begin{aligned} \delta = & 0.3723 \\ & + 23.2567 \sin D - 0.758 \cos D \\ & + 0.1149 \sin 2D + 0.3656 \cos 2D \\ & - 0.1712 \sin 3D + 0.0201 \cos 3D \end{aligned} \quad (4.21)$$

where D is the day number :

$$D = (360/365.25) \times (J - 79.346) \quad (4.22)$$

and J is the Julian day, 1 on the first of January and 365 on the 31st of December (more strictly, the difference between the Julian day in consideration and the Julian day on January the first at noon for that given year, plus 1).

The maximum daily variation in declination is less than 0.5 degrees of arc at the equinoxes and less than 1 minute of arc at the solstices (Spencer 1971), thus, when accuracy to the nearest degree is required, a single value of δ can be used over a whole day, with considerable simplification in the calculations. To keep within an error similar to that of the selected method of calculating declination, the coordinates of the sun vector at noon (\hat{s}_0) can be recalculated every time, adding to the day number $t/24$ days, where t is the number of hours from noon LAT.

In order to integrate the amount of solar radiation over the whole day, it is necessary to know the duration of daylight and therefore the time of sunrise and sunset. Astronomical sunrise and sunset will occur at the time when the z coordinate of the sun vector equals zero. Thus, solving for z in Equation 4.18:

$$z = \cos \varphi \cos \omega \cos \delta + \sin \varphi \sin \delta = 0 \quad (4.23)$$

gives:

$$\cos \omega = \frac{-\sin \varphi \sin \delta}{\cos \varphi \cos \delta} \quad (4.24)$$

$$\omega = \cos^{-1}(-\tan \varphi \tan \delta) \quad (4.25)$$

which is the absolute value of the hour angle at sunrise or sunset. Note that this solution is in agreement with the results derived following spherical trigonometrical equations (e.g. Iqbal 1983, page 16).

The sunrise will be at $t = 12(1 - \omega/\pi)$ hours and the sunset at $t = 12(1 + \omega/\pi)$. The day length will be $2\omega 2\pi/24$. The equation has no solution if $|\tan \varphi \tan \delta| > 1$, in this case, if the latitude has the same sign of the declination, that is, $\varphi / |\varphi| = \delta / |\delta|$ it is the polar day, and if they are of different sign then it is the polar night. These equations do not take into account the height of the observer above the horizon or crepuscular diffuse solar irradiation: for a detailed treatment of the astronomical parameters involved in this case, see the Nautical Almanac Office (1974).

4.4.1 Angle of incidence of the sun on inclined surfaces

The fraction of light intercepted by the inclined surface will be proportional to the cosine of the angle between the normal to the surface and the sun rays. Having calculated a unit vector gradient normal to the surface and a unit vector in the direction of the sun, the dot product of both gives the cosine of the angle between them; thus the angle between the sun and the normal to surface, θ_s is:

$$\theta_s = \cos^{-1}(\hat{s} \cdot \mathbf{n}_u) \quad (4.26)$$

Figure 4.8 shows the application of these algorithms to produce a map of solar radiation over an area of high relief, the Mont Blanc Massif in the French Alps. Incoming solar radiation was modelled for clear skies at 15 minute intervals from sunrise to sunset at the time of the spring equinox, following an updated parametric model based on Iqbal (1983). Irradiation at every grid cell is evaluated according to the angle of incidence of the sun and the shading of surrounding terrain as described in Section 4.5. Diffuse incoming solar radiation is evaluated according to the hemispherical portion of sky visible from every grid cell as described in Section 4.6.

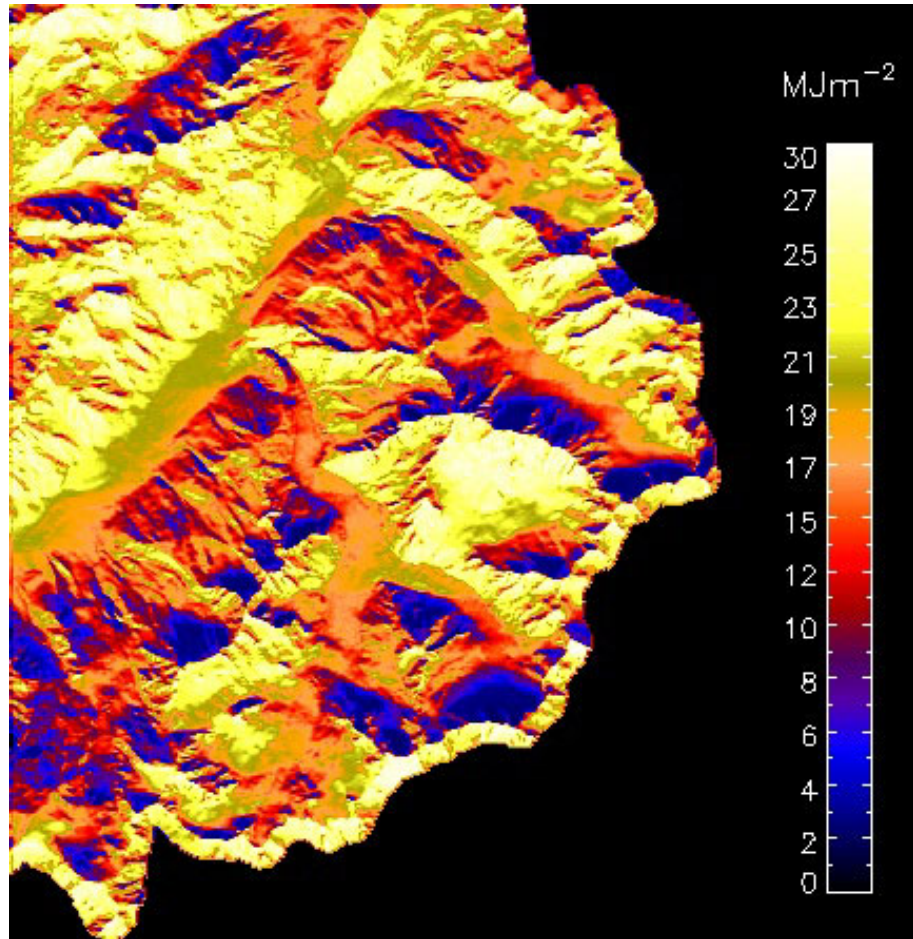


Figure 4.8. Color coded map of insolation received at the Mont Blanc Massif at the spring equinox. Incoming solar radiation is modelled for clear skies at 15 minutes interval from sunrise to sunset following Iqbal's (1983) parametric model. Incident solar radiation for every grid cell is evaluated according to the angle of incidence of the sun and the shading of surrounding terrain. Diffuse incoming solar radiation is evaluated according to the hemispherical portion of sky visible from every grid cell. Reflected radiation from surrounded terrain is not computed. Values range from 2.2 to 29.96 MJm^{-2} .

4.5 Shaded relief

The sun can be considered as a point light source at infinite distance, and thus, all illumination rays arriving at a grid can be considered parallel. For computational convenience we consider an ‘illumination plane’ perpendicular to the solar rays (Figure 4.9). All solar rays traverse this plane at a right angle. By checking the projection of a grid cell over this plane, following the direction of the sun, we can determine whether a point is in the sun or in the shade of another cell. In Figure 4.9 this is illustrated for a two dimensional example: the projection of P_1 , that is, P'_1 , has a value higher than any previous one (as it is the first point to be scanned), so it is in the sun. Similarly for P'_2 and P'_3 , however, P'_4 has a lower value than P'_3 and therefore is in its shadow. The projection of a point P'_i on the solar plane \mathbf{SP} is the dot product of the vector $\overrightarrow{OP_i}$ and the unit vector \hat{s}_p , which is a vector in the direction of the plane \mathbf{SP} and perpendicular to the solar vector \hat{s} . A cell will shade itself if the angle between the sun and the vector normal to the cell’s surface is higher than $\pi/2$.

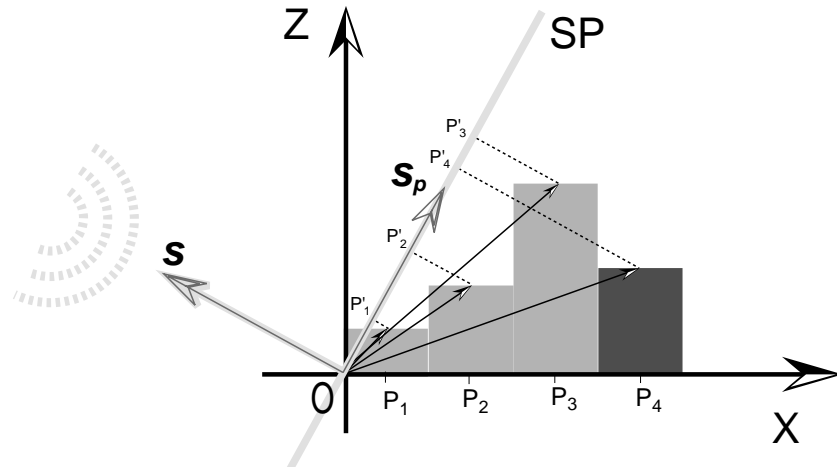


Figure 4.9. Hillshading. As the sun can be considered as a point source at infinite distance, all solar rays are parallel and cross the plane \mathbf{SP} perpendicularly. By checking the projection of a grid cell over this plane we can determine whether a point is in the sun or in the shade of a previous cell. In the figure the projection of P_1 , that is, P'_1 , has a value higher than any previous one (as it is the first point to be scanned), so it is in the sun. Similarly for P'_2 and P'_3 , however, P'_4 has a lower value than P'_3 and therefore is in its shadow. The projection of a point P'_i on the ‘solar plane’ \mathbf{SP} is the dot product of the vector $\overrightarrow{OP_i}$ and the vector s_p , which is a unit vector perpendicular to s , the unit vector in the direction of the sun.

By scanning the grid across the sun path, we can determine which cells are shaded or not by comparing their projection values. In order to speed up the implementation of the algorithm, an array of cells is defined for every cell on the sun side of the grid border. The length of this array is given by the first intersection of a line along the vector opposite to the sun and the DEM boundaries. The x,y position of the cells under consideration in the original grid are estimated by integer increments of the vector opposite to the sun for the largest x,y coordinate. Figure 4.10 shows the application of the hill-

shading algorithm to the Mont Blanc Massif DEM. The sun is assumed to be at 315^0 (northwest) and the zenith angle is 45^0 , an unrealistic position traditionally chosen to avoid a pseudoscopic effect, that is the reversal of the relief or valleys appearing like mountains and mountains looking like valleys when illumination is applied from the south. The image has a minimum illuminance of 18% to account for diffuse radiation and the reflected light is modified according to $\cos \theta_s$. Computation time was about one sixth of a second for a grid of 150 000 cells (Figure 4.10) on a Intel Xeon CPU 2 GHz 523,276 KB RAM and 1.6 seconds on a SunSparc 450.



Figure 4.10. Hillshading of Mont Blanc DEM . The incident light is modified according to the cosine angle of incidence of the sun on the slope. A minimum illuminance of 18% is introduced to account for diffuse radiation. Illumination is from the northwest at 45^0 elevation.

The coordinates of the vectors involved in these calculations for the three dimensional case are as follows:

The vector from the origin to any point $P_{i,j}$ at column i , row j is:

$$\overrightarrow{OP}_{i,j} = (\ell i, \ell j, z_{i,j}) \quad (4.27)$$

where ℓ is the cell size and $z_{i,j}$ the elevation of cell at i, j . For simplicity we assume that the solar plane crosses the grid at the origin $(0, 0, 0)$. The unit vector in the direction of the solar plane is calculated as a combination of two cross products:

$$\hat{s}_p = \hat{s} \times \frac{\hat{s} \times \hat{s}_{xy0}}{|\hat{s} \times \hat{s}_{xy0}|} \quad (4.28)$$

where the second term is the unit vector perpendicular to the sun in the horizontal direction and \hat{s}_{xy0} is the projection of \hat{s} on the horizontal (XY) plane. The projection $P'_{i,j}$ of $P_{i,j}$ is:

$$P'_{i,j} = \overrightarrow{OP}_{i,j} \cdot \hat{s}_p \quad (4.29)$$

4.6 Sky view factor

The sky view factor is defined as the hemispherical fraction of unobstructed sky visible from any point. This is an important parameter for the calculation of incoming diffuse radiation and for the net balance of long-wave radiation (Dubayah and Rich 1995, Duguay 1995, Varley et al. 1996). The complementary parameter, 'ground view factor', is important in the evaluation of diffuse and multiple scattered short wave radiation, especially in areas of high albedo, like snow covered mountains, as well as for the long-wave radiative budget (Olyphant 1986a, Olyphant 1986b, Greuell et al. 1997). It is also important in other fields, such as cosmogenic dating, in order to evaluate the topographical shielding from cosmic radiation (Dunne et al. 1999). It is a common practice to measure the zenithal angle of the horizon at a given azimuth interval and then average for all the compass directions to compute the ratio of visible hemisphere to the whole hemisphere (Nuñez 1980, Dozier and Frew 1990).

Following the unit-sphere method (Iqbal 1983, p. 298) the sky view factor is evaluated as the ratio of the projected surface of the visible part of the hemisphere, to the area of a whole hemisphere of unitary radius (Figure 4.11). The radius of the projection of the visible part of the hemisphere is equal to the sine of the average zenithal angles in all azimuth directions. Here a variation of the hillshading algorithm described above is used to find the horizon zenithal angles for selected azimuths. By repeating the shading algorithm from a given azimuth direction in decreasing steps of elevation values, we can find the horizon angles for every cell in that direction: this angle will be complementary to the current elevation angle at the cell's transition from sun to shadow. The initial elevation value need not be higher than the maximum cell slope in the grid. This is repeated at the required azimuth interval over 360^0 degrees and the results averaged. The area of the circle of the projected visible hemisphere is calculated for every circular segment corresponding to the azimuth increments, and the sky view factor is computed

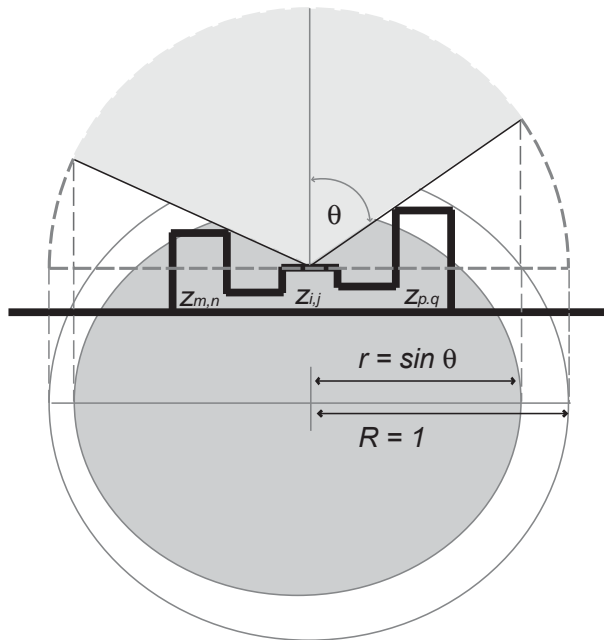


Figure 4.11. Sky view factor: the fraction of sky visible from any point is evaluated as the ratio of the projected area of the visible hemisphere to the area of the base of a unit sphere. The figure illustrates the calculation for a given cell $z_{i,j}$ with visibility obstructed by neighbouring cells $z_{m,n}$ and $z_{p,q}$, where the portion of visible sky is the shaded area. The sky view factor will be $r^2/R^2 = r^2 = \sin^2 \bar{\theta}$, where $\bar{\theta}$ is the average zenithal angle for all azimuth directions. Note that for clarity in the illustration the projected visible surface area is selected only for two points and not for the average, thus the resulting geometry is an ellipse instead of a circle.

as the finite sum:

$$f_{sk} = \sum_{\varphi=0}^{2\pi} \pi \cos^2 \theta \frac{\Delta\varphi}{2\pi} \quad (4.30)$$

where θ is the local horizon angle, including the slope of the cell itself, for a given azimuth, φ .

A typical calculation for a terrain with slopes up to 45^0 and at 15^0 degrees azimuthal intervals will require $45 \times 24 \times N$ operations if N is the number of cells in the DEM, which is considerably faster than the N^2 operations required for a rigorous estimation of all the angles subtended by every cell with any other cell in the grid. The results for the Mont Blanc area are visualised in Figure 4.12

Averaging $\bar{\theta}$ implies the assumption of isotropy in the diffuse radiation field, which is an unrealistic simplification. If this were not acceptable, the suggested algorithm can be used to store horizon angles at any given direction, at the expense of more memory requirements. For a rigorous evaluation of the influence of surrounding terrain on the radiation falling on any cell, it would be necessary to perform a viewshed analysis, rather than the simplified parameter “ground view factor”. This point is not addressed here, but the reader is directed to the work of Wang, Robinson and White (2000), which is probably the most efficient viewshed algorithm to date.

Dozier, Bruno and Downey (1981) have developed a very efficient algorithm for the calculation of local horizons, that can be applied to the calculation of casted shadows. The shading algorithm in this paper might be more suitable for the calculation of shades at a limited number of illumination angles, as it is fast and does not need to store horizon information for every azimuth direction.

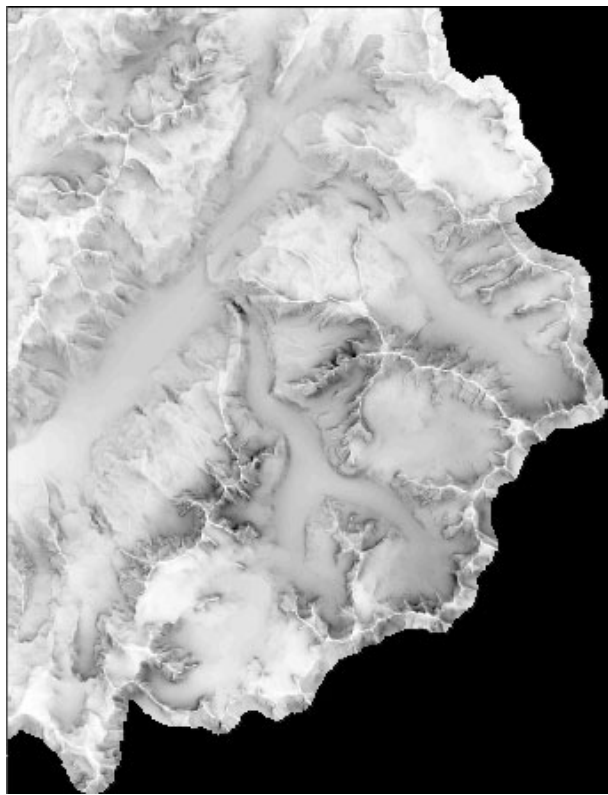


Figure 4.12. Relative grey-scale representation of sky view factor for the Mont Blanc DEM. Dark areas have lower sky visibility, while white ones, such as higher ridges, have unobstructed visibility of the upper hemisphere. Values range from 0.5 to 1, with the lowest value corresponding to the steepest slope, 81° , on the western face of Les Drus, centre right of the image.

Chapter 5

Modelling solar radiation over complex topography: II. Albedo estimation using terrestrial photography

5.1 Aim

The overall aim of the work in this chapter is developing a practical and inexpensive remote sensing tool for the estimation of temporal and spatial variations of surface albedo on glacier and snow covered mountainous areas. Given that the maximum energy reflected by the snow lies on the visible band of the electromagnetic spectrum, and given the widespread use of photographic cameras, the good spectral response of modern films and the increasing availability of digital photography, the use of conventional photography was explored for this purpose.

5.2 Introduction

On low and mid-latitude glaciers and on high mountains, solar radiation is the main source of energy for the melting of ice and snow (e.g. de la Casinière 1974, Marks and Dozier 1992, Cline 1997). Thus an accurate measurement of the temporal and spatial variation of albedo, which is the ratio of incoming to outgoing hemispherical short-wave radiation, is necessary to estimate snow ablation, which conse-

quently influences the glacier mass balance dynamics and runoff. Albedo is, therefore, a very important parameter for the study of the hydrological resources derived from snow and for the study of glacier behaviour and its climatic response. It is an essential input for the physically based estimation of the energy balance of glaciers and snow cover basins (e.g. Strasser et al. 2002).

In order to estimate the albedo distribution over a basin, a standard approach is the interpolation of values from a few point measurements. However, the high spatial variability of albedo may introduce a large error (Knap et al. 1999). Furthermore, *in situ* measurements may be difficult or even impossible due to avalanche risk, which makes remote sensing tools an attractive solution. Satellite remote sensing has the potential to provide the necessary information of spatial and temporal variations of albedo, and therefore considerable research is being done in this area (e.g. Dubayah 1992, Knap et al. 1999, Grover et al. 2000). Although satellite derived data is very cost effective it is still expensive in absolute terms. Additionally, in areas of high relief, cloud cover and shadows may reduce the efficiency of satellite imagery in the optical band, and it is impossible to get a temporal resolution higher than the repeat coverage cycle of the satellite.

An economic and either alternative or complementary approach to satellite imagery is the use of oblique terrestrial photography, which allows high temporal and spatial resolution. Furthermore, the combination of both techniques, satellite and photography, may enhance the quality of the satellite data. By testing smaller sites at higher resolution the results can be validated for the the whole coverage area. The proposed technique is suitable for mountain regions where views at a steep incidence angle result in better precision and larger ground coverage. The technique was evaluated by using the Mer de Glace Glacier, in the French Alps, as a test site (Figure 5.12).

5.3 Methodology

Firstly we describe the georeferencing of oblique photographic images, using a viewing transformation and perspective projection of a digital elevation model (DEM) and a mapping function between pixels in the photograph and cells in the DEM. In this section the mathematical approach to defining the camera coordinate system is explained, together with the geometric transformations needed for georeferencing oblique photography. Visibility analysis is performed and basic photo orientation and corrections for camera movements are considered. Problems arising from using non metric cameras and conventional film and scanner are addressed. Then we deal with the estimation of albedo from reflectance values recorded by the camera. This is done by obtaining the ratio between the reflectance normalised values of the georeferenced photograph and a surface of known albedo. The effect of topography on the global solar radiation arriving at the ground is studied, accounting for direct cast shadows, diffuse radiation from the sky and diffuse reflected radiation from the surrounding terrain, which can be important in snow covered areas. The attenuation of solar radiation reflected from the target pixels when traversing the intervening atmosphere is evaluated with the help of the radiative transfer model MODTRAN (Berk

et al. 1989). A simple empirical relationship was found for the effect of the camera optics, scan and film developing on the final product, the digital reflectance values in the image of the studied area. Finally the preferred data storage format is justified.

5.3.1 Georeferencing terrestrial photography

In order to georeference terrestrial photographs we need to find a function relating two-dimensional pixels in the photograph to three-dimensional points in the digital elevation model. This is achieved by applying a perspective projection after transforming the coordinates of the DEM to camera coordinate system. In this way we produce a “virtual” photograph of the digital elevation model, that is, a two-dimensional representation of the relief information contained in the DEM, as seen from the point of view of the camera. By scaling this representation according to the resolution of the photograph, we can establish the necessary correspondence between pixels in the image, screen coordinates of the perspective projection of the DEM and their geographic location.

Simultaneous development of a similar technique has been carried out by different authors (Corripio 2000, Corripio 2001, Aschenwald et al. 2001). The details of the transformations are not explicitly given by Aschenwald et al. (2001), who derived them from classical photogrammetry theory (Slama et al. 1980). The present work follows computer graphics theory and, for completeness and repeatability, the detailed procedure is explained in the following paragraphs.

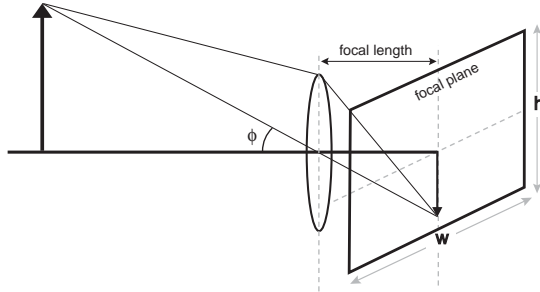


Figure 5.1. Simplified scheme of image formation in the camera. ϕ is half the angle of the vertical field of view, w is the width of the film (36 mm) and h is its height (24 mm).

Firstly, we select the visible portion of the DEM according to the angular field of view. This is derived from the the focal length of the camera lens and the dimensions of the film. The angle ϕ in Figure 5.1, is half the vertical field of view, and its value is:

$$\phi = \arctan \frac{(1/2)h}{f} \quad (5.1)$$

where f is the focal length and h is the vertical dimension of the film, which is 24 mm for 35 mm

photography. Similarly, the half value of the horizontal field of view, φ , is:

$$\varphi = \arctan \frac{(1/2)w}{f} \quad (5.2)$$

where w is the horizontal dimension of the exposed film or 36 mm for this format.

Within this viewing window there are surfaces facing the observer and others facing away or hidden by nearer ground. These surfaces are, obviously, not seen by the camera, and in order to avoid duplicate or erroneous mapping of the photographic pixels to non visible DEM cells a viewshed analysis was performed with ArcInfo, a commercially available GIS package. Future work will be done toward the implementation of a viewshed algorithm by Wang, Robinson and White (2000), so that the whole procedure is a stand-alone routine coded in a single programming language.

Once visibility has been calculated, we apply a viewing transformation that maps points in the world coordinate system (that of the DEM) to points in the camera coordinate system, representing the viewing geometry of the camera in three-dimensional space, as shown in Figure 5.2. A viewing transformation is parameterised by a viewing direction vector \vec{N} , a vector \vec{V} indicating which way is up, a vector \vec{U} positive in the direction of the X-axis and a viewing position C (Fiume 1989). This is a standard procedure for obtaining perspective views in computer graphics (e.g. Foley et al. 1990). Firstly, we apply a translation transformation to set the origin at C , the camera position. The transformation matrix, in homogeneous coordinates, representing this translation, T_t would be:

$$\begin{pmatrix} P_{tx} \\ P_{ty} \\ P_{tz} \\ 1 \end{pmatrix} = \begin{pmatrix} 1 & 0 & 0 & -C_x \\ 0 & 1 & 0 & -C_y \\ 0 & 0 & 1 & -C_z \\ 0 & 0 & 0 & 1 \end{pmatrix} \begin{pmatrix} P_{wx} \\ P_{wy} \\ P_{wz} \\ 1 \end{pmatrix} \quad (5.3)$$

where P_w is any given point in world coordinates and P_t is the translated point to a reference system with origin at C , the camera position.

Lastly, the viewing transformation is completed by multiplying the result of Equation 5.3 by the following transformation matrix, which rotates the translated coordinates according to the viewing reference system:

$$\begin{pmatrix} P_{cx} \\ P_{cy} \\ P_{cz} \\ 1 \end{pmatrix} = \begin{pmatrix} U_x & U_y & U_z & 0 \\ V_x & V_y & V_z & 0 \\ N_x & N_y & N_z & 0 \\ 0 & 0 & 1/f & 1 \end{pmatrix} \begin{pmatrix} P_{tx} \\ P_{ty} \\ P_{tz} \\ 1 \end{pmatrix} \quad (5.4)$$

where f is the focal length of the lens and P_c is the resulting coordinates of a point in camera coordinate system.

The calculation of the unit vectors defining the viewing geometry is as follows. The viewing direc-

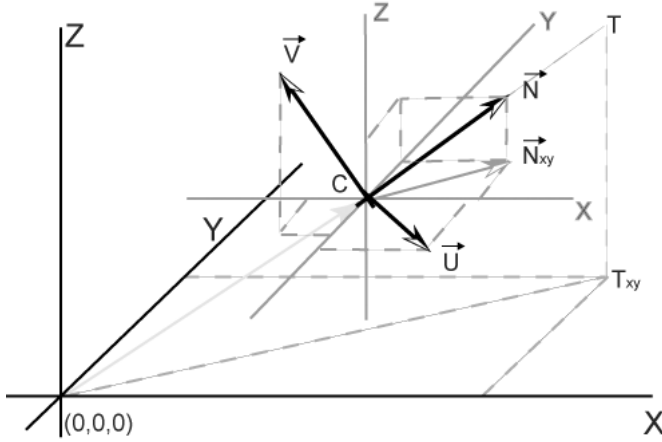


Figure 5.2. Change from world to camera coordinate system. DEM coordinates are referenced to the main reference system XYZ in the figure, while the image taken by camera at point C is referenced to the coordinate system defined by the three orthogonal unit vectors $\vec{U} \vec{N} \vec{V}$. \vec{N} is the viewing direction of the camera, calculated from the camera and target positions. \vec{U} is the unit vector of the cross product of \vec{N} and \vec{N}_{xy} , which is the projection of \vec{N} on the horizontal plane. \vec{V} is $\vec{U} \times \vec{N}$. See Section 5.3.1.

tion or vector \vec{N} is :

$$\vec{N}_0 = T - C, \quad (5.5)$$

$$\vec{N} = \frac{\vec{N}_0}{|\vec{N}_0|} \quad (5.6)$$

where T is the coordinates of the the target (aim of the camera) and C the coordinates of the camera with respect to the DEM origin of coordinates.

From this vector, and applying a procedure slightly modified from that used by Fiume (1989) or Watt and Pollicarpo (1998), \vec{U} and \vec{V} are calculated using simple vector calculus, by finding the cross products:

$$\vec{U} = \begin{cases} \vec{N} \times \frac{\vec{N}_{xy}}{|\vec{N}_{xy}|} & \text{if } N_z > 0 \\ \frac{\vec{N}_{xy}}{|\vec{N}_{xy}|} \times \vec{N} & \text{if } N_z < 0 \end{cases} \quad (5.7)$$

$$\vec{V} = \vec{N} \times \vec{U} \quad (5.8)$$

where \vec{N}_{xy} is the projection of \vec{N} onto the horizontal plane, or $(N_x, N_y, 0)$, and N_z the z coordinate of vector \vec{N} .

After the viewing transformation a perspective projection is applied. This is a mapping function of the points in three-dimensional space to a flat two-dimensional space representing the window of the camera vision. A simplified geometry of the projection is shown in Figure 5.3. Following Watt and Watt (1992) the resulting x, y coordinates are calculated as:

$$P_{px} = \frac{f P_{cx}}{\frac{1}{2} w P_{cz}} \quad \text{and} \quad P_{py} = \frac{f P_{cy}}{\frac{1}{2} w P_{cz}} \quad (5.9)$$

where $P_{p(x,y)}$ are the new x, y coordinates of the perspective projection of the point $P_{c(x,y,z)}$ onto the projection plane, which in this case is the film. The factor $1/2$ is introduced in the denominator to set the origin of coordinates in the projection plane to the centre of the film.

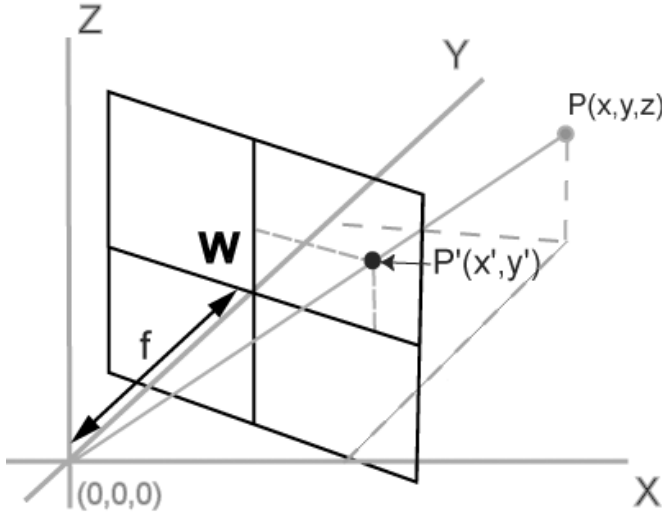


Figure 5.3. Simplified geometry of the perspective projection for one single point. A point P in tridimensional space is mapped (projected) to a point P' in a two-dimensional viewing window representing the camera film. The distance f to the origin of coordinates C in camera coordinate system is equivalent to the lens focal length. This perspective projection produces a virtual photograph of the DEM, which is then mapped to the pixels in the photograph. By conserving the link between P and P' the information in the flat two dimensional photograph can be mapped to the original three-dimensional points in the DEM. See Section 5.3.1 for details.

The resulting set of x and y coordinates after the perspective projection recreate, at a lower resolution and at a different scale, the terrain surface captured by the film (Figure 5.4). It is, in fact, a virtual photograph of the digital elevation model. In order to map it to the original photograph it has to be scaled according to the resolution of the scanned picture. This is a simple linear transformation.

If the position of the camera and the viewing direction is correct, the projection of the DEM grid points should match the image in the photograph, as in Figure 5.5, then the visual information of the picture can be extracted and mapped onto the digital elevation model. This is straightforward if, during the viewing and perspective transformation of the DEM, the link to the original coordinates of the grid cells is always preserved. When implementing the algorithm this is attained by constructing a five dimensional matrix with three dimensions (x, y, z) representing the original coordinates and two additional ones for those of the perspective projection.

Figure 5.4 shows the result of this perspective transformation, projection and scaling for a section of the Mer de Glace. Dots are the perspective projections of the original DEM grid cells, the frame is the camera field of view. The photograph in Figure 5.5 shows the superposition of the projected DEM (red dots) onto the original photograph. Green crosses are ground control points (GCPs), used for fast photo orientation when the target coordinates are not precisely known and to assess the fitness of the match between the photography and the perspective projection of the DEM. Usually a visual inspection of the resulting image is sufficient. In general there are no more than one or two pixel displacement between the GCPs perspective projection and the corresponding photographic points. Higher errors are possible when using low quality DEMs or lenses with poorly defined focal length. In these cases the code implementation allows the registration of the matching images to perform a better measurement of the displacements. If there were any uncertainty on the exact position of the point towards the camera is aiming (the target), the viewing direction vector will not be precisely defined, and this will result in a displaced perspective projection of the DEM. In order to avoid the more lengthy computation of the

5.3. Methodology

whole DEM, it is sufficient to compute only a few well defined GCPs to assess the accuracy of photo-orientation. Figure 5.6 shows a flow chart of the georeferencing process, where the first loop is done initially only for the ground control points in order to speed up the computation, and only when the match between GCPs and the corresponding points in the photograph is satisfactory, the computation is applied to the whole DEM.

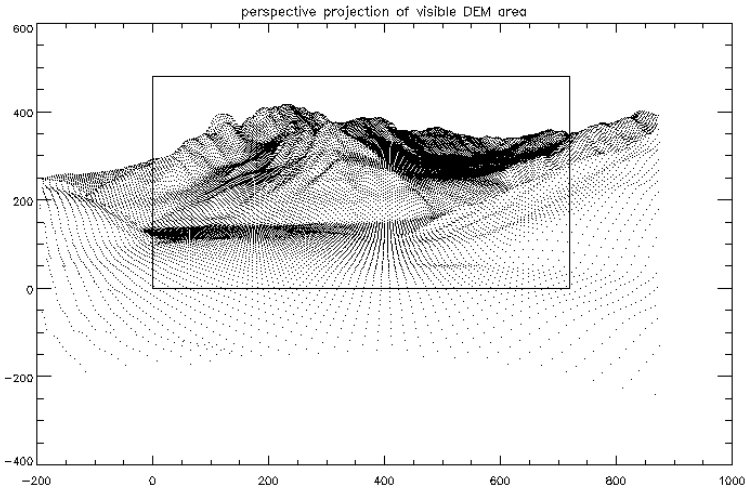


Figure 5.4. Perspective projection of a DEM of the lower section of the Mer de Glace, Mont Blanc. Every dot represent a grid cell after a viewing transformation and perspective projection. The frame is the camera field of view. Axis units are pixels in the original photograph: 720x480 within the frame, at a resolution of 200 dots per cm.



Figure 5.5. Super imposition of the perspective projection of a DEM of the Mer de Glace glacier (Figure 5.4) over a photograph of the area. Red dots are the perspective projections of the original DEM grid cells, green dots are ground control points. The photograph is taken from the Refuge du Requin looking east-northeast.

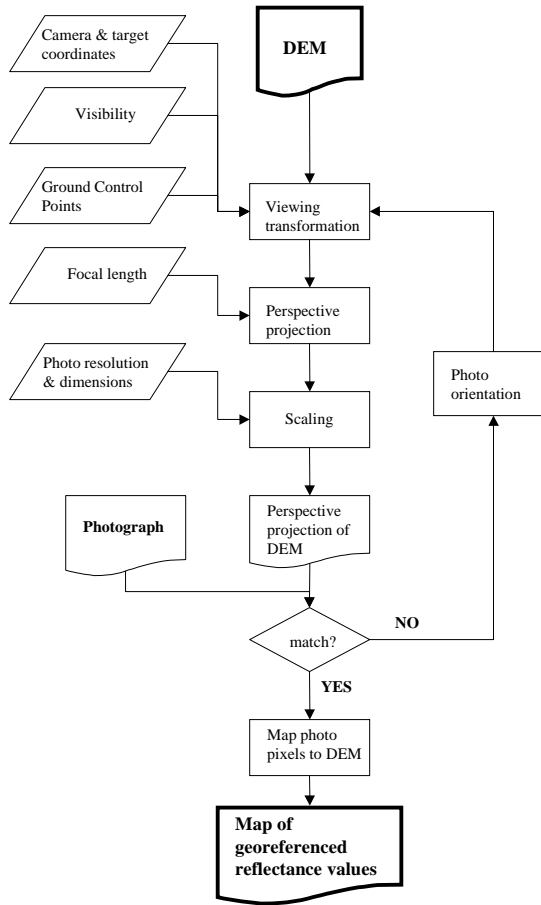


Figure 5.6. Flow chart of the georeferencing process.

The end result of this first process is a georeferenced image of reflectance values, shown in Figure 5.7. Reflectance in the case of visible photography refers to the three optical bands in the red, green and blue to which the film is sensitive, though the technique is of application to any other ground based sensor able to record images in any spectral band. A more detailed georeferenced image, for the lower section of the glacier is shown in Figure 5.8, in this case using a DEM resampled to 10 m resolution in order to show the potential of this technique to recognise and geolocate surface features.

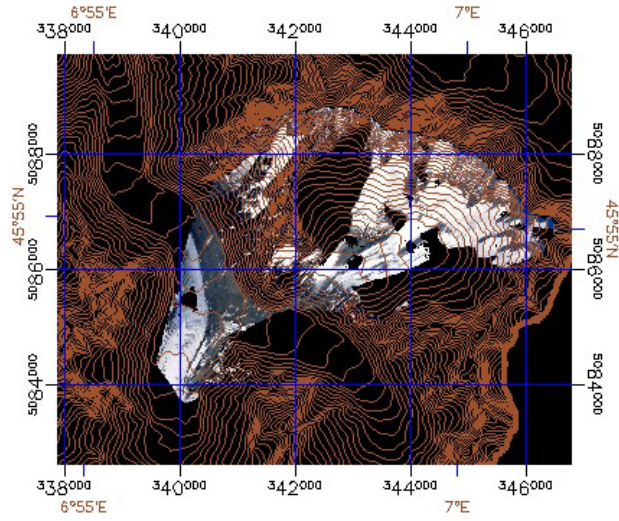


Figure 5.7. Georeferenced image of the lower middle section of the Mer de Glace. Reflectance values are extracted from photograph in Figure 5.5. Black areas (holes) are not visible from the camera position.

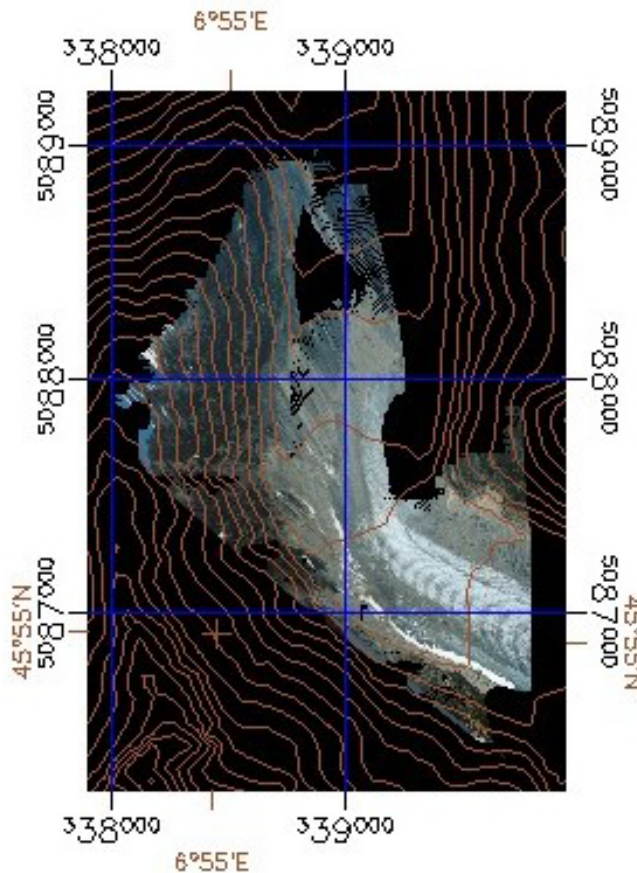


Figure 5.8. Detail of lower section of Mer de Glace. Georeferenced image using a resampled 10 m resolution DEM to show the potential of this technique for landform and pattern recognition. Note the dark and white ojives or Forbes bands on the glacier, which are characteristic of the lower tongue of the Mer de Glace.

Photo orientation

Unless the camera is mounted on a theodolite or a similar apparatus, it is very difficult to keep its X-axis (vector \vec{U}) in a strictly horizontal position at the time of taking the photograph, specially under adverse terrain and weather conditions. To cope with this problem a simple algorithm for correction of camera rotation is implemented.

The simplest correction is for the distortion due to roll of the camera around the viewing direction axis. Figure 5.9 shows the calculation of the angle of rotation. The discontinuous line represents the projected terrain points for a viewing coordinate system rotated approximately 15 degrees anti clockwise (note that an anti clockwise roll of the camera results in a clockwise roll of the image). The continuous line would be the photographed terrain. By measuring the pixel positions of both, the actual image P_i and the projected elevation points P_p relative to the center of the image, we can calculate angles ψ and γ and their difference, which is angle ζ , the actual roll of the camera. By rotating the camera coordinate system $C\vec{U}\vec{V}\vec{N}$ an angle ζ , the distortion due to roll is corrected. As we are dealing with unit vectors, the operation is reduced to adding a vertical vector of magnitude $-\tan \zeta$ to \vec{U} (recall from Equation 5.7) and finding the unit vector in the resulting direction:

$$\psi = \arctan \frac{P_{iy}}{P_{ix}} \quad (5.10)$$

$$\gamma = \arctan \frac{P_{py}}{P_{px}} \quad (5.11)$$

$$\zeta = \psi - \gamma \quad (5.12)$$

$$\mathbf{u}_\zeta = (0, 0, -\tan \zeta) \quad (5.13)$$

$$\vec{U}' = \frac{\vec{U} + \mathbf{u}_\zeta}{|\vec{U} + \mathbf{u}_\zeta|} \quad (5.14)$$

$$\vec{V}' = \vec{N} \times \vec{U}' \quad (5.15)$$

The new, rotated camera coordinate system will be $C\vec{U}'\vec{V}'\vec{N}$.

The differences between expected (due only to rotation) and measured values of the displacement of P_p along the X-axis will give us information on the yaw of the camera, or horizontal displacement of the estimated target. Extensive work is been done toward the elaboration of precise photo orientation algorithms (e.g. Croitoru and Ethrog 2001), although it was found that the use of precise ground control points, for example, collected by differential GPS (global positioning system), allows fast manual photo orientation by trial and error.

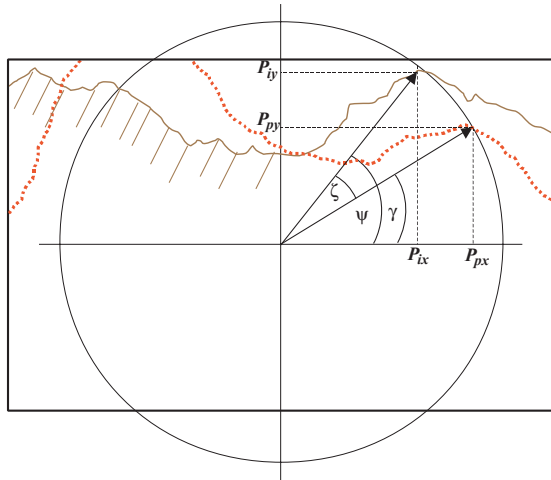


Figure 5.9. Example of mismatch between the perspective projection of the DEM (dotted line) and the photographic image (continuous line) due to roll of the camera. The correction for this displacement is explained in Section 5.3.1

Additional corrections

Additional corrections to account for the curvature of the earth and the refraction of light through the atmosphere need to be taken into account in some cases. Curvature of the earth may be important for images taken from a long distance. Simple trigonometry shows that the depression of the observed point or dip (Δz), is related to the distance to the observer by:

$$\Delta z = R_e - \frac{R_e}{\sqrt{R_e^2 + d^2}} \quad (5.16)$$

where R_e is the radius of the Earth, (mean value: 6,367,450 m) and d is the distance to the observer. For a distance of 10 km the dip would be 7.85 m, which should be subtracted from the cells' heights at that range prior to the georeferencing process.

The refraction of light is only important for paths through the atmosphere where the target and the observer are at very different altitudes, and therefore at significantly different air densities. Refraction is evaluated using the MODTRAN radiative transfer model (Berk et al. 1989). In the present study, for typical atmospheric conditions and maximum difference in height, the cumulative bending of the light rays is about 0.012° , which for the maximum distance range within the DEM amounts to an error of 2 m. However, the photographs are taken for smaller areas and elevation ranges, which made refraction and curvature in this case negligible.

Radial distortions are highly variable depending on the quality of the lenses used. This type of distortion alters the geometry of the image, typically in an exponential way as we move away from the centre of the image. Access to this information is not easy, as manufacturers normally classify it as confidential, but typical values are in the range of up to tens of μm (Cooper and Robson 1996, Fryer 1996). For a scanned digital image at 200 dots per cm (512 dpi), the radial distortion would be smaller than one pixel, and therefore negligible. An alternative solution if the radial distortion is

expected to be high, is to discharge the margins of the photograph and cover the area with another photograph centered around the discharged area. Tangential distortion is typically small compared to radial distortion (Jacobson 1978).

Other errors due to coma, astigmatism, barrel and pincushion distortion of the lens, curvature of field (Jacobson 1978) and for film deformation due to unflatness (Fryer 1996) are minimised by using high quality lenses and cameras.

5.3.2 Conversion from reflectance to albedo

A pixel in a photograph contains information on the reflected radiation coming from a determined surface area. This reflected radiation will depend on the incoming global radiation, the albedo of the surface, the intervening atmosphere and the viewing geometry. The global radiation is the result of multiple interactions of the solar radiation field with the atmosphere, the target and the surrounding terrain. Thus, the main factors affecting the solar radiation falling on a surface are:

- Ratio of direct to diffuse radiation. - Angle of incidence of the solar beam on the surface.
- Local horizons to the surrounding ground and the nature of this ground.
- Fraction of visible sky in the upper hemisphere or skyview factor.
- Multiple scattering of solar radiation between the sky and the ground.

The main factors affecting the measurement and recording of reflected solar radiation arriving to the film are:

- Atmospheric transmittance between the object and the camera.
- Anisotropy of the reflected radiation.
- Input/output relationship between the incoming light and the response of the lens-camera-film-scanner system.

A photograph contains a large amount of information at a very high resolution, but it is not a system designed for retrieving quantitative information from the original incoming radiation. However, this work assumes that there is a direct relationship between the albedo of a surface and the camera output of the recorded reflected flux radiance. Then, by comparing the values of pixels in a photograph to a determined reference pixel corresponding to a surface of known albedo, we can estimate the albedo of the remaining surfaces, even when it is not possible to estimate the actual value of the radiative flux arriving to the film.

The surface albedo is defined as the ratio of the hemispheric reflected (I_r) and incoming (I_i) radiative fluxes (e.g. Knap and Reijmer 1998):

$$\alpha = \frac{I_r}{I_i} \quad (5.17)$$

The incoming radiative fluxes are calculated as:

$$I_i = ((R_0/R)^2 I_{sc} \tau_i (F_t + F_{sk} + F_{ms} + F_{sn})) \quad (5.18)$$

where I_{sc} is the solar constant or 1366.1 Wm^{-2} (Fröhlich and Lean 1998); $(r/r_0)^2$ is the reciprocal of the square of the radius vector of the earth, or correction for the eccentricity of the earth's orbit, which here is calculated using Fourier series derived by Spencer (1971), Equation 5.19; and τ_i represents atmospheric transmittance functions, both for diffuse and direct radiation, which take into account Rayleigh scattering, transmittance by ozone, by uniformly mixed gases, by water vapour and by aerosols, and are computed following a parametric model by Iqbal (1983). The τ -functions incorporate the relative optical path length and pressure corrected air mass, depending on solar zenith angle and altitude. Further updates to Iqbal's model are introduced for the calculation of precipitable water, following Prata (1996), for ozone layer thickness, which is extracted from the NASA Total Ozone Mapping Spectrometer dataset (TOMS-EP 2001) and for increased transmittance with altitude, computed statistically after several runs of the model and in accordance with values recommended by Bintanja (1996), as explained in Chapter 3.

The eccentricity correction is:

$$\begin{aligned} (R_0/R)^2 &= 1.00011 \\ &+ 0.034221 \cos \theta_J + 0.00128 \sin \theta_J \\ &+ 0.000719 \cos 2\theta_J + 0.000077 \sin 2\theta_J \end{aligned} \quad (5.19)$$

where θ_J is the dayangle, calculated as:

$$\theta_J = \frac{2.0 \pi (J - 1.0)}{365.0} \quad (5.20)$$

with J the day of the year: 1 on the first of January, 365 on the 31st of December.

The model has been tested successfully at high altitude in the Andes and at lower altitudes in the Alps during the work for this thesis (see Figures 3.4 and 3.5 in section 3.7.1). In both cases the differences between modelled and measured data were smaller than the error introduced by pyranometer accuracy (3%), This model also gives the best results in a comparative study of radiative flux parameterizations for short-wave radiation published by Niemelä et al. (2001b).

The terms of the last factor in Equation 5.18 represent the corrections for the influence of topography and diffuse radiation. These are:

$$F_t = f_{dt} \hat{n} \cdot \hat{s} = f_{dt} \cos \theta_s \quad (5.21)$$

is a correction term for the angle of incidence of sun on the slope, where f_{dt} is the ratio of direct to total incoming radiation, \hat{n} is the unit vector normal to the surface and \hat{s} is the unit vector in the direction of

the sun. This dot product is equivalent to the cosine of the relative solar zenith angle θ_s . F_t is computed only for cells in the sun, not in the shadow.

$$F_{sk} = f_{df} f_v \quad (5.22)$$

is diffuse radiation from the sky, f_{df} is the ratio of diffuse to total incoming radiation, calculated from Iqbal's model, and f_v is the hemispherical fraction of visible sky, or skyview factor. f_v and \hat{n} are calculated from a digital elevation model of the area, these two terms and \hat{s} are computed following the algorithms developed in Chapter 4.

$$F_{ms} = \alpha_{sk} (f_s \alpha_s + (1 - f_s) \alpha_g) f_{sh} \quad (5.23)$$

is diffuse radiation due to multiple scattering between the ground and the sky, where α_{sk} is the albedo of the atmosphere, which depends on atmospheric conditions and is calculated according to Iqbal (1983); f_s is the fraction of surrounding terrain covered by snow with albedo α_s ; the remaining terrain has an estimated albedo of α_g ; and f_{sh} is a shadow factor:

$$f_{sh} = f_{dr} f_{st} + f_{df} \quad (5.24)$$

where f_{st} is the ratio of cells in the sun to total number of cells.

A rigorous computation of reflected diffuse radiation will require an exhaustive evaluation of viewing geometry and illumination conditions of the surrounding terrain, which is computationally expensive. Therefore, a simplified approach is suggested in the form of the following equation:

$$F_{sn} = (1 - f_v) (f_{sv} \alpha_s + (1 - f_{sv}) \alpha_g) f_{sh} \quad (5.25)$$

where the term f_{sv} is the ratio of snow covered to total visible surrounding terrain. Following Greuell et al. (1997), a distinction is made between f_s and f_{sv} , as reflected diffuse radiation from snow will come from those surfaces which are visible, while the diffuse radiation due to multiple scattering with the sky might come from surrounding snow covered terrain which is not visible from the area under consideration.

The snow albedo is not isotropic, and variations might be important, especially at low relative solar zenith angles. It is generally agreed that the albedo of the snow is independent of θ_s for θ_s smaller than 50° (Wiscombe and Warren 1980, Brock, Willis and Sharp 2000). In any other cases, and for the albedo of the ice, bidirectional reflectance distribution functions should be applied (see for example: Greuell and de Ruyter de Wildt 1999, Knap and Reijmer 1998).

The reflected radiation arriving at the camera or recording device per pixel will be:

$$R = I_i \alpha \Omega \tau_t \quad (5.26)$$

where Ω is the ratio of the solid angle of a receptor's pixel field of view to 2π (the whole hemisphere solid angle), and τ_t is a transmittance function to account for atmospheric attenuation between the target and the camera. τ_t is calculated using MODTRAN and general knowledge of the local atmospheric conditions. Running the MODTRAN model for all the cells would be extremely time consuming if not impossible. Thus, a feasible solution is to run the model for a set of points containing the boundaries of the DEM, clusters of points in the regions of more interest and randomly selected points. From the results of these runs a statistical fit is interpolated as a surface of minimum curvature passing through the given values. Transmittances for all the remaining grid cells are obtained by reference to this interpolated surface.

The ratio of the reflectance of any given pixel R_n to a reference pixel reflectance R_{ref} whose albedo is known, will be:

$$\frac{R_n}{R_{ref}} = \frac{(I_i \alpha \Omega \tau_t)_n}{(I_i \alpha \Omega \tau_t)_{ref}} \quad (5.27)$$

Rearranging terms, combining with Equation 5.18 and noting that $\Omega_n = \Omega_{ref}$, as the camera pixels are uniform and their field of view solid angles are identical, we have:

$$\alpha_n = \alpha_{ref} \frac{R_n}{R_{ref}} \frac{(\tau_i \tau_t)_n (F_t + F_{sk} + F_{ms} + F_{sn})_{ref}}{(\tau_i \tau_t)_{ref} (F_t + F_{sk} + F_{ms} + F_{sn})_n} \quad (5.28)$$

where $(\tau_i)_n$ and $(\tau_i)_{ref}$ may cancel each other if altitudinal variations within the area under consideration are small.

The ratio R_n/R_{ref} is calculated directly from the digital numbers of the digitised (scanned) photograph. α_{ref} is known by direct measurement and the rest of terms are calculated following equations 5.18 to 5.25. Thus, it is sufficient to know a reference albedo, which is measured at one single point, in order to estimate the albedo of the whole area in the image. The reference albedo is one single measurement and can be located at any point visible in the image, although it is better to select an area of uniform albedo and slope to minimise errors derived from georeferencing inaccuracies. If no direct measurement of a reference point is possible, then a surface of known reflectance such as a Kodak grey card or a spectralon panel could be introduced at the time of taking the image and follow the same procedure to calculate the albedo of the remaining pixels.

Narrow band versus broadband albedo

The recording device used in this work is slide film for visible light, sensitive to radiation in the range of 400 to 700 nm. However, the snow absorbs energy in the form of short-wave radiation in a wider

5.3. Methodology

spectrum, and the albedo is generally measured in the range 300 to 2800 nm. A conversion between the narrow visible band to the wide short-wave band is desirable.

Snow may present large variation in albedo in the near infrared, depending mainly on snow grain size (Wiscombe and Warren 1980, Dozier, Schneider and McGinnis 1981). However, the corresponding variations in the visible band are too small to detect with normal photographic film, therefore it is not possible to extend the visible albedo to a wider band using only information on the visible range. None the less, the actual energy inputs in the regions 300–400 nm and 700–2800 nm, for the usual atmospheric conditions in which we were working, are 10% and 25% respectively of the total short-wave energy, according to MODTRAN model outputs. The maximum range of albedo variation is very small in the ultraviolet and up to approximately 40% in some region of the infrared for varying snow grain size (Wiscombe and Warren 1980, Figure 8). Thus, the maximum error in the estimation of energy inputs in the case of extreme variations of snow grain size, considering only the visible band, would be about 9% and typically smaller. During the present work snow grain size was practically uniform on the whole area except for the upper section of Mont Blanc de Tacul, above 4,000 m a.s.l. Ground above 4,000 m represented only 2% of the total surface and images used for the computation normally contains only one uniform type of snow. Therefore, the extension of albedo values derived from reflectance comparisons in the visible region band to broad band albedo is a reasonable assumption in this particular case. Further research will focus on ways of improving the estimation of albedo by using digital or spectral cameras sensitive to near infrared radiation.

Film-scanner input/output relationship

The relationship between incident light on the camera and film response depends on the emulsion used, the type of lens, the exposure, brightness of the object and film development. Additionally, the accurate response of the scanner to the light transmitted through the processed film is difficult to quantify, as scanner manufacturers normally do not provide the necessary information. These processes introduce uncertainties and non-linearities in the evaluation of the scanned digital image.

To deal with this problem an empirical approach was followed, to obtain a function that relates input (incoming light) to output (digital values produced by the scanner), for a given combination of lens-film-scanner. The procedure is similar to sensitometric analysis in photography (Jacobson 1978) and consists of finding a statistical fit between known illumination values and resulting output from the scanner.

In the present work a graded grey-scale card (Kodak Grayscale Q-13) was photographed and used as a calibration input. This card is a rectangle divided into 25 boxes of varying shades of grey, from near white to near black at 0.05 density steps, from nominal values of 0.05 to 1.95. Density is a magnitude normally used in photography, whose value is the logarithm of light flux intensity, either transmitted through the film, or reflected from a surface. Thus, the grey-scale card densities correspond to re-

flectance values between 1% and 89%. Values below 10% were ignored, as the response of the film in this area is non-linear and we are dealing with snow, which has always higher reflectance. In case we are interested in very dirty and debries-covered ice with lower reflectance values, the image should be slightly over-exposed to avoid dealing with images in the nonlinear part of the response curve. Values for the scanned test photograph are plotted in Figure 5.10. Most photographic films present characteristic response curves that shows a straight line between a toe of increasing slope in the darker region of the image and a shoulder of decreasing slope near saturation. Therefore, a correctly exposed film, with density values within these two thresholds, should present a linear response, although slightly modified by the development and scanning. For a film scanned at gamma = 1, Figure 5.10 shows a linear relationship close to 1:1 (slope = 1.111, $r^2=0.998$) for digital numbers corresponding to reflectances in the snow region. This linear relationship simplifies the correction between original reflectance values and the DN values produced after scanning the film. It is sufficient to solve for the x in the regression equation and apply it to the reflectance values.

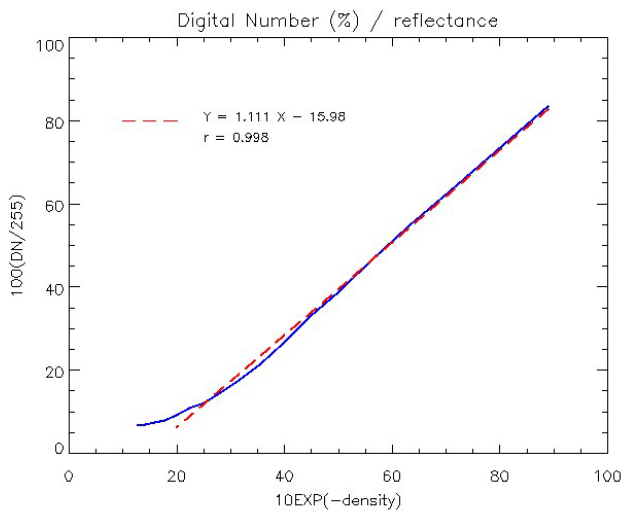


Figure 5.10. Digital Number (DN) versus reflectance. The output of the scanned photographic image is conditioned by the whole photographic process, camera, lenses and scanner characteristics. In order to relate the input light to the output values an empirical approach was followed. Solid line shows the relationship between input light and output DN values and dashed line is a regression fit excluding areas of very low reflectance. The regression is then linear, and the exclusion of very low (dark) values is justified as we are dealing with snow, which high reflectance values, in the region where the function is linear.

5.3.3 Data format

To facilitate data portability and to integrate digital elevation models and image files, the GeoTIFF data format was chosen for digital analysis and storage. GeoTIFF represents an effort by over 160 different remote sensing, GIS, cartographic, and surveying related companies and organizations, to establish a TIFF based interchange format for georeferenced raster imagery (Ritter and Ruth 1997, Ritter and Ruth 2000).

5.4 Experimental set up

Photographs and direct albedo measurements were taken on the Mer de Glace on different days from the 6th to the 26th of June 2000. The Mer de Glace is the largest glacier in the French Alps and the third largest in the whole Alps (Figure 5.12). It is located east of the Mont Blanc, with a length of 12.3 km, and a surface area of 32.09 km² (Hoelzle and Haeberli 1999). The altitude ranges from 4,248 m above sea level to 1,470 m a.s.l. The location was selected taking into account the variability of snow and ice surface albedos, different orientations, accessibility, safety and efficiency of time allocation.

The orientation of the principal glacier slopes range from 0 to 180 degrees, with the largest sections of the glacier facing S, SE and N. This range of orientations makes possible studying the glacier at different times and with different solar illumination conditions. The upper section of the glacier, above 4000 m, had fresh snow that had not suffered intense metamorphism processes, and consequently had a higher albedo. However, most of the glacier was covered in well metamorphosed granular snow. The lower section was bare glacier ice partially covered in debris.



Figure 5.11. Albedometer setting. The white oval, above and left the camera tripod is the albedometer, made up of two Kipp & Zonen opposed pyranometers. The output is read in two voltmeters connected at the extreme of the cable, held by the skier-operator in the image.

Albedo measurements were taken using a Kipp & Zonen CM 7B albedometer, which consists of two opposed pyranometers sensitive to hemispherical incoming and reflected short-wave radiation in the range 300–2800 nm. The albedometer was attached to a photographic camera tripod, as shown in Figure 5.11, and positioned parallel to the surface to minimise measuring errors due to the inclination of the surface (Mannstein 1985, Sicart et al. 2001). Measurements were taken on the widest possible range of surface types, orientations and time of the day. The location of every site was determined using a GPS with a nominal precision of 15 m. The actual precision, especially at the bottom of the valleys with poor satellite visibility and geometry was estimated in the range of 25 to 100 m by comparison of actual readings on the GPS receiver with points whose location was well known.

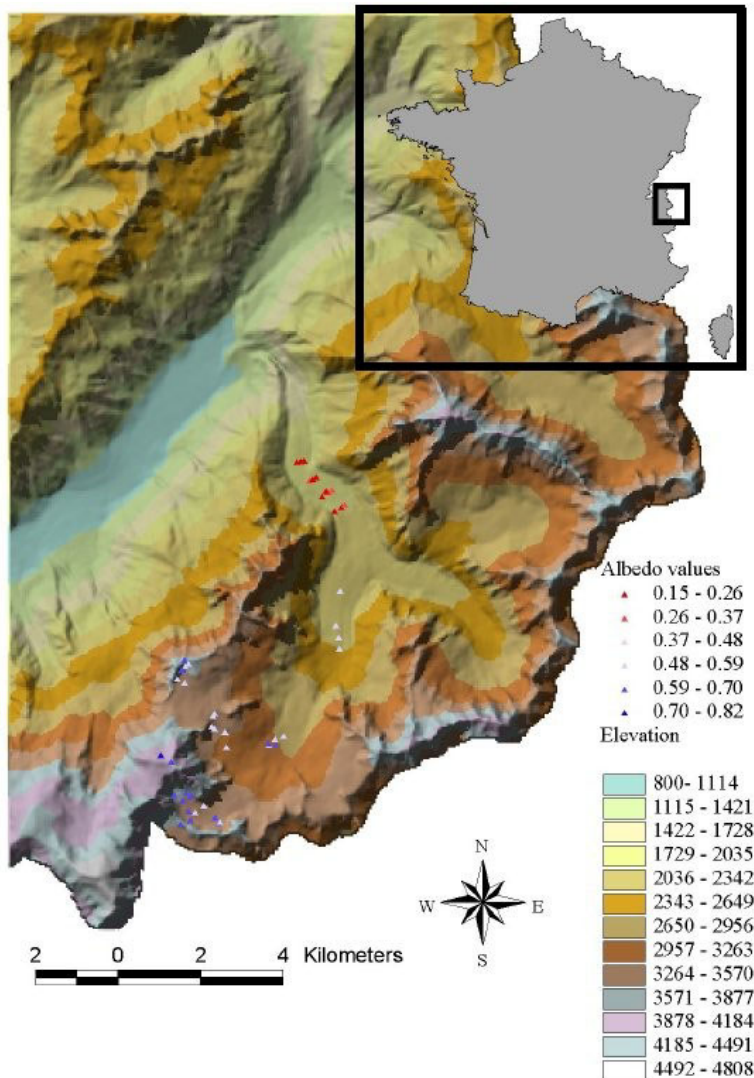


Figure 5.12. Map of the area of study in the French Alps, $45^{\circ} 50' \text{ N}$, 7° E . Mer de Glace glacier is the inverted Y-shaped glacier in the lower centre of the image. Coloured dots are albedo measurements. The DEM only covers the French side of the area, with no values for Italy and Switzerland.

A digital elevation model at 50 m grid resolution was purchased from the French Institute Géographique National. Photographs were taken with a Nikon F4 camera and lenses in the range 35–80 mm. The film used was Kodak Ektachrome E100SW for visible light, which shows a good overlapping of spectral bands and extended linear response over its sensitivity range (Kodak 2001). A Kodak grey card was used as a reference card, both for the intensity of reflected light and for spectral balance. Although the grey card is not a perfectly diffuse reflector, it has small variations in reflectance over the optical wavelengths according to Milton (1989) and to tests with a GER 3700 spectrometer performed by the author.

5.5 Results and discussion

The result of the georeferencing process for this test site have already been introduced in Section 5.3.1, Figures 5.7 and 5.8. The accuracy of the georeferencing process decreases with shallow viewing angles (areas of closely packed red dots in Figure 5.5), and is better for viewing directions approaching the normal. This fact makes the technique more appropriate for mountain terrain, where images can be taken from ridges and peaks with steep viewing angles to the valley.

The final result of the albedo estimation is shown in Figure 5.13 as a color coded georeferenced composite image of estimated albedo values derived from three different photographs of the Mer de Glace. Coloured crosses representing the measured values are superimposed, so that discrepancies can be easily highlighted, although none is obvious in this case. The inset, extracted from a resampled DEM at higher resolution, is a detail of the lower section, showing the albedo variations among the glacier ogives. Black areas are either areas not visible from the photo or with relative solar zenithal angles higher than 60°. Figure 5.14 shows the differences between estimated and measured albedo values. The maximum error in the estimation of albedo is 6.5%, while the average error is only 2.2%.

In general errors are small and most of them are derived from displacements between photograph and DEM during the georeferencing process, especially in areas where there is an abrupt change of slope. This is because the angle between the sun and the normal to the slope is the most important parameter affecting the conversion between reflectance values and albedo. Thus, a small displacement may cause a relatively flat pixel being corrected for an excessively steep slope. This type of error can be avoided improving the georeferencing process by providing more precise and a larger number of ground control points. Uncertainties in the exact geolocation of the photo-pixels, together with ambiguous assignation of image pixels to DEM cells, specially for low resolution DEMs, may lead to errors due to high albedo variability over the glacier. As Figure 5.15 shows, inter-pixel variability of albedo values is in the same range as the maximum error in the albedo estimation. This variability is maximum in areas partially covered with debris and on patchy surfaces, with intermixing of snow and glacier ice. The date of DEM production is important too, given the fast retreat and thinning rate of some Alpine glaciers.

When using normal film and additional scanning of the image on non metric cameras, there is always some mismatch between the actual borders of the film and the origin of the image. If the film is scanned from a framed slide, there may be some additional inaccuracies due to internal displacements of the film inside the slide mount. Additionally, the corners of the photographic emulsions are not perfectly square (Croitoru and Ethrog 2001), which may add an uncertainty of a few pixels, reducing the accuracy of the georeferencing step. This problem can be easily solved using digital photography.

As there was limited information on the anisotropy of the reflected solar radiation over the snow, the traditional rule of thumb considering albedo independent of the relative solar zenith angles for angles smaller than 50° (Wiscombe and Warren 1980) was applied, and cells falling outside this condition were masked out. Work by Gruell (2002) shows that there is still insufficient knowledge about the an-

gular distribution of the reflected radiation over the snow and that bidirectional reflectance distribution functions (BRDFs) may not be of universal application. Therefore the masking out option was considered safer than applying corrections from BRDFs derived at other locations and with different snow characteristics. A further project using a modified application of the photographic technique described in this paper for the derivation of suitable BRDFs is under consideration. Albedo was estimated only for the visible part of the spectrum, which may lead to some errors (see Section 5.3.2), although the uniformity of grain size in the case study suggests that these errors are likely to be small.

Further work to assess the accuracy of the georeferencing process was carried out in the Swiss Alps, at the Haut Glacier d'Arolla, in cooperation with the Swiss ETH. Here a higher resolution DEM and GCP collection with differential GPS was possible, which resulted in improved geolocation. The albedo was measured at five AWS on the glacier and the value of one of them used as reference value. The derived albedos for Arolla compared well to simple parameterisations of albedo derived from ageing curves (Corripio et al. 2002). In Arolla photographic images were taken on a daily basis, this allowed the study of a temporal series of georeferenced images and the study of the snow line retreat and advances. Two examples of the results are shown in Figure 5.16, a three-dimensional representation of the area covered by the photographic image; and in Figure 5.17, which shows the evolution of snow cover during the ablation season. An animation of the process is available at:

<http://tsunami.geo.ed.ac.uk/~jgc/temp/arollaanimation.html>.

This georeferencing technique was not fully developed until the completion of the field work in the Andes, thus, application to the area was limited.

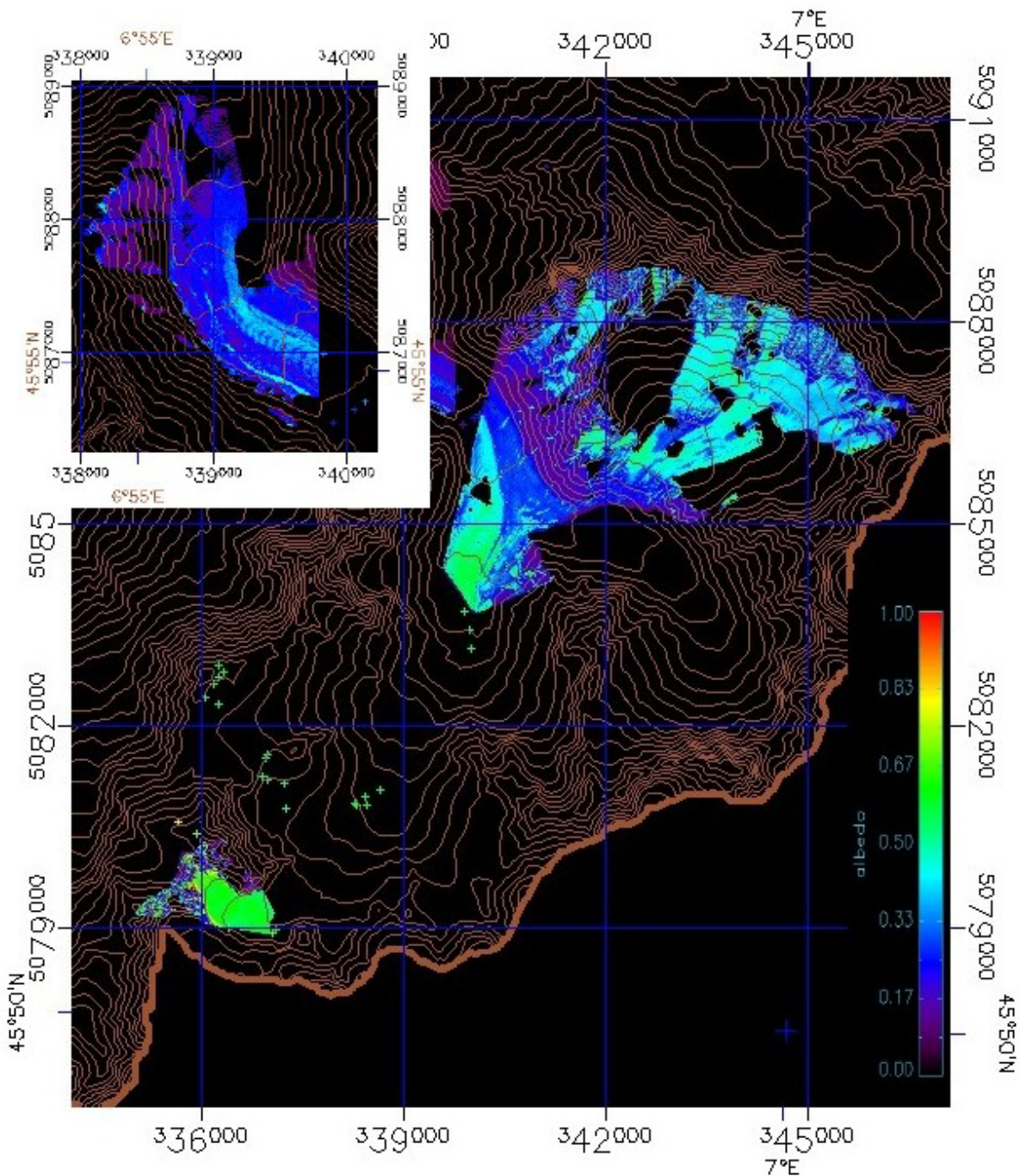


Figure 5.13. Colour coded composite map of albedo values derived from three georeferenced photographs of the Mer de Glace. Coloured crosses are measured values, a first inspection reveals good agreement between measured and estimated values. Actual values are plotted in Figure 5.15. The inset is a detail of the lower section of the Mer de Glace, corresponding to Figure 5.8, showing the albedo variability among the glacier ogives.

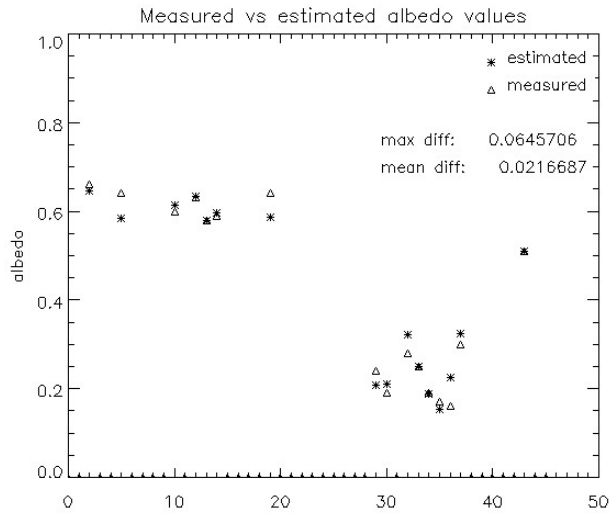


Figure 5.14. Measured versus estimated albedo values for areas in Figure 5.13. The maximum difference is 6.5%, while the average is 2%, which is less than the accuracy of the albedometer. Measured points on the X-axis are ordered from west to east.

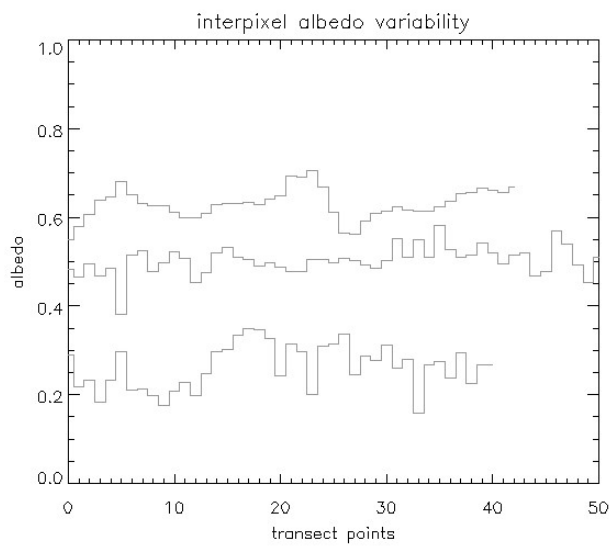


Figure 5.15. Inter-pixel variability of the albedo values for three arbitrary transects on the upper, medium and lower (ice covered) areas of the glacier. High variability in a relative small space is a large source of errors in the photography derived albedos.

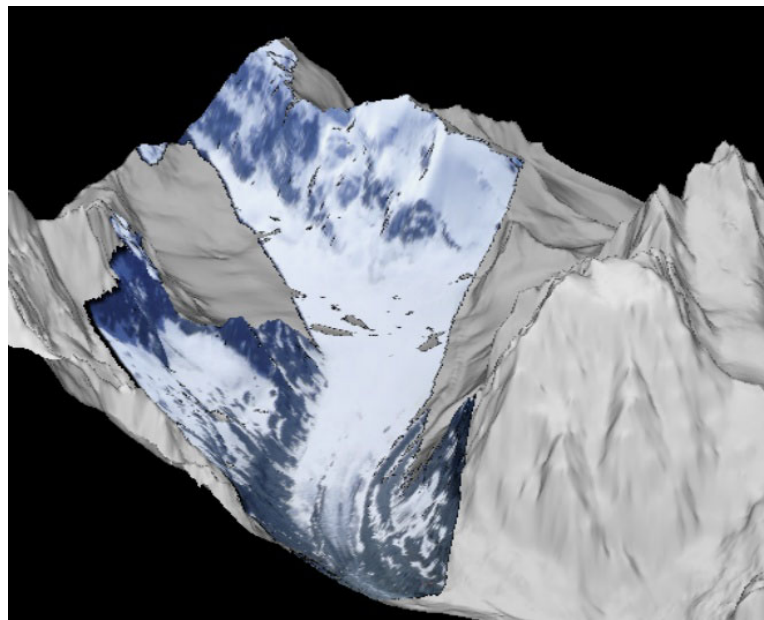


Figure 5.16. Relief representation of a georeferenced photograph taken from the north of Haut Glacier d'Arolla looking south, wrapped over the digital elevation model of the area.

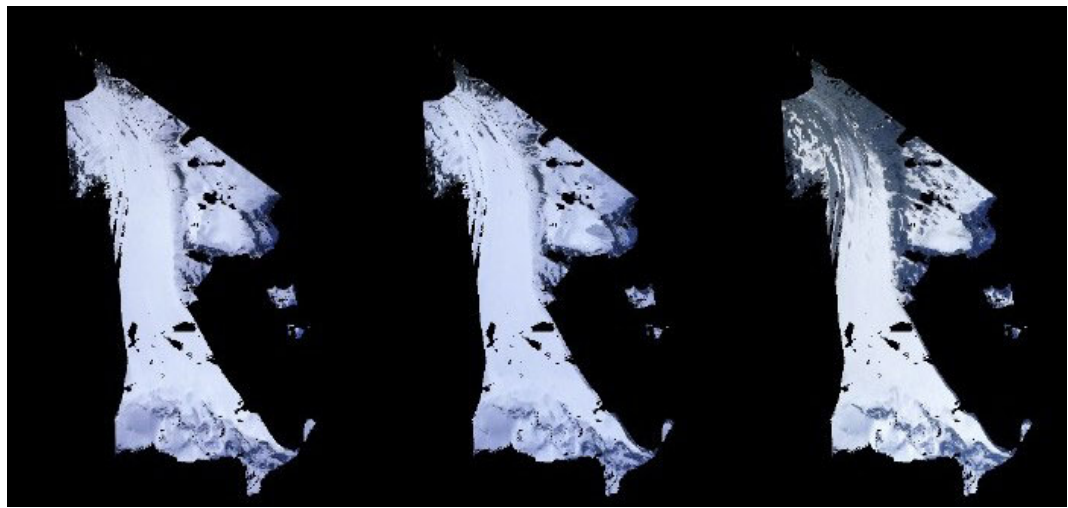


Figure 5.17. Evolution of snow cover during from 25 May 2001 to 25 July 2001 on the Haut Glacier d'Arolla, Swiss Alps. Note that the image has enough resolution to detect small avalanches on the rightmost section of the central image.

Chapter 6

Model implementation and results

This chapter discusses the implementation of a distributed energy balance model to a high altitude basin in the Central Andes. The chapter also assesses the energy balance components, their spatial variation, the effect of penitentes on snow melt, and infers the effects of any possible changing climatic conditions on the snow ablation and water resources.

We need a distributed model to gain useful information of the ablation, runoff and climatic sensitivity of the whole glacierised basin, yet, most of the data are generally gathered at one or at most few points on the surface of the glacier. The step from point to distributed modelling poses two main problems. Firstly, there is a problem of scale, which translates into a strong computational demand, as we need to repeat complicated calculations for the many hundreds of thousand cells that integrate the digital elevation model. Secondly, there is the problem of uncertainties in the data input. If we knew perfectly well the exact behaviour of the atmosphere, one single point measurement would give us full insight on the state of all variables and their change in space and time. This, unfortunately, is not the case; therefore, we need to resort to either extensive measurements, remote sensing or further modelling to generate the distributed data input. Chapter 5 developed one of such remote sensing tools to measure albedo at the basin scale. It will be of limited use when the snow is covered in penitentes, but is fully applicable early in the season or at elevations where penitentes have not developed.

In Chapter 3 we reviewed the best available point modelling approaches that can be applied to assess the snow surface energy balance. In this chapter we assess the application of those approaches to distributed modelling when feasible, and suggest alternative simplifications when their computational demands make their implementation unrealistic.

As we have seen in Chapter 2, the case of the Dry Central Andes is further complicated by the presence of penitentes. This problem will be treated using a digital elevation model of the microscale topography that replicates the local surface penitentes. The treatment of these complex surfaces, espe-

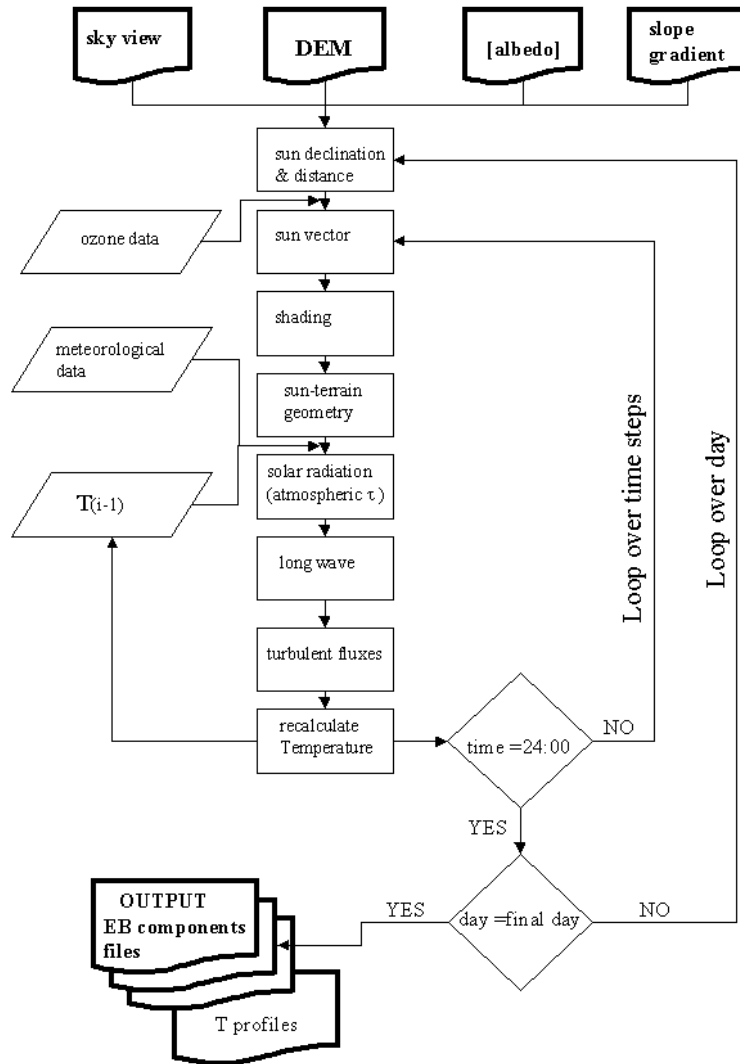


Figure 6.1. Schematic flow diagram of the energy balance modelling. Albedo in brackets indicates an optional input when it is available or an estimation or extrapolation when direct or derived measurements are not available.

cially when they have overhanging sections, is possible thanks to the algorithms developed in chapter 4. The implementation of the distributed model is described schematically in Figure 6.1.

6.1 Boundary and initial conditions

The implementation of the model assumes the conservation of energy:

$$I_G(1 - \alpha) + L \downarrow - L \uparrow + H + L_v E + Q_s + M = 0 \quad (6.1)$$

where I_G is global short-wave radiation (direct, diffuse and reflected from surrounding slopes), M is the energy used for snow melt and Q_s is energy to change the temperature of the snow pack. Mass balance is not addressed, so the snow melted simply leaves the system. Evaporation is added to the computation of total ablation and is taken into account as the latent heat component ($L_v E$). The temperature of the snow is allowed to fluctuate but never can exceed 273.15 K. Once it reaches this temperature all energy surplus is redirected to melting. The conditions at the boundaries of any DEM are not well defined, as we do not have any information of the topography beyond this area. This affects the computation of the terrain parameters and the incoming solar radiation. For example, the eastern side of any DEM representing any rough terrain on the surface of the earth is directly illuminated by the rising sun, when in reality could be shadowed by mountains located further east. To minimise errors derived from this uncertainty, the two first and last columns and rows of the DEMs used here replicate the value of the immediately inner row or column, and the values of the 5 outer rows and columns are ignored in the final evaluation of results. This value of five columns was chosen after visual and statistical evaluation of the results, by using plots of profile values and by studying the color representation of diverse parameters such as shadows or cumulative insolation.

The temperature of the snow for every grid cell is initially set equal to that of the air, then recalculated at every time step and subsequently fed into the model as the initial snow temperature for the following time step calculation. The temperature of the snow-free ground is set equal to that of the surrounding air for the calculation of the intercepted long-wave radiation emitted by surrounding slopes. This is a simplification, but as ground emissivity is smaller than snow emissivity and much of the surrounding ground is snow-covered, the errors are expected to be small. For the calculation of the intercepted long-wave radiated by snow-covered surrounded slopes, the temperature of the snow is set equal to the temperature of the local cell. This is likely to overestimate incoming long-wave radiation at lower elevations and underestimate it at higher elevations. The error will only be appreciable in areas of very low sky visibility. A rigorous evaluation requires detailed viewshed analysis that make the running times of the model impractical for present research.

6.2 Input data

The available data are those recorded by one automatic weather station on the glacier. This is suitable for a point model but further elaboration is needed to input them into a distributed model. Variables such

as albedo and surface temperature could be obtained using remote sensing techniques, either satellite or land-based. Air temperature would require knowledge of vertical profiles and wind distribution. The former was not available. An attempt was made to estimate the latter using simplified wind models (e.g. Ryan 1977), however, the model tested are found to be highly site-specific, and therefore of no application to the Andes area. In the absence of better modelled or measured values, wind will be considered constant over the whole area and equal to those measured at the AWS.

The model design allows either the incorporation of distributed data inputs in the form of arrays corresponding to the cells of the DEM, or the simplified extrapolation from point measurements. When no measurements are available, as in the Andes study, meteorological variables are extrapolated assuming standard profiles of relative humidity and lapse rates with elevation (U.S. NOAA 1976). Additional data for daily ozone values were retrieved from the total Ozone Mapping spectrometer (TOMS-EP 2001).

The recorded meteorological variables are summarised in Table 6.1. The most remarkable aspect is the very low relative humidity. Occasional high values were associated with the presence of clouds, sometimes at the AWS level. Relative humidity follows a diurnal cycle, with maxima due to nocturnal cooling and minima normally related to katabatic winds. Winds were light to moderate and fairly constant. Wind direction on Juncal Norte glacier had a clear bimodal distribution matching the upvalley–downvalley orientation. Downvalley winds were stronger than in Loma Larga, as Juncal Norte is a larger glacier in a deeper valley and it is surrounded by higher peaks. In the Loma Larga glacier the downvalley direction seems to have two components: one is the general downvalley direction, and the other is the influence of downslope flow from the Northeast. This latter is due to the main snow covered slope in the valley, which is facing south and therefore receiving less solar radiation, which leads to more intense cooling of the surrounding air, and is likely to cause an important downward density flow affecting the local winds. Incoming solar radiation was very intense, with average values close to those of perfectly clear days and peaks exceeding 1700 Wm^{-2} at the upper AWS. These peaks were higher than the exoatmospheric radiation and were probably caused by enhanced downward flux due to forward scattering of light by large cumulonimbus. Albedo was fairly constant during the whole measurement period, and typically 8% lower on the upper station, where the site was completely covered in penitentes. The calculated dew point was well below zero, with very rare exceptions.

It should be pointed out that reliable measurements of ablation in the penitente-covered area of the upper meteorological station were not available. This proved very difficult because measuring changes in penitente dimensions relative to a changing surface is a non-trivial task.

The values of measured meteorological variables and calculated dew point on the two glaciers are given in Figures 6.2 to 6.13. The values for Juncal Glacier were recorded by an AWS installed at 3335 m on relatively flat and melting snow near the glacier snout. This snow was composed of large rounded grains about 2 mm in diameter. The upper AWS was installed at 4667 m on an area of the glacier completely covered in penitentes. These penitentes were between 1 m and 2 m deep, with an average depth of 1.35 m. As the peaks of the penitentes were rather irregular, it is difficult to estimate the slope

Table 6.1. Recorded meteorological variables and calculated dew point.

Juncal glacier, 3035 m	T °C	RH %	u ms ⁻¹	SWin Wm ⁻²	SWout Wm ⁻²	α	dew point °C
min	1.2	10.4	0.1	—	—	—	-19.2
mean	7.7	35.7	3.9	353	184	0.52	-7.6
max	17.3	80.2	13.6	1564	810	0.52	1.6
std. dev.	3.2	15.4	1.8	—	—	—	4.3
Loma Larga gl., 4667 m							
min	-8.4	5.0	0.0	—	—	—	-34.3
mean	0.1	39.3	2.5	383	163	0.44	-13.6
max	12.7	97.0	9.5	1727	737	0.43	1.7
std. dev.	3.8	18.5	1.5	—	—	—	7.6

of the area. The qualitative impression and the slope derived from the DEM cell suggest that it was flat. The elevation of the AWS was estimated from GPS, watch altimeter and the map location. The watch altimeter proved to be unreliable. The actual height is expected to be within $\pm 90\text{ m}$ of the given value. For clarity, only the first week of data is plotted, although the whole period was used for the model runs, validation and calibration. Calibration refers to the corrections made to Greuell and Konzelmann's (1994) formulation of turbulent fluxes (Section 6.3.3). No further calibration was made. All the data are plotted in the Appendix A.

6.2. Input data

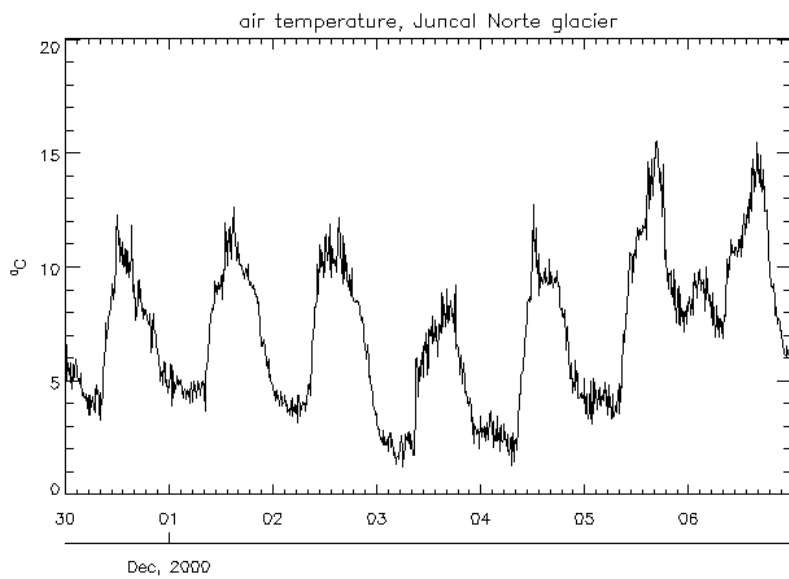


Figure 6.2. Air temperature measured on Juncal Norte glacier at 3335 m.

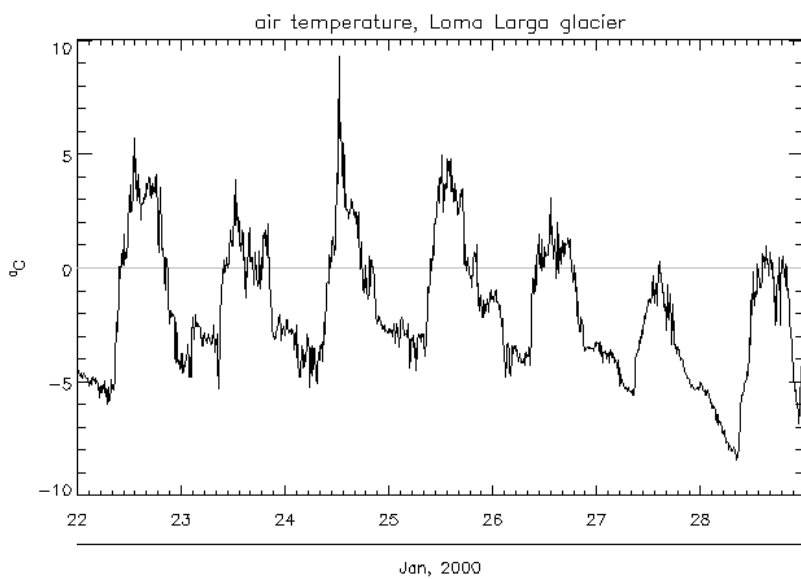


Figure 6.3. Air temperature measured on Loma Larga glacier at 4667 m.

6.2. Input data

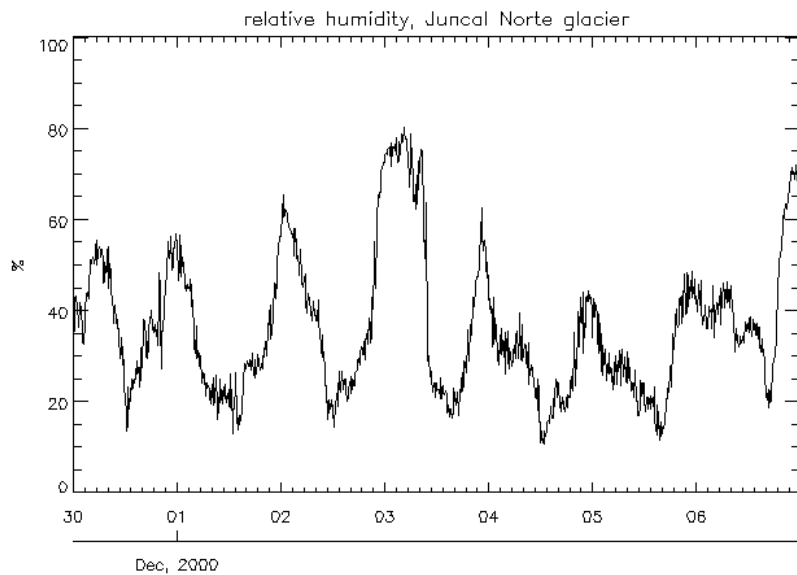


Figure 6.4. Relative humidity measured on Juncal Norte glacier at 3335 m.

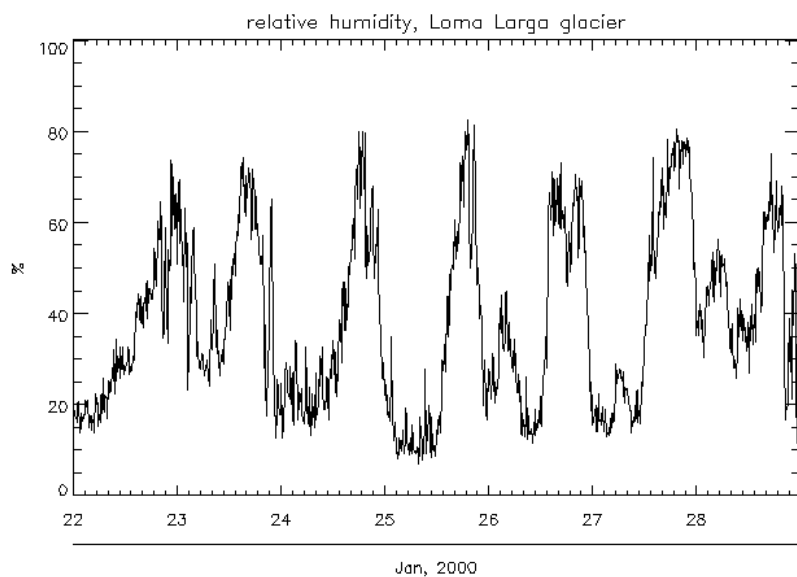


Figure 6.5. Relative humidity measured on Loma Larga glacier at 4667 m.

6.2. Input data

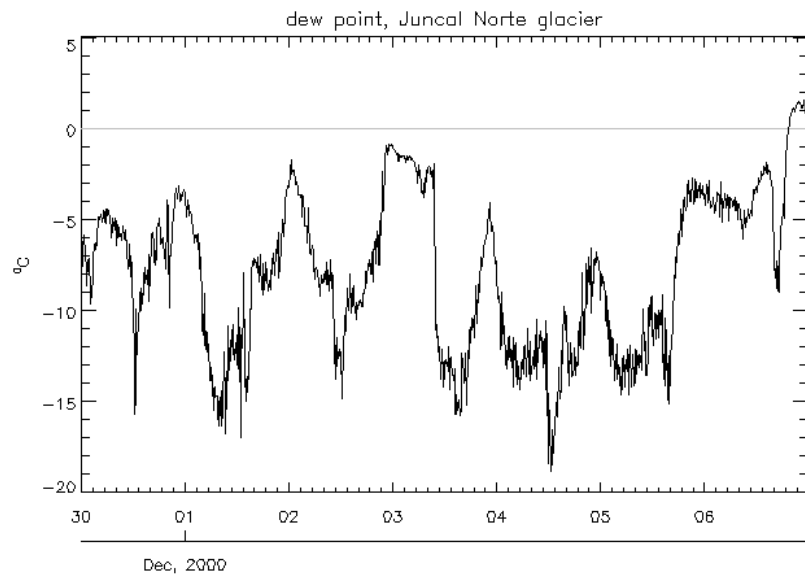


Figure 6.6. Dew point calculated according to Jacobson (1999) 2.56 on Juncal Norte glacier at 3335 m.

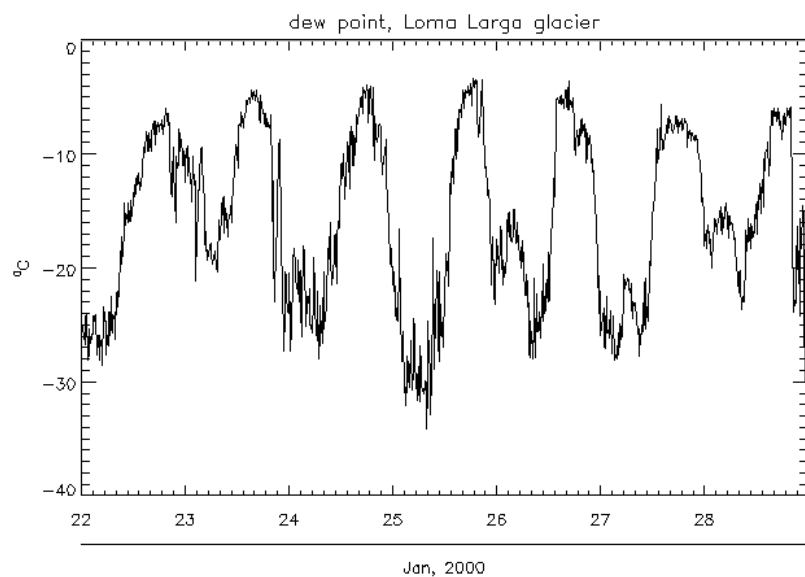


Figure 6.7. Dew point calculated according to Jacobson (1999) 2.56 on Loma Larga glacier at 4667 m.

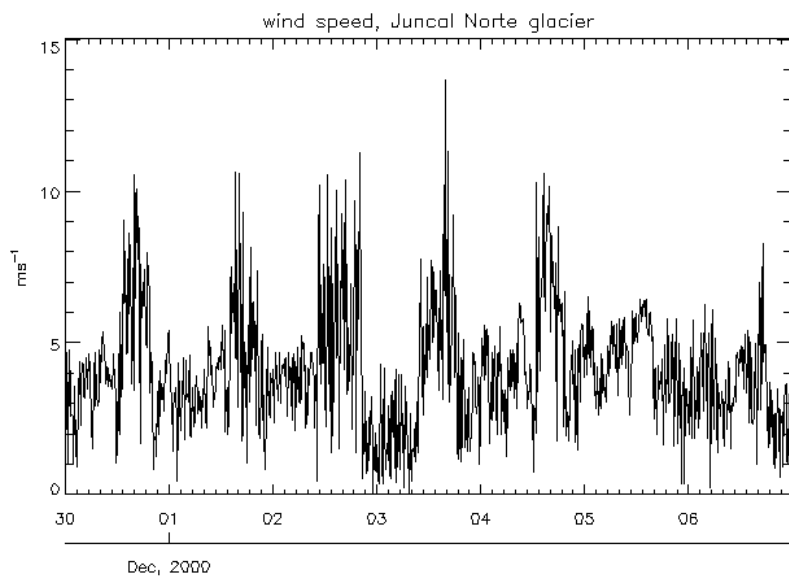


Figure 6.8. Wind speed measured on Juncal Norte glacier at 3335 m.

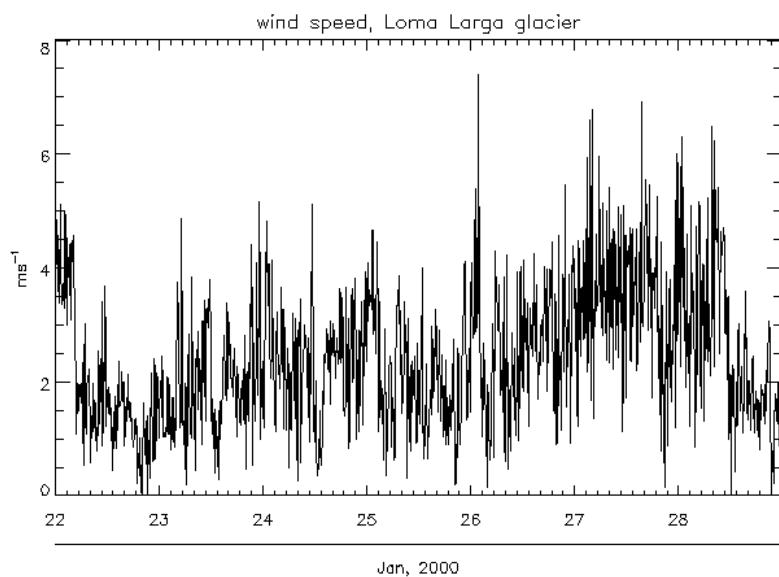


Figure 6.9. Wind speed measured on Loma Larga glacier at 4667 m.

6.2. Input data

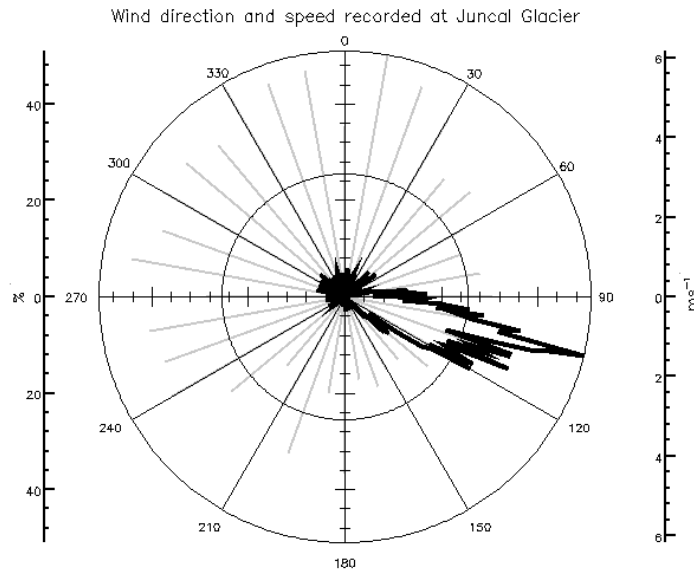


Figure 6.10. Wind rose of relative frequency for all the measuring period (day 335 to 346) on Juncal Norte glacier at 3335 m. Grey lines indicate wind mean speed for every radial sector. The maximum frequency follows the orientation of the lower section of glacier, as can be seen in Figure 2.2

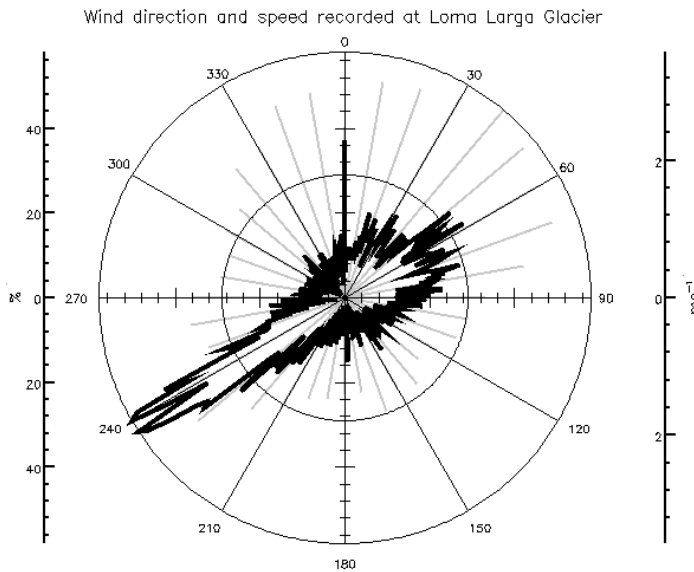


Figure 6.11. Wind rose of relative frequency for all the measuring period (day 22 to 53) on Loma Larga glacier at 4667 m. Grey lines indicate wind mean speed for every radial sector. The main orientation of the glacier is East–West and the predominant winds in this case seems to be from the valley, the northeast component of the glacier winds may be influenced by the more extent snow cover of the south-facing slopes, to the north of the AWS.

6.2. Input data

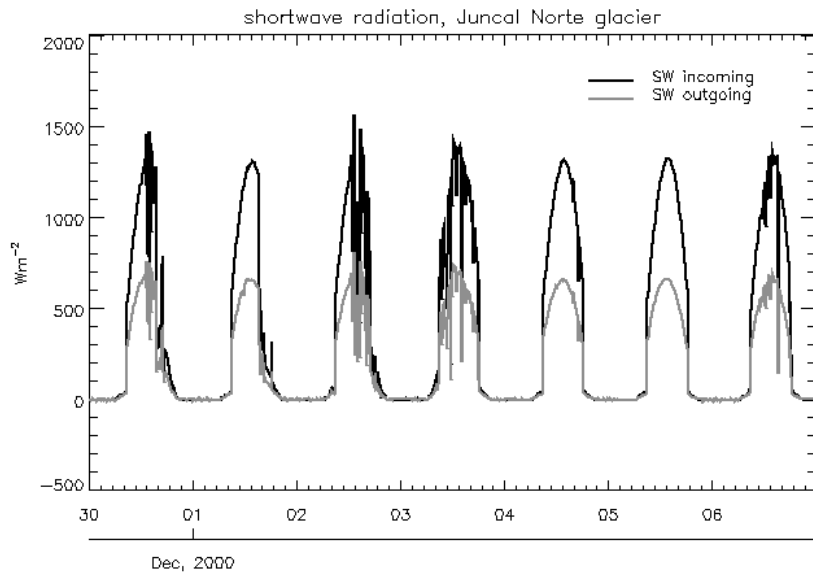


Figure 6.12. Shortwave incoming and outgoing solar radiation measured on Juncal Norte glacier at 3335 m.

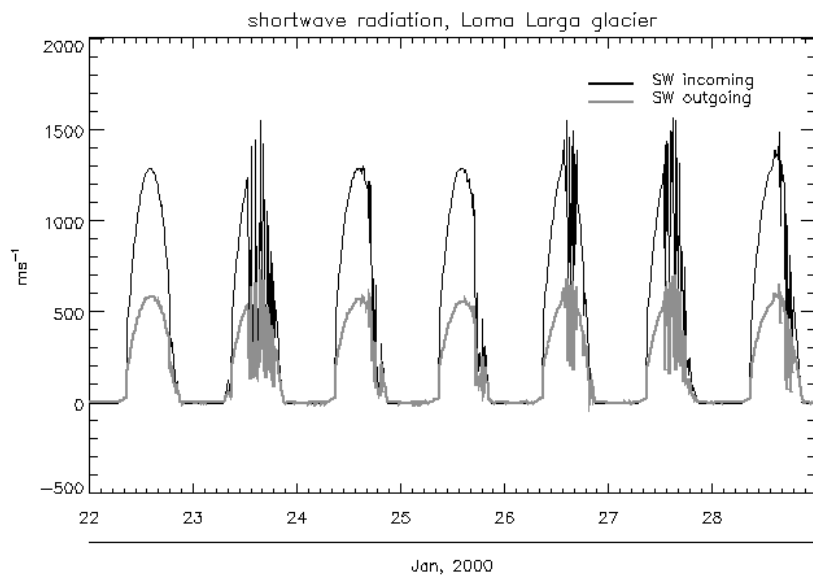


Figure 6.13. Shortwave incoming and outgoing solar radiation measured on Loma Larga glacier at 4667 m.

6.2.1 Elevation data

One input to the model is elevation data, which in turn control the interpolation of temperature data if these are derived from the lapse rate. Elevation data are obtained from a digital elevation model purchased from the Instituto Geográfico Militar Chileno, the Chilean military cartographic office. The DEM was generated from a digitised contour map of the region based on a photogrammetric flight in 1954. From the original contour map at scale 1:50,000 m a digital elevation model was generated at 20 m resolution. This resolution was chosen as a compromise between the scale of the original map and a suitable cell size to represent rapid changes in relief. The interpolation algorithm used is the ArcInfo routine *topogrid*, which gives the best results among commercially available software in an intercomparison study by Wise (1998).

Lliboutry (1998, p. 1119) has noted that “glaciologists and geographers should not trust any elevation that is indicated on maps of the Andes Mountains”. This notwithstanding, and despite the inaccuracies in elevation data, the DEM will be useful in assessing the general influence of topography on the energy balance. Despite the elevation inaccuracies of the DEMs, relative heights are not expected to be erroneous and thus the modelling exercise will be useful to study the spatial variation of energy balance. Figure 6.14 shows a shaded relief representation of the DEM with overlying contours at 50 m interval.

6.3 Distributed energy balance model

6.3.1 Distributed modelling of short-wave radiation

The short-wave radiation was modelled at one metre interval for the whole range of altitudes found on the basin and for the given meteorological conditions. During all the observations it was noted that any discernible dust layers due to atmospheric inversion were below the altitude of the glacier, therefore the visibility profile was assumed invariant with altitude. Figure 6.15 shows the modelled variation in incoming direct and diffuse radiation from 3000 to 7000 m on the 37th day of the year for a zenith angle of 60°. These modelled values revealed the atmospheric transmittances to be a strongly linear function of altitude, with the slope of the line varying slightly at different zenith angles (The model was run for different angles, only one is plotted in Figure 6.15). The correlation coefficients of the linear fit are better than 0.999 for direct solar radiation and better than 0.998 for the diffuse component. These values degrade only slightly for zenith angles bigger than 85°. The zenith angle is calculated at every time step as explained in section 4.4. The variation of the solar zenith angle for the same day at the given latitude and longitude is illustrated in Figure 3.10.

The linear variation of solar radiation as a function of altitude permits the simplification of the distributed model. The linear fit is calculated at every time step and one metre interval for the range of

elevations in the DEM, then the normal to beam and diffuse short-wave radiation in the proximity of every cell in the DEM is calculated as a function of its altitude. Even if we calculate the radiation at one metre interval, this requires about 4000 calculations instead of over half a million, if we compute it for every grid cell on a typical DEM of the area. The radiation values are further modified for the angle of incidence of the sun on the slope, shading of surrounding topography and reflected radiation from surrounding terrain as explained in Chapter 4. The diffuse radiation was further modified according to

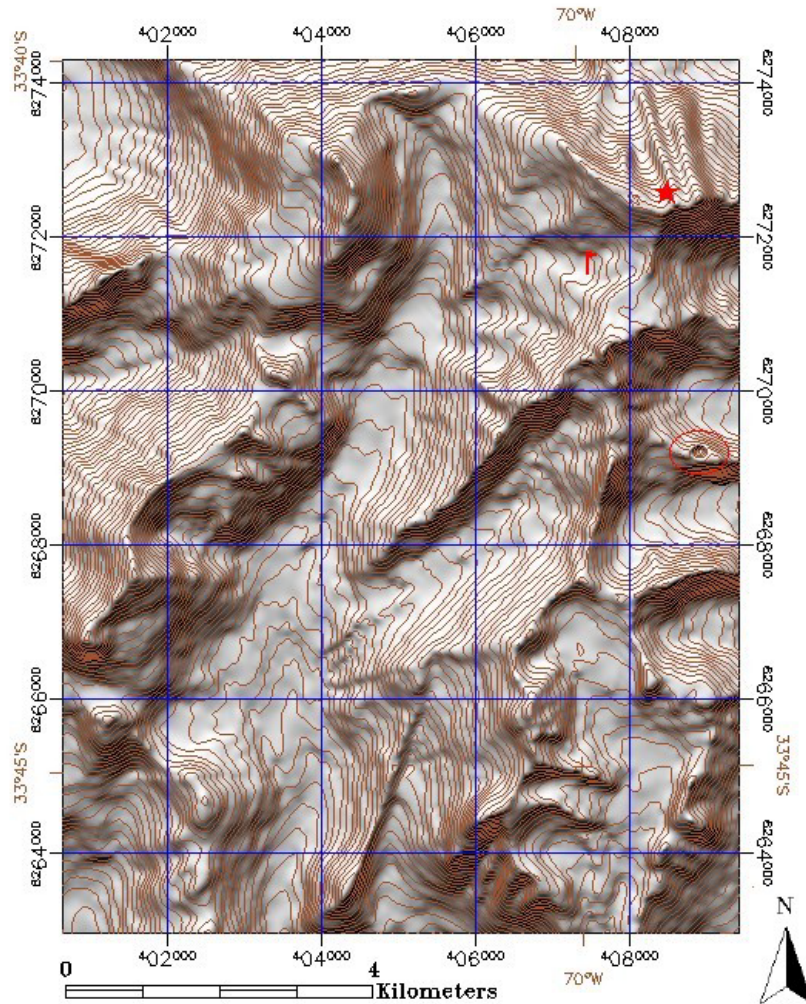


Figure 6.14. Relief shading and contour map of the Loma Larga area. The AWS is indicated by the red flag and the red star shows Cerro Loma Larga, at 5404 m. Projection is UTM, grids are 2 km apart, as indicated by the labels. A close inspection of the DEM reveals artifacts following the contour levels, generated by the interpolating algorithm. Note as well the spurious data on grid 408000,6268000 (circled), due to a missing contour value in the original map, which also shows large blank areas, probably due to poor definition of steep regions in the original aerial photograph. For these reasons detailed conclusions derived from the analysis of digital elevation models in the area should be treated with care.

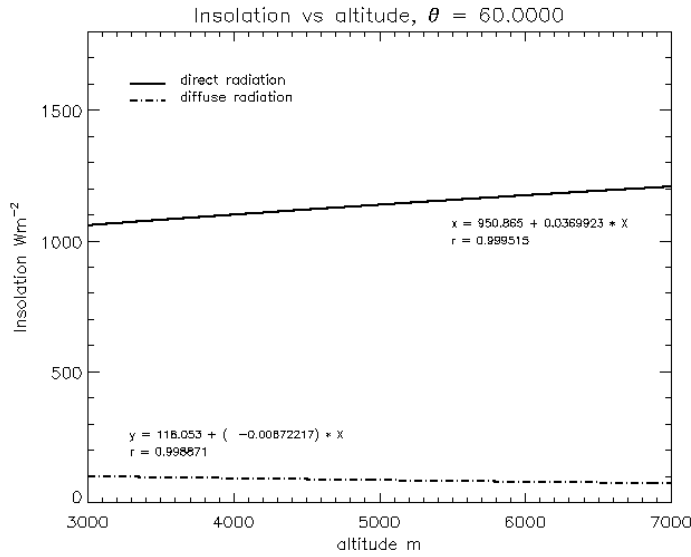


Figure 6.15. Variation of short-wave atmospheric direct and diffuse radiation with altitude, independent of topography. The line shows the modelled values at 1 m interval, while the equation shows the best linear fit and correlation coefficient.

the local horizon of every grid cell and land cover of those cells (snow or bare ground). To compute the ratio of snow cover to bare ground photographs of the surrounding slopes were used if available, and the visible pixels classified into snow or ground according to threshold reflectance values. If no photographs are available a local approximation can be inferred from local knowledge of the site. This approximation is justified if we consider that the mean values of reflected radiation from surrounding slopes are never higher than 10% of global radiation, thus an error in the snow/ground ratio estimation would only produce an error of one order of magnitude smaller in the global radiation estimation.

6.3.2 Distributed modelling of long-wave radiation

The step from point modelling to distributed grid modelling for long-wave radiation is straightforward. The formulation is exactly as in section 3.3, assuming no clouds, and it can be applied to the whole array at once. Incoming long-wave radiation depends on sky visibility and air temperature. The former is computed from the DEM (Section 4.6) and the latter is computed according to the local lapse rate or to the available knowledge of atmospheric profiles. Outgoing long-wave radiation depends on the snow temperature at every grid cell. The snow temperature was recalculated at every time step after the computation of the energy fluxes as explained in section 3.6.

6.3.3 Distributed modelling of turbulent fluxes

As mentioned in Chapter 3, the best approximation to the calculation of energy fluxes involves using the Monin-Obukhov length, which is computed in an iterative manner. Applying these iterations to

every cell of a DEM proves to be an extremely lengthy process. To speed up the process, the fluxes were calculated using the bulk Richardson number instead of the Monin-Obukhov length. The approach is similar to that used by Greuell and Konzelmann (1994) for the numerical modelling of the energy balance of the Greenland Ice Sheet, with the suggested correction for stratification. The advantage is that it has no need of iterative calculations, and the whole array of cells can be processed simultaneously. This approach was found to underestimate both sensible and latent fluxes in comparison with the Monin-Obukhov approach. Differences were smaller for the latent heat fluxes, resulting in more negative net turbulent fluxes, and therefore lower modelled temperatures. To correct for this, Greuell and Konzelmann's (1994) model was further calibrated with the data recorded in the Andes and the formulation slightly modified by introducing the zero-plane displacement term (Brutsaert 1982). An additional modification was taking into consideration the density of the air and substituting the original terms of vapour pressure, temperature and specific heat of dry air for the specific humidity in the computation of latent heat fluxes. Thus, equations 8 and 9 in Greuell and Konzelmann (1994) for sensible and latent turbulent heat fluxes become:

$$H = \rho_a c_{pa} a_h f_s \frac{k^2 \bar{u} (\theta_a - \theta_s)}{\ln \frac{z_u - d_0}{z_0} \ln \frac{z_T - d_0}{z_{0h}}} \quad (6.2)$$

$$LE = L_s \rho a_v f_s \frac{k^2 \bar{u} (q_a - q_s)}{\ln \frac{z_u - d_0}{z_0} \ln \frac{z_q - d_0}{z_{0q}}} \quad (6.3)$$

where H is sensible heat flux, LE is latent heat flux, ρ_a is air density, a_h is the ratio of eddy diffusivity to eddy viscosity for heat and a_v for water vapour, k is the von Karman's constant taken as 0.40, \bar{u} is average wind speed at height z_u , θ is potential temperature, q is specific humidity with subscripts a and s for screen level and snow surface respectively, L_s is the latent heat of sublimation, d_0 is the zero-displacement plane, z_0 are roughness lengths for momentum, heat (z_{0h}) or water vapour (z_{0q}), and $z_T z_q$ are the measurement heights of temperature and relative humidity respectively. Following Brutsaert (1982) $d_0 = (2/3.0)7.35z_0$, and following Smeets et al. (1999) $d_0 = -d_0$ if measurement heights are taken from the top of the surface roughness elements. The roughness length for momentum was computed from the ratio of the roughness element height to the frontal area index (Lettau 1969, Smeets et al. 1999), and from this, the roughness lengths for heat and water vapour are calculated after Andreas (1987), as explained in Section 3.4. The additional term f_s is the correction for the influence of stratification (Greuell and Oerlemans 1986, Greuell and Konzelmann 1994):

$$\text{if } R_i \geq 0 \quad f_s = \left(1 + 15R_i \sqrt{1 + R_i}\right)^{-1} \quad (6.4)$$

$$\text{if } R_i < 0 \quad f_s = 1 - 15R_i \left(1 + 75C_{H0} \sqrt{\frac{z_T - d_0}{z_{0h}}}\right)^{-1} \quad (6.5)$$

6.3. Distributed energy balance model

The bulk Richardson number was computed as

$$R_i = \frac{g}{T_m} \frac{(\theta_a - \theta_s) z_u^2}{\bar{u}^2 z_T} \quad (6.6)$$

and the term C_{H0} is also modified for the zero-plane displacement

$$C_{H0} = \left(\frac{k}{\ln \frac{z_T - d_0}{z_{0h}}} \right)^2 \quad (6.7)$$

At this stage the mode is simplistic in assuming that roughness length is uniform over the whole glacier. However, there are not enough measurements, either during this field campaign or from any other study to estimate its spatial variations on the glaciers of the Central Andes.

Figure 6.16 shows the effect of calibrating this model by comparing modelled and measured snow surface temperatures on the penitentes. As in Figure 3.7, initial temperature was set at an extremely low value (200 K) to test the stability of the model and the speed at which it converged to measured values. The model is run over the whole DEM, but only the values corresponding to the cell of reference are plotted and compared to the measured temperature using thermistors.

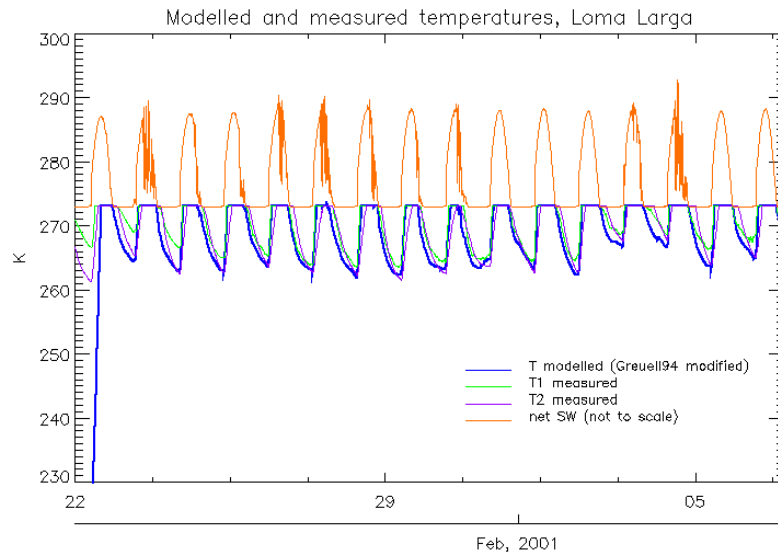


Figure 6.16. Comparison between modelled and measured temperatures on the surface of Loma Larga glacier, 4667 m. using Greuell and Konzelmann's (1994) modified formulation. Compared with Figure 3.7, here minimum values are slightly lower, but realistic, and the convergence of the model to measured values is slower than using the Monin-Obukhov length. Net short wave radiation (not to scale) is plotted to show day and night periods

6.4 Sensitivity analysis

Given the uncertainties in the measurements, it is advisable to assess the sensitivity of the model to changes in the input variables, to determine its stability and whether the behaviour of the model corresponds well with observations.

A simplified analysis was made to evaluate the response of the model to changes in one variable keeping all the rest constant. If the output of the model shows low sensitivity to changes in input parameters, we can confidently say that measurement errors in that parameter are not going to produce large errors in the modelling results. If the situation is the opposite, a small variation in the input produces large variations in the results, then the model outputs need to be treated with care whenever there are uncertainties in the measurement or estimation of the given parameter. Some of the input variables are related, while others are independent, and in some cases keeping a parameter constant is not the most realistic situation when other parameters change. For example air warming or cooling adiabatically is likely to conserve the specific humidity, which implies a change in relative humidity. The former parameter is related to the ratio of masses, which is conserved, while the second one is related to pressure and saturation pressure which changes with temperature. Thus, care should be taken using a simple analysis like this.

6.4.1 short-wave radiation model sensitivity

Figure 6.17a shows the variation of incoming short-wave radiation, direct and diffuse, with altitude. It seems to be strongly linear for the interval considered and directly proportional to altitude, as it would be expected when the solar beam traverses a thinner medium. The maximum variation in this case is about 5% for direct radiation. Figure 6.17b shows the change related to visibility, which is very marked for low visibility but more attenuated for clearer conditions. In fact, for visibilities better than 50 km, as it was the case in the Andes, variation is never higher than 5%.

Figure 6.18a is the variation due to ozone for a rather extreme range. Real values in the area of study are likely to be between 200 and 350 dobson units (between 0.250 cm and 0.350 cm), according to data recorded by the Earth Probe–Total Ozone Mapping Spectrometer–Earth Probe (URL for source data in references). The maximum variation is a 2% decrease in both direct and diffuse radiation with increasing ozone. For the restricted range of ozone values the variation is less than 1%. Figure 6.18b shows the change due to variations in relative humidity, which can be quite large, up to 10%, indicating the importance of water vapour in the absorptance of solar radiation. Maximum change is at low relative humidities, as in the study area, therefore, this is an important parameter to measure correctly.

Figure 6.19a shows the proportional decrease of solar radiation with temperature. This case needs to be considered carefully. It is hard to imagine the physical basis by which a warmer atmosphere of equal

6.4. Sensitivity analysis

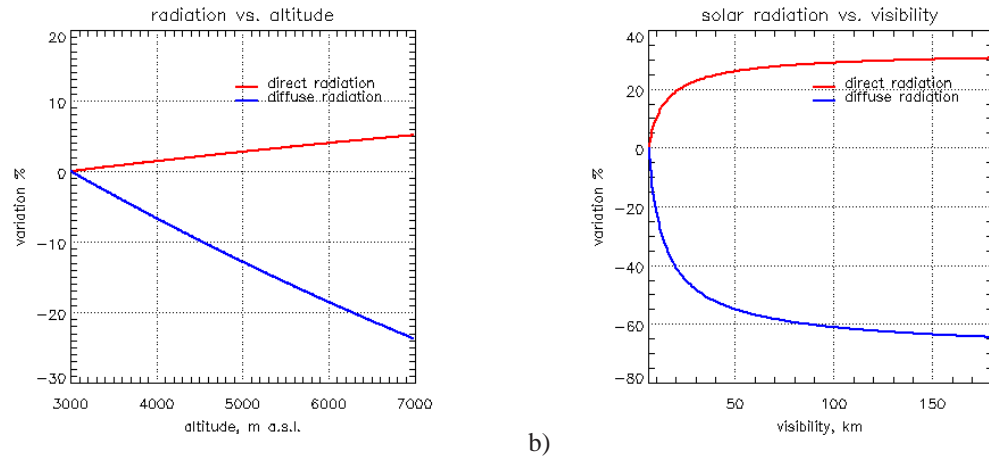


Figure 6.17. Modelled variation of incoming solar radiation, direct and diffuse components, for increasing altitude (a) and for increasing visibility(b).

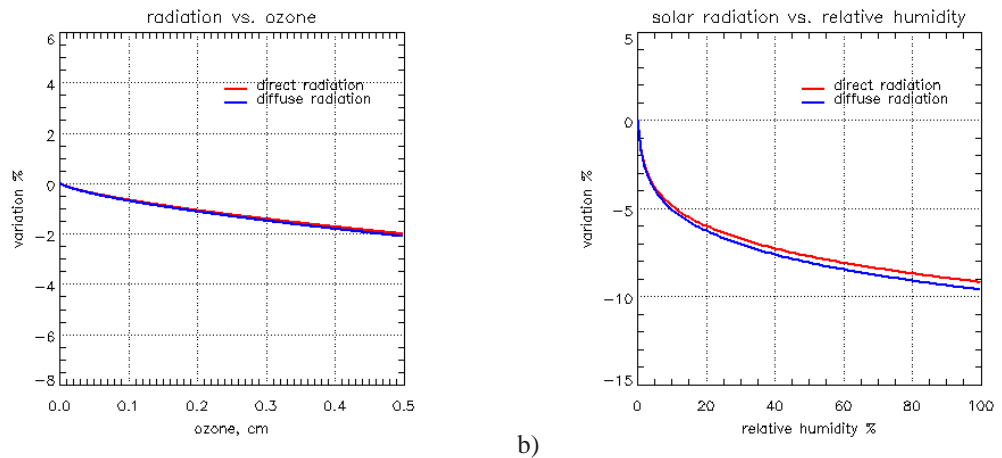


Figure 6.18. Modelled variation of the direct and diffuse components of incoming solar radiation for changing values of O_3 and relative humidity

mass and constituents should be less transparent than a colder one. If we look in detail at the reason for this decrease in radiation transmissivity, we can see in Figure 6.19b that the only cause is a similar decrease in the transmittance due to water vapour. This is an artifact of the analytical tool, as it has been pointed out before. We are using relative humidity as a proxy of water vapour content, keeping its value constant with increasing temperature results in an increase of specific humidity (mass of water vapour per mass of dry air), which is unrealistic. Thus, temperature does not affect transmittance unless it is related to changes in actual mass of water vapour content of the atmosphere.

6.4. Sensitivity analysis

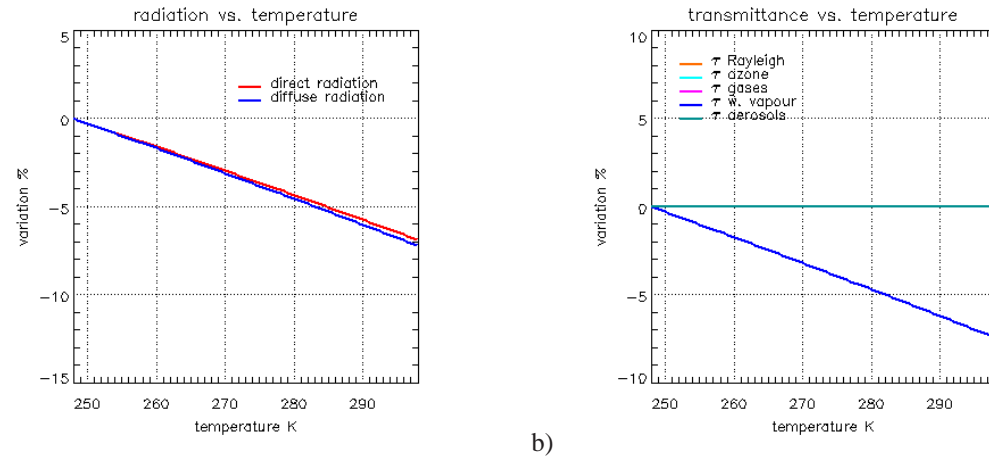


Figure 6.19. Modelled variation of the direct and diffuse components of incoming solar radiation for increasing temperature (a) and the corresponding change in individual transmittances. In (b) all transmittances overlap except for water vapour.

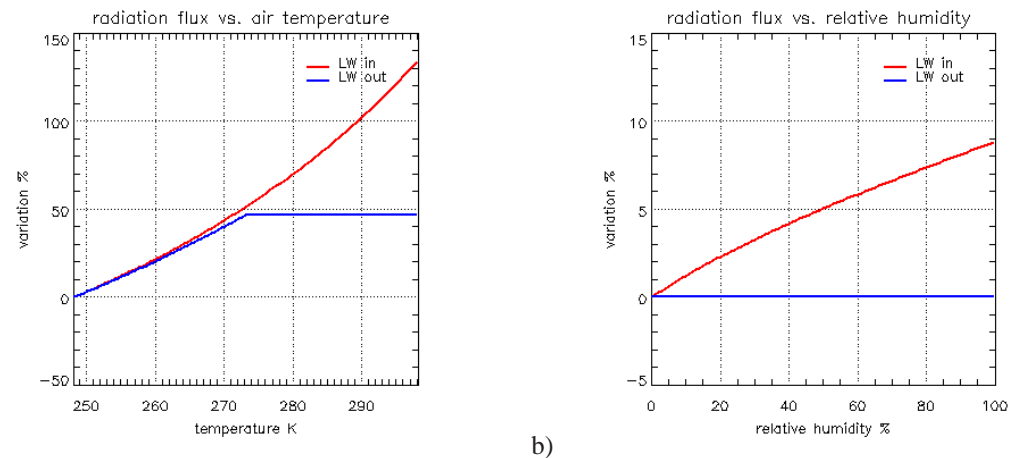


Figure 6.20. Modelled variation of long-wave radiation as a function of air and snow temperature (a) and as a function of relative humidity (b).

6.4.2 Long-wave radiation model sensitivity

Figure 6.20a shows the change in both upward and downward long-wave radiative flux due to temperature. As the thermal radiative emission is proportional to the temperature of the emitter to the fourth power, this is obviously the most important parameter. The analysis is somehow simplified in that snow temperature follows air temperature until it reaches 0°C. Figure 6.20b shows the change with relative humidity. It does not affect outgoing long-wave radiation but can increase the downward emission from

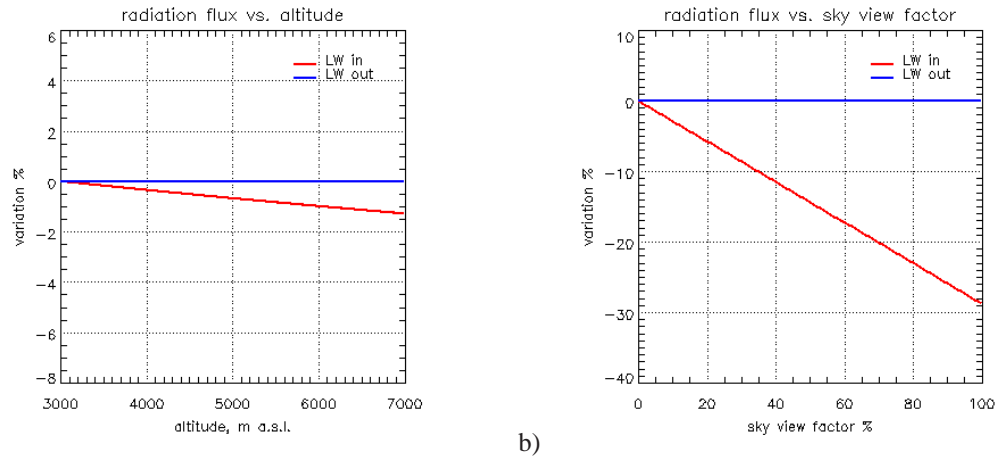


Figure 6.21. Modelled variation of long-wave radiation as a function of altitude (a) and sky view factor (b).

the atmosphere up to almost 10% for saturated air.

The effect of altitude is shown in Figure 6.21a. As the volume of overlying emitting atmosphere decreases with elevation, so does the thermal radiation, up to a variation of less than 2%. An additional parameter considered here, and related to topography, is the sky view factor. Incoming long-wave at high altitude and clear skies is minimum for surfaces surrounded by flat unobstructed horizons, as there is no interception of radiation emitted by the surrounding terrain. As the sky view factor decreases the incoming long-wave radiation increases, up to almost 30%. Sky view factor values in the areas of study range from 1.0 on the ridges to a minimum of 0.5 in very steep and deep ravines, corresponding to an increase in incoming long-wave radiation of 15% from the highest to the lowest sky view factor.

6.4.3 Turbulent heat fluxes model sensitivity

Finally, the sensitivity of turbulent fluxes to two variables is illustrated in the next figures. The effect of wind speed, the most important parameter, is shown in Figure 6.22a. With the estimated surface roughness at the upper AWS at Loma Larga glacier ($z_0 = 0.2$ m), changes in wind speed from 1 ms^{-1} to 11 ms^{-1} can produce an 6-fold increase in turbulent fluxes, both sensible and latent. The effect of surface roughness is also important, but at a smaller scale, as already noted by Denby and Greuell (2000). In this case, a variation bigger than two orders of magnitude, from 0.001 m to 0.2 m, will bring about a 150% increase in turbulent fluxes.

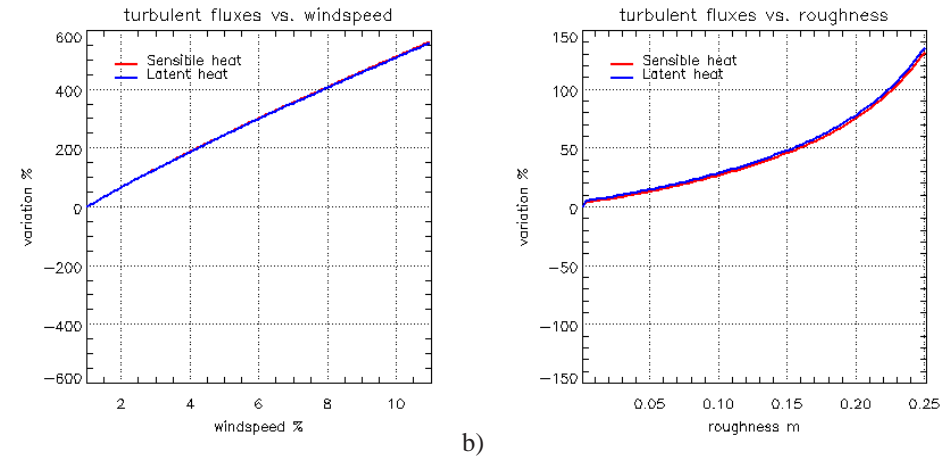


Figure 6.22. Modelled variation of the turbulent heat fluxes for changes in the the wind speed (a) and in the roughness parameter(b).

6.5 Energy balance at the microtopographical scale

The previous sections illustrate the distributed computation of the energy balance at a basin scale. This modelling exercise is a useful tool at the beginning of the ablation season, when the snow surface is smooth. As the season advances, penitentes become widespread on the Central Andes glaciers. At this point the results from such models need to be treated with care because this change in the surface morphology alters the surface roughness, changes the local slope angle and the temperature distribution on the snow surface, which consequently produces a change in the whole energy balance of the snow cover. As Lliboutry (1998) has noted, the available mathematical models in hydrology are of no application to this case.

To assess the effect of penitentes on all the components of energy balance, short-wave interception and reflection, long-wave emission and reception and the changing surface roughness, a high resolution digital elevation model of the surface with 1 cm grid cell spacing was generated and the distributed energy balance model applied to it.

When wind blows over very rough elements a gradient in cooling rates and evaporation would be expected, with stronger values on the windward and the upper section of the roughness elements. This fact was confirmed by direct measurements of the temperature of the penitentes surface with a hand-held infrared thermometer, which revealed temperature gradients of up to 1 Km^{-1} , warmer at the base and cooler at the peaks. Some modelling attempts have been performed to assess the partition of wind generated stress over rough surfaces (Raupach 1992). The author is unaware of any modelling or experiment assessing the partition of turbulent heat interchange over rough snow or ice surface elements. Some interpolation from the modelled stress partition could be made to this study, but it was considered

safer to do it when reliable measurements can give an indication of how adequate such extrapolation is. Therefore, the turbulent heat interchange was modelled as a function of surface roughness, without any attempt to estimate local differences.

6.5.1 Penitentes digital elevation model

A model of the penitente-covered snow surface was generated according to measured penitente distribution and size, with an average height of 1.35 m, wavelength of 0.80 m and radius of curvature 3 m. Penitentes are represented as blades which corresponds better to the initial stage in their formation. Later the peaks become sharper although the blade structure is partly maintained (Figure 6.23). The scale is similar in small penitentes and in fully developed ones, so the model is applicable to both cases. The base of the troughs was made flat, as there is frequent melting and even small water ponds in these areas. A smoothing filter was passed over the whole surface to avoid unrealistically sharp angles, but resulted in excessive flattening of the peaks. Field measurements show that penitentes are slightly concave and tilted 11° to the north, the midday sun position in the southern hemisphere summer solstice (note the arrows in Figure 6.24). As real penitentes have overhanging surfaces, these can not be represented by a mathematical function, which requires a single z-value for every (x,y) pair, and it is therefore impossible to represent them as a digital elevation model. By rotating the reference system an equivalent angle, the z-axis will be in line with the vertical axis of the penitentes and we can build the DEM with no overhanging surfaces, and then rotate the world according to this new reference system. For the calculation of solar irradiation on the penitentes surface (Figure 6.24) we only need to rotate the sun vector through the original reference system an opposite angle by applying the appropriate rotational matrices (for a review of rotational matrices see Goldstein 1980, Weisstein 1999). The rotated sun vector \hat{s}_r in the new reference system is:

$$\hat{s}_r = \mathbf{r}_z(-\phi)\mathbf{r}_x(-11^\circ)\mathbf{r}_z(\phi)\hat{s} \quad (6.8)$$

where ϕ is the solar azimuth, \mathbf{r} are rotational matrices and the subscripts denote the axis of rotation.

The penitentes' walls act as a 'solar trap' due to multiple reflection of incident light. Thus reflected radiation was computed for several multiple reflections, in this case for 5 reflections that, given the local snow albedo, accounts for more than 97% of the energy from this source. The reflected light after a first reflection affects the opposite slope, not the local one; a second reflection on the opposite slope is intercepted by the local slope; the third reflection is treated as the first, and so on. Thus, only even reflections for a given wall are computed, as odd reflections are 'reflected-out' (Peterson et al. 1985). The computation takes into account the angle of incidence of the first beam on the surface and then considers successive reflected radiation as isotropic. The effect of shading on reflected radiation is taken into account by introducing a ratio between the number of cells in the sun and the total number of cells. The modified incoming long-wave radiation is a function of the sky view factor, its value outside the penitentes layer and the long-wave emission of surrounding walls.



Figure 6.23. Details of penitentes on a snow field about 4300 m. The tops tend to sharpen into a peak shape, but the overall blade structure is conserved.

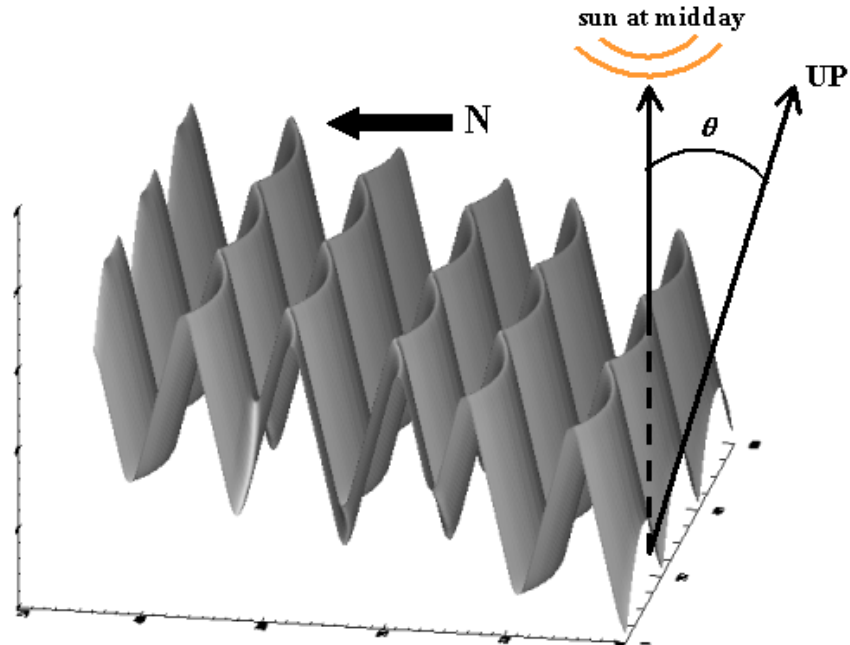


Figure 6.24. Digital elevation model at 1 cm resolution of the penitentes-covered snow surface. The world reference system is rotated southth to avoid overhanging surfaces, to model the solar radiation the solar vector is defined according to the new reference system.

6.6 Results and discussion

The result of the distributed model applied to the Loma Larga and surrounding glaciers is illustrated in the following figures as color coded map of energy fluxes. Values are daily averages after the computation of the whole period for which meteorological data are available, from day 22 to day 53 or 22 January to 22 February 2001. Discussion and analysis are based on Loma Larga data. The measurement site in Juncal corresponds better to situations found in the Alps, where snow ablates more uniformly. The contribution of every component to the net energy balance is illustrated in Figure 6.25.

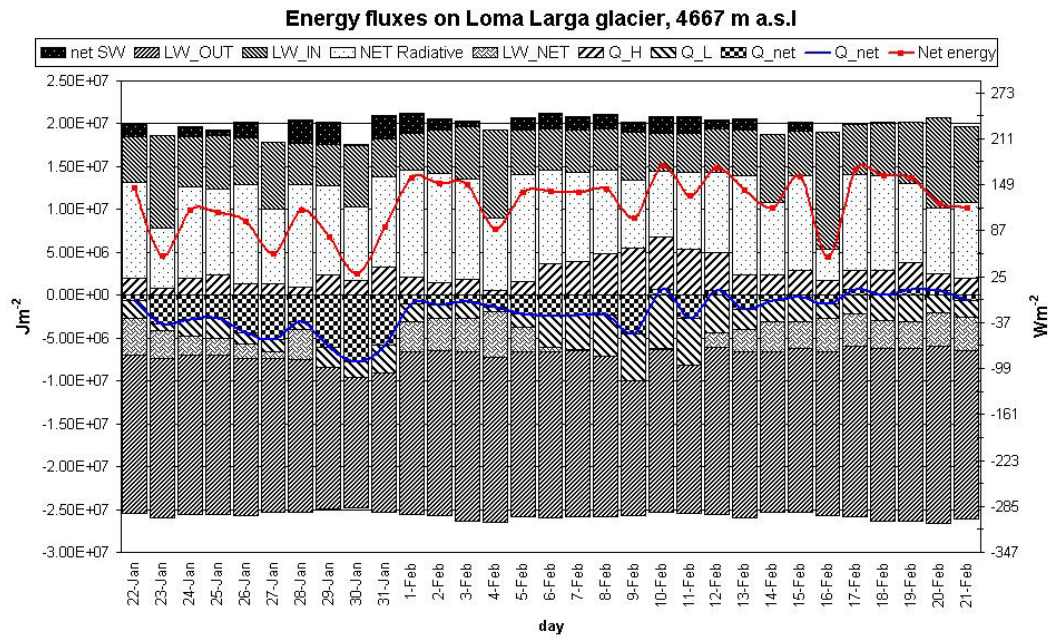


Figure 6.25. Energy contributions of every component in the energy balance for the whole recording period at Loma Larga glacier. SW is short-wave, LW long-wave, Q_S turbulent sensible heat flux, Q_L turbulent latent heat flux, Q_net is turbulent net heat flux and Net energy is for the local measured albedo.

6.6. Results and discussion

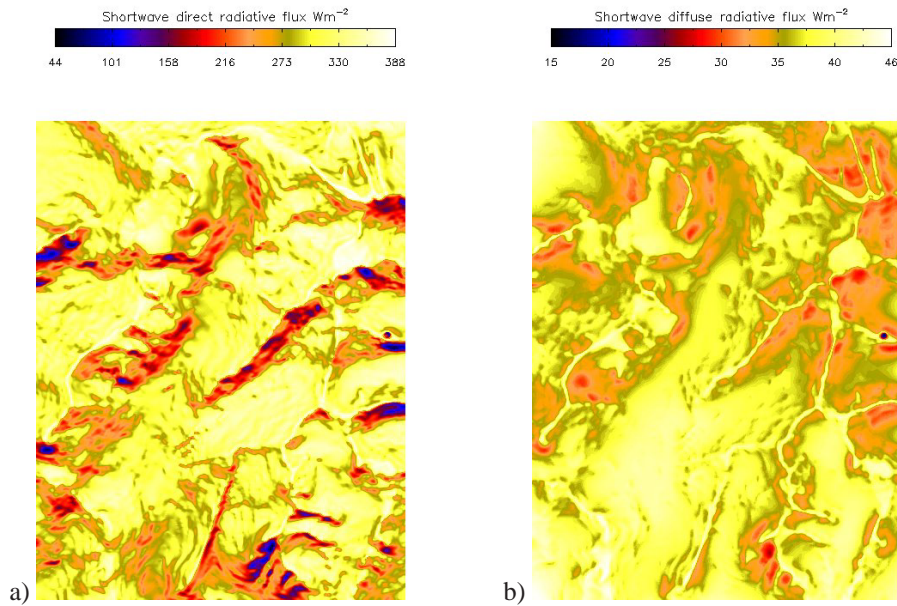


Figure 6.26. Spatial distribution of the daily cumulative short-wave direct (a) and diffuse (b) components of incoming solar radiation. Loma Larga site, averaged from day of the year (DOY) 22 to day 53.

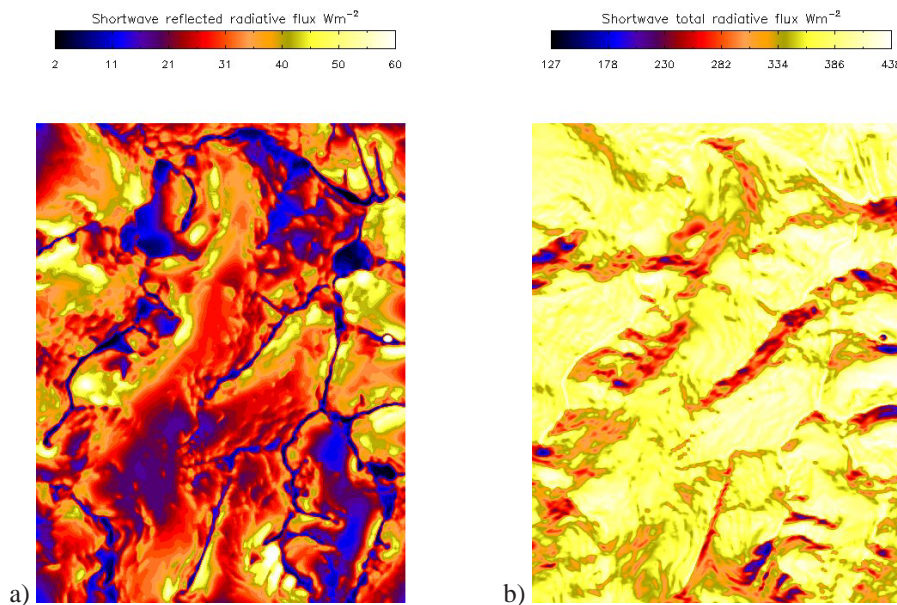


Figure 6.27. Spatial distribution of the daily cumulative incoming short-wave radiation reflected from surrounding slopes (a) and the total value (b). Loma Larga site, averaged from DOY 22 to day 53.

6.6. Results and discussion

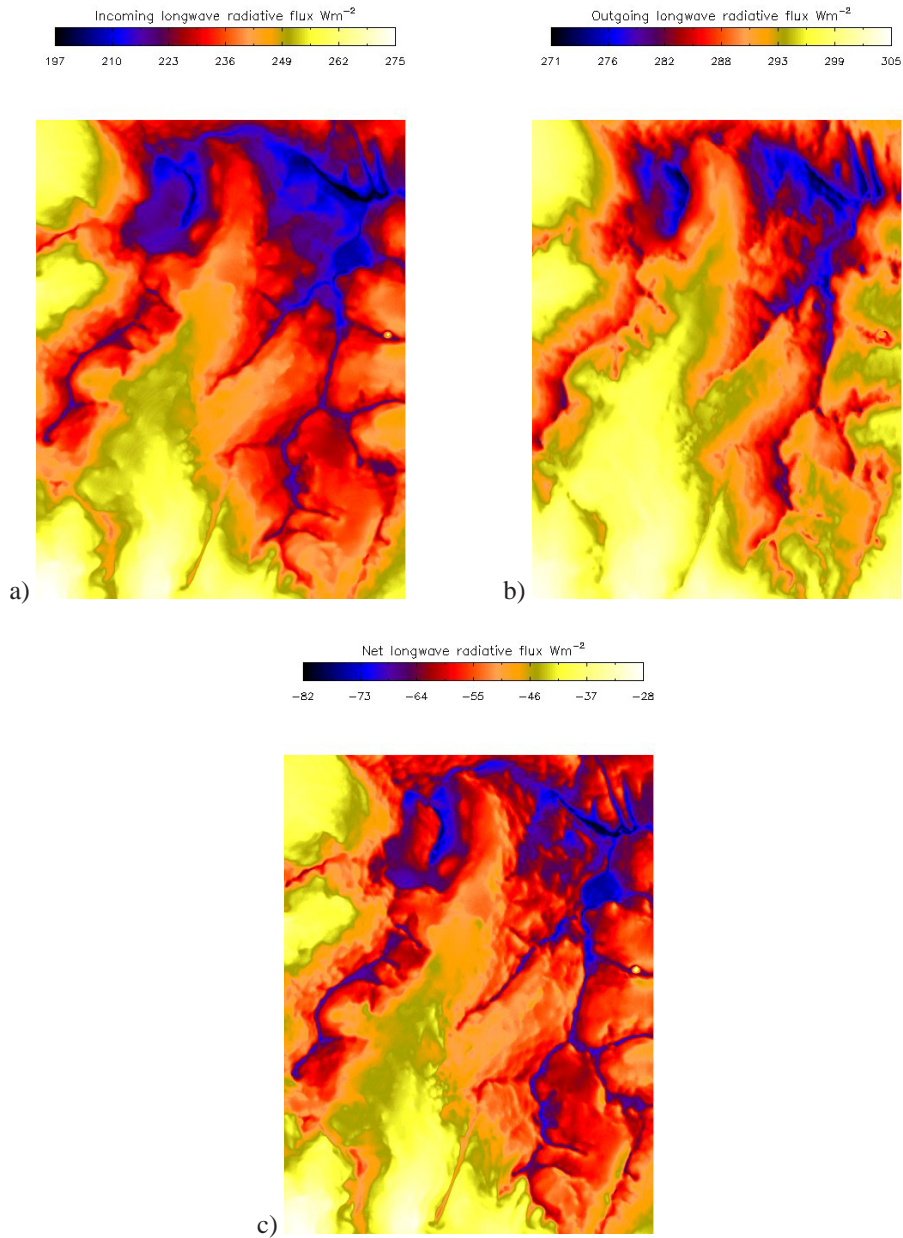


Figure 6.28. Spatial distribution of the daily cumulative long-wave radiation, (a) is incoming flux, (b) is outgoing and (c) is net flux. Loma Larga site, averaged from DOY 22 to day 53.

6.6. Results and discussion

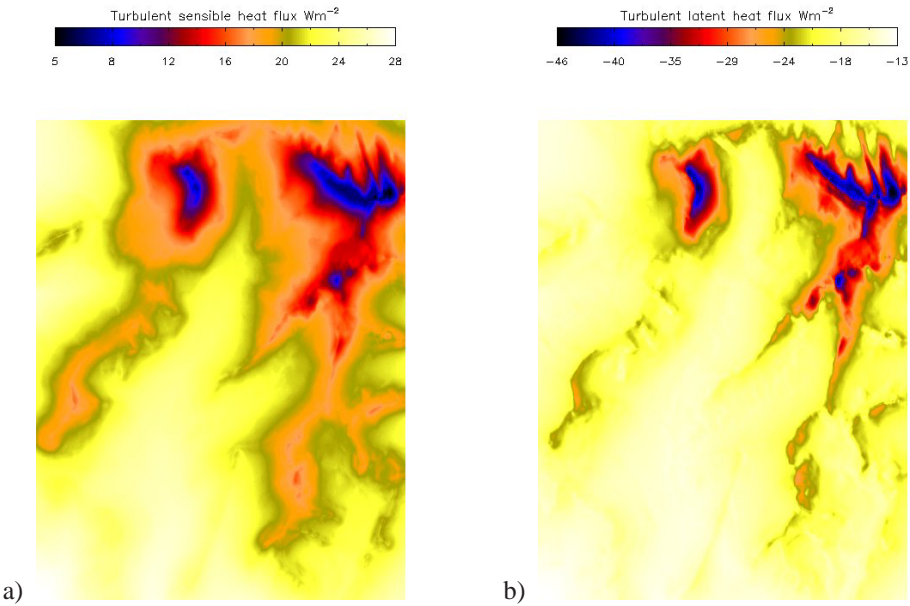


Figure 6.29. Spatial distribution of the daily cumulative turbulent sensible and latent heat flux on Loma Larga glacier. Loma Larga site, averaged from DOY 22 to day 53.

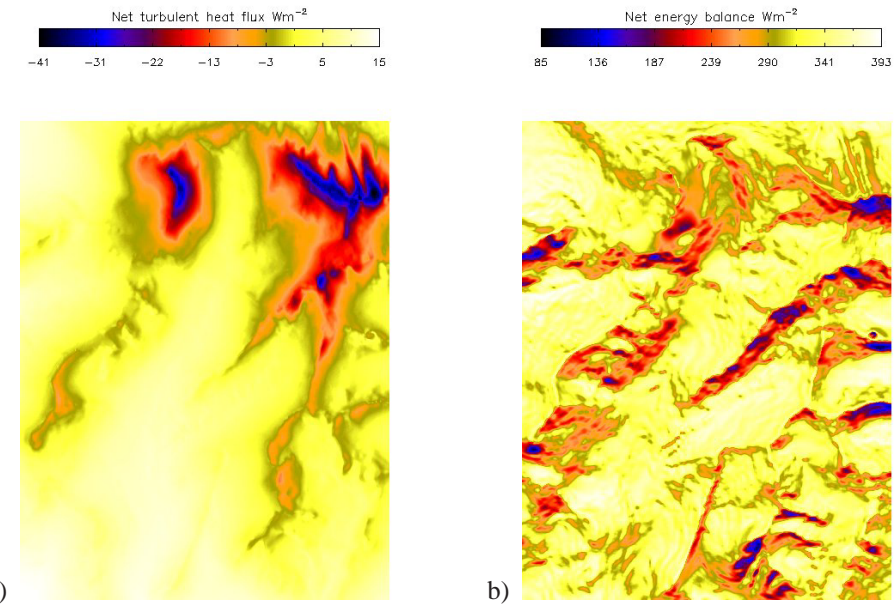


Figure 6.30. Spatial distribution of the daily cumulative net turbulent and total net heat flux on Loma Larga glacier. Loma Larga site, averaged from DOY 22 to day 53.

6.6.1 Effect of topography

A first visual inspection of the results, either for one day or for the whole recording period, shows most clearly the variation according to topography. Changes in long-wave and turbulent fluxes maps are associated with changes in elevation, while the maps of short-wave radiation reveal the finer detail topography. The importance of topography in computing the energy balance of mountain glaciers has already been stressed by Klok and Oerlemans (2002) for an Alpine case study. Their study is very specific, for one single glacier facing north, which enhances even more the effect of topography due the preferential orientation of slopes. In the cases studied here topography is of paramount importance locally, but at the scale of the whole basin, the multiple orientations of the slopes tend to cancel directional effects and there is not a clear correlation between altitude and insolation when considering mean values over the whole area. In Figure 6.26, for example, it can be seen that maxima and minima of solar radiation are at both sides of the same peak (Cerro Cortaderas, grid 408000,6270000 in Figure 6.14). The situation is better illustrated in Figure 6.31 that shows the variation of energy balance components with altitude. Short-wave direct radiation (SW dir) increases slightly with altitude, but in general has little variation; turbulent fluxes become more negative with height and sensible fluxes follow a decreasing tendency but with a very gentle slope; diffuse radiation is rather unaffected, while short-wave reflected follows an inverse pattern than short-wave direct. The general tendency of decreasing net energy flux is caused by the more accentuated decrease in downward long-wave flux, which is not compensated by the moderate increase of outgoing long-wave radiation. A similar situation but more exaggerated occurs in Juncal Norte. The differences are due to the stronger winds in Juncal Norte (average 3.95 ms^{-1} in Juncal and 2.51 ms^{-1} in Loma Larga). These stronger winds are probably due to stronger katabatic forcing in a larger and higher glacier with a deeper and a better defined valley. The importance of wind on the energy balance is stressed by the results of a simple experiment, showed in Figure 6.32. A simple increase in wind speed of 2 ms^{-1} lower the net energy balance in excess of 140 Wm^{-2} .

If we plot the values of the energy balance components against the slope and aspect of the terrain, then a more distinctive pattern arises for the short-wave radiation component, as illustrated in figures 6.33 and 6.34. Direct short-wave decreases considerably with increasing slope, a direct consequence of the cosine law applied to the interception solar radiation by the slope. Diffuse short-wave decreases slightly with increasing slope, while reflected short-wave follows an inverse pattern, due to smaller sky view factor for steeper slopes. Long-wave radiation values are unrelated to slope and the variation of turbulent fluxes is minimal, just a small decrease that may be related to colder snow surfaces on steeper slopes with lower saturation vapour pressure at the snow and therefore smaller gradient with the air vapor pressure. Steep slopes tend to be at higher elevations, which also means lower air density and reduced turbulent fluxes, but the effect is very small.

The relationship between aspect and radiation shows a distinctive minimum in net energy and direct radiation for those slopes facing south, away from the sun in the Southern Hemisphere. The effect on the other components is minimal. A very small fluctuation in the turbulent fluxes on Juncal area may be

6.6. Results and discussion

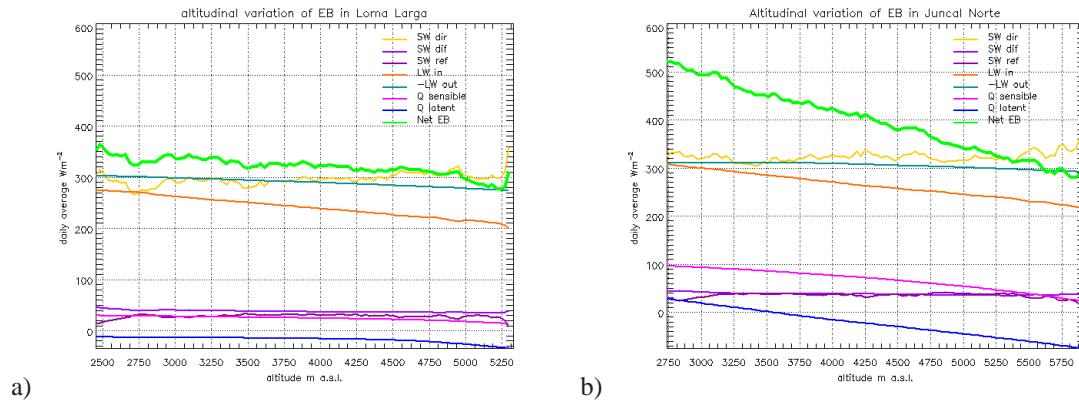


Figure 6.31. Variation with elevation of the mean daily distributed values at different altitudinal belts of the energy balance components for the whole recording periods on the Loma Larga (days 22 to 54) and the Juncal Norte areas (days 345 to 355). Outgoing long-wave are absolute values, the actual value is negative. Main differences are due to increased absolute values of turbulent fluxes in Juncal Norte due to stronger winds.

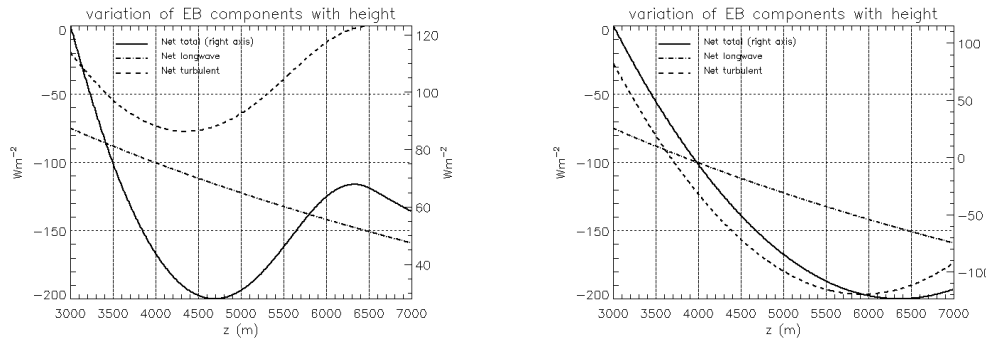


Figure 6.32. Variation of the energy balance components with height for mean recorded values at the lower AWS (3035 m) applying a standard lapse rate (-0.0065 Km^{-1}). Net values are right axis. Values do not take into account energy absorbed at different surface or subsurface layers in this case. Short-wave global radiation is modified primarily by albedo, which in this case was simplified to a constant value. The right figure shows the results for an average increase in wind speed of 2 ms^{-1} .

related to the fact that many cells facing south east correspond to the large Río Plomo Basin, the largest glacial basin in the Central Andes, which produce an average higher elevation and lower temperature for cells in this region.

6.6.2 Effect of penitentes

The energy balance model was applied to the microtopography DEM and run for the whole recording period with ten minute time steps to asses the effect of penitentes on the interception of solar radia-

6.6. Results and discussion

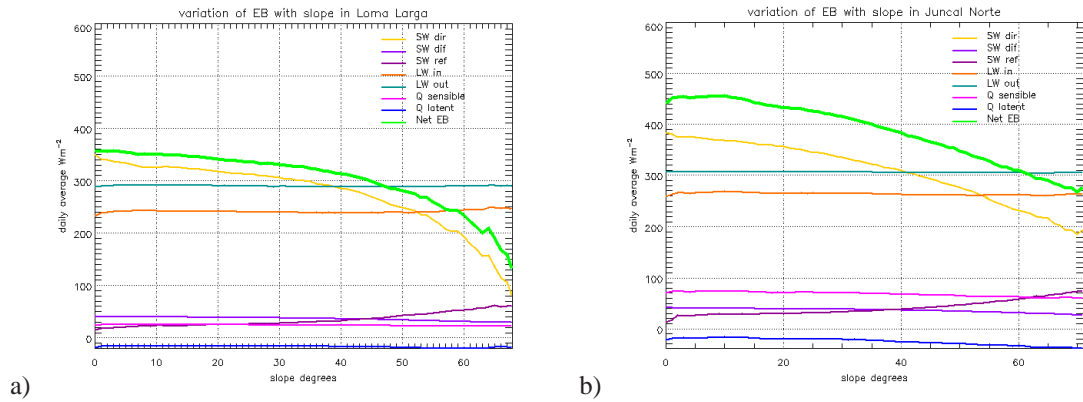


Figure 6.33. Variation with slope of the mean daily distributed values of the energy balance components on Loma Larga and Juncal glaciers.

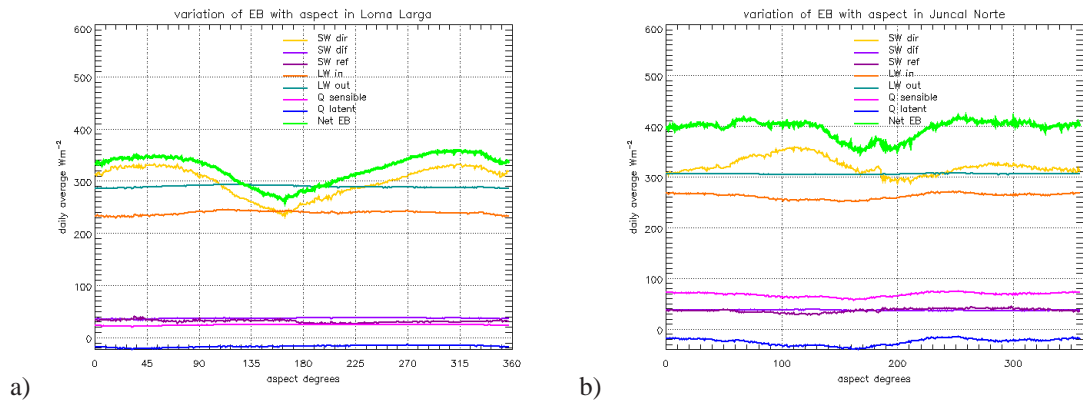


Figure 6.34. Variation with aspect of the slope of the mean daily distributed values of the energy balance components on Loma Larga and Juncal glaciers.

tion. The results for day 37 are shown in Figure 6.35. The maximum total daily value is 42.2 MJm^{-2} (488 Wm^{-2}), while the mean value is only 16.65 MJm^{-2} (193 Wm^{-2}). The histogram of values shows a bimodal distribution with two peaks at 10 MJm^{-2} (116 Wm^{-2}) and 18 MJm^{-2} (208 Wm^{-2}) corresponding to the north and south facing walls. The same day on a flat surface the modelled (and measured) radiation was 435 Wm^{-2} . The mean values for the summer solstice (21 December) were 230 Wm^{-2} and 486 Wm^{-2} for the penitentes and a flat surface respectively. An inspection of the results for diffuse and reflected radiation reveals that the latter increases downwards and the former increases upwards, with a maximum at the peaks.

The net energy balance is shown in Figure 6.38. In general terms average values of net long-wave radiation increased its mean value from -77 Wm^{-2} on a flat surface to -39 Wm^{-2} on the penitentes, due

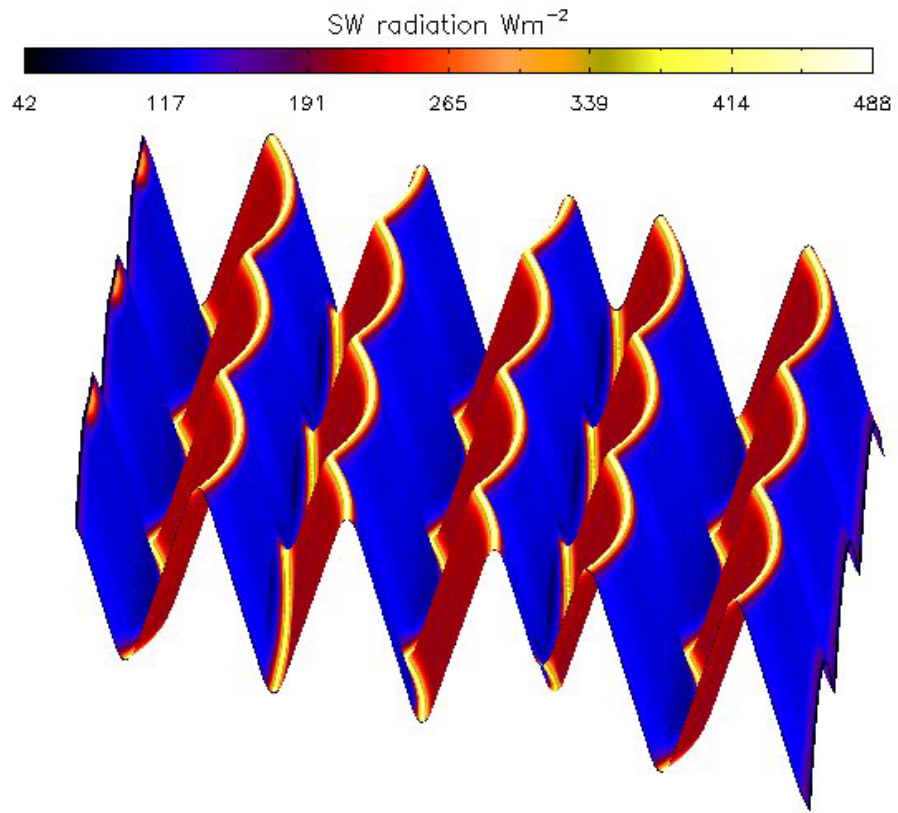


Figure 6.35. Average daily value of total insolation (direct, diffuse and reflected) modelled on penitentes for the 37th day of the year at Loma Larga glacier.

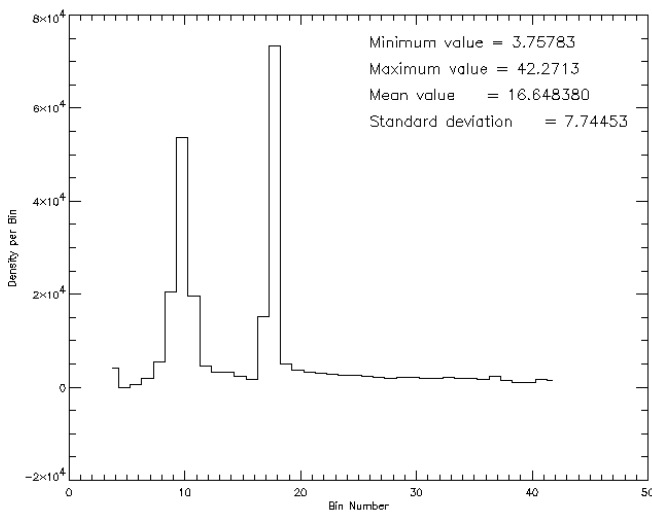


Figure 6.36. Histogram of insolation values in Figure 6.35 showing a bimodal distribution corresponding to the north facing and south facing slopes. Values are MJm^{-2} .

to emitted radiation from the surrounding snow walls. Turbulent fluxes decreased their net value from -17 to -28 Wm^{-2} on average (Table 6.2). These values are averages for all grid cells, however surface area is different according to the slope of the cell, and total area is increased on a rough surface, in this case by a factor of 2.8. The change in the overall energy balance due only to the increased absolute values of turbulent fluxes because of increased roughness, would represent a reduction of about 2.85 mm of water equivalent melt (mm w.e.) per day. This means that an additional 342 mm w.e. of snow are preserved during the four principal months of the ablation season.

Table 6.2. Energy balance partition for flat snow and penitentes (Wm^{-2})

	SWin	SWnet	LWnet	Heat flux net	Total
Flat snow	435	209	-77	-17	115
Penitentes (mean)	193	106	-39	-28	39

The partition of the energy balance components on the snow surface is also important. Thus, the penitentes' walls receive about half of the incoming solar radiation with respect to a flat surface. This compensates for the increase in long-wave radiation and keeps the penitentes' walls generally frozen and dry, while melting occurs only at the bottom of the troughs. The localized melting favours percolation of water, with almost no supraglacial drainage, which in turn reduces loss of water by further evaporation. This corresponds well with the observed situation, although small streams may form lower down and later in the ablation season, as seen on the Horcones glacier on Aconcagua in a different year. Nonetheless these streams are much smaller than supraglacial rivers observed in the Alps or in the lower section of Juncal Norte glacier, with no penitentes but wet snow. Comparing modelled melting for flat and penitentes surfaces we get a maximum of $31 \text{ kgm}^{-2}\text{day}^{-1}$ (8 cm for the measured density of 400 kgm^{-3}) and an average of $4.7 \text{ kgm}^{-2}\text{day}^{-1}$ (1 cm) for the penitentes and for a flat surface with $z_0 = 0.002\text{m}$ a value of $41.3 \text{ kgm}^{-2}\text{day}^{-1}$ or 10 cm. For the whole measuring period, mean values for penitentes are maximum 8.6 cm day^{-1} and average 1.6 cm day^{-1} , data are summarised in Table 6.3. The maximum value for the penitentes area tends to increase toward the solstice and decrease at lower maximum zenith angles, as the sun will not reach the bottom of the troughs. However, these values seem to be higher than observed. If we compare modelled temperatures on the penitentes (Figure 6.39), we can see that the south facing wall hardly reaches 0° , while the skin temperature is actually lower, the troughs reach melting point during most of the day and the north wall during a shorter period. This correspond well with reality, though most of the time the walls were frozen. This situation is better replicated when modelling the temperature for a thin surface layer. The fact that the snow thickness of the penitentes decrease upwards suggest a more effective heat interchange between colder and warmer wall, and the net effect is that most of the energy input is redirected to temperature fluctuations instead of melting. This observation is supported by Kotlyakov and Lebedeva (1974) who compared theoretical and observed melt values in penitente snow in the Pamirs, while theoretical values suggested 55 mm w.e. of melt, observed values were zero. They reported 2mm day^{-1} of evaporation in the Pamirs, in the Andes modelled results suggest up to 6mm day^{-1} maximum and an average of 2.1 mm day^{-1} for the

whole recording period. The efficiency of snow preservation under the form of penitentes is illustrated in Figure 6.40: in the vicinity of this area small ponds of water were observed, indicating temperatures above freezing, yet the pinnacles of ice survived for a long time under the strong solar radiation and generally were dry, indicating little or no melting. The spatial distribution of ablation, both at the basin scale, for non-penitente snow and for penitentes is given in Figure 6.37. The increased ablation on the west facing side of the north wall is because the snow is already warmer when it gets hit by the rays of the afternoon sun. The effect is asymmetrical, as the morning sun is intercepted by colder snow. This effect may be responsible in part for the weaker definition of the concave form in bigger penitentes compared to the initial stages of growth. The large ablation values on the peaks are unrealistic and due to the excessive flattening of the area in the ‘virtual’ penitentes used in the model.

Table 6.3. Modelled melt and evaporation on flat snow and penitente snow at Loma Larga, 4667m on day 37.

	melting (mm w.e.)	(cm)	evaporation (mm w.e.)	(cm)
Flat snow	41.3	10.3	0.51	0.13
Penitentes (max)	31.0	7.75	2.47	0.62
Penitentes (mean)	4.7	1.2	0.84	0.21

Further comparison between modelled and observed melt values were made for the Juncal Norte glacier, using the data collected by the lower AWS during a 11 day period in November-December 2000. Results here, on relatively flat granular snow and assumed $z_0 = 0.002$ m, are in good agreement with observed snow melt derived from ablation stakes and measured snow density around 625kg m^{-3} , differences for the whole period were less than 2 cm as it has already been indicated in Figure 3.12.

6.6. Results and discussion

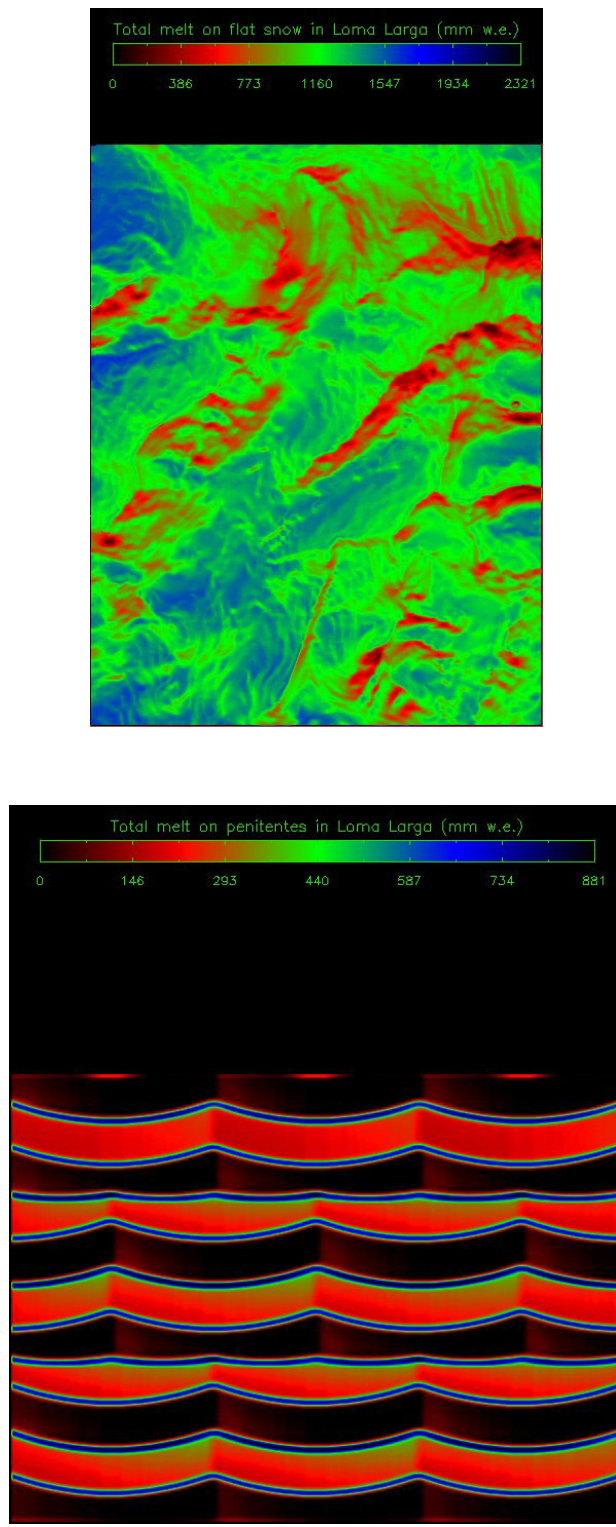


Figure 6.37. Spatial distribution of snow ablation, including evaporation, both at the basin scale and the penitentes scale. Note increased ablation on the right side of the north walls of penitentes.

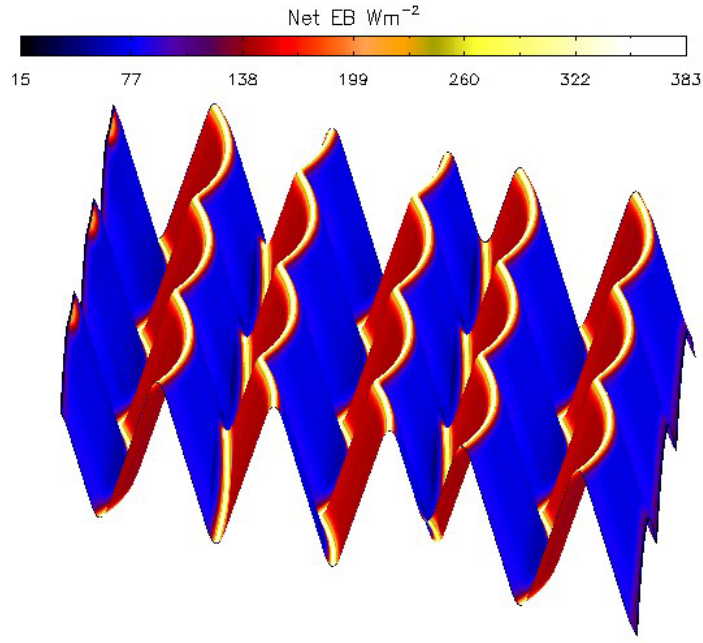


Figure 6.38. Net energy balance of penitentes for the 37th day of the year.

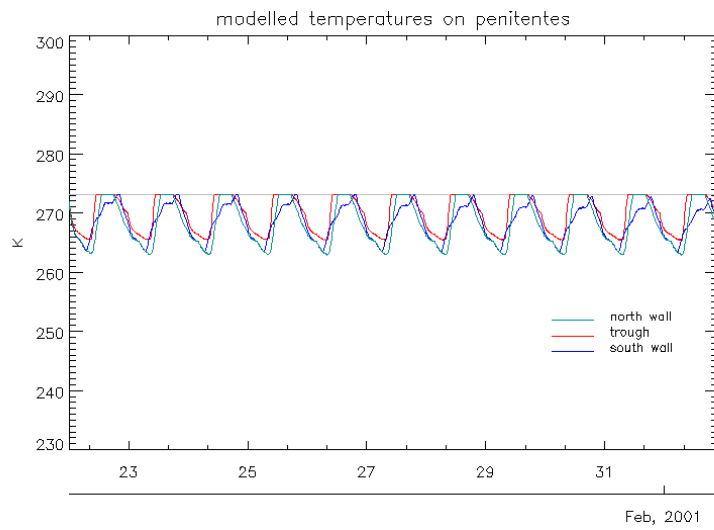


Figure 6.39. Temperature fluctuations for a two week period modelled on the surface of penitentes at Loma Larga glacier. Temperature on the south facing walls (away from the sun) barely reaches 0°C, indicating little or no melting, despite positive air temperatures and strong solar radiation.



Figure 6.40. Penitentes on a former shallow snow field at 4300 m Snow in the troughs has disappeared, but the penitentes survive for a long time despite the strong solar radiation and day temperatures above freezing level.

6.7 Response under changing climatic conditions

The implications of possible climatic change, the sensitivity of the energy balance to different parameters and its variation with altitude are studied in relation to the sensitivity analyses of previous sections and the distributed net energy balance over the glacier surface. We have seen that penitentes form under well defined climatic conditions, *i.e.*: stable weather, intense solar radiation, moderate wind, low relative humidity and negative dew point. These conditions are confirmed by previous studies (Lliboutry 1954b, Kotlyakov and Lebedeva 1974).

Variations in these conditions will hinder the particular ablation processes leading to the formation of penitentes in the following way:

Unstable weather will bring snow precipitations. Observations show that penitentes are formed in granular snow and require some continuous days of sunny weather to form. New snow will make the surface uniform, will increase the albedo and slow the metamorphism of snow grains, retarding or suppressing the formation of penitentes. Weather perturbations are associated to cloud cover, blocking the direct sunlight that is the main element in this ablation process. Increased cloud cover will also increase the downward long-wave radiative flux. We have seen that radiative cooling plays an important role in the energy balance of the snow surface, that will be very much modified under cloudy conditions. We have also seen that there is a direct relationship between the orientation of penitentes and the main source of energy, that of direct solar radiation. This source is highly directional, and hence the impression of penitentes being "carved" by the sun. An increase of downward long-wave flux, which is diffuse

and hence non-directional, will make the effect of the direct solar radiation less relevant.

Moderate wind is necessary to cool the surface of the snow and the pinnacles once penitentes are formed. Too strong winds will cool the surface in excess. Strong winds are also associated to snow transport and resurfacing of subsurface layers. The detailed study of these processes are out of the scope of the present work. However, the effect of wind suppressing the formation of penitentes has been confirmed by observation by the author on different Andean massifs. This was observed on the upper section of the Juncal Glacier, where wind is higher on unsheltered slopes and snow is less metamorphosed. However, penitentes were found not far below the summit of Nevado Juncal (6100 m) on a very sheltered location. A similar situation was observed on Cerro Aconcagua, where the snow ablated into penitentes up to an altitude of 5800 m except on the very wind-exposed eastern section (Polish Glacier). Furthermore turbulent fluxes are very dependent on surface roughness, thus even if the initial stages on the formation of penitentes take place, their development will be constrained by excessively strong winds.

Low humidity and low dew point are related, their effect is increased ablation, which is an energy demanding process that has the effect of cooling the surface. Negative dew point means that snow will sublime rather than melt (except when air becomes locally saturated, which bring about a rising of dew point temperature). The lack of liquid water has also a thermal insulating effect, as snow and air are worse heat conductors than water. This favours differential ablation, while the presence of liquid water will tend to make the local thermal and energy imbalances more diffuse.

We have an upper limit to the occurrence of penitentes and the extension of snow cover, the absolute limit being the height of the mountains. This absolute limit, however, is lowered when the sheltering effect of surrounding topography disappears, resulting in a wind regime closer to that of the free atmosphere. It could be observed and measured that while in the glacier valleys wind was moderate and constant, on the upper section winds were much stronger. These observations are punctual, during the ascents of Nevado Juncal (6100 m), Aconcagua (6954 m) and Loma Larga (5404 m), but they agree with a long record of experience by other mountaineers in the region and make sense from a basic interpretation of wind dynamics over rough topography.

From the previous exposition we can see that there is a climatic lower limit and a topographic upper limit to the particular ablation forms of the region. The upper limit is likely to be constant, except at geological time scales, and the lower limit will be influenced by changing global climatic conditions. To assess these last, the outputs of two coupled atmosphere-ocean general circulation models (AOGCMs) were studied. The first model is the HadCM2 developed at the Hadley Centre (Johns et al. 1997). HadCM2 has a spatial resolution of 2.5° latitude by 3.75° longitude, the atmospheric component of HadCM2 has 19 levels and the ocean component 20. The second model is the HadCM3 (Gordon et al. 2000) also developed at Hadley, which does not need flux adjustment as it has a higher ocean resolution. HadCM3 seems to be a stable model, with little drift in model runs over a thousand years and its run according to the latest special report on emission scenarios (SRES) of the Intergovernmental

6.7. Response under changing climatic conditions

Panel on Climate Change (IPCC). The model outputs for surface temperature changes at the end of the century are shown in figures 6.42 and 6.41. Other variables such as cloud cover or wind speed show no changes in the HadCM2 model outputs or a slight decrease (-0.5%) in the HadCM3 model.

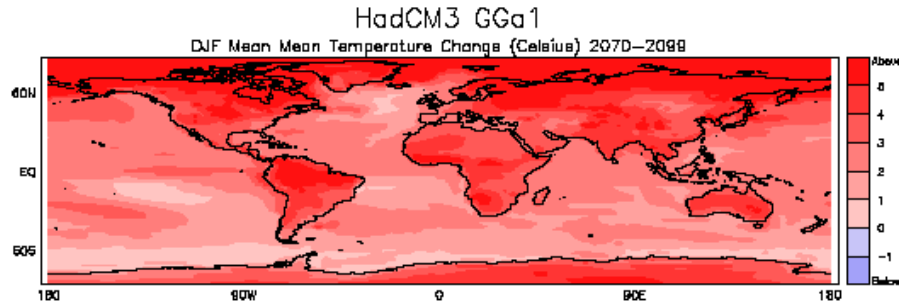


Figure 6.41. Output of the HadCM3 coupled atmosphere-ocean general circulation model showing the differences between present and projected surface temperature by the end of the 21st Century. URL: <http://www.cru.uea.ac.uk/>

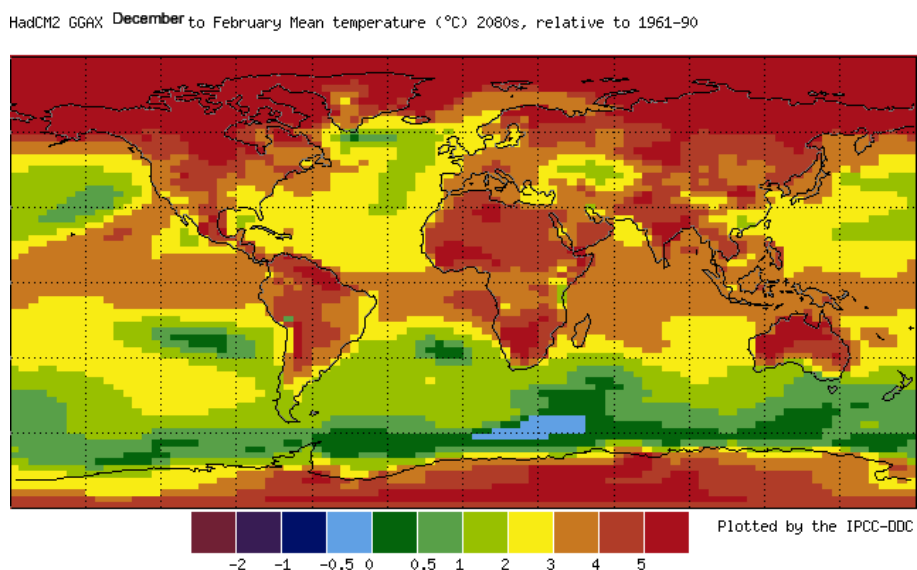


Figure 6.42. Output of the HadCM2 coupled atmosphere-ocean general circulation model showing the differences between mean temperatures from 1961-1990 and projected surface temperature by 2080. URL: <http://www.cru.uea.ac.uk/>

Although the initial process of penitentes formation is not yet well understood, they seem to start at the level when the uppermost layer surface energy balance becomes zero or negative. This is associated to the formation of surface crust subsurface processes of melting, hoar formation and water vapor transport (Ozeki and Akitaya 1996). This fact is confirmed by modelling results and direct observations, both in the Andes and under anticyclonic conditions in the Alps. In the Andes, modelled energy balance for

the uppermost surface layer becomes zero at an approximate height of 3800 m, as shown in Figure 6.43, the same altitude where the first penitentes and micropenitentes were observed. In the Alps, extensive areas covered in a mixture of radiative crust and small penitentes were observed by the author in the winter 2003-2004 after a long spell of stable, sunny and moderately cold weather. The phenomenon was widespread in the Mont Blanc massif and in the Berner Oberland at heights around 2800 m a.s.l. Once penitentes form, there is a feedback mechanism (increasing cooling due to increased roughness, solar trap) that makes them more stable, even under a changing meteorological situation. Thus initial conditions are probably the most important factor in the generation of these ablation forms. From the climatic models we see that temperature is likely to rise about four degrees during the ablation season in the Central Andes by the end of the 21st century. The result will be an upward migration of the line of penitentes between 400 and 600 m in height. Given the effect of penitentes in snow preservation, and the fact that they occurred at the heights where the largest volumes of ice are located in the central Andes, the consequences are likely to be enhanced ablation of the glaciers of the Dry Central Andes, the disappearance of some small glaciers at lower altitudes and the faster depletion of water resources.

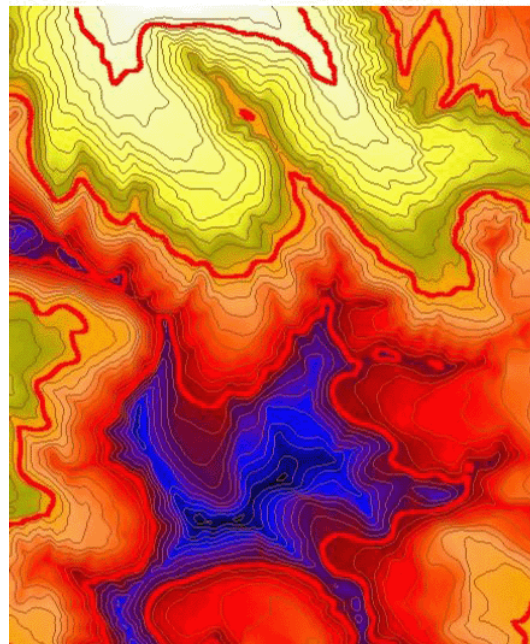
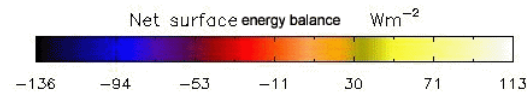


Figure 6.43. Uppermost surface layer net energy balance at Juncal Norte Glacier on the day of the year 335 (1st December). Thick contours are 3000 m, 4000 m and 5000 m, The net energy balance becomes negative at about 3800 m, the height where first penitentes were observed.

Chapter 7

Conclusions and future work

The unique characteristic of the snow cover in the Central Andes is the presence of penitentes. These pinnacles of snow and ice preclude the application of standard energy balance and melt models and require a more sophisticated treatment of the snow surface microtopography in the implementation of distributed energy balance models.

The work carried out for this thesis represents a contribution to the available meteorological data in the Central Andes. Although the contribution is modest in absolute terms it is important in relative ones, given the general paucity of data in the region. These data together with data collected in the Alps were used to test the suitability of models to evaluate the snow surface energy balance and its components. Solar radiation is the variable the modelling of which seems more reliable for clear skies, in the stable climatic conditions in the Dry Central Andes. However, determination of cloud cover extension and frequency remains an unsolved problem. The maximum uncertainty is the estimation of turbulent fluxes and the computation of roughness lengths under variable winds. Despite these limitations this model is a useful approach, given the intense solar radiation in the region, which is the main contribution to the energy balance, and the abundance of clear skies during the ablation season.

Several tools were developed to improve the application of spatially distributed energy balance models. The first of these tools is a set of mathematical algorithms applied to digital elevation models to derive terrain parameters such as gradient (slope and aspect), horizon configuration (skyview factor), sun position and shading. These algorithms are particularly suitable for surfaces of high and variable relief such as mountainous terrain. They minimize the area under evaluation, keeping extreme slope values with minimum smoothing. This is important in cases where thresholds play an important role, such as in slope stability assessment or avalanche forecasting. The vectorial approach allows simple treatment of otherwise difficult geometries and terrain characteristics such as overhanging surfaces. The main advantages of the algorithms described are the facility to operate vectors, the consistency of vector

representation for all the procedures involved, easier conceptual visualisation in three dimensions and optimisation of array handling capabilities in computer languages, which results in a fast and efficient implementation. They can be used to model overhanging surfaces, such as penitentes. Therefore they constitute the most realistic approach to the numerical treatment of this problem.

The second tool consists of two complementary techniques. The first one is the georeferencing of terrestrial photography, a flexible and inexpensive remote sensing tool that has potential applications in many environmental and monitoring fields, such as snow mapping, vegetation surveys, erosion monitoring, geomorphological mapping and visualisation in GIS; it could also improve previous applications of photography to land cover mapping and monitoring (e.g. Christiansen 2001). It provides an economical tool to assess temporal variation of land cover properties at a high temporal resolution, with a spatial resolution and accuracy limited only by the scale and quality of the available digital elevation models. The second complementary technique is a simple, yet effective, way of estimating the distribution of snow surface albedo from one single reference measurement using terrestrial photography. The input of a map of surface albedo with high temporal resolution is likely to improve the output of distributed snow energy balance models. The full development of this technique was achieved after the field campaign in the Andes, and thus it was only of limited application there, but its potential use is demonstrated by satisfactory results on two Alpine glaciers. Although the tool is useful to estimate snow cover extension and snow change in the Andes, at this stage it is not suitable for the albedo estimation of penitente snow. The reason is the partial visibility of penitentes troughs from an oblique perspective.

Finally, we have seen that the climatic characteristics of the Dry Central Andes – low humidity and high solar radiation inputs in stable summers coupled with high evaporation rates and strong radiative cooling – results in a unique snow ablation morphology: penitentes. Modelling and field data suggest that any changes in the meteorological conditions during the initial stages of growth of penitentes early in the ablation season, for example, increased humidity, longwave radiation or stronger winds may suppress or hinder their formation. Since the growth of penitentes is sustained by a positive feedback mechanism, the consequences of a small change in meteorological conditions may result in a disproportionate change in overall ablation. Modelling work suggests that penitentes enhance conservation of snow cover and that a consequence of their loss might be increased ablation over the whole season, decreased glacier mass balance and faster depletion of water resources. Given the critical nature of snow and ice melt in relation to water resources for human consumption and agricultural resources in the Central Andes, any potential change is worthy of further research.

7.1 Future work

A logical step forward is moving from energy balance modelling to mass balance modelling, which has the additional problem of calculating the distribution and amount of precipitation in the Andes. Direct measurement of flow discharge associated with energy balance studies would permit the development

and better validation of melt models suitable for application to areas where the surface energy balance is altered by the presence of penitentes. This task is important not only from a scientific perspective but also for its direct social and economical implications, as in these areas mountains, glaciers and snow cover play a vital role as water reservoirs.

It would be desirable to assess the suitability of general circulation models, coupled with satellite observation, to model the cloud cover, its spatial and temporal distribution, type, and frequency; in this way the modelling of incoming short-wave and long-wave radiation could be improved. Downscaling these GCMs to the appropriate resolution over such a complicated orography as the Andes is not expected to be a trivial task. A detailed measurement of ablation or the direct measurement of turbulent fluxes is desirable to improve the modelling of energy interchange between the atmosphere and the snow surface covered by penitentes.

The development of the remote sensing photographic technique to date has some limitations due to the limited spectral sensitivity of the photographic film and the uncertainties introduced by the anisotropy of the snow albedo. These limitations could be overcome using digital spectral photography and building suitable bidirectional reflectance distribution functions for the observed spectral bands.

The actual implications and extent of any climatic change in the region can not be fully evaluated without understanding the initial processes of snow ablation that leads to the formation of penitentes. This understanding could be improved by the replication of these processes in a cold laboratory under controlled circumstances and the rigorous testing of different hypotheses about their formation.

The above mentioned hypotheses are at this moment at a very speculative stage. However, from direct observation and modelling results it seems that initial stage of penitentes formation is associated to the formation of sun (or radiative) crust at the snow surface. This process occurs when surface energy balance is zero or negative, but intense solar radiation penetrates underneath the surface, which produces subsurface melting. Water then refreezes near the surface, forming a thin crust that can remain for days. The actual crust can form by regelation of liquid water or by sintering of granular snow. Even if sublimation takes place on the surface of the crust, water vapour from the subsurface snow migrates to the crust layer where it refreezes maintaining the crust for a longer time (Ozeki and Akitaya 1996). Underneath the crust a vertical arrangement of snow crystal and structures up to a few cm tall and a few mm wide can be observed. The exact formation is yet unclear, but probably it is similar to the formation of deep hoar. Once the surface crust disappears these vertical structures are further modelled by direct sunlight, leading to the formation of micropenitentes first and later to the growth of full size penitentes as explained in section 2.3.1. It would be necessary to evaluate the propagation of direct sunlight through the crust, which presents a random distribution of density, and in some cases pores of the size of a snow grain. A directional forcing, such as the daily path of sun rays upon this material of randomly variable density and therefore light transmittance, may have a shaping effect on the subsurface layer. Areas of repeated (through a daily cycle) differential illumination may generate differential distribution of temperature and vapour pressure, leading to different rates of subsurface ablation and vapour migration,

7.1. Future work

that can be influence the formation of this subsurface structures. The repeated observation of sun crust simultaneously to the formation of penitentes, both in the Andes and the Alps, and the likelihood of the process outlined here makes worth pursuing this line of research.

Appendix A

Meteorological data collected on Juncal Norte glacier (32.986 S, 69.956 W) from 30 November to 11 DEcember 2000 and in Loma Larga glacier (33.6917 S, 70.0 W) from 22 January to 22 February 2001.

For the calculation of dew point, Jacobson (1999) formulation was followed:

Solving for Bolton (1980) in Jacobson (1999, 2.62) dew point in K is:

$$T_d = (4880.357 - 29.66 * \log e_0) / (19.48 - \log e_0) \quad (\text{A.1})$$

where the actual vapour pressure is $e_0 = e^* RH$, and e^* is saturated vapour pressure computed following Lowe's (1977) polynomials (Equation 3.30), and RH is relative humidity from 0.0 to 1.0.

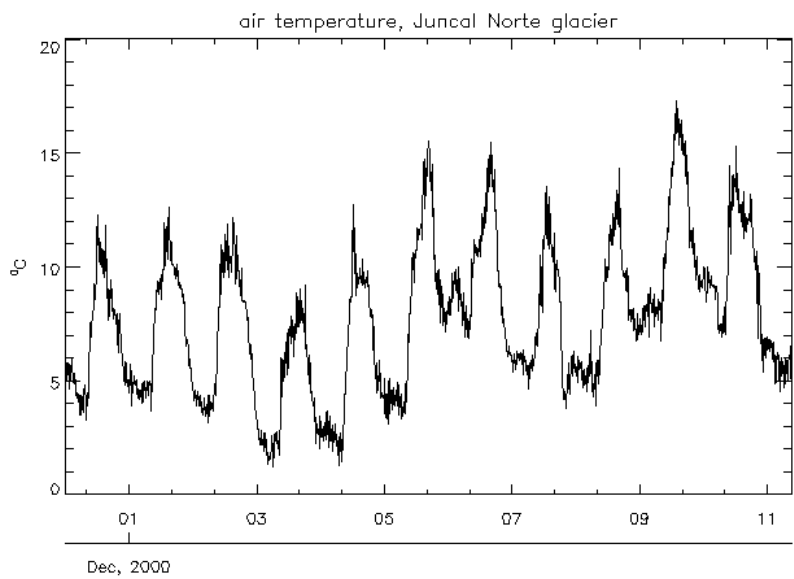


Figure A.1. Air temperature measured on Juncal Norte glacier at 3335 m.

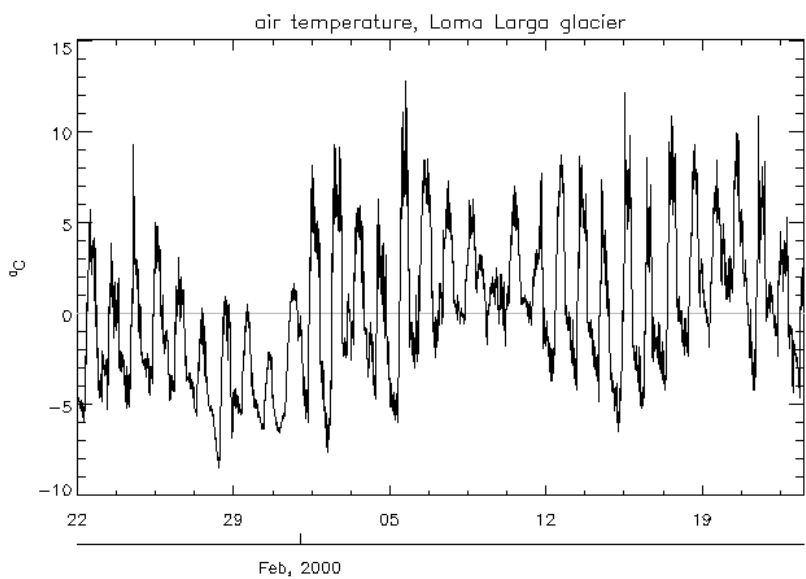


Figure A.2. Air temperature measured on Loma Larga glacier at 4667 m.

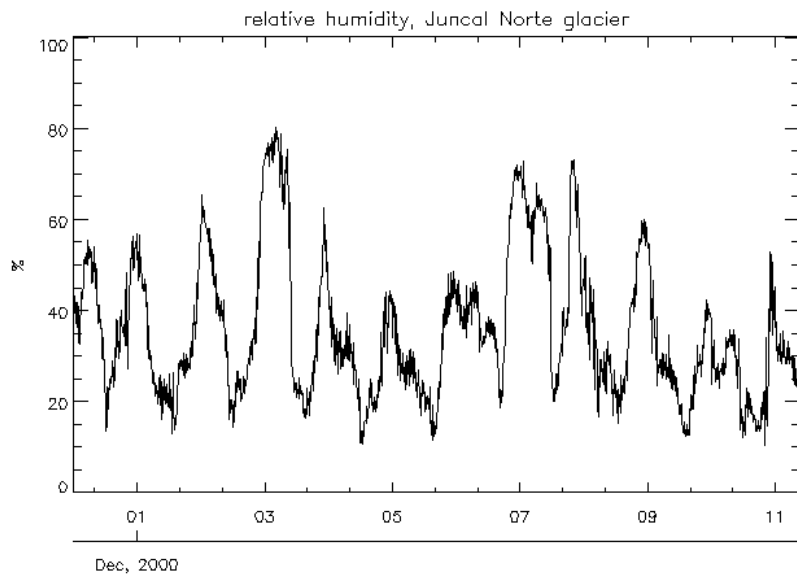


Figure A.3. Relative humidity measured on Juncal Norte glacier at 3335 m.

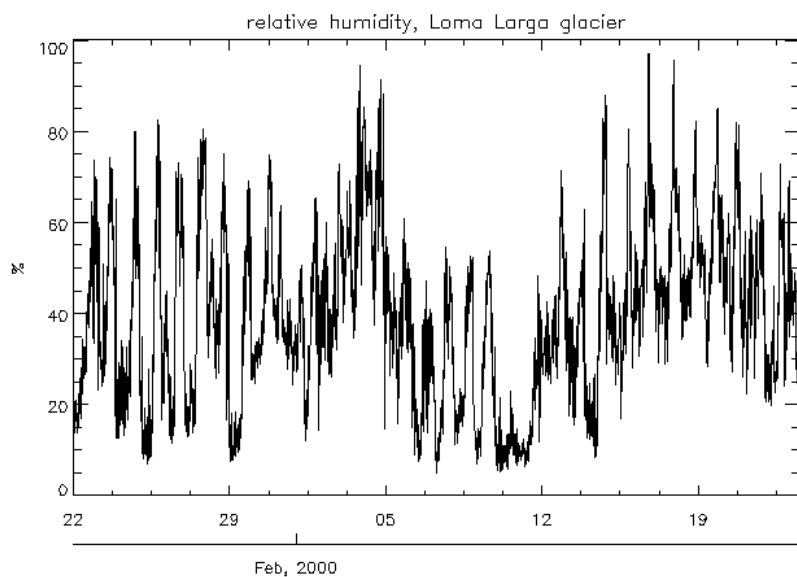


Figure A.4. Relative humidity measured on Loma Larga glacier at 4667 m.

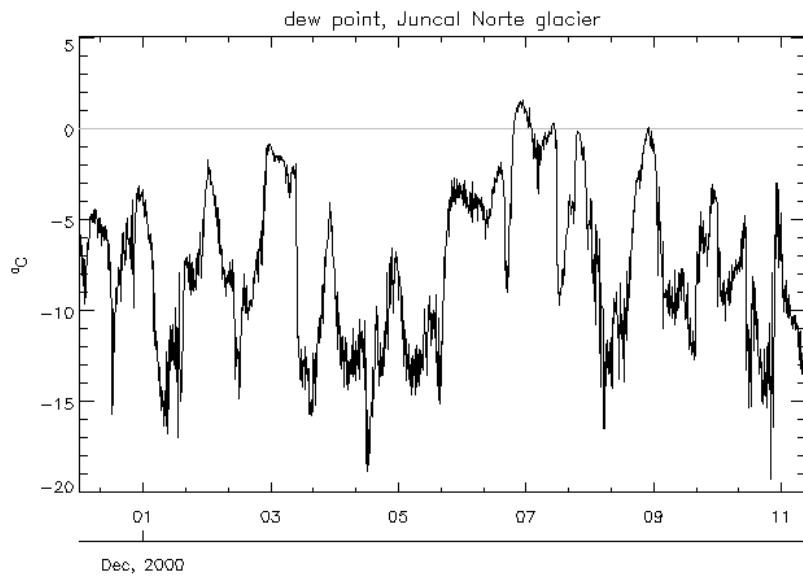


Figure A.5. Dew point calculated according to Jacobson (1999) 2.56 on Juncal Norte glacier at 3335 m.

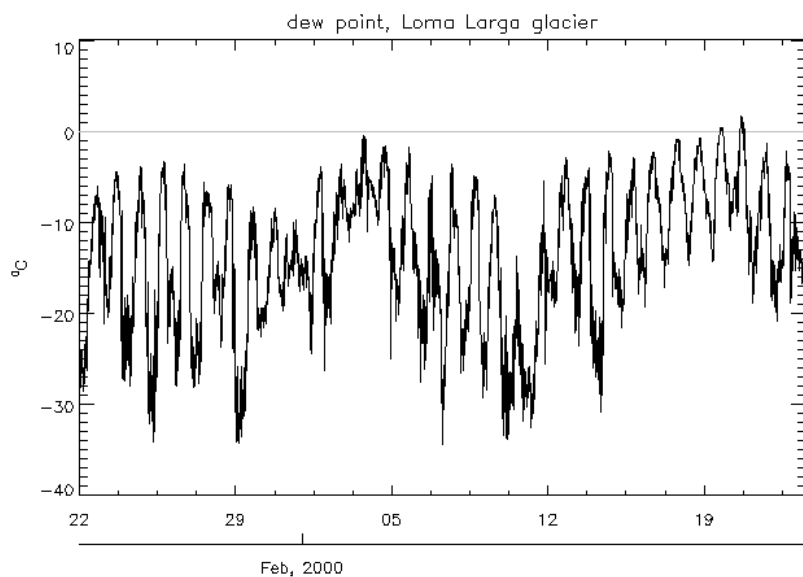


Figure A.6. Dew point calculated according to Jacobson (1999) 2.56 on Loma Larga glacier at 4667 m.

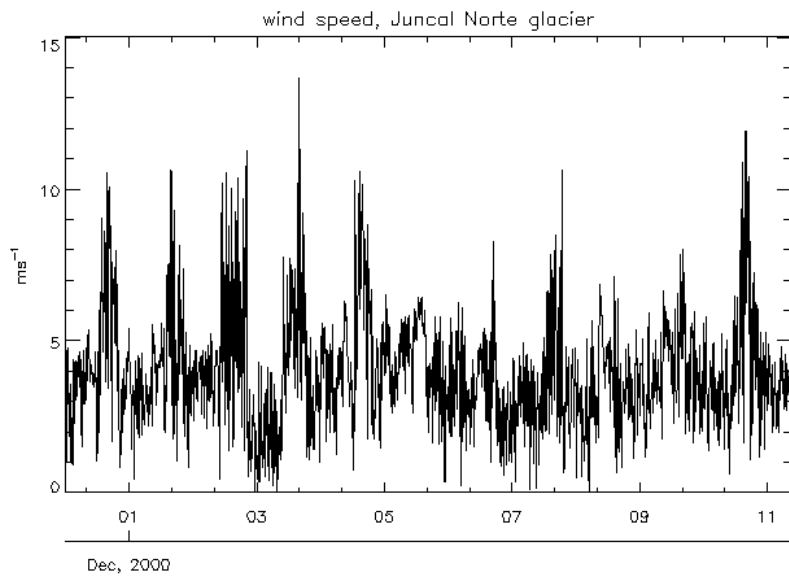


Figure A.7. Wind speed measured on Juncal Norte glacier at 3335 m.

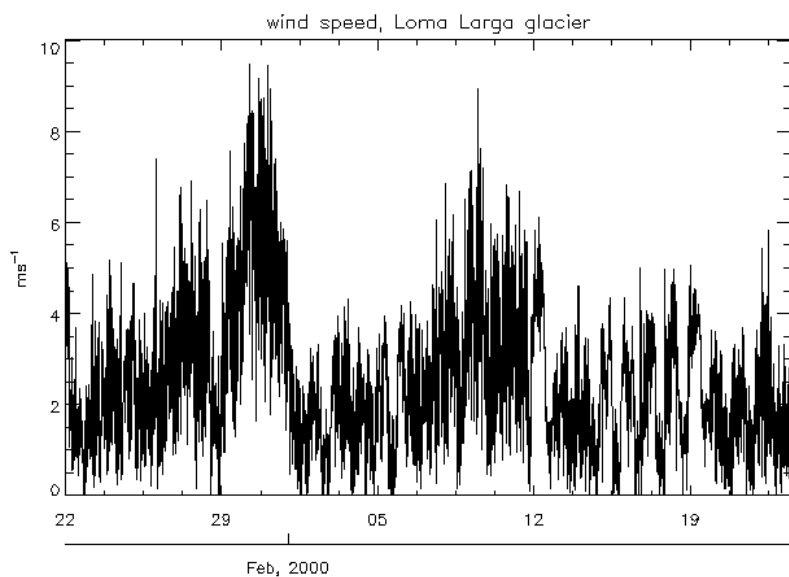


Figure A.8. Wind speed measured on Loma Larga glacier at 4667 m.

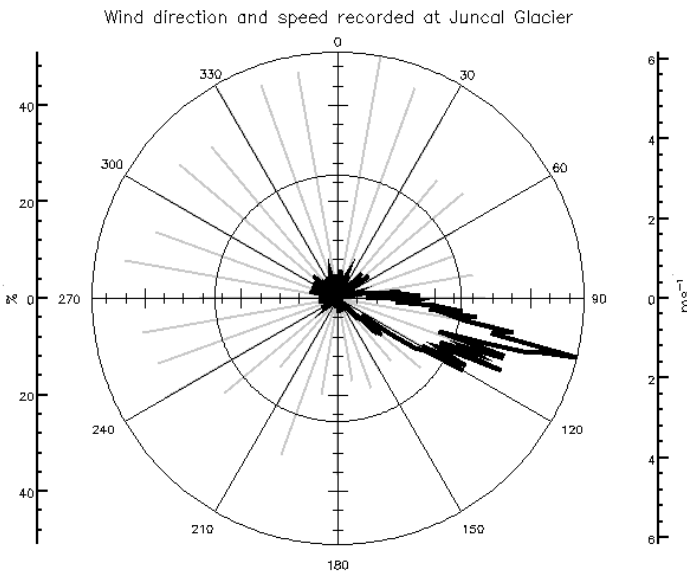


Figure A.9. Wind rose of relative frequency for all the measuring period (day 335 to 346) on Juncal Norte glacier at 3335 m a.s.l. Grey lines indicate wind mean speed for every radial sector. The maximum frequency follows the orientation of the lower section of glacier, as can be seen in Figure 2.2 This figure is repeated from Figure 6.10 for completeness.

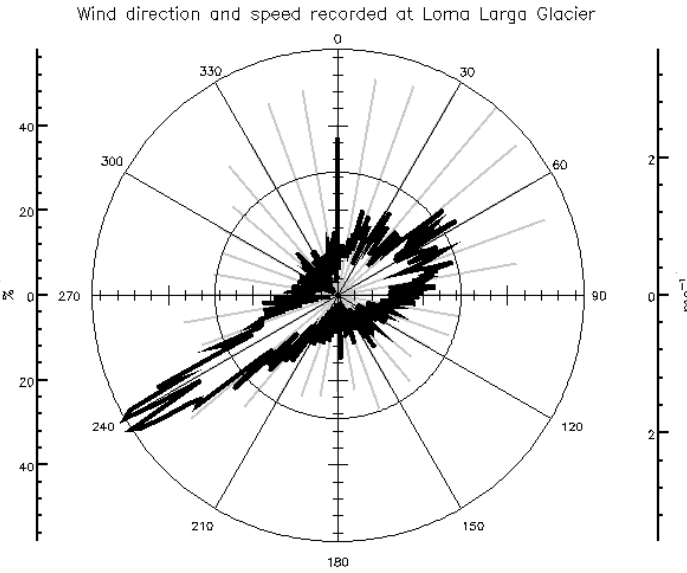


Figure A.10. Wind rose of relative frequency for all the measuring period (day 22 to 53) on Loma Larga glacier at 4667 m. Grey lines indicate wind mean speed for every radial sector. The main orientation of the glacier is East–West and the predominant winds in this case seems to be from the valley, the northeast component of the glacier winds may be influenced by the more extent snow cover of the south-facing slopes, to the north of the AWS. This figure is repeated from Figure 6.11 for completeness.

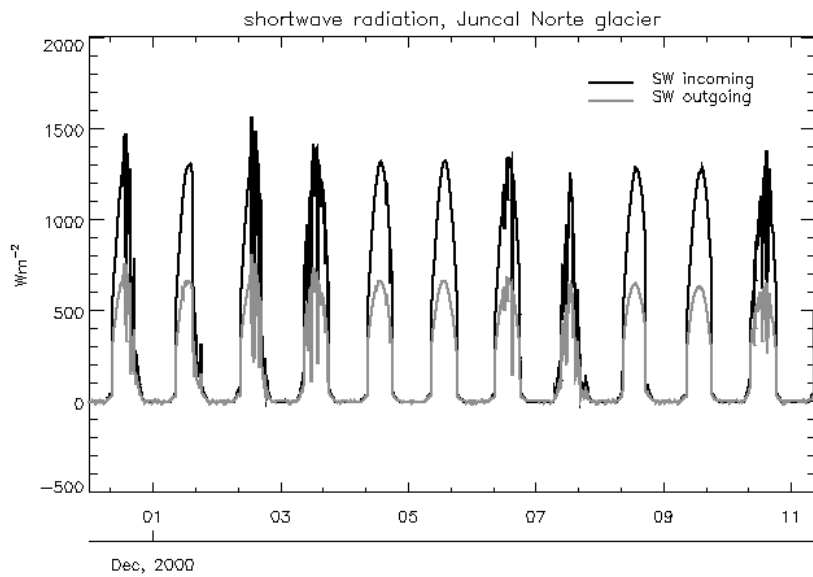


Figure A.11. Shortwave incoming and outgoing solar radiation measured on Juncal Norte glacier at 3335 m.

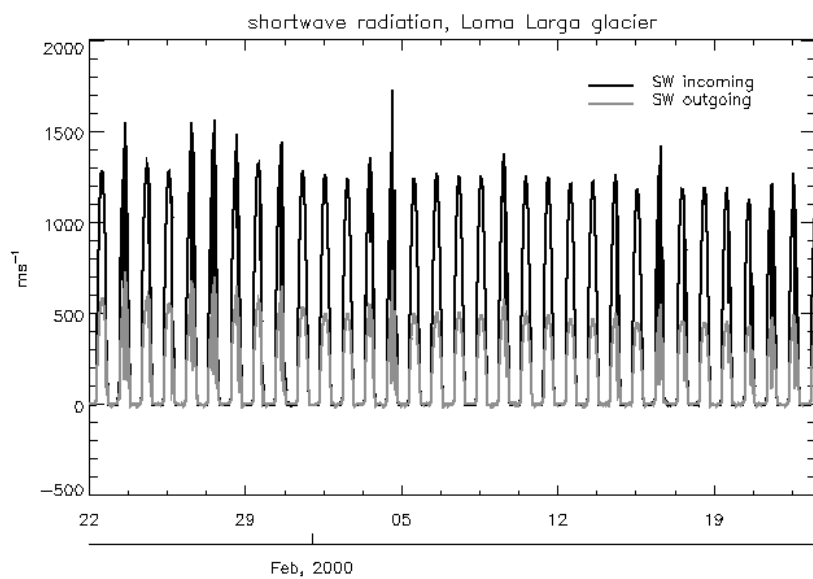


Figure A.12. Shortwave incoming and outgoing solar radiation measured on Loma Larga glacier at 4667 m.

Bibliography

- Aizen, V. B., Aizen, E. M., Dozier, J., Melack, J. M., Sexton, D. D. and Nesterov, V.: 1997, Glacial regime of the highest Tien Shan Mountain, Pobeda–Khan Tengry Massif, *Journal of Glaciology* **43**(145), 503–512.
- Amstutz, G. C.: 1955, On the formation of snow penitentes, *Journal of Glaciology* **3**(24), 304–311. number and pages not sure.
- Andreas, E. L.: 1986, A new method of measuring the snow surface temperature, *Cold Regions Science and Technology* **12**(12), 139–156.
- Andreas, E. L.: 1987, A theory for the scalar roughness and the scalar transfer coefficients over snow and sea ice, *Boundary layer Meteorology* **38**, 159–184.
- Arnold, N. S., Willis, I. C., Sharp, M. J., Richards, K. S. and Lawson, M. J.: 1996, A distributed surface energy–balance model for a small valley glacier, *Journal of Glaciology* **42**(140), 77–89.
- Aschenwald, J., Leighter, K., Tasser, E. and Tappeiner, U.: 2001, Spatio-temporal landscape analysis in mountainous terrain by means of small format photography: a methodological approach, *IEEE Transactions on Geoscience and Remote Sensing* **39**(4), 885–893.
- Atkinson, K. B. (ed.): 1996, *Close range photogrammetry and machine vision*, Whittles Publishing, Caithness, Scotland.
- Barry, R. G.: 1992, *Mountain weather and climate*, Routledge, London.
- Becht, M.: 1991, Schneehydrologische Untersuchungen am Pico de Teide (Teneriffa) (Snow hydrology at Pico de Teide, Tenerife), *Erdkunde* **4**, 264–276.
- Berk, A., Bernstein, L. S. and Robertson, D. C.: 1989, MODTRAN: A Moderate Resolution Model for LOWTRAN 7, *Technical Report GL-TR-89-012*, Air Force Geophysics Laboratory.
- Betterton, M. D.: 2001, Theory of structure formation in snowfields motivated by penitentes, suncups, and dirt cones, *Physical Review E* **63**(056129), 12 pages.
- *<http://prola.aps.org/>

BIBLIOGRAPHY

- Bintanja, R.: 1996, The parameterization of shortwave and longwave radiative fluxes for use in zonally averaged climate models, *Journal of Climate* **9**, 439–454.
- Bird, R. E. and Hulstrom, R. L.: 1981a, Review, evaluation and improvements of direct irradiance models, *Trans. ASME J. Solar Energy Eng.* **103**, 182–192.
- Bird, R. E. and Hulstrom, R. L.: 1981b, A simplified clear sky model for direct and diffuse insolation on horizontal surfaces, *Technical Report SERI/TR-642-761*, Solar Research Institute, Golden, Colorado.
- Bolton, D.: 1980, The computation of equivalent potential temperature, *Monthly Weather Review* **108**, 1046–1053.
- Bourges, B.: 1985, Improvement in solar declination computation, *Solar Energy* **35**(4), 367–369.
- Brandt, R. and Warren, S.: 1993, Solar-heating rates and temperature profiles in Antarctic snow and ice, *Journal of Glaciology* **39**(131), 99–110.
- Brock, B. W. and Arnold, N. S.: 2000, A spreadsheet-based (microsoft excel) point surface energy balance model for glacier and snow melt studies, *Earth Surface Processes and Landforms* **25**(6), 649–658.
- Brock, B. W., Willis, I. C. and Sharp, M. J.: 2000, Measurements and parameterization of albedo variations at Haut Glacier d'Arolla, Switzerland, *Journal of Glaciology* **46**(155), 675–688.
- Brock, B. W., Willis, I. C., Sharp, M. J. and Arnold, N. S.: 2000, Modelling seasonal and spatial variations in the surface energy balance of Haut Glacier d'Arolla, Switzerland, *Annals of Glaciology* **31**, 53–62.
- Brun, E., Martin, E., Gendre, V. S. C. and Coleou, C.: 1989, An energy and mass model of snow cover suitable for operational avalanche forecasting, *Journal of Glaciology* **35**(121), 333–342.
- Brutsaert, W.: 1982, *Evaporation into the atmosphere : theory, history, and applications*, 1984 edn, Reidel, Dordrecht.
- Burrough, P. A.: 1986, *Principles of Geographical Information Systems for Land Resources Assessment*, Oxford University press, New York.
- Businger, J. A. and Yaglom, A. M.: 1971, Introduction to Obukhov's paper on 'Turbulence in an atmosphere with non-uniform temperature', *Boundary Layer Meteorology* **2**, 3–6.
- Chang, K. and Tsai, B.: 1991, The effect of DEM resolution on slope and aspect mapping, *Cartography and Geographic Information Systems* **18**(1), 69–77.
- Christiansen, H.: 2001, Snow-cover depth, distribution and duration data from northeast Greenland obtained by continuous automatic digital photography, *Annals of Glaciology* **32**, 102–108.

BIBLIOGRAPHY

- Cline, D. W.: 1997, Snow surface energy exchanges and snowmelt at a continental midlatitude Alpine site, *Water Resources Research* **33**(4), 689–701.
- Cooper, M. A. R. and Robson, S.: 1996, Theory of close range photogrammetry, in K. B. Atkinson (ed.), *Close range photogrammetry and machine vision*, Whittles Publishing, Caithness, Scotland.
- Corripio, J. G.: 2000, Snow surface albedo estimation using 35 mm terrestrial photography, *Technical report*, Kodak (Research and Development), Harrow, England.
- Corripio, J. G.: 2001, Snow surface albedo estimation using 35 mm terrestrial photography, *Geophysical Research Abstracts, abstracts of the European Geophysical Society 26th General Assembly, Nice, France 25–30 March 2001*, Vol. 3.
*<http://www.copernicus.org/EGS/egsga/nice01/programme/abstracts/aai5922.pdf>
- Corripio, J. G.: 2003, Vectorial algebra algorithms for calculating terrain parameters from DEMs and the position of the sun for solar radiation modelling in mountainous terrain, *International Journal of Geographical Information Science* **17**(1), 1–23.
- Corripio, J. G. and Purves, R. S.: 2003, Energy balance of high altitude glacierised basins in the Central Andes: climatic and hydrological aspects, in D. Collins, C. de Jong and R. Ranzi (eds), *Climate and Hydrology in Mountain Areas*, Springer, London. Submitted.
- Corripio, J., Strasser, U., Burlando, P., Funk, M., Pellicciotti, F. and Brock, B.: 2002, Comparison of a time series of snow albedo fields derived from ageing curve parameterization and 35mm terrestrial photography for Haut Glacier d'Arolla, Switzerland., *Geophysical Research Abstracts, abstracts of the European Geophysical Society 27th General Assembly, Nice, France, 21–26 April, 2002*, Vol. 4.
*<http://www.cosis.net/abstracts/EGS02/00138/EGS02-A-00138-1.pdf>
- Coulson, K. L.: 1959, Characteristics of the radiation emerging from the top of a rayleigh atmosphere, *Planetary and Space Science* pp. 256–284.
- Croitoru, A. and Ethrog, U.: 2001, Photo orientation under unstable conditions: a robust approach using range ratios, *Photogrammetric Record* **17**(97), 63–87.
- Dakhal, A. M., Amada, T. and Aniya, M.: 2000, Landslide hazard mapping and its evaluation using GIS: an investigation of sampling schemes for a grid-cell based quantitative method, *Photogrammetric Engineering and Remote Sensing* **66**(8), 981–989.
- Darwin, C.: 1839, *Journal of researches into the geology and natural history of the various countries visited by H. M. S. Beagle, under the command of Captain Fitz Roy, R.N., 1832 to 1836*, H. Colburn, London.
- de la Casinière, A. C.: 1974, Heat exchange over a melting snow surface, *Journal of Glaciology* **13**(67), 55–72.

BIBLIOGRAPHY

- Denby, B. and Greuell, W.: 2000, The use of bulk and profile methods for determining surface heat fluxes in the presence of glacier winds, *Journal of Glaciology* **46**(154), 445–452.
- Dilley, A. C. and O'Brien, M. O.: 1998, Estimating downward clear sky long-wave irradiance at the surface from screen temperature and precipitable water, *Quarterly Journal of the Royal Meteorological Society* **124**(549), 1391–1401.
- Dozier, J., Bruno, J. and Downey, P.: 1981, A faster solution to the horizon problem, *Computers & Geosciences* **7**, 145–151.
- Dozier, J. and Frew, J.: 1990, Rapid calculation of terrain parameters for radiation modelling from digital elevation data, *IEEE Transactions on Geoscience and Remote Sensing* **28**(5), 963–969.
- Dozier, J., Schneider, S. R. and McGinnis, D. F.: 1981, Effect of grain size and snowpack water equivalence on visible and near-infrared satellite observations of snow, *Water Resources Research* **17**(4), 1213–1221.
- Dubayah, R.: 1992, Estimating net solar radiation using Landsat Thematic Mapper and digital elevation data, *Water Resources Research* **28**(9), 2469–2484.
- Dubayah, R. and Rich, P.: 1995, Topographic solar radiation models for GIS, *International Journal of Geographical Information Systems* **9**(4), 405–419.
- Duguay, C. R.: 1995, An approach to the estimation of surface net radiation in mountain areas using remote sensing and digital terrain data, *Theoretical and Applied Climatology* **52**(1-2), 55–68.
- Dunne, J., Elmore, D. and Muzikar, P.: 1999, Scaling factors for the rates of production of cosmogenic nuclides for geometric shielding and attenuation at depth on sloped surfaces, *Geomorphology* **27**(1-2), 3–11.
- Dyurgerov, M.: 2002, Glacier mass balance and regime: Data of measurements and analysis, in M. Meier and R. Armstrong (eds), *INSTAAR Occasional Paper No. 55*, Institute of Arctic and Alpine Research, University of Colorado, Boulder, CO. Distributed by National Snow and Ice Data Center, Boulder, CO.
*http://instaar.colorado.edu/other/download/OP55_glaciers.pdf
- Espizúa, L.: 1986, Fluctuations of the Río Plomo glaciers, *Geografika Annaler* **68**(A), 317–327.
- ESRI: 2000, Arc Info online documentation ArcDoc Version 8.0.2. Environmental Systems Research Institute technical documentation, Redlands, California.
- Evans, I. S.: 1980, An integrated system of terrain analysis and slope mapping, *Zeitschrift für Geomorphologie Suppl-Bd* **36**, 274–295.
- Fiume, E. L.: 1989, *The mathematical structure of raster graphics*, Academic Press, Boston.

BIBLIOGRAPHY

- Foley, J. D., van Dam, A., Feiner, S. K. and Hughes, J. F.: 1990, *Computer graphics, principles and practice*, Adison-Wesley, Reading, Massachusetts.
- Fröhlich, C. and Lean, J.: 1998, The sun's total irradiance: Cycles, trends and climate change uncertainties since 1976, *Geophysical Research Letters* **25**, 4377–4380.
- Fryer, J. G.: 1996, Camera calibration, in K. B. Atkinson (ed.), *Close range photogrammetry and machine vision*, Whittles Publishing, Caithness, Scotland.
- Gao, J.: 1997, Resolution and accuracy of terrain representation by grid DEMs at a micro-scale, *International Journal of Geographical Information Science* **11**(2), 199–212.
- Georges, C. and Kaser, G.: 2002, Ventilated and unventilated air temperature measurements for glacier-climate studies on a tropical high mountain site, *Journal of Geophysical Research*. Accepted.
- Goldstein, H.: 1980, *Classical mechanics*, 2 edn, Addison-Wesley, Reading, Mass. 672 p.
- Gordon, C., Cooper, C., Senior, C. A., Banks, H., Gregory, J. M., Johns, T. C., Mitchell, J. F. and Wood, R. A.: 2000, The Simulation of SST, Sea Ice Extents and Ocean Heat Transports in aversion of the Hadley Centre Coupled Model without Flux Adjustments, *Climate Dynamics* **16**, 147–168.
- Gradshteyn, I. S. and Ryzhik, I. M.: 1980, *Tables of Integrals, Series and Products*, Academic Press, New York.
- Greuell, W.: 2002, Validation of satellite derived surface albedos with measurements from a helicopter, *European Geophysical Society 27th General Assembly, Nice, France, 21–26 April, 2002*.
*<http://www.cosis.net/abstracts/EGS02/00689/EGS02-A-00689.pdf>
- Greuell, W. and de Ruyter de Wildt, M.: 1999, Anisotropic reflection by melting glacier ice: measurements and parameterizations in Landsat TM bands 2 and 4, *Remote Sensing of Environment* **70**, 265–277.
- Greuell, W., Knap, W. H. and Smeets, P. C.: 1997, Elevational changes in meteorological variables along a midlatitude glacier during summer, *Journal of Geophysical Research* **102**(D22), 25941–25954.
- Greuell, W. and Konzelmann, T.: 1994, Numerical modelling of the energy balance and the englacial temperature of the Greenland Ice Sheet. Calculations for the ETH-Camp location (West Greenland, 115 m a.s.l.), *Global and Planetary Change* **9**, 91–114.
- Greuell, W. and Oerlemans, J.: 1986, Sensitivity studies with a mass balance model including temperature profile calculations inside the glacier, *Zeitschrift für Gletscherkunde un Glazialgeologie Band 22*(Heft 2), 101–124.
- Greuell, W. and Smeets, P.: 2001, Variations with elevation in the surface energy balance on the Pasterze, Austria, *Journal of Geophysical Research* **106**(D23), 31,717–31,727.

BIBLIOGRAPHY

- Grover, K. D., Steven, M. D., Rondeaux, G. and Clark, J. A.: 2000, Estimating albedo from limited espectral and angular data, *International Journal of Remote Sensing* **21**(1), 155–165.
- Haeberli, W., Frauenfelder, R. and Hoelzle, M.: 2001, Glacier mass balance bulletin, World Glacier Monitoring Service. IAHS (ICSI) UNEP UNESCO WMO 2001. Digital media.
*<http://www.geo.unizh.ch/wgms/mgb/mgb6/MBB6.pdf>
- Hastenrath, S. and Koci, B.: 1981, Micro-morphology of the snow surface at the Quelccaya ice cap, Peru, *Journal of Glaciology* **27**(97), 439–444.
- Helbling, R.: 1935, The origing of the Río Plomo ice-dam, *Geographical Journal* **85**(1), 41–49.
- Hock, R.: 1998, *Modelling glacier melt and discharge*, PhD thesis, Geographisches Institut ETH, Zurich. Zürcher Geographische Schriften 70, pp. 126.
- Hock, R.: 2002, A distributed energy blance model for complex topography and its application to Storglaciären, Sweden, *Journal of Glaciology* **Submitted**.
- Hodgson, M. E.: 1995, What cell size does the computed slope/aspect angle represent?, *Photogrammetric Engineering and Remote Sensing* **65**(5), 513–517.
- Hodgson, M. E.: 1998, Comparison of angles from surface slope/aspect algorithms, *Cartography and Geographic Information Systems* **25**(3), 173–185.
- Hoelzle, M. and Haeberli, W.: 1999, World Glacier Inventory, World Glacier Monitoring Service and National Snow and Ice Data Center for Glaciology, Boulder, CO. Digital media.
*http://www-nsic.colorado.edu/NOAA/wgms_inventory/
- Horn, B. K. P.: 1981, Hillshading and the reflectance map, *Proceedings of the IEEE* **69**(1), 41–47.
- Hoyt, D. V.: 1978, A model for the calculation of solar global insolation, *Solar energy* **21**(1), 27–35.
- Hulton, N., Sugden, D. and Purvess, R.: 2002, Role of icesheet/climate models in Quaternary research: response to G. Wenzens,, *Quaternary Science Reviews* . In press.
- Iqbal, M.: 1983, *An Introduction to Solar Radiation*, Academic Press, Toronto.
- Jackson, B. and Carroll, J.: 1977, Aerodynamic roughness as a function of wind direction over asymmetric surface elements, *Boundary Layer Meteorology* **14**, 323–330.
- Jacobson, M. Z.: 1999, *Fundamentals of Atmospheric Modeling*, Cambridge University Press, Cambridge.
- Jacobson, R. E. (ed.): 1978, *The Manual of Photography*, 7th edn, Focal Press, London.
- Johns, T. C., Carnell, R. E., Crossley, J. F., Gregory, J. M., Mitchell, J. F. B., Senior, C. A., Tett, S. F. B. and Wood, R. A.: 1997, The Second Hadley Centre Coupled Ocean-Atmosphere GCM: Model description, Spinup and Validation, *Climate Dynamics* **13**, 103–134.

BIBLIOGRAPHY

- King, W. D. V. O.: 1934, The Mendoza river flood of 10–11 January 1934 – Argentina, *Geographical Journal* **85**, 321–326.
- Kirckpatrick, J. B. and Nuñez, M.: 1980, Vegetation–radiation relationships in mountainous terrain: eucalyptus dominated vegetation in the Risdon Hill, Tasmania, *Journal of Biogeography* **7**, 197–208.
- Kirkbride, M. P.: 1995, Processes of transportation, in J. Menzies (ed.), *Modern Glacial Environments. Processes, dynamics and sediments*, Butterworth–Heinemann, Oxford.
- Klok, E. J. and Oerlemans, J.: 2002, Model study of the spatial distribution of the energy and mass balance of the Morteratschgletscher, Switzerland, *International Journal of Glaciology*. Accepted.
- Knap, W. H., Brock, B. W., Oerlemans, J. and Willis, I.: 1999, Comparison of Landsat TM-derived and ground-based albedos of Haut Glacier d’Arolla, Switzerland, *International Journal of Remote Sensing* **20**(17), 3293–3310.
- Knap, W. H. and Reijmer, C. H.: 1998, Anisotropy of the reflected radiation field over melting glacier ice: measurements in Landsat TM bands 2 and 4, *Remote Sensing of the Environment* **65**, 93–104.
- Kodak: 2001, Kodak technical data: Kodak professional ektachrome films E100S and E100SW.
*<http://www.kodak.co.uk/global/en/professional/support/techPubs/e164/e164>
- Koh, G. and Jordan, R.: 1995, Sub-surface melting in a seasonal snow cover, *Journal of Glaciology* **41**(139), 474–482.
- Kondratiev, K. Y.: 1969, *Radiation in the Atmosphere*, Academic Press, New York. 912 p.
- Kotlyakov, V. M. and Lebedeva, I. M.: 1974, Nieve and ice penitentes, their way of formation and indicative significance, *Zeitschrift für Gletscherkunde und Glazialgeologie* **Bd X**, 111–127.
- Kumar, L. and Skidmore, A. K.: 2000, Radiation–vegetation relationships in a eucalyptus forest, *Photogrammetric Engineering and Remote Sensing* **66**(2), 193–204.
- Kumar, L., Skidmore, A. K. and Nowles, E. K.: 1997, Modelling topographic variation in solar radiation in a GIS environment, *GIS International* pp. 475–497.
- Leiva, J. C., Lenzano, L. E., Cabrera, G. A. and Suarez, J. P.: 1989, Variations of the Río Plomo glaciers, Andes Centrales Argentinos, in J. Oerlemans (ed.), *Glacier fluctuations and climate change*, Kluwer, Dordrecht.
- Lettau, H.: 1969, Note on aerodynamic roughness-parameter estimation on the basis of roughness-element description, *Journal of Applied Meteorology* **8**, 828–832.
- Liniger, H., Weingartner, R. and Grosjean, M. (eds): 1998, *Mountains of the World – Water Towers for the 21st Century*, Mountain Agenda for the Commission on Sustainable Development (CSD), University of Bern.

BIBLIOGRAPHY

- Lliboutry, L.: 1954a, Le Massif du Nevado Juncal ses penitentes et ses glaciers, *Revue de Géographie Alpine* **42**, 465–495.
- Lliboutry, L.: 1954b, The origin of penitentes, *Journal of Glaciology* **2**(15), 331–338.
- Lliboutry, L.: 1956, *Nieve y glaciares de Chile. Fundamentos de glaciología*, Universidad de Chile, Santiago de Chile.
- Lliboutry, L.: 1965, *Traité de Glaciologie*, Vol. I & II, Masson, Paris.
- Lliboutry, L.: 1998, Glaciers of the Dry Andes, in R. S. J. Williams and J. G. Ferrigno (eds), *Satellite Image Atlas of Glaciers of the World SOUTH AMERICA*, United States Geological Survey Professional Paper 1386–I.
*<http://pubs.usgs.gov/prof/p1386i/index.html>
- Lowe, P. R.: 1977, An approximating polynomial for the computation of saturation vapor pressure, *Journal of Applied Meteorology* **16**, 100–103.
- Mächler, M.: 1983, *Parameterization of solar radiation under clear skies*, Master's thesis, University of British Columbia, Vancouver, Canada.
- Mannstein, H.: 1985, The interpretation of albedo measurements of a snowcovered slope, *Archiv für Meteorologie, Geophysik und Bioklimatologie* **36**(Series B), 73–81.
- Marks, D. and Dozier, J.: 1992, Climate and energy exchange at the snow surface in the alpine region of the Sierra Nevada. 2. Snow cover energy balance, *Water Resources Research* **28**(11), 3043–3054.
- Miller, A.: 1976, The climate of Chile, in W. Schwerdtfeger (ed.), *World survey of climatology. Climates of Central and South America*, Elsevier, Amsterdam.
- Milton, E. J.: 1989, On the suitability of Kodak neutral test cards as reflectance standards, *International Journal of Remote Sensing* **10**(6), 1041–1047.
- Monin, A. S. and Obukhov, A. M.: 1954, Basic laws of turbulent mixing in the ground layer of the atmosphere, *Tr. Geofiz. Instit. Akad. Nauk. S.S.R.* **24**(151), 163–187.
- Moore, I. D., Gallant, J. C., Guerra, L. and Kalma, J. D.: 1993, Modelling the spatial variability of hydrological processes using GIS, *HydroGIS 93: Applications of Geographic Information Systems in Hydrology and Water Resources Management (Proceedings of the Vienna Conference, April 1993)*, IAHS Publication no 211, International Association of Hydrological Sciences, pp. 161–169.
- Munro, D. S.: 1989, Surface roughness and bulk heat transfer on a glacier: comparison with eddy correlation, *Journal of Glaciology* **35**(121), 343–348.
- Naruse, R. and Leiva, J. C.: 1997, Preliminary study on the shape of snow penitents at Piloto Glacier, the Central Andes, *Bulletin of Glacier Research* **15**, 99–104.

BIBLIOGRAPHY

- Nautical Almanac Office: 1974, *Explanatory Supplement to the Astronomical Ephemeris and the American Ephemeris and Nautical Almanac*, HMSO, London.
- Niemelä, S., Räisänen, P. and Savijärvi, H.: 2001a, Comparison of surface radiative flux parameterizations. Part I: Longwave radiation, *Atmospheric Research* **58**, 1–18.
- Niemelä, S., Räisänen, P. and Savijärvi, H.: 2001b, Comparison of surface radiative flux parameterizations. Part II: Shortwave radiation, *Atmospheric Research* **58**, 141–154.
- Nuñez, M.: 1980, The calculation of solar and net radiation in mountainous terrain (Risdon, Tasmania), *Journal of Biogeography* **7**(2), 173–186.
- Obleitner, F.: 2000, The energy budget of snow and ice at Breidamerkurjökull, Vatnajökull, Iceland, *Boundary Layer Meteorology* **97**, 385–410.
- Obukhov, A. M.: 1946, Turbulence in an atmosphere with non-uniform temperature, *Trudy Instit. Teoret. Geofiz.: AN-S.S.S.R. No. 1*. (English translation: (1971) *Boundary Layer Meteorology* **2**, 7–29.
- Oerlemans, J.: 1986, Glaciers as indicators of a carbon dioxide warming, *Nature* **320**, 607–609.
- Oerlemans, J.: 1994, Quantifying global warming from the retreat of glaciers, *Science* **264**, 243–245.
- Oerlemans, J.: 2001, *Glaciers and climate change: A meteorologist's view*, Balkema, Lisse, the Netherlands.
- Oerlemans, J., Anderson, B., Hubbard, A., Huybretschs, P., Johannesson, T., Knap, W. H., Schmeits, M., Stroeven, A. P., van de Wal, R. S. W., Wallinga, J. and Zuo, Z.: 1998, Modelling the response of glaciers to climate warming, *Climate Dynamics* **14**, 267–274.
- Oerlemans, J. (ed.): 1989, *Glacier fluctuations and climatic change : proceedings of the Symposium on Glacier Fluctuations and Climatic Change, held in Amsterdam, 1–15 June 1987*, Kluwer Academic, Dordrecht; London.
- Oke, T. J.: 1987, *Boundary layer climates*, Methuen, London.
- Olyphant, G. A.: 1986a, The components of incoming radiation within a mid-latitude Alpine watershed during the snowmelt season, *Arctic and Alpine Research* **18**(2), 163–169.
- Olyphant, G. A.: 1986b, Longwave radiation in mountainous areas and its influence on the energy balance of alpine snowfields, *Water Resources Research* **22**(1), 62–66.
- Ozeki, T. and Akitaya, E.: 1996, Field observations of sun crust formation in Hokkaido, Japan, *Arctic and Alpine Research* **28**(2), 244–248.
- Paeschke, W.: 1937, Experimentelle Untersuchungen zum Rauhigkeits- und Stabilitätsproblem in der bodennahen Luftschicht, *Beiträge zur Physik der Freie Atmosphäre*.

BIBLIOGRAPHY

- Page, J. K. (ed.): 1986, *Prediction of solar radiation on inclined surfaces.*, Solar energy R & D in the European Community. Series F. Solar radiation data; v. 3, Dordrecht; Lancaster: Reidel for the Commission of the European Communities.
- Paltridge, G. W. and Platt, C. M. R.: 1976, *Radiative Processes in Meteorology and Climatology*, American Elsevier, New York.
- Paterson, W. S. B.: 1994, *The physics of glaciers*, Elsevier, Oxford. 3rd edition.
- Peterson, W. A., Dirmhirn, I. and Hurst, R. L.: 1985, A theoretical model to determine solar and diffuse irradiance in valleys, *Solar Energy* **35**(6), 503–510.
- Plüss, C. and Mazzoni, R.: 1994, The role of turbulent heat fluxes in the energy balance of high Alpine snow cover, *Nordic Hydrology* **25**(1-2), 25–38.
- Plüss, C. and Ohmura, A.: 1997, Longwave radiation on snow-covered mountainous surfaces, *Journal of Applied Meteorology* **36**, 818–824.
- Prandtl, L.: 1904, Über Flüssigkeitsbewegung bei sehr kleiner Reibung, *Verhandlungen des dritten Internationalen Mathematiker-Kongresses in Heidelberg vom 8 bis 13 August 1904*. (1905) (also in *Gesammelte Abhandlungen*, Vol. 2, Springer-Verlag, Berlin, 1961, pp. 575–584, English in NACA Technical Mem. No. 452).
- Prandtl, L.: 1932, Meteorologische Anwendungen der Strömungslehre, *Beitr. Phys. Fr. Atmosph.* **18**, 188–202.
- Prata, A. J.: 1996, A new long-wave formula for estimating downward clear-sky radiation at the surface, *Quarterly Journal of the Royal Meteorological Society* **122**, 1127–1151.
- Prohaska, F.: 1976, The climate of Argentina, Uruguay and Paraguay, in W. Schwerdtfeger (ed.), *World survey of climatology. Climates of Central and South America*, Elsevier, Amsterdam.
- Purves, R. S., Barton, J. S., Mackaness, W. A. and Sugden, D. E.: 1998, The development of a rule-based spatial model of wind transport and deposition of snow, *Annals of Glaciology* **26**, 197–202.
- Raupach, M. R.: 1992, Drag and drag partition on rough surfaces, *Boundary Layer Meteorology* **60**, 375–395.
- Rhodes, J. J., Armstrong, R. L. and Warren, S. G.: 1987, Mode of formation of "ablation holows" controlled by dirt content of snow, *Journal of Glaciology* **33**(114), 135–139.
- Richards, K., Sharp, M., Arnold, N., Gurnell, A., Clark, M., Tranter, M., Nienow, P., Brown, G. and Lawson, W.: 1996, An integrated approach to modelling hydrology and water quality in glacierized catchments, *Hydrological processes* **10**, 479–508.
- Ritter, N. and Ruth, M.: 1997, The GeoTiff data interchange standard for raster geographic images, *International Journal of Remote Sensing* **18**(7), 1637–1647.

BIBLIOGRAPHY

- Ritter, N. and Ruth, M.: 2000, GeoTIFF format specification. GeoTIFF revision 1.0.
*<http://www.remotesensing.org/geotiff/spec/geotiffhome.html>
- Ritter, P.: 1987, A vector-based slope and aspect generation algorithm, *Photogrammetric Engineering and Remote Sensing* **53**(8), 1109–1111.
- Robison, N.: 1966, *Solar Radiation*, Elsevier, Amsterdam.
- Roch, A.: 1954, The glaciers, snow and avalanches of Mount Everest, *Journal of Glaciology* **2**(16), 428–430.
- Ryan, B. C.: 1977, A mathematical model for diagnosis and prediction of surface winds in mountainous terrain, *Journal of Applied Meteorology* **16**(6), 571–584.
- Schwerdtfeger, W.: 1976, *World survey of climatology. Climates of Central and South America*, Elsevier, Amsterdam.
- Sicart, J. E., Ribstein, P., Wagnon, P. and Brunstein, D.: 2001, Clear-sky albedo measurements on a sloping glacier surface: a case study in the Bolivian Andes, *Journal of Geophysical Research* **106**(D23), 31,729–31,737.
- Skidmore, A. K.: 1989, A comparison of techniques for calculating gradient and aspect from a gridded digital elevation model, *International Journal of Geographical Information Systems* **3**(4), 323–334.
- Slama, C. C., Theurer, C. and Henriksen, S. W. (eds): 1980, *Manual of Photogrammetry*, American Society of Photogrammetry, Falls Church, Va. xv, 1056 p.
- Smeets, C., Duynkerke, P. and Vugts, H.: 1999, Observed wind profiles and turbulence over an ice surface with changing surface roughness, *Boundary Layer Meteorology* **92**, 101–123.
- Spencer, J. W.: 1971, Fourier series representation of the position of the sun, *Search* **2**, 172.
- Stefanovič, P. and Wiersema, G.: 1985, Insolation from digital elevation models for mountain habitat evaluation, *ITC Journal* **3**, 177–186.
- Stocks, A. M.: 1994, Mountain regions and geographical information systems, an overview, in M. F. Price and D. I. Heywood (eds), *Mountain environments and geographic information systems*, Taylor & Francis, London, pp. 1–24.
- Strasser, U., Etchevers, P. and Y., L.: 2002, Inter-comparison of two snow models with different complexity using data from an alpine site, *Nordic Hydrology* **1**, 15–26.
- Stull, R.: 1988, *An introduction to boundary layer meteorology*, Kluwer Academic, Dordrecht.
- Thekaekara, M. P.: 1973, Extraterrestrial spectral irradiance, in A. J. Drummond and M. P. Thekaekara (eds), *The Extraterrestrial Solar Spectrum*, Mount Prospect: Institute of Environmental Sciences, pp. 71–133.

BIBLIOGRAPHY

- TOMS–EP: 2001, Total Ozone Mapping Spectrometer–Earth Probe data sets.
*<http://toms.gsfc.nasa.gov/epioms/ep.html>
- Troll, C.: 1942, *Büßerschnee in den Hochgebirgen der Erde*, Patermanns Geographische Mitteilungen Ergdnzungsheft Nr. 240, Justus Perthes, Ghota.
- U.S. NOAA: 1976, *U.S. standard atmosphere, 1976*, NOAA-S/T; 76-1562, U.S. National Oceanic and Atmospheric Administration, National Aeronautics and Space Administration, United States Air Force, Washington. 227 pp.
- Varley, M. J., Beven, K. J. and Oliver, H. R.: 1996, Modelling solar radiation in steeply sloping terrain, *International Journal of Climatology* **16**, 93–104.
- Vermote, E., Tanré, D., Deuzé, J. L., Herman, M. and Morcette, J. J.: 1994, Second simulation of the satellite signal in the solar spectrum: User manual, *Technical report*, University of Maryland/Laboratoire d'Optique Atmosphérique, Lille.
- Vermote, E., Tanré, D., Deuzé, J. L., Herman, M. and Morcette, J. J.: 1997, Second simulation of the satellite signal in the solar spectrum: an overview, *IEEE Transactions on Geoscience and Remote Sensing* **35**(3), 675–686.
- Vuille, M., Hardy, D. R., Braun, C., Keimig, F. and R Bradley, R.: 1998, Atmospheric circulation anomalies associated with 1996/1997 summer precipitation events on Sajama Ice Cap, Bolivia, *Journal of Geophysical Research* **103**(D10), 11191–11204.
- Wadge, G.: 1988, The potential of GIS modelling of gravity flows and slope instabilities, *International Journal of Geographical Information Science* **2**(2), 143–152.
- Wagnon, P.: 1999, *Analyse du bilan d'énergie d'un glacier tropical . Application à la relation glacier-climat.*, PhD thesis, Laboratoire de Glaciologie et Géophysique de l'Environnement, Université Joseph-Fourier, Grenoble 1.
- Wagnon, P., Ribstein, P., Kaser, G. and Berton, P.: 1999, Energy balance and runoff seasonality of a bolivian glacier, *Global and Planetary Change* **22**, 49–58.
- Walraven, R.: 1977, Calculating the position of the Sun, *Solar Energy* **20**, 393–397.
- Wang, J., Robinson, G. J. and White, K.: 2000, Generating viewsheds without using sightlines, *Photogrammetric Engineering and Remote Sensing* **66**(1), 87–90.
- Wang, J., White, K. and Robinson, G.: 2000, Estimating surface net solar radiation by use of Landsat–5 TM and digital elevation models, *International Journal of Remote Sensing* **21**(1), 31–43.
- Warren, S. G.: 1982, Optical properties of snow, *Reviews of Geophysics and Space Physics* **20**(1), 67–89.
- Watt, A. H. and Policarpo, F.: 1998, *The computer image*, Addison–Wesley, Harlow.

- Watt, A. H. and Watt, M.: 1992, *Advanced animation and rendering techniques: theory and practice*, ACM Press: Addison-Wesley, New York.
- Weisstein, E. W.: 1999, *CRC concise encyclopedia of mathematics*, CRC publisher, London. 1969 p.
 *<http://mathworld.wolfram.com>
- Williams, L. D., Barry, R. G. and Andrews, J. T.: 1972, Application of computed global radiation for areas of high relief, *Journal of Applied Meteorology* **11**, 526–533.
- Willis, I., Arnold, N., Sharp, M., Bonvin, J. M. and Hubbard, B. P.: 1998, Mass balance and flow variations in Haut Glacier d'Arolla, Switzerland, calculated using digital terrain modelling, in S. Lane, K. Richards and J. Chandlers (eds), *Landform monitoring, modelling and analysis*, Wiley, Chichester, pp. 343–362.
- Wiscombe, W. J. and Warren, S. G.: 1980, A model for the spectral albedo of snow, I: pure snow, *Journal of the Atmospheric Sciences* **37**, 2712–2733.
- Wise, S. M.: 1998, The effect of GIS interpolation errors on the use of digital elevation models in Geomorphology, in S. Lane, K. Richards and J. Chandlers (eds), *Landform monitoring, modelling and analysis*, Wiley, Chichester.
- Workman, W.: 1914, Nieve penitente and allied formations in himalaya, or surface-forms of neve and ice created or modelled by melting, *Zeitschrift für Gletscherkunde und Glaziageologie* **8**, 289–330.
- Zevenbergen, L. W. and Thorne, C. R.: 1987, Quantitative analysis of land surface topography, *Earth Surface Processes and Landforms* **12**, 47–56.